Spring 1-1-2017

Dual Comb Spectroscopy of High Temperature Environments

Paul James Schroeder
University of Colorado at Boulder, paul.j.schroeder@colorado.edu

Dual comb spectroscopy of high temperature environments

by

Paul James Schroeder

B.S. San Diego State University, 2011

M.S. University of Colorado Boulder, 2013

A thesis submitted to the

Faculty of the Graduate School of the

University of Colorado in partial fulfillment

of the requirements for the degree of

Doctor of Philosophy

Department of Mechanical Engineering

2017

This dissertation entitled:

Dual comb spectroscopy of high temperature environments

written by Paul James Schroeder

has been approved for the Department of Mechanical Engineering

---

Professor Gregory B. Rieker (Principal Advisor)

Professor John Daily

Date: _____

The final copy of this thesis has been examined by the signatories, and we find that both the content and the form meet acceptable presentation standards of scholarly work in the above mentioned discipline.

Abstract

Schroeder, Paul James (Ph.D., Department of Mechanical Engineering)

Dual comb spectroscopy of high temperature environments

Dissertation directed by Assistant Professor Gregory B. Rieker

A frequency comb is a laser whose output is composed of many narrow linewidth, precisely spaced optical frequencies. Robust designs and dual comb interference techniques have recently enabled tooth-by-tooth resolved absorption spectroscopy in a compact and flexible package. In this work, we present both the first mobilization of a dual comb spectrometer in harsh environments and the first broadband, high-resolution investigation of high temperature water vapor lineshapes. The instrument was deployed to the basement of a 16MW natural gas turbine facility at CU Boulder to simultaneously measure H_2O and CO_2 concentrations and gas temperature in the exhaust stream. This revealed errors in the two most common spectroscopic databases used for high temperature studies, HITRAN2012 and HITEMP2010. These databases are accurate at room temperature, though their accuracy diminishes at elevated temperatures. We used the dual comb spectrometer at NIST Boulder to compare, for the first time, spectra of pure and air-broadened water at temperatures up to 1000ºC with models generated by both databases. Their data is almost entirely extracted using Voigt lineshape profiles while advanced profiles that fix problems with the Voigt have not been broadly tested at elevated temperatures. We fit the spectra from the above comparison with Voigt, Rautian, and quadratic speed dependent Voigt lineshapes to examine their effect on 232 extracted temperature-scaling exponents. Only the quadratic speed dependent Voigt produced values that validated external computations while only requiring a single exponent to fit each transition up to 1000ºC. We then utilized these fits to generate a new database of spectral parameters to increase high temperature accuracy of spectroscopic measurements. The database contains line centers, linestrengths, self-broadening coefficients, temperature-scaling exponents, and speed dependence parameters for 625 water vapor absorption transitions. Finally, we deployed the mobile spectrometer to Colorado School of the Mines to measure water mole fraction and temperature in the core of an entrained flow gasifier. We used measurements of the water vapor temperature up to 1400ºC and 15atm using argon as the entrainment gas to elucidate char gasification kinetics models. Without the newly created databases, measurements in this argon rich environment would have been impossible.

Acknowledgments

My family, Jim, Lori, Kate, Grandpa Bill and Grandma Sue, deserve the highest praise and recognition that I could ever hope to offer. Because of this, this paragraph has been difficult to compose. No matter how I write it, it will fail to capture how truly thankful I am to have such an amazing support group and how influential you all have been in ways you could never have imagined. Any positive trait that I may have can be traced back to you and because of this, you should consider the completion of this Ph.D. as much yours as it is mine.

I would like to acknowledge the support that my girlfriend Katie Primm has given me over the years. She has only known me as a stressed Ph.D. student always worried about writing a paper or an upcoming project. Despite this, she has unwaveringly supported me, from cooking occasional dinners after long nights in the lab to listening to the problem of the day. Her passion and alacrity for her own work has driven me to become better at what I do. I cannot thank her sincerely enough for all she has and continues to do.

Before I started graduate school, I was told to "never join a new professor, you never know when they might lose money or get fired." Thankfully, I completely disregarded that advice and joined Dr. Rieker, along with Torrey Hayden, in an empty box of a lab. My relationship with him as my direct mentor and coworker has been more influential than I ever could have imagined. He has taught me how to be a researcher focusing producing high quality, reputable work who also focuses on clear presentation through a variety of media. Perhaps more importantly, he has taught me just as much about professionalism and how to be an adult. He has given me numerous responsibilities, trusted my opinions, allowed me to lead undergraduates, taught me about the inner workings of professorial life, shown me the balance that should be struck with one's personal life, while unknowingly providing opportunities year-after-year to play April Fool's Day pranks. I never hesitated broaching personal topics with him and he was openly forthcoming with Rieker Life Advice. He has not simply been an academic advisor to me but a role model and for this, I am eternally grateful.

The people that compose the Precision Laser Diagnostic Lab are the most well rounded, intelligent, interesting, and good-natured people that I have ever had the fortune to work with. I was humbled on a daily basis with their clever ideas, the work they produced, and the open and supportive way in which they presented their thoughts….even during the two-page evisceration of my practice defense talk by Torrey. I feel fortunate to have been able to spend so much time with such an impressive group of people so early in my career and will always consider you my friends and colleagues.

I would like to acknowledge and thank the Department of Mechanical Engineering for accepting me into the program and valuing student involvement and opinion as highly as they do. In addition, the administrative staff does exceptional work and I cannot begin to count the number of times they have helped me navigate various paperwork requirements and formalities.

My friends, both in San Diego and Colorado, deserve immense credit and acknowledgment as well. It is often overlooked just how vitally important time *away* from the lab is as time *in* the lab. From countless Moab trips to watching Breaking Bad in San Diego via a webcam, you were all there to freshen my mind and keep work in perspective. Your friendly competition and support was a large driver in my completion of this degree.

The scientists and technicians at NIST Boulder in Nathan Newbury's group have had significant impact on my trajectory as a researcher. When I began with Dr. Rieker most of my time was spent at NIST trying to learn how to operate the dual comb spectrometer. The employees at NIST immediately

welcomed me and always answered any question I posed. I feel immensely fortunate to have been able to work so closely with them. Specifically, I would like to thank: Dr. Nathan Newbury, Dr. Ian Coddington, Dr. Fabrizio Giorgetta, Bill Swann, Dr. Esther Baumann, Dr. Laura Sinclair, Dr. Kevin Cossel, Dr. Stefan Droste, Dr. Gar-Wing Truong, Mick Cermak, Isaac Khader, and Joe Thompson as well as the amazing administrative staff who keep NIST's gears running.

The measurements in Chapter 6 were completed at Colorado School of Mines in Dr. Jason Porter's lab with his graduate student Madison Kelley. I would like to thank them for opening their lab and impressive equipment to us and the dual comb spectrometer. Though it took Madison and I three 24 hour data runs, we ended up getting a useful and unique dataset. I would like to thank them both for their patience dealing with a spectrometer that could be very temperamental at times.

Craig Joy from the Physics Trades Teaching Shop has had an important role in turning me into a professional mechanical engineer. He has taught me enough machining, dimensioning, and part design that I feel comfortable discussing design considerations with machinists. He was always patient when I chipped his drill bits or broke his 2-56 taps and I thank him for that.

I would also thank Ken Morse, Victor Ferreira, Jeffery Fisher, Steve Burke, and the control room staff at the CU power plant who were immensely helpful in allowing us to set up the spectrometer in their basement enabling the measurements in Chapter 2.

List of Tables

List of Figures

1 Introduction

1.1 Background and motivation

1.1.1 Laser Diagnostics in high temperature environments

As a larger fraction of the global population continues to modernize, access to clean energy and accurate knowledge of pollutant sources will become increasingly vital. Even with the rapid development of renewable technologies, a significant portion of our energy, particularly in developing countries, will be derived from combustion sources like gas turbines, coal gasifiers [1], and other combustion devices [2,3]. Improving the efficiency and reducing the emissions from combustion systems requires detailed understanding of combustion processes along with the ability to monitor and control them in real time [4]. However, measurement of these systems is difficult because they operate at high temperature, high pressure, have varying species mole fractions, and are typically subject to poor instrument accessibility [5]. Laser diagnostics are able to directly probe the internal dynamics in combustors and are well positioned to have an important role in combustion efficiency improvements, combustion chemistry knowledge, and pollutant characterization far into the future. High-speed, in-situ measurements of water vapor temperature, pressure, and concentration measurements are of particular interest in these fields [6]. Many diagnostics used in these research areas are based on water vapor absorption because water vapor is both present in ambient air and is a key product of combustion.

In addition to combustion systems, exoplanetary studies of planets orbiting close to their parent star are dependent on accurate, high temperature spectroscopic data to correctly interpret collected spectral signatures [7–9]. The absorption spectrum of starlight that has passed through the exoplanet atmosphere is used to remotely study its environmental composition and atmospheric temperature.

1.1.2 Direct Absorption Spectroscopy

Direct absorption spectroscopy is an optical diagnostic technique used to probe the thermodynamic properties of gases in the systems mentioned above. The technique can be time resolved, quantitative, and can measure *in* situ concentrations and temperatures of gasses that would otherwise be difficult or impossible to measure. All of these properties are vital to combustion measurements, though direct absorption does have drawbacks. The measured properties are averaged along the beam line-of-sight so they do not provide multidimensional spatial resolution and measurement interpretation requires accurate knowledge of the quantum mechanical transition information.

Absorption of light by molecules, such as H_2O, CO_2, CH_4, and CO, is represented by the Beer-Lambert Law. This law allows experimenters to extract thermodynamic parameters by quantitatively describing the frequency dependent magnitude of light absorption by a molecule. In the systems studied in this work, we typically extract temperature and concentration and use the form of the Beer-Lambert Law:

$$\left(\frac{I}{I_o}\right)_\nu = \exp\left(\sum_j \left(S_j(T) P X_i L \phi_j(\nu)\right)\right) \tag{1}$$

where $(I/I_o)_\nu$ is the frequency dependent ratio of laser intensity before and after interaction with a gas, $S_j(T)$ is the linestrength of transition j, P is system pressure, X_i is the molar fraction of absorbing gas i, L is the interaction pathlength of the laser through the gas, and $\phi_j(\nu)$ is the frequency dependent line shape function for transition j. The argument in the exponential is known as absorbance. Classically, the Voigt profile is used for $\phi_j(\nu)$. It considers broadening due to Doppler shifts of the molecules relative to the beam propagation direction and Lorentz (collisional) broadening to account for the effect collisions have on the internal energy state of the molecule. However, these two mechanisms fail to account for well-known second order broadening effects such as speed dependence and Dicke narrowing. These effects narrow the transition profile, thus decreasing measurement accuracy if not accounted for in the line shape profile. However, they require high resolution spectrometers for accurate measurement. In this work, we employ various line shapes depending on the desired level of accuracy. See Chapters 4 and 11 for a more detailed description of the Voigt and modern line shapes and Figure 1-1 for a graphical description of the direct absorption process.

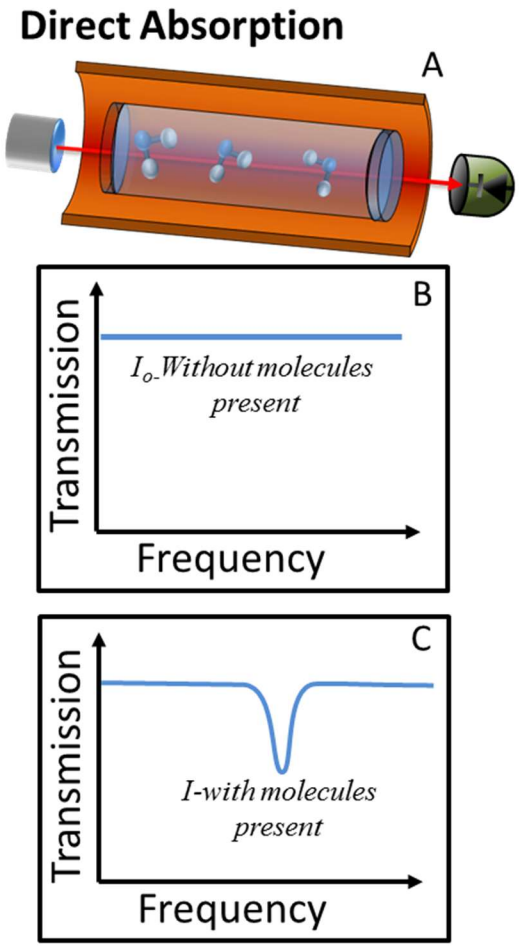

Figure 1-1-Graphic of direct absorption. A-Laser of known frequency is passed through a gas of interest. B-The laser intensity without the gas in the beam path is recorded. C-The absorption profile is then recorded with the gas present.

The key to extracting quantitative information from direct absorption measurements is accurate knowledge of the strength and shape of the transitions that are being probed. When solving Equation (1), data such as the linestrength, the line shape's full width at half maximum (FWHM), and natural center frequency, among many others, are required and can be found in publicly accessible databases. The two most commonly used in engineering diagnostics are studied in this dissertation. They are HITRAN2012 (HITRAN) [10] and HITEMP2010 (HITEMP) [11]. Note that much of the HITRAN2012 data is currently in the online repository, HITRAN Online [12]. These databases are highly accurate near room temperature, where the parameters have been directly measured for most strong transitions, though at high temperatures there are far fewer direct measurements [13]. At temperatures near 1000K there are some validated transitions [14–18] but most line shape data is dependent upon quantum mechanical calculations, which can be subject to limitations on theoretical understanding or computational resources [11,19]. See Section 3.2.6 for a detailed explanation of the development and progression of HITRAN and HITEMP. The high temperature knowledge gap is especially true for water vapor, despite being a heavily studied molecule. Water is present in ambient air, and is a major product of combustion and is therefore commonly used to measure temperature, assess combustion processes, or in the study of the atmospheres of distant planets.

In this dissertation, we aim to fill that knowledge gap by developing high temperature water vapor databases in the near infrared (NIR) wavelength region. To accurately extract line shape parameters, one must fully constrain every variable in Equation (1) except for $\phi(\nu)$. This is

accomplished here by controlling the temperature, water vapor mole fraction, system pressure, and pathlength in a spectroscopic cell placed inside a uniform, high temperature tube furnace. Various line shape profiles are then multispectral fit to each transition at each experimental condition to determine the temperature and pressure dependence of the line shape parameter of interest [14,20,21]. One can extrapolate these room temperature properties to higher temperatures with power law scaling approximations using the expression, $(296K/T)^n$, where T is a temperature of interest and n is a computationally, theoretically, or experimentally derived value. This scaling approximation is based on simplified physical models, so experiments are often the most reliable method of extracting accurate values or checking computed values. This need for high temperature water transition data and scaling approximations is emphasized by Tennyson *et al.* in their paper describing the state-of-the-art line shape and databases: "Available experimental studies usually span ranges of about 100K to about room temperature…" followed by "Obviously, it would be desirable to have experimental studies over more extended temperature ranges, but these are unlikely to be forthcoming in the immediate future" [13].

1.1.3 Frequency Comb Spectroscopy

1.1.3.1 Fiber frequency comb

A frequency comb is a laser source with an output composed of many distinct, evenly spaced optical frequencies. It can be created in many ways, from modulation of a single wavelength source to stabilization of the output frequencies of a mode-locked laser.

For the work in this dissertation, we focus on stabilized mode-locked comb sources since they are capable of generating extremely broad output spectra with very well known optical frequencies. In the time domain, a mode-locked laser is one that emits a constant train of short pulses. The pulses are generated by forcing the light from thousands of longitudinal modes in the cavity to be in phase or "locked". This generates a very narrow (of order femtoseconds), large amplitude pulse. In this situation, the pulse repetition rate is defined by the laser cavity length [22].

In the frequency domain, the pulse train is composed of many discrete optical frequencies or cavity modes separated by the laser repetition rate, which covers a broad spectral range. The tooth frequencies are defined by $\nu_n = f_{ceo} + nf_{rep}$ where ν_n is the frequency of the nth comb tooth, f_{ceo} is the carrier envelope offset frequency, and f_{rep} is the comb's repetition rate. The progression from a mode-locked laser to a frequency comb comes when the two degrees of freedom, f_{ceo} and f_{rep}, of the comb teeth are controlled. Once they are stabilized at known values (or precisely measured in real time), all tooth frequencies in the spectrum are known. The combs used in this dissertation are exclusively made from fiber optic components. Figure 1-2 graphically illustrates the density of comb teeth and the ability to resolve absorption features.

There are many methods for stabilization of the comb teeth [23–25]. The method employed here is active stabilization through feedback loops that control the length of the comb cavity and the intensity of the cavity pump lasers. Other methods closely monitor tooth drift and correct the tooth frequencies in real-time or post processing [26].

Though frequency combs are relatively new devices [27,28], research has advanced quickly, and since 1999 researchers have built combs to generate light from the extreme ultraviolet to the mid IR [29]. We employ fiber frequency combs spanning wavelengths from approximately 1.2-1.8 μm. Their tooth spacing is either 100 or 200MHz, and we leverage their broadband design to conduct highly resolved spectroscopy in engineering environments for the first time.

1.1.3.2 Dual Comb Spectroscopy

To benefit from the broadband spectra generated by frequency combs in spectroscopic measurements, one needs a broadband, high resolution detection method. The comb tooth absolute frequencies are too large to differentiate directly with a detector (hundreds of THz), and their dense spacing requires a detection method with spectral resolution at least as high as the repetition rate (100-200 MHz, 0.0033cm^{-1}-0.0067cm^{-1}, and 0.67-1.4 picometers (pm) at 1430nm). A Fourier Transform Infrared Spectrometer (FTIR) could resolve the teeth individually, but would require a scanning arm of approximately 300cm in length and take between 2 and 30 minutes to complete a single scan for the 100MHz combs [30]. An instrument of this size is not applicable in an industrial environment and the scan time prohibits time-resolved gas characterization. Therefore, we employ an interference technique known as dual comb spectroscopy that allows tooth-by-tooth resolution at combustion-relevant sampling rates [23,26,31–39].

A dual-comb spectrometer (DCS) relies on optical heterodyning, which requires a square law detector and incident light composed of a local oscillator, LO, and signal, each at slightly different frequencies. When the LO and signal light combine on the detector, a beat signal is generated at their frequency difference. If the difference between the LO and signal sources is in the radio frequency regime (RF) (e.g. 10s of MHz), the beat signal can be acquired by fast photodetectors and RF electronics. We apply this technique simultaneously to all comb teeth of two mutually phase locked combs over a spectral region of interest to measure gas spectra. We set the combs to have a repetition rate difference, Δf_{rep}, of order 1kHz. At the start of the desired spectral window for an absorption measurement, a comb tooth pair

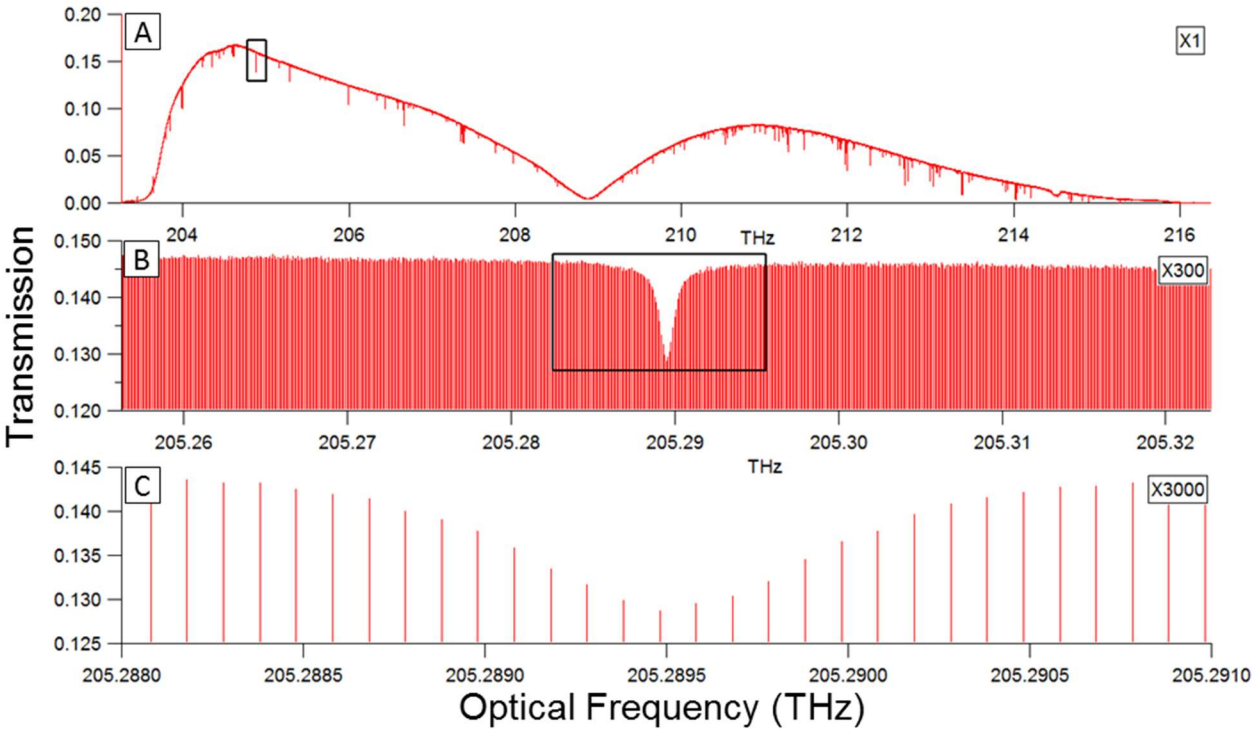

Figure 1-2-An example of the resolution and tooth density of the 100MHz combs discussed in this work. A-Transmission spectrum of the NIST linked frequency combs through a water vapor absorption cell. The overall spectral shape is intrinsic to the comb light and can vary depending on comb settings and transmission optics. B-300x expansion of the transmission spectrum in A with the comb teeth represented by vertical bars – the density of the teeth becomes apparent. The absorption feature is highly resolved and can be accurately fit. C- 3000x expansion relative to A.

is set to exactly overlap, see the leftmost comb tooth pair in Panel A of Figure 1-3. Each subsequent comb tooth pair then creates a unique heterodyne beat note separated by an integer multiple of Δf_{rep}, $f_{beat} = m\Delta f_{rep}$ where m is the mth comb tooth pair, as illustrated in Panel B of Figure 1-3. f_{beat} is necessarily less than $f_{rep}/2$, which means that all f_{beat} frequencies are in the RF domain for a 100 or 200 MHz repetition rate comb. When the magnitude of a comb tooth is reduced by absorption, the corresponding RF beat is also reduced. Thus the spectral absorption is encoded in these RF beats, allowing us to resolve the entire spectrum on a tooth-by-tooth basis [25,38,40–42]. A DCS requires that the two frequency combs be phase-locked to one another and the wavelengths of the comb teeth be referenced to a known wavelength in order to construct an accurate wavelength axis on the spectrum. See Section 1.1.4 for descriptions about how we phase lock and wavelength reference the comb teeth for each system used in this dissertation.

When both pulses from the LO and signal combs overlap in time on the photodetector, a strong interference signal is generated (centerburst). The time domain signal is called an interferogram (IG) and is similar to those measured in FTIR spectrometry. After digitization and collection, the IG is Fourier transformed to obtain the individual beat frequencies spaced by Δf_{rep}. We then scale the measured beat frequencies back to their original optical frequencies using the set-points of the frequency combs. Interferograms repeat every $1/\Delta f_{rep}$ seconds, are coherently averaged, and phase corrected in post processing to increase the final single-to-noise ratio (SNR). Here, we use the DCS systems and the heterodyne technique to probe high temperature systems with an unprecedented combination of frequency accuracy, resolution, and bandwidth. The systems can simultaneously produce and resolve 100,000+ distinct comb teeth over the near infrared (NIR) spectral range using this technique.

1.1.3.3 Fundamental tradeoff off between acquisition speed and bandwidth

The resolvable spectral bandwidth for a DCS is defined to be between two frequencies where comb tooth pairs from comb 1 and comb 2 exactly overlap, for example, the first pair of comb teeth on the left side of Figure 1-3. This defines two Nyquist windows, one from 0Hz to $f_{rep}/2$ and a second one from $f_{rep}/2$ back to 0Hz. Though the beat frequencies in both Nyquist windows are identical, they result from comb teeth at different optical frequencies. If the light covering one Nyquist window is not removed with a filter, the absorption from two different pairs of comb teeth is encoded on one beat note, distorting the measured absorption profiles. This occurs because the detector cannot discriminate between "positive" and "negative" frequencies. Alternately stated, the detector cannot uniquely identify a beat frequency from Nyquist window 1 from the same beat frequency in Nyquist window 2. If this aliasing effect is not accounted for, their unique absorption values are mixed, thus ruining the retrieved spectral profiles. In the optical regime, the width of one Nyquist window (the spectral bandwidth) is the product of the comb tooth spacing (which is the repetition rate of the signal comb) and the number of comb teeth in the Nyquist window [41]:

$$Spectral\ Bandwdith = f_{rep} * m \tag{2}$$

where f_{rep} is the average repetition rate of the combs and m is the number of resolvable beat frequencies in a spectrum. Each beat frequency is spaced by Δf_{rep} so the number of resolvable beat frequencies in the RF domain is therefore:

$$m = \frac{f_{rep}}{2 * \Delta f_{rep}} \tag{3}$$

Combining equations (2) and (3):

$$Spectral\ Bandwidth = \frac{f_{rep}^2}{2 * \Delta f_{rep}} \quad (4)$$

Therefore, a higher Δf_{rep} yields a faster acquisition rate for a single spectrum, at the expense of spectral bandwidth. The reciprocal nature of IG acquisition rate and spectral bandwidth is apparent and something that must be considered before, and tailored to, any experiment. Figure 1-4 plots the tradeoff for regions of operation applicable to the DCS systems investigated here and it highlights the flexibility of the spectrometer since its operable points can be quickly changed in the field.

1.1.4 DCS systems employed in this dissertation

1.1.4.1 Metrology comb system at NIST Boulder

The comb system used for Chapters 3, 4, and 5 of this dissertation is a ring cavity design located at NIST in Boulder. It consists of two fiber frequency combs set at nominal repetition rates of 100MHz built using single mode, NIR fiber [39–41]. They are mode-locked using the Kerr effect through nonlinear polarization rotation. Briefly, when the polarization of the cavity is correctly set, the high intensity peak of a light pulse will be preferentially propagated around the cavity. As the pulse travels, its low intensity wings experience more loss in the fiber, thus continuing the propagation of the high intensity center. The preferential loss is created by exploiting the slight birefringence of a single mode optical fiber and pulse polarization to create a cavity that selectively propagates high intensity light [43]. The comb teeth are stabilized by comparison of two individual teeth against two narrow linewidth, single frequency lasers that are themselves Pound-Drever-Hall (PDH) locked to a stable optical cavity. These optical cavities are periodically referenced to the NIST hydrogen maser to create an absolute frequency reference [37,40]. Phase coherence between the combs is achieved by referencing both combs to the same stable cavity modes with phase locked loops. We reference the comb tooth wavelengths by locking two teeth from each comb at two defined frequency offsets from the cavity stabilized lasers, corresponding to the two degrees of freedom for each comb spectrum. The loop that controls the comb repetition rate operates at approximately 10kHz and controls the cavity pump power. The carrier envelope offset frequency is controlled by a combination of a fast acousto-optic-modulator, bandwidth of >100kHz, and a slow piezo-electric block that removes low frequency noise of the repetition rate lock

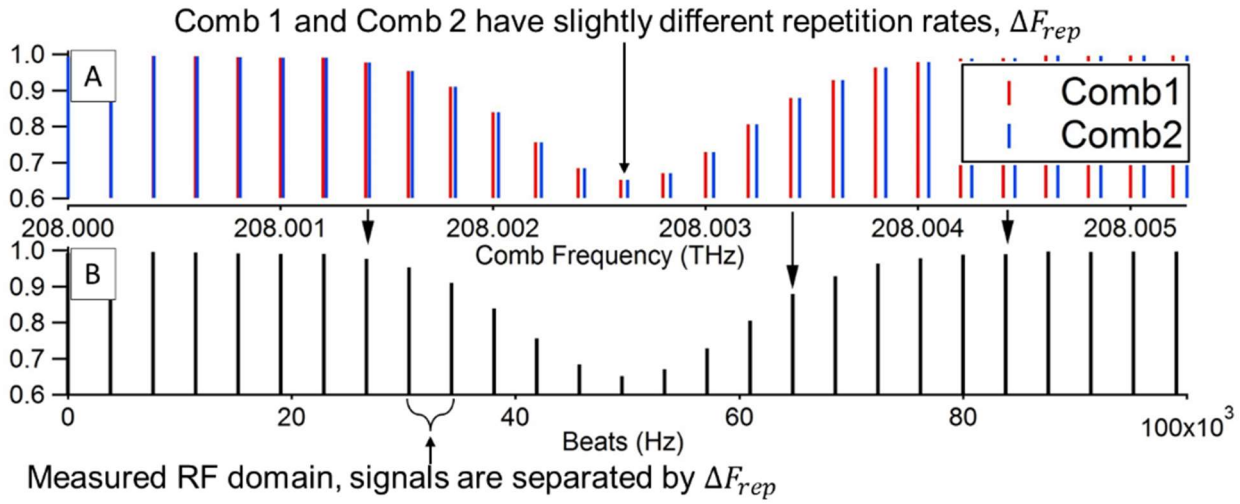

Figure 1-3-Graphic of multiheterodyne spectroscopy. A- The difference in repetition rate between two combs creates a unique frequency difference between subsequent comb tooth pairs. B- The frequency difference of each comb tooth pair generates a unique beat note recorded in the RF frequency domain. The absorption that occurred in the NIR is encoded in the RF beats and in post processing we scale them back to their original optical frequencies.

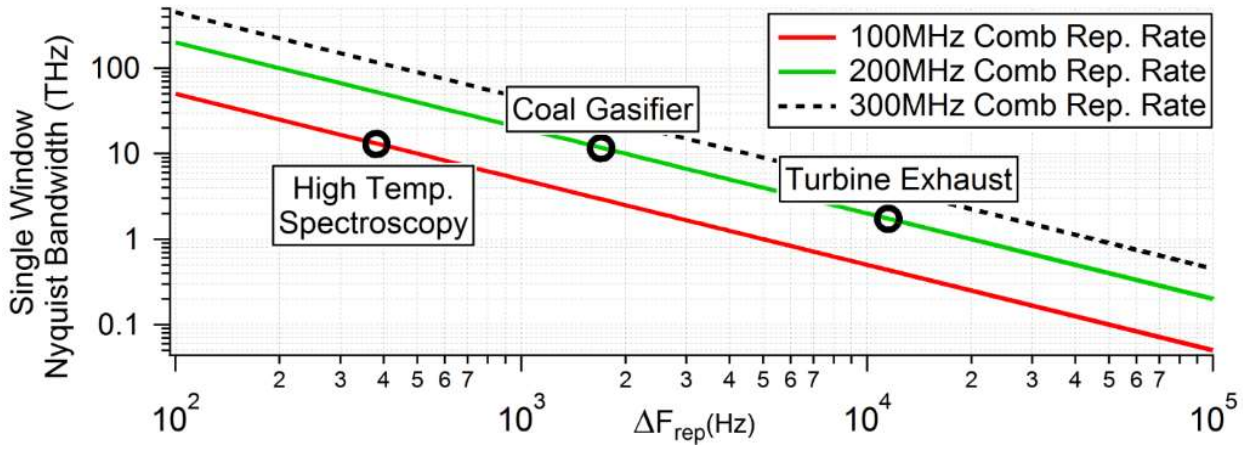

Figure 1-4-Reciprocal nature of the usable dual comb bandwidth versus Δf_{rep} (the difference in repetition rate of the two combs), where Δf_{rep} defines measurement acquisition rate of the experiment. The 100 and 200MHz systems used in this work are shown, as well as a potential, higher speed system.

[40]. These loops are not completely independent and slightly influence each other. The stable comb spectra are amplified in erbium-doped fiber, pulse compressed in a large mode area fiber, and broadened in highly nonlinear fiber (HNLF) to create a spectrum that spans from approximately 5500-8300cm^{-1} (1200-1800nm). We optically filter the broadened spectrum to only the water absorption region of interest with a spectral grating filter [39]. The comb light is transmitted to the University of Colorado Boulder (CU) in an underground fiber link described in 3.2.2. At CU, we combine the light, pass it through our gas of interest, and resolve the teeth as described in 1.1.3.2. This system is flexible in its control of the teeth but is completely immobile.

1.1.4.2 Mobile dual comb spectrometer utilizing linear PM cavities

While referenced to an absolute standard, the fiber ring lasers of the previous system are highly sensitive to ambient temperature and humidity fluctuations, long-term polarizer drift, and loud noises in the optics laboratory. Therefore, to use a DCS in industrial, uncontrolled environments requires a more robust laser design. The comb system presented in this section is based on a 200MHz linear cavity design using polarization-maintaining (PM) fiber and a saturable absorbing mirror [44]. The saturable absorbing mirror absorbs low intensity light while reflecting the high intensity part of the pulse thus mode-locking the laser [43]. The PM fiber in the cavity constrains the cavity polarization and makes the system far more resistant to environmental perturbations [45,46]. See Figure 1-5 for a schematic of the mobile frequency comb design.

The stabilization of f_{ceo} is accomplished with $f-2f$ interferometry, see Section 2.2, while f_{rep} is referenced by locking against a narrow linewidth diode laser. This diode laser naturally drifts and will therefore shift the frequencies of all comb teeth. We account for the drift of the diode in two ways: 1- In Chapter 2, we measured the drift of the repetition rate of one comb to mHz precision with a counter referenced to an ovenized quartz oscillator. This allows wavelength axis adjustment in post processing of each of our measured spectra with the MHz-level optical frequency accuracy set by the quartz oscillator. Unconstrained diode drift can cause the phase lock to fail due to lack of dynamic range adjustment of the cavity length over long periods of time. Alternatively, in Chapter 6, we again measure the repetition rate of one of the combs but instead of letting the diode naturally drift, we slightly vary its temperature to maintain the repetition rate required for the heterodyne detection method. Method 2 is preferred over Method 1 because it can be maintained indefinitely. Both Methods 1 and 2 result in optical frequency errors of approximately 2MHz. Typical spectral linewidths at atmospheric pressures are >1GHz so the

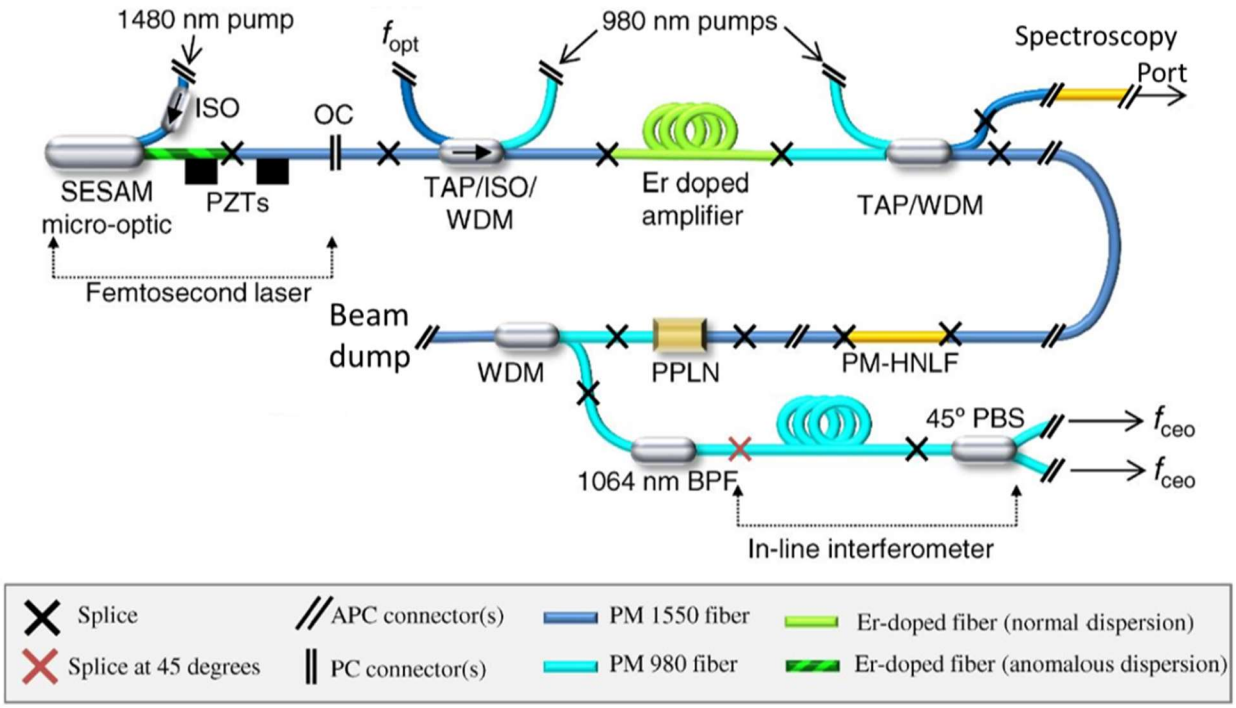

Figure 1-5-Adapted from Ref. [44], this is a schematic of the mobile dual comb system. The locations of the taps for the optical and carrier envelope offset locks are indicated as is the comb generating mode locked cavity. The system is made using PM fiber and it fits inside a 20 X 20 X 2.5cm box. See the reference for more detail about the specific cavity design.

frequency error of the mobile system is negligible. Other methods exist which allow correction for the frequency drift of comb teeth, which could prove useful for mobile dual frequency comb spectroscopy [26,36,47].

The stabilized spectrum of each comb is amplified and broadened as in 1.1.4.1, but without the large mode area fiber, prior to use for spectroscopy. The mobile frequency combs each produce approximately 300 mW of optical power and their enclosures are temperature controlled with thermoelectric coolers to coarsely control their repetition rates prior to phase lock implementation. The PM fiber and saturable absorber mode locking makes the system robust against environmental changes and vibrations and the whole system is easily portable; it occupies about the same volume as a miniature refrigerator. Section 2.2 contains additional detail about this system.

1.1.5 Comparison with Other Absorption Spectroscopy Systems

There are many types of laser diagnostics and techniques in use for both combustion and high temperature metrology measurements. A detailed review of either field would be too broad for this dissertation but a brief review of the technologies related to a DCS will be presented here.

A DCS combines: 1) wide wavelength coverage (enabling simultaneous measurement of multiple molecules while minimizing interference from overlapping absorption features), 2) high spectral resolution (resulting in well-resolved, undistorted molecular spectra), and 3) high time resolution (enabling the characterization of short timescale processes). DCS systems with these traits have been realized in a handful of carefully controlled metrology laboratories worldwide [26,34,36,48–50].

In light of this being the first demonstration of this technique in an engineering setting or for high temperature metrology, a DCS compares well against techniques that share similar qualities with the closest analog being an FTIR. The resolution and sample time of an FTIR are determined by the length of its mechanically scanned Michelson interferometer arm and an instrument with comparable resolution to the mobile comb spectrometer presented in this work would require a 300cm long scanning arm, and thus is not robust and easily portable [30]. More importantly, the sampling rate for such an instrument is more than three orders of magnitude slower than the comb spectrometer. If individual spectra are not captured on timescales faster than the turbulence-induced laser intensity fluctuations in a combustion system, the result is apodization (an effective loss of resolution and introduction of potential distortion) [51]. Supercontinuum sources and high-speed swept sources are capable of similar wavelength coverage and higher sample rates than DCS systems, but are limited by some combination of unknown/broad laser linewidth (for scanned sources), difficult wavelength characterization (to establish an accurate, undistorted wavelength axis), and low spectral resolution (e.g. from the grating spectrometer used for detection) [15,51–57]. TDLAS measurements are known for high spectral and time resolution, but can cover only 1-2 absorption features at a time [1,2,58–60]. It is possible to multiplex diode lasers to measure multiple species, but our dual comb spectrometer uses only six pump diodes to generate hundreds of thousands of unique optical frequencies spanning from about 1200nm to 1800nm at a spacing of 100 or 200 MHz, 0.7 pm or 1.4 pm at 1440nm, respectively depending on the system [61,62]. Thus as the dual comb technique becomes more accessible for industrial environments, it fills a unique niche by providing flexible, broad spectral coverage, high resolution, and reasonably high acquisition rates.

1.2 Dissertation Overview

Here we present the progression of work and major results contained in the dissertation to clarify how and why the work was completed.

The goal at the beginning of this dissertation was to measure water vapor temperature and mole fraction in an argon buffered high temperature, high pressure coal gasifier to inform reaction kinetics and models. However, we knew argon-water line shape databases did not exist, so we linked the DCS at NIST to CU and collected the spectral data for water-water and argon-water systems. During this time, NIST finished developing a robust and portable comb design. Extending that design, our group built our own system to make measurements in locations other than controlled optics labs. We then tested and deployed the system by measuring CO_2 and water temperature and concentration through the turbine exhaust in the CU natural gas turbine facility. We saw that the high temperature air-broadened water models and the turbine spectra did not match sufficiently and could be improved. We collected additional air-water data with the NIST linked system and qualitatively compared the HTIRAN/HITEMP models to our DCS spectra. With the 50 experimental spectra, 25 water-water and 25 argon-water measurements, we set out to then extract line shape parameters. We collaborated with Brian Drouin and Matt Cich at the Jet Propulsion Laboratory (JPL) to use their well-vetted and community-accepted multispectral fitting software. Upon examining the results of the fits, we saw that the only profile to extract realistic line shape data and validated previous computational models was the quadratic speed dependent Voigt. We had also finished analyzing the water-water and water-argon line shape parameters. With the argon-water and water-water database in-hand, we were able to examine the behavior of water in the coal gasifier. We then used the mobile DCS to measure high temperature, high pressure argon-water mixtures in March 2017 and utilized the in-house database to analyze the spectra.

This dissertation achieves the following major goals:

- **First demonstration of DCS in an industrial environment (Chapter 2).** We measured gas temperature and H_2O and CO_2 mole fraction in the exhaust of a 16MW gas turbine and demonstrate down to 10 second temporal resolution, illustrating instrument viability for combustion system transient measurements. Some of the shortcomings of the HITRAN2012 database were also apparent, thus driving the need for the development of more accurate high temperature spectroscopic databases. This is the first published example of a DCS deployed outside of an optics laboratory.
- **Compare the performance of the two most commonly used spectral databases, HITEMP2010 and HITRAN2012, to predict high temperature water vapor absorption (Chapter 3).** We overlay broadband, accurate absorption data with models generated from HITRAN and HITEMP to categorize and track the differences between the data and models. The improvements to model predictions using simple temperature scaling relationships are also investigated to improve and inform their use by other researchers.
- **Study various line shapes and their ability to model high temperature water vapor (Chapter 4).** Using the data from the comparison work in Chapter 3, we use multispectral fitting software to extract the self-broadening temperature-scaling exponents for 232 transitions using Voigt, Rautian, and quadratic speed dependent Voigt spectral line shapes. These models account for line shape narrowing mechanisms but have primarily been tested at room temperature and below. The limitations of the Voigt are well known but until this study, there had been no large-scale fitting of line shape parameters over large temperature ranges. We show that only the quadratic speed dependent Voigt adequately modeled these effects. We also show that the retrieved values validated previous computed broadening exponents, and that a single temperature-scaling exponent was adequate to fit the data over the whole temperature range.
- **Improve high temperature water vapor absorption databases (Chapters 4 and 5).** Measuring line shape scaling parameters for self-broadened water vapor is vital to further increase the accuracy of the spectroscopic databases at elevated temperatures. This will be an improvement on the current values, which are mostly unmeasured approximations applied at elevated temperatures. Data extracted over our 296-1305K temperature range does not exist in the community and will improve measurements of high temperature systems. Additionally, we will publish a companion paper presenting argon-water broadening, shifting, temperature dependencies, and speed dependence parameters.
- **Utilize a DCS in a high pressure, high temperature flow in an experimental scale coal gasifier (Chapter 6).** Upon publication, we will provide simultaneous, *in situ* measurements of gas temperature and water mole fraction in an argon rich environment in an experimental gasifier reactor column in Professor Jason Porter's lab at Colorado School of Mines. Quantitative measurements will be made possible by the implementation of our in-house measured water-argon broadened database and the unique mobile spectrometer described above. These measurements will be enabled by our in-house databases since there are no broadly available argon-water line shape parameters available in the community. This work will validate the current models of temperature distributions in the core of the gasifier and inform gasification kinetics.

2 Dual comb spectroscopy in a 16MW gas turbine exhaust

A majority of text in this chapter is identical to the published version of the cited paper.

2.1 Introduction

Though frequency combs were initially developed for time and frequency metrology, researchers quickly recognized that they could be a useful tool for broadband laser absorption spectroscopy. They allowed many absorption features from several molecules to be measured with one laser. Simultaneously measuring multiple molecules gives researchers valuable information about the condition of combustion systems and increases their ability to optimize and improve the system of interest. To accurately resolve molecular spectra with ~GHz absorption linewidths at atmospheric pressure, it is desirable to use frequency comb sources with a comb tooth spacing on the order of a few hundred MHz – a few picometers in wavelength space. The utility of these laser sources has previously only been applicable in controlled optics laboratories but this chapter demonstrates their use in an industrial environment.

Recently, comb-tooth-resolved dual comb spectroscopy was demonstrated in practical environments, despite decohering effects induced by turbulence [39]. These prior experiments were performed with a laboratory-based DCS built around ring cavity laser oscillators that utilize nonlinear polarization rotation mode-locking, and which were phase-locked to two cavity-stabilized, narrow-linewidth, single-frequency lasers [37]. A hydrogen maser (ultra-stable frequency reference) provided the timebase for all electronics. The mode-locking was highly sensitive to vibration, temperature, and humidity changes and the combs where incompatible with field operation. Phase-locking the combs to cavity-stabilized lasers and referencing them to the hydrogen maser provided a high degree of frequency accuracy and stability (Hz linewidth comb teeth and knowledge of the absolute comb tooth frequency to <10 kHz), but came with high cost and complexity.

Here we present the first demonstration of a mobile DCS for measurements in an industrial environment, Figure 2-1. The mobile spectrometer takes advantage of several recent advancements in environmentally robust frequency comb lasers [44,46] to untether the dual comb system from the laboratory. These frequency combs demonstrate stable mode-locking despite large changes in environmental conditions while the spectrometer configuration eliminates the need for both the cavity-stabilized lasers and the hydrogen maser for phase locking and wavelength referencing, see 1.1.4.2.

We characterize the exhaust of a 16 MW stationary gas turbine in the University of Colorado cogeneration facility by recording absorption spectra composed of 16,000 comb teeth spanning 1435.5 nm to 1445.1 nm with 1.6 picometer wavelength spacing. The instrument resolution is less than 1 picometer because the tooth linewidth is considerably narrower than the spacing and the frequencies are conservatively known to better than 10 MHz. Spectra containing 279 absorption features of H_2O and 43 features of CO_2 are acquired at 12.4 kHz. Spectra are averaged for up to 60 seconds to achieve high signal-to-noise ratio. They are simultaneously fit with HITRAN2012 based absorption models to extract temperature and species concentrations. H_2O and CO_2 concentration levels are consistent with expectations based on turbine operating parameters. Temperature and concentration trends follow operational variations of the gas turbine and periodic operation of an auxiliary burner located in the duct upstream of the beam location.

These measurements demonstrate the feasibility of a DCS system for combustion environments. The kHz acquisition rates of the spectrometer are faster than turbulence-induced beam fluctuations in these environments, which enables undistorted full resolution spectra. This is not possible with high

resolution Fourier transform spectrometers (FTS/FTIR), which are several orders of magnitude slower. With the current system, any species with absorption features in the 1.2 to 1.8 μm wavelength region can be probed simultaneously. Future systems will further enhance the signal-to-noise ratio of the DCS for short averaging times. Systems operating in the mid-infrared where stronger absorption features of even more molecules are located, are fast evolving [63].

2.2 Mobile dual frequency comb spectrometer

A description of the mobile DCS in this chapter is presented in section 1.1.4.2 though more specific details about the system are presented here.

In order to perform accurate heterodyne spectroscopy, the two frequency combs must be phase-locked to one another and the wavelengths of the comb teeth must be referenced to a known wavelength. The mobile implementation achieves phase-locking and wavelength-referencing using portable components, which achieve accuracy and stability appropriate for atmospheric pressure absorption spectroscopy measurements. Comb tooth resolution and accurate wavelength scaling was enabled by use of the heterodyne technique discussed in 1.1.3.2.

The two degrees of freedom, f_{ceo} and f_{rep} of the comb teeth are controlled in the following ways. f_{ceo} is detected through a standard $f-2f$ interferometry technique that compares a frequency-doubled comb tooth from the 2µm region to a tooth at 1µm [27,28,44,64]. Once detected, f_{ceo} can be phase locked to a reference oscillator through feedback to the comb oscillator pump power. The phase-lock between the combs and control of f_{rep} is established by phase-locking one tooth near 1560nm from each comb to a narrow linewidth reference laser (2kHz linewidth, RIO Planex RIO0195-3-01-3). The comb structure is modulated through feedback to a piezoelectric stack that stretches the laser cavity. The particular tooth from each comb that is used for the lock is chosen judiciously for multi-heterodyne detection between the two combs, similar to the method outlined in [41] and 1.1.3.2. The accuracy and stability of the frequency locks depends on the radiofrequency oscillator that is used to reference the timebase of the electronics. For the implementations described in this Chapters 3, 4, and 5 the reference oscillator was a hydrogen maser with exceptional stability. Here and in Chapter 6, we use a compact ovenized quartz oscillator (Wenzel 501-09451) with stability better than 1ppm per day [65]. In our wavelength range, this translates to MHz-level optical frequency stability. While lower than previous frequency comb implementations, this stability is comparable to a well-calibrated high-end FTIR

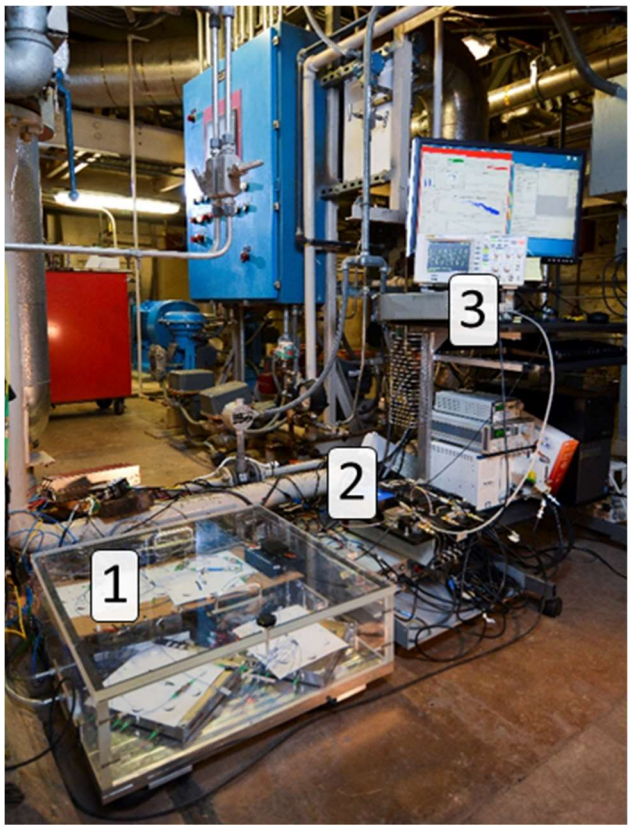

Figure 2-1- First demonstration of a mobile DCS. (1) Dual frequency combs (2) Reference laser, and (3) FPGA control electronics and data acquisition. The access port to the turbine exhaust is one floor above the spectrometer, and the spectral filters are out of the frame. The system is not isolated from the industrial environment.

and three orders of magnitude below the GHz absorption linewidths of typical atmospheric absorption features.

The narrow-linewidth reference laser itself drifts slowly by up to 100MHz (depending on environmental conditions) over a several hour period. This drift is transferred to the comb teeth. We measure the repetition rate of the frequency combs to mHz precision with a counter referenced to the quartz oscillator to measure the drift. This measurement, combined with the slow nature of the drift allows the proper wavelength scaling of each of our measured spectra with the MHz-level optical frequency accuracy set by the quartz oscillator. The mobile dual-frequency comb spectrometer as installed at the power plant is shown in Figure 2-1. Other methods exist which allow correction for the frequency drift of comb teeth. These methods could also prove useful for a mobile DCS [26,36].

The system was setup in less than one day in the basement of the power plant facility and was operated for four days without any environmental control or vibration isolation. Figure 2-1 illustrates a photo of how the spectrometer was arranged in the power plant. The system consisted of two, 200MHz combs yielding a resolution of $0.0067 cm^{-1}$.

2.3 Power plant facility measurements

2.3.1 Stationary gas turbine facility

The power plant at the University of Colorado Boulder is a cogeneration plant powered by two Mitsubishi MF111A/B 16MW natural gas turbines. The independent turbines use auxiliary steam injection into the combustor to lower peak temperatures and reduce NOx emissions. Combustor bypass air leads to overall lean operation (16% excess O_2). The exhaust passes through a heat exchanger to generate steam for turbine injection, additional power generation in a secondary steam turbine, and/or campus heating. Downstream of the turbine exit, there is a supplemental burner that is fired on demand to add energy to the exhaust for additional steam generation. Our measurement location was approximately 3.6m downstream of this burner, before the steam generation unit. The duct cross section at our measurement location was 4.6 x3.7m. See Figure 2-2 for an experimental schematic.

2.3.2 Optical setup

The mobile DCS rested on small inflated innertubes directly on the floor of the power plant, without further vibration isolation or control of the ambient temperature (see Figure 2-1). Heavy machinery and large water pumps were continuously operating nearby during the course of the measurements and the ambient temperature varied from 12ºC to 22ºC. These severe external perturbations did not affect spectrometer operation.

The light from the combs was combined, spectrally filtered to our region of interest (1435.5 to 1445.1 nm), and sent through 10m of SMF-28 optical fiber to existing windows in the turbine exhaust duct, located one story above the spectrometer. The light was collimated into a 2.2 mm diameter freespace beam with an off-axis parabolic mirror. The beam passed across the duct and was reflected back by a plane mirror for a roundtrip pathlength of 723cm. A 35mm plano-convex lens focused up to 175µW of return light onto a single photodetector (Thorlabs PDA10CF). A National Instruments field programmable gate array (FPGA) sampled the detector at a rate of 200MHz, hardware-averaging 1000 IGs before writing the data to disk.

With this technique, there is a tradeoff between the spectral bandwidth and the acquisition rate of an individual spectrum, section 1.1.3.3. Here, we chose a relatively narrow spectral bandwidth (10nm) to increase the acquisition rate of an individual spectrum to 12.4kHz. We average this acquisition rate to 10

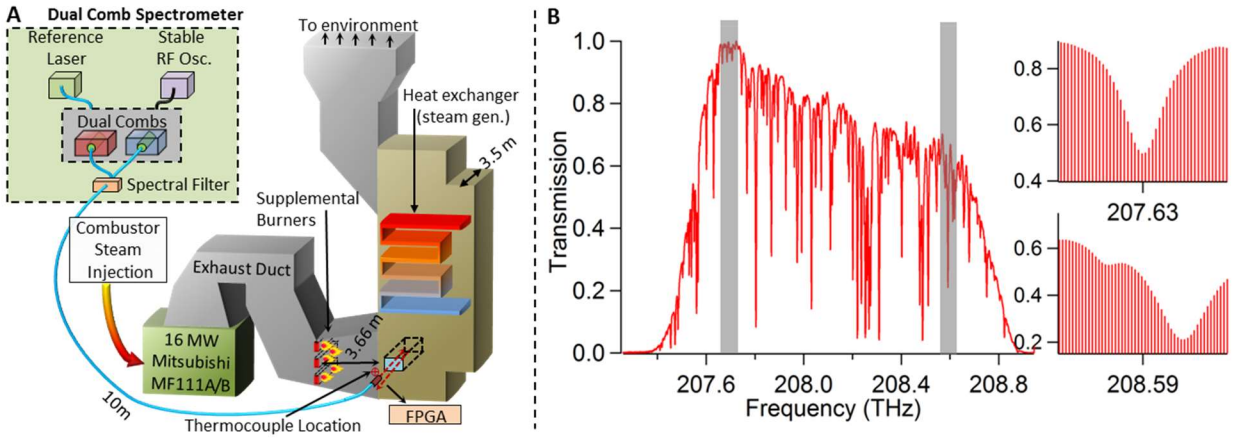

Figure 2-2-(A) Experimental schematic of the dual comb spectrometer and gas turbine facility. (B) Example transmission spectrum with insets of two absorption features (vertical bars represent heterodyne beat signals from individual comb tooth pairs).

and 60 second time stamps to increase the SNR. A broader spectral range could be covered with the same system if a lower per spectrum acquisition rate is acceptable.

The existing 1cm-thick plane windows of the exhaust ports could not be modified with a wedged face, so they imparted a distinct etalon (interference) structure onto the recorded spectra. The structure was fit with a sine wave and removed during post processing.

2.4 Gas turbine Exhaust Results

2.4.1 Absorption spectra and fitting

Panel B of Figure 2-2 shows an example measured laser transmission spectrum from 207.46THz (1445.1nm) to 208.84THz (1435.5nm), after 60s of averaging. The comb tooth spacing is 200MHz (1.6 picometers). Temperature and species concentrations are inferred by simultaneously fitting the broad measured spectra with an absorbance model for each absorbing species, a polynomial function to account for broadband baseline variation, and a sine function to account for the etalon structure in the baseline.

Accurate absorption models that include the temperature and pressure dependence of the absorption features are vital to this process. Several databases catalogue molecular absorption feature strengths, widths, and locations, and are combined with a line shape profile to create an absorption model. Here, we use a Voigt line shape profile and absorption feature data from HITRAN2012 to generate an absorption spectrum for our measured region. HITRAN 2012 was chosen because it contains many high temperature absorption features from the HITEMP2010 database, in addition to newer experimental data, Section 3.2.6. Careful laboratory experiments using frequency combs to measure water vapor absorption spectra at known high temperature conditions show that HITRAN2012 is as good as or better at predicting high temperature spectra than HITEMP2010, see Chapter 3 and [66]. However, HITRAN2012 was developed without broadband high temperature experimental data, so the accuracy of absorption-feature strengths and air-broadening temperature-dependence at high temperatures still lags behind the accuracy of the corresponding data at room temperature. In addition, the database does not yet include

the temperature dependence of pressure-shift and self-broadening coefficients. We are present measured line shape parameters for several hundred water features from 204THz to 215THz in Chapters 3, 4, and 5. In the absence of these data, we use the following scaling relations for the self-broadening and pressure-shift coefficients, respectively [67]:

$$2\gamma_{self} = 2\gamma(T_o)\left(\frac{296}{T}\right)^{.5}, \qquad \delta_{air\ \&\ self} = \delta_{air\ \&\ self}(T_o)\left(\frac{296}{T}\right)^{1} \quad (1)$$

We fit the spectra in two distinct steps – a piecewise fit to correct the baseline, and then a bandwide fit to extract the temperature and species concentrations as described in detail in Section 3.2.4. Note that incorporating improved high temperature spectral parameters in the model should enable simultaneous fitting of pressure in the future. For these data, we fixed the pressure at a value of 645Torr, which was bracketed by local atmospheric pressure (about 635Torr) and the duct overpressure valve (set at 26Torr gauge pressure). Setting the fit pressure to these bounds resulted in a 2.2K rms difference in measured temperature.

Panel A in Figure 2-3 shows a typical spectrum, model fit, and residual. We excluded residuals from the strongly saturated portions of features (absorbance greater than 3). Panel B of Figure 2-3 shows two narrow regions of the fit. The extremely weak CO_2 absorption is resolvable and easily incorporated

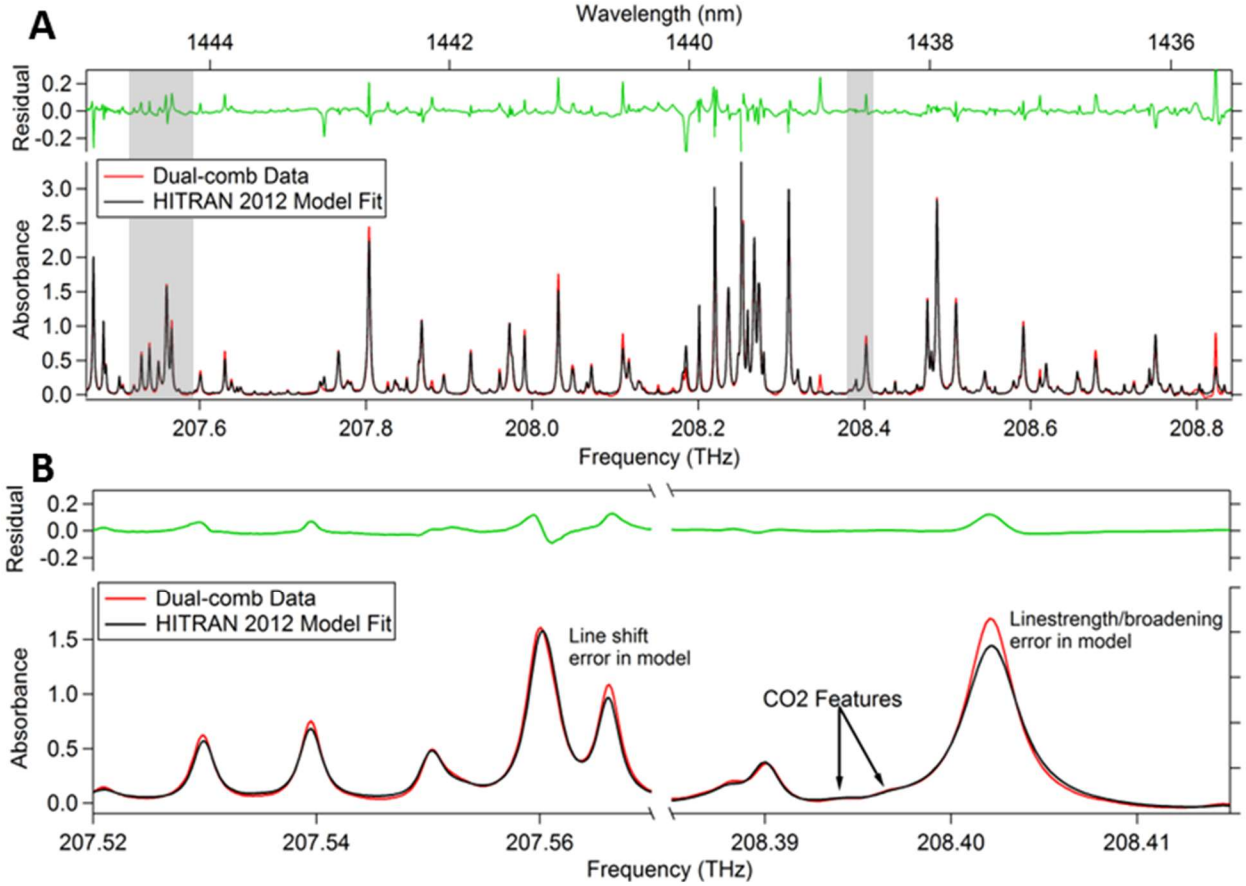

Figure 2-3-(A) Measured absorbance spectrum (60s average) with absorption model fit and residual. (B) Two example narrow spectral regions showing model fit and examples of common errors associated with the absorption database when used for high temperature environment. The right side of (B) shows two weak CO_2 features resolvable on the wings of strong neighboring water features.

in the fit despite the strong neighboring water vapor absorption features. Water vapor overlap is typical for all the CO_2 features in our spectra. This illustrates one strength of the broadband capability of the spectrometer – the ability to simultaneously fit multiple interfering absorbing species. The decreased accuracy of many HITRAN2012 spectral parameters at high temperatures is apparent in Figure 2-3. Because the temperature and species concentrations are extracted from a bandwide fit to hundreds of features, sensitivity to error in individual lines is greatly reduced. The spectrometer is mainly sensitive to overall systematic biases in the database parameters.

2.4.2 Time-resolved results

Figure 2-4 shows time-resolved temperature, H_2O and CO_2 concentrations during a 2.5 hour period that includes a temporary ignition of the supplementary burners and gas turbine shutdown. Each point represents a parameter extracted from a fit to a 60s average spectrum similar to Figure 2-3.

The temperature results are compared to an uncalibrated thermocouple approximately 0.8m below the laser beam and protruding an unknown distance into the exhaust flow. The plots show trend agreement between the frequency comb measurement and the thermocouple except for thermocouple lag during transients. We do not expect absolute temperature agreement because the thermocouple is uncalibrated and sampling a different region of the flow.

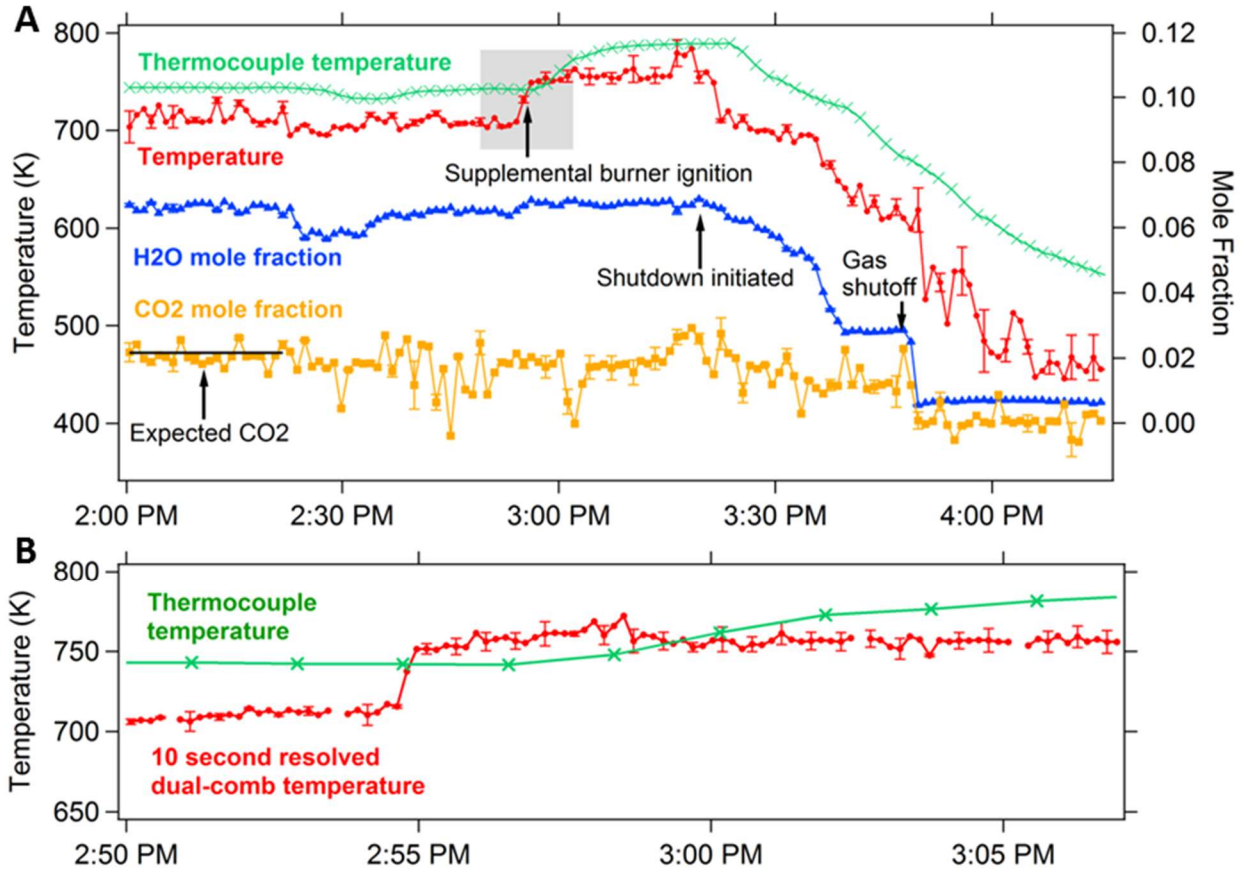

Figure 2-4-(A) Time-resolved measurements using the dual comb spectrometer (60s averages). Temperature from nearest uncalibrated thermocouples to the measurement location (1m separation). The horizontal line at early times on the CO_2 trace represents the expected value based on the measured excess oxygen. (B) 10 second averaged temperature data during supplemental burner ignition.

From 2:55 P.M. to 3:21 P.M. local time, the auxiliary exhaust duct burner was ignited, causing a rapid temperature increase immediately apparent with the frequency comb data but with some lag in the thermocouple data. Panel B of Figure 2-4 shows the measured temperature with 10 s average data during the startup transient of the exhaust duct burner. Four points were removed from the 10 s average data because of poor convergence of the spectral fit. At 3:21 P.M. the auxiliary burner was shut off and the turbine shutdown sequence commenced. This lasted until the fuel flow to the turbine was completely shut off at 3:49 P.M.. The post processing fitting routine was seeded with an initial temperature guess of 700K +/- 10K (randomly generated) for the entire data run, so no a priori temperature profile information was required to seed the fitting routine and track the temperature trend.

Figure 2-4 also shows the frequency comb-measured water and CO_2 concentrations. The expected CO_2 concentration based on the measured excess O_2 is represented by a horizontal line during the stable period prior to 2:30PM. The mean laser-measured CO_2 concentration matches the expected concentration to within 4.4%. The mean laser-measured H_2O concentration is higher than a simple stoichiometry calculation would suggest, which is expected given ambient water vapor in the intake air and steam injection into the combustor. At 3:49 PM, the natural gas flow to the turbine was shut off, and CO_2 concentrations fall to zero while the water concentration falls to the ambient level.

We iterated the calculations in post processing 15 times to obtain the standard deviation of the measured temperatures and concentrations at each step in the time series (represented by the uncertainty bars in Figure 2-4). Figure 2-4 shows every third deviation for clarity and the averages of all the deviations are : 1.2%, 1.0%, and 17.8% for temperature, H_2O, and CO_2, respectively. Note that the increased CO_2 deviation is due to the relatively weak CO_2 absorbance signal.

2.5 Summary

We demonstrate the first industrial application of a dual frequency comb spectrometer by measuring temperature, H_2O, and CO_2 concentration transients in the exhaust of a 16MW stationary natural gas turbine at the University of Colorado Boulder. The spectrometer was completely untethered from the laboratory, maintaining phase and mode locks for over six hours in a noisy industrial environment without the need for significant vibration isolation, ambient temperature control, cavity-stabilized reference lasers or an ultra-stable RF reference. Individual spectra measuring absorption on 16,000 distinct comb teeth were recorded at a rate of 12.4kHz and averaged for 10 or 60s. We simultaneously fit 279 H_2O and 43 CO_2 absorption features to obtain temperature and species concentrations. The measurements demonstrate the potential for a fieldable dual comb spectrometer with a unique combination of speed, bandwidth, and resolution that had so far only been exploited in a stable optics laboratory.

The published version of this chapter can be cited as:

Schroeder, P. J., R. J. Wright, S. Coburn, B. Sodergren, K. C. Cossel, S. Droste, G. W. Truong, et al. 2016. “Dual Frequency Comb Laser Absorption Spectroscopy in a 16 MW Gas Turbine Exhaust.” *Proceedings of the Combustion Institute*.

2.6 Acknowledgements

The work in this chapter was funded by the National Science Foundation under Grant Number CBET 1454496 and by the Advanced Research Projects Agency-Energy (ARPA-E), U.S. Department of Energy, under Award Number DE-AR0000539. The views and opinions of authors expressed herein do not necessarily state or reflect those of the United States Government or any agency thereof. The authors

would like to thank Torrey Hayden, Amanda Makowiecki, David Pfotenhauer, and Jinyu Yang for their help during the measurement campaign. We also thank Ken Morse, Victor Ferreira, Jeffery Fisher, Steve Burke, and the control room staff at the CU power plant for help and access to their equipment.

3 High temperature comparison of the HITRAN2012 and HITEMP2010 water vapor absorption databases to frequency comb measurements

A majority of text in this chapter is identical to the published version of the cited paper.

3.1 Introduction

As discussed in 1.1.2, gas properties are extracted from measured absorption spectra through comparison with an absorption model. The model is generated by combining a line shape function (e.g. Voigt, Lorentzian, etc.) with database values of the intensity, position, and broadening parameters for each transition. Water vapor absorption transition information repositories relevant to high temperatures are HITRAN2012 [10], HITEMP2010 [11], HITRAN2008 [68], and BT2 [19], which are composed of both measured and computed transition parameters spanning from 0-25,000cm^{-1}. We focus in this chapter on HITRAN2012 (HITRAN) and HITEMP2010 (HITEMP) because they combine BT2 and older versions of HITRAN and HITEMP with newer data and calculations. Additionally, these databases are carefully vetted and widely used by researchers from various fields.

A majority of the experimental data incorporated in HITRAN and HITEMP are collected with high resolution Fourier-transform infrared (FTIR) spectrometers in well-controlled optical cells at temperatures below 400K [69–72]. Experimental investigations of the databases at higher temperature are crucial because many line shape temperature-scaling effects – particularly line shift and broadening – cannot be easily computed nor accurately extrapolated from room temperature measurements. The line shape parameters for a small number of water vapor transitions have been measured at up to 2500K in shock tubes with narrow bandwidth diode laser sources, [89] or up to 3000K in flames with lower resolution spectrometers, [90]. Liu *et al.* [15] studied a similar temperature and pressure range as this chapter but examined fewer transitions at a lower frequency accuracy. They extracted line shape parameters from fits to 47 transitions and compared their results to HITRAN2004 [73], HITRAN2000 [74], and Toth [70]. Their fit intensities and air-broadening coefficients were typically within approximately 20% and 50% of the published data, respectively. They showed that the parameters could widely vary between databases and do not always extrapolate well above room temperature.

The databases have evolved significantly since the Liu et al. work (see Section 3.2.6). In this paper, we examine the ability of simulations using the HITRAN2012 and HITEMP2010 databases to accurately predict the absorption of more than 600 transitions measured with a broadband, high resolution dual frequency comb spectrometer at up to 1300K. Our measured spectra span from 6780cm^{-1} (1475nm) to 7217cm^{-1} (1385nm) with a point spacing of 0.0033cm^{-1} (0.68pm at 1429nm). The data were collected under carefully controlled conditions in a quartz optical cell contained within a high-uniformity furnace. To our knowledge, this is the broadest high resolution/accuracy test of high temperature absorption under carefully controlled conditions in an optical cell.

We demonstrate that at 1300K, HITEMP and HITRAN accurately predict the existence and position (within 0.033cm^{-1}) of >99% of transitions with intensity >1E-28 (cm^{-1}/molecule cm^{-2}) in the measured spectral region, despite having been developed without broadband high temperature experimental data. Further results of this paper include:

1) HITEMP more often predicts transitions that are not observed in the absorption spectra, while HITRAN more often fails to predict an observed line. Combined, both of these error types account for less than 1% of the more than 600 transitions examined in this chapter and fall

between a maximum intensity of 1e-23 (cm^{-1}/molecule cm^{-2}) and our approximate minimum detectable intensity of 1e-28 (cm^{-1}/molecule cm^{-2}).

2) The MARVEL line position updates [75] from HITEMP to HITRAN significantly improve the predicted line positions of weak transitions in HITRAN.
3) HITRAN more accurately predicts the air-broadened width of water vapor absorption features at high temperature thanks to improved power-law temperature scaling coefficients for air-broadening [76].
4) Both databases do not contain temperature scaling of the air-pressure shift parameters and self-broadening parameters. This leads to consistent, significant error in the line shape prediction at high temperature. The inclusion of a simple temperature scaling relationship for these parameters significantly improves simulations using both databases.

The results contained in this paper are valid up to 1300K. Measurements in much higher temperature flames suggest that HITRAN and HITEMP still require further refinement to predict spectra at those conditions [77].

3.2 Methods

We collect high resolution absorption spectra for pure water vapor and air-water vapor mixtures at five temperatures using dual frequency comb spectroscopy. This section describes the dual comb spectrometer, the high temperature optical facility, and the data collection and analysis methods.

3.2.1 Dual Frequency Comb Spectroscopy (DCS)

The DCS used in this chapter is detailed in 1.1.4.1 with 100MHz pulse repetition rates and, after filtering with a grating-based filter, spans from 6780.3cm^{-1} to 7217.7cm^{-1} [39,78]. This range encompasses 131,073 comb teeth spaced at 0.0033cm^{-1} (100MHz), and was chosen because it contains transitions that have been previously validated at high temperature and because the transitions in this region have highly variable lower state energy values (which is desirable for temperature sensing). We use dual comb spectroscopy to detect the absorption on each comb tooth across the spectrum after transmission through the high temperature cell by employing the techniques described in 1.1.3.2. In this chapter, interferograms are averaged for approximately 90 minutes for each measured spectrum to obtain absorbance SNR values of approximately 2000:1 across the 101,372 comb teeth spanning the central 400cm^{-1} of the spectrum.

3.2.2 Remote DCS

The experimental setup is detailed in Figure 3-1. At the time this data was taken, mobile DCS systems were not yet available [64,65]. The fixed DCS used here is located at NIST Boulder and the spectroscopic cell and high temperature furnace are located at the University of Colorado Boulder (CU). The dual comb spectrometer and spectroscopic cell are connected via two telecommunications optical fibers in the Boulder Research and Administration Network (BRAN) fiber bundle that join the separate labs over a distance of ~3km [79]. As shown in Figure 3-1 d-e, the light from the two frequency comb lasers is passed through these fibers to the CU laboratory. To avoid cross phase modulation, one fiber was used for each comb. Thermal gradients, nonequivalent strains, and mechanical vibrations induce a varying optical path difference between these fibers, resulting in differential phase noise between the two combs upon arrival at CU. To combat this, a portion of the cavity-stabilized 1535nm reference laser light is co-propagated in each BRAN fiber. After passing over the link, the 1535nm light in each fiber is separated from the frequency comb light with dense wavelength division multiplexers and interfered to create an error signal that represents the phase difference between the two fiber links. A servo loop and piezoelectric fiber stretcher (General Photonics FST-002) are used to null the error signal, effectively

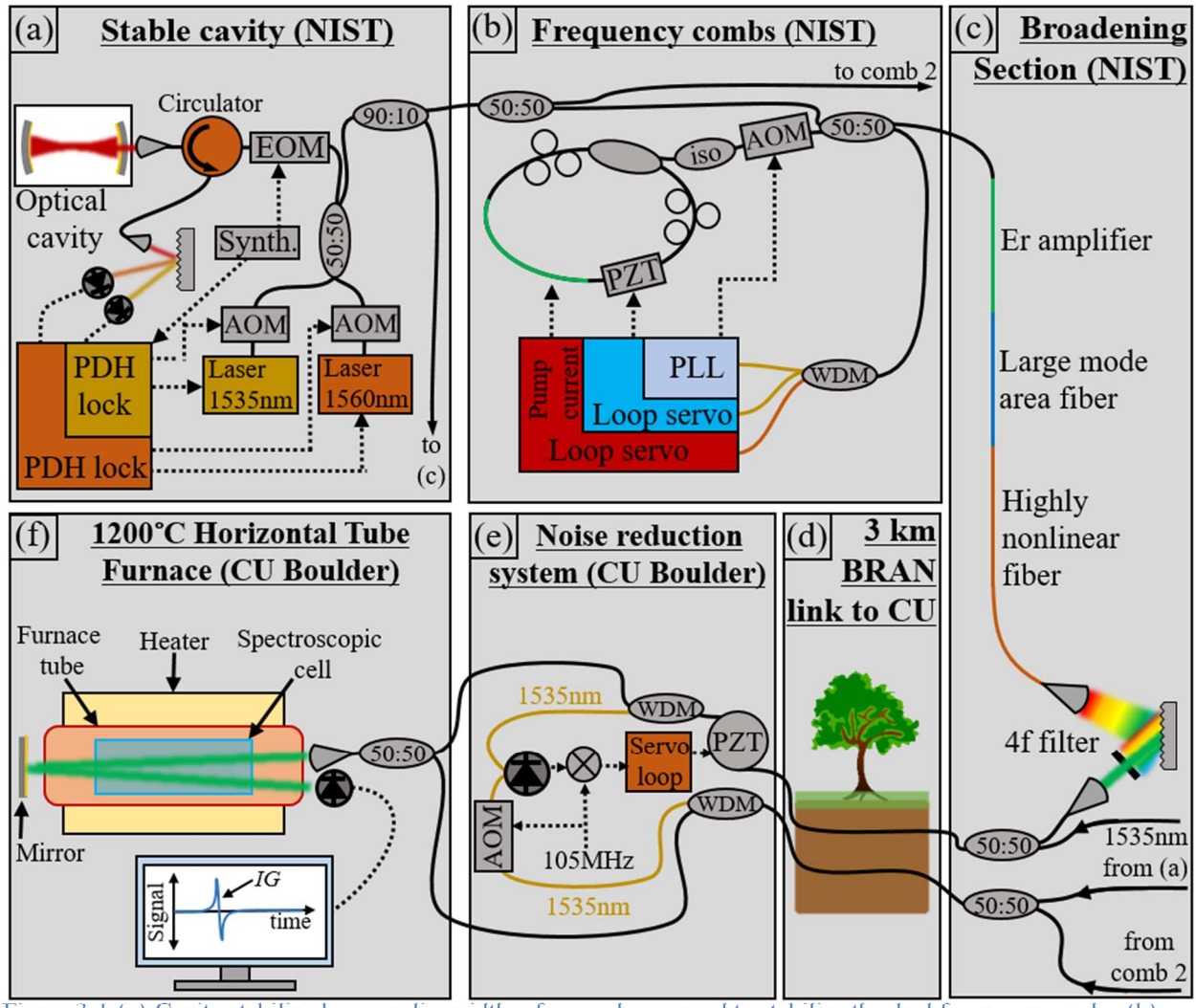

Figure 3-1-(a)-Cavity stabilized narrow linewidth reference lasers used to stabilize the dual frequency combs. (b)-Ring cavity frequency comb phaselocked to the two cavity-stabilized lasers. (c)- Amplification, pulse compression, broadening, and optical filtering. Only one comb system is shown in parts a-c, but the output from a second identical comb (with an offset repetition rate) is also transmitted over the BRAN link. In addition, 1535nm stable cavity light is added to the frequency comb light before transmission over the link. (d)-the 3km link between NIST and CU in the BRAN fiber network. (e)-The system employed to reduce noise on the combs from the BRAN fiber. The homodyne beat between the 1535nm light added to both fibers in (c) controls a piezoelectric stretcher that corrects for small optical path differences between the two fibers. (f)- Combined dual comb beam passing through the furnace and gas mixture of interest. The detected dual comb signal is then analyzed to generate a comb-tooth resolved absorption spectrum. Figure Key: AOM: acousto-optic modulator, EOM: electro-optic modulator, WDM: wavelength division multiplexer, PZT: piezoelectric stretcher, PLL: phase lock loop, PDH: Pound-Drever-Hall lock, 50:50 or 90:10: proportional splitter.

cancelling any differential optical path variations between fibers with a servo loop bandwidth of approximately 2kHz. This is adequate to control most noise sources imparted to the fibers between NIST and CU and increases the interferogram signal-to-noise (SNR) by a factor of 5 to 10. The BRAN link also exhibits typical telecom fiber OH absorption at 1397nm so that section of the spectrum is removed prior to data analysis (see Figure 3-2). The design and operation of the dual comb spectrometer apparatus is discussed in more detail in references [39,41].

3.2.3 High Temperature Optical Cell and Experimental Conditions

In the CU Boulder lab, the dual frequency comb light is combined onto a single, 1m long fiber and launched with an off-axis parabolic collimator through a three-zone horizontal tube furnace containing a fused silica optical cell (Figure 3-1f). The cell is 45.7cm in length and 5 cm in diameter, and located within the 47cm uniform-temperature central region of the furnace. Circulation of external cold air is prevented with end caps on the furnace tube. Each window on the cell is wedged at 3 degrees and mounted at a 1-degree tilt relative to the cell axis to reduce etalon effects. The light is double passed through the cell, creating a total path length of 91.4cm. All free space sections of the beam path outside of the cell are continuously purged with dry nitrogen to reduce ambient water absorption.

The experimental conditions are listed in Table 3-1. The temperature of the external wall of the gas cell was measured at six locations along its length with a Type K thermocouple and confirmed to vary less than +/- 5K from the set point (the total reported temperature uncertainty is described in Section 9.1). The reported temperatures assume that the temperature of the static gas mixture within the cell is in equilibrium with the cell wall temperature. Pressure is measured with a calibrated capacitance manometer (MKS Baratron 628C).

Mixtures are created with synthetic air (Airgas Ultra Zero Air, <2 ppm of H_2O and <1ppm of CO_2+CO) and high-purity, vacuum-degassed water (Honeywell CAS 7732-18-5) in a three-gallon stainless steel mixing chamber containing loose stainless steel ball bearings. After filling to the desired H_2O partial pressure and adding air to reach the desired total pressure, we vigorously agitate the mixture with the ball bearings for 15 minutes, followed by a 12-hour waiting period before introduction to the experiment.

To account for the well-known adsorption and desorption of water by surfaces in the tank and gas handling manifold [80], we extract the water vapor number density from the measured DCS spectra of the air-water vapor mixtures at each temperature. We use the HITRAN/HITEMP intensities of four water vapor absorption features that were previously validated at high temperature [14,56]. The measured DCS spectrum is fit with a Voigt profile with both the Doppler and Lorentz width floating for each of the four transitions. The area of each of the four fitted Voigt profiles is compared to the HITRAN/HITEMP intensity at the measured experimental temperature and pathlength to retrieve the water vapor number density using each transition. The reported number density is the mean of the number density retrievals from each transition. The number density uncertainty is reported as the standard deviation of the retrieved number densities from each different transition. Water vapor number density uncertainty for the pure water cases is based on the measured pressure drift in the cell over the course of an experiment (under the assumption that the only gas in the system is water vapor). The reader is referred to Chapter 9 for

Table 3-1- All experimental conditions and their uncertainties. All experiments span 6780-7217cm^{-1}, and an averaging time of 87 minutes. The pathlength for all measurements was 91.4±0.1cm.

	Experimental conditions and uncertainties		
	Temperature (K)	Pressure (Torr)	H_2O number density /1e17 (cm-3)
Air-Broadened	296 ± 2.2	581 ± 1.5	3.52±0.048
	549 ± 4.8	575 ± 1.5	1.84±0.010
	801 ± 6.2	578 ± 1.5	1.28±0.014
	1053 ± 8.3	574 ± 1.5	0.93±0.022
	1305 ± 9.9	578 ± 1.5	0.75±0.013
Pure Water	296 ± 2.2	9.00 ± 0.02	2.94±0.050
	549 ± 4.8	9.00 ± 0.02	1.58±0.027
	801 ± 6.2	9.00 ± 0.02	1.09±0.018
	1053 ± 8.3	9.00 ± 0.02	0.83±0.014
	1305 ± 9.9	9.00 ± 0.02	0.67±0.011

more details on the experimental uncertainty sources and calculations.

3.2.4 Background Subtraction and Baseline Correction

Figure 3-2 shows the data processing steps to get from the measured transmission spectrum to the final absorbance spectrum. The transmission spectra is a combination of the wavelength-dependent variations of the comb intensity, transmission optics, and detector response, small absorption features

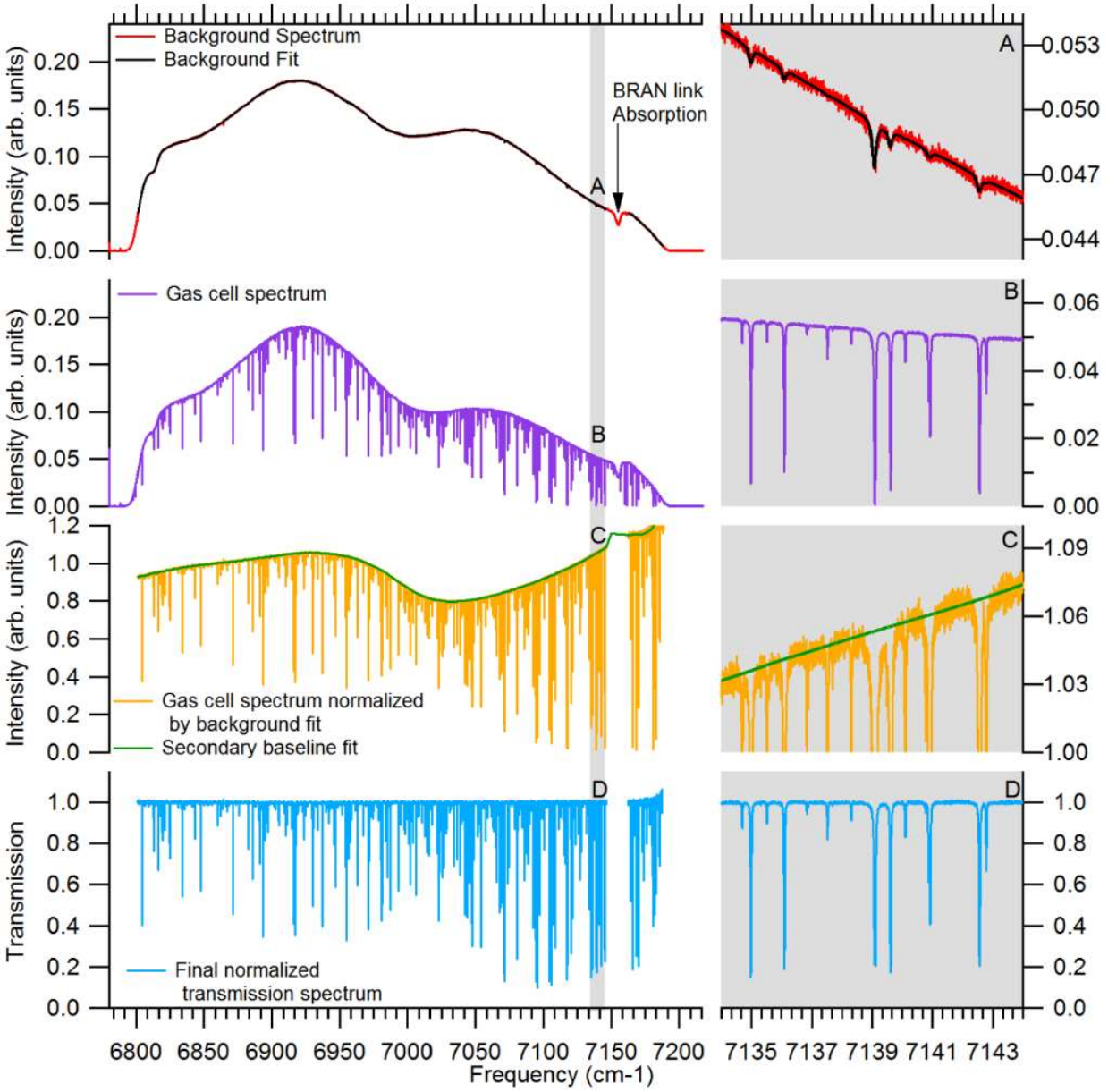

Figure 3-2- Processing steps for dual comb data. Panel A shows the measured background transmission spectrum acquired with the optical cell evacuated. Panel B shows an example spectrum with the optical cell filled with 9Torr of water vapor. The fiber OH absorption profile is removed from analysis. Panel C shows the normalized spectrum generated from the ratio of the trace in Panel B and the fit to the background spectrum of Panel A. Also, Panel C shows the fit, green trace, to the remaining slowly varying spectral variations using the technique mentioned in the text. Panel D is the final transmission spectrum after normalizing by the baseline fit in Panel C (green trace) Panel D is used in the comparison studies when transformed to absorbance. The insets show more detail in one region of the spectrum.

from residual water vapor in the purged regions outside of the optical cell, and finally the desired water absorption from the cell. As shown in Figure 3-2, the analysis has two steps to isolate the desired absorbance spectrum from the water vapor in the cell.

First, we acquire a background transmission spectrum measured with the cell under vacuum, Panel A. We maintain steady flow in the purge regions until the residual absorption is both small and stable before starting measurements. The small absorption features that remain are due to residual water vapor in the freespace regions of the beam path outside of the optical cell.

We then acquire a transmission spectrum with water vapor in the cell under the desired conditions. Panel B shows an example transmission spectrum with 9Torr of pure water vapor in the optical cell. The spectrum is typical of the spectra collected at other conditions.

A ratio of this spectrum to the background spectrum yields a partially normalized transmission spectrum, as shown in Panel C. (In practice we fit the background spectrum, shown as the black line in Panel A, and use this fit for the normalization to eliminate the transfer of noise from the background spectrum to the measurement spectrum.) The normalization removes the small influence of the background water vapor from the transmission spectrum, and partially removes the laser intensity variation. However, the comb intensity spectrum varies slowly over time (minutes to hours) so that the normalization of the measured spectrum by the background spectrum does not fully remove the laser intensity profile.

We remove the remaining "baseline" intensity variation using a similar method to the one described in the supplement to [39]. Spectra are divided into 25.35cm^{-1} (760GHz) windows (each containing approximately 250 individual absorption features) and fit simultaneously with a 10th order polynomial baseline and an absorption model based on temperature-scaled HITRAN data, discussed in Section 3.2.6. We tested varying window widths and polynomial baseline orders. A 25.35cm^{-1} wide window and a 10th order polynomial was chosen as it generates a fitted baseline (green line in Panel C) that did not respond to small differences between the modeled and measured absorption features (which appear as much sharper variations than the natural intensity variation of the combs, optics, and detector response). The blue trace in Panel D shows the final transmission spectrum after normalization by the baseline in Panel C, green trace. This final transmission spectrum is compared with models generated from HITRAN and HITEMP to extract the results in Section 3.3.

3.2.5 Spectrometer Uncertainty

We discuss the fidelity of the measured spectrum along three metrics: the wavelength accuracy of each spectral sample, the instrument line shape, and the instrument nonlinearity. Together these three metrics drive the ability of the DCS instrument to accurately reproduce the true absorption spectrum.

Wavelength referencing of the comb teeth and phase coherence between the combs is achieved by phase locking both combs to two cavity-stabilized reference lasers near 1535nm and 1560nm. The absolute optical frequency of the cavity-stabilized lasers is periodically measured against a hydrogen maser, using a fully self-referenced comb at NIST Boulder. In this way, the frequency accuracy of each DCS spectral sample point is better than 3.34e-6cm^{-1} (100kHz). Thus, the wavelength uncertainty of the system is very low compared to the line center uncertainties of the databases.

The spacing between points on a measured absorption spectrum is set by the comb tooth spacing of 0.0033cm^{-1} (100MHz). The resolution of each sample point is set by the comb tooth linewidth, which is approximately 3.34e-7cm^{-1} (10kHz) at the comb source, and <3.34e-6cm^{-1} (100kHz) after delivery of

the laser light to the experiment over the BRAN link. Thus the instrument line shape is negligible, given the ~GHz linewidths of water vapor absorption features.

Phase noise, detector, amplifier, and analog-to-digital conversion nonlinearities can lead to very slight distortion of the measured spectrum. We maintain low phase noise, and limit average power on the detector to <100μW to achieve very low spectral distortion. Using the same spectrometer and similar detector power limitations as presented here, references [41] showed that fits to narrow Doppler profiles resulted in no residual structure above the experimental noise. Based on this we estimate the nonlinearities contribute to less than 1e-3 absorbance (0.1%) uncertainty in the retrieved absorption magnitude.

Finally, the absorbance uncertainty due to the baseline removal procedure detailed in Section 3.2.4 and [66] is estimated to be 1e-3 absorbance. This value was computed as the maximum deviation of the baseline across a range of baseline fit window widths (7.7cm^{-1}-76.7cm^{-1}) and polynomial orders (4th to 14th order). There is additional baseline noise due to residual phase noise between the combs, but this effect should be negligible here because of the low residual phase noise of this dual comb system and the long averaging times [81].

3.2.6 HITEMP/HITRAN Source Data

This section will briefly discuss the relationship of HITRAN and HITEMP to each other and earlier databases. We also summarize specific updates and modifications relevant to the primary isotopologue of water over the wavenumber range studied in this chapter.

Figure 3-3 illustrates the evolution of HITEMP to HITRAN with the published databases. HITEMP2010 stems from BT2. BT2 contains over 505 million transitions for water vapor, so the HITEMP authors included only transitions with "significant intensity" between 296 and 4000K and with J<50 [11]. This intensity limit created the base dataset for HITEMP and reduced the size of the database to 111 million transitions, including 2.2 million in the spectral frequency range investigated here with intensities as low as 1e-70 (cm^{-1}/molecule cm^{-2}). Next, the HITEMP authors replaced any BT2 position and intensity entries with data from HITRAN2008 if the HITRAN2008 transition line centers were within 2cm^{-1} of the BT2 values. If there was a known doublet in the HITRAN2008 data, the HITRAN2008 position was used with the BT2 intensity. The Semi-Empirical Line Position (SELP) list, which calculated line centers using experimentally measured transition energy levels, supplanted the BT2 data where available [11,82]. The primary position assignments for weak transitions in HITEMP come from BT2 and Gordon *et al.* [19,83], while the work of Toth *et al.* [84] covers the strong, room temperature active lines. This progression is shown in Panel A of Figure 3-3. Table 3-2 shows the line position and intensity content of the HITEMP and HITRAN databases. The transition from BT2 line positions in HITEMP to the use of MARVEL for line position information in HITRAN is apparent. Intensities still primarily come from Toth [84] and BT2 in HITRAN. When no accurate self- or air-

Table 3-2-Number of lines and their sources in the HITRAN and HITEMP databases for the frequency range investigated in this chapter. The inclusion of the MARVEL database is apparent in HITRAN as well as extensive use of BT2 for intensities for both databases.

	HITEMP2010 Content		HITRAN2012 Content	
	Position	Intensity	Position	Intensity
BT2 [19]	25,523	44,826	93	4,249
MARVEL [75]	-	-	4,188	-
Toth Database [84]	1,488	1,488	1,449	1,488
Gordon [83]	22,303	-	77	-
Total modeled lines	46,314		5,737	

broadening parameters existed for a transition, coefficients were calculated using the technique of Gordon *et al.* [85]. They calculated the broadening coefficients by combining experimental and computational data in a filtering algorithm, as outlined in the reference. Finally, the temperature dependence of the air-broadening exponent, n, was calculated using complex Robert-Bonamy (CRB) theory [86] unless HITRAN2008 already contained accurately measured values. For the comparisons in our work, we employed an intensity cutoff of 1e-38 (cm^{-1}/molecule cm^{-2}) – approximately 10 orders of magnitude lower than the smallest detectable features in our measured absorption spectra – to reduce the size of HITEMP to 46,314 lines for computational convenience.

Perhaps not widely known in the applied spectroscopic community, HITRAN2012 utilizes HITEMP2010 as its base dataset, as shown in Panel B of Figure 3-3. HITRAN broadly employs the MARVEL procedure developed by Tennyson *et. al*, [75] which generates a list of allowed transitions between empirically derived energy levels. MARVEL mostly replaced the BT2 positions, except where accurate HITRAN2008 values were already present. The HITRAN authors used an intensity cutoff of room temperature intensity values of 1e-29 (cm^{-1}/molecule cm^{-2}) to reduce the extremely large number of lines in HITEMP to a more computationally manageable number (5,737 over our region). The HITRAN authors again employed the method by Gordon *et al.* [85] to calculate the self- and air-broadening coefficients, excluding known outliers and including experimental data when available. Over the wavenumber region examined here, CRB calculations of n were widely replaced. Birk and Wagner studied pure water and water/air mixtures from 1250-1750cm^{-1} at 205-315K to determine n for a range of rotational quantum numbers [76]. As described in HITRAN2012 (and its references and source file), transitions in HITRAN2012 that share the same rotational quantum assignment as transitions studied by

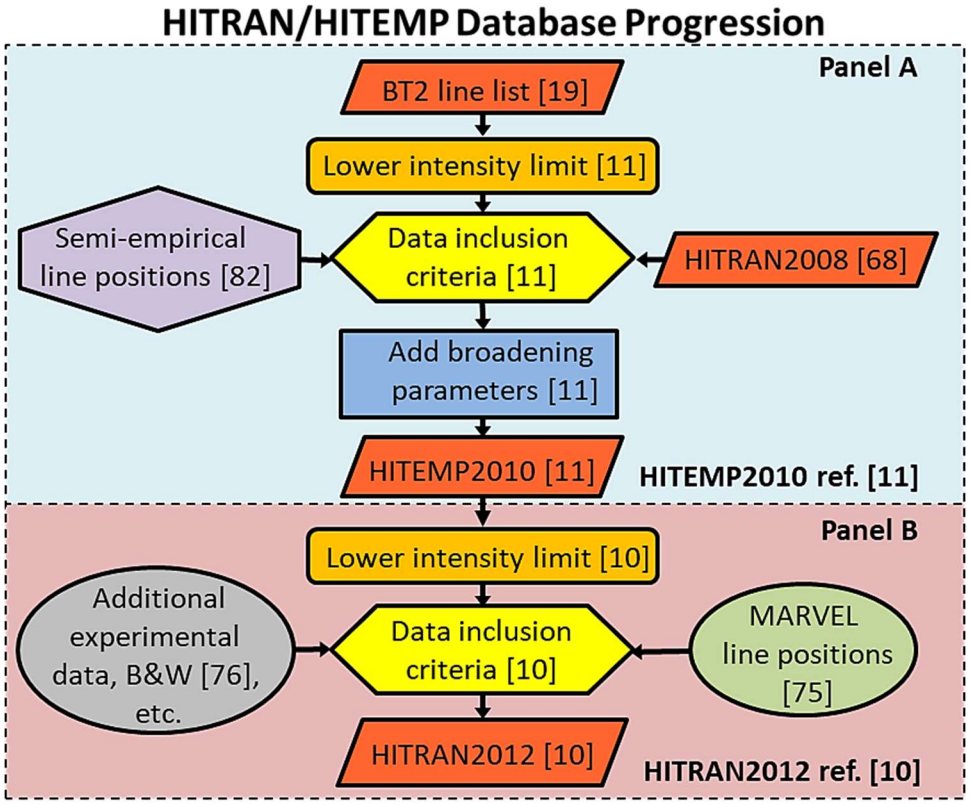

Figure 3-3- Evolution of HITEMP2010 and HITRAN2012 databases. The orange-red trapezoids indicate the final databases in their published form.

Birk and Wagner adopt their n value [76] (reference 20 in the HITRAN references and sources file). If there was no direct match between the rotational states of a HITRAN line and a line studied by Birk and Wagner, the HITRAN line was given the value corresponding to the average of n as a function of J" from Birk and Wagner's data (reference 22 in the HITRAN references and sources file). Finally, over this range, a few weak lines retain n from HITEMP. Readers are referred to the HITRAN2012 publication for more information about modifications and data sources for lines outside of our wavenumber range and molecules other than the primary isotopologue of water. As described in 3.3, these updates of n significantly improved the accuracy of predicted line shapes at all elevated temperatures.

Neither HITRAN nor HITEMP has been systematically tested with controlled high temperature, high resolution, broadband water vapor absorption data, which motivates the work described in this paper.

3.3 Results and Discussion

3.3.1 Water Vapor in Air Mixture

This section compares spectra collected for air/water vapor mixtures at the conditions presented in Table 3-1 with absorption models calculated using Voigt profiles and HITRAN and HITEMP data.

3.3.1.1 Database Assessment

The performance of the HITEMP- and HITRAN-based absorbance models was first assessed by overlaying measured spectra, (e.g. see panel D of Figure 3-2) with models generated at each corresponding temperature/pressure/concentration condition. The entire spectrum was analyzed on a line-by-line basis for transitions with SNR values greater than 2.5.

Four types of prediction errors were categorized and recorded:

1) Data No Model (DNM) describes lines that are observed experimentally, but are not predicted by the model.
2) Model No Data (MND) describes lines that appear in the model, but are not observed experimentally.
3) Shift describes a line that is measured at a different wavelength than predicted in the HITRAN model. This includes frequency shifts induced by the lack of a temperature-dependent air-pressure shift in HITRAN and HITEMP (see next section).
4) Not Clear is used to describe an error between the data and the model which does not fall clearly into one of these categories.

Figure 3-4 shows examples of each of the types of database errors, and Table 9-2 lists all identified error occurrences, type, and wavenumber for each database.

Table 3-3- Summary of recorded errors as presented in Section 9.2. See Section 3.3.1.1 for a brief description of each error type.

	296 K			549K			801K			1053K			1305K		
	HITEMP	HITRAN	Common	HITEMP	HITRAN	Common	HITEMP	HITRAN	Common	HITEMP	HITRAN	Common	HITEMP	HITRAN	Common
DNM	0	1	0	1	1	0	6	2	2	8	4	5	8	16	9
MND	0	0	0	4	1	3	9	2	3	14	1	5	22	1	6
Shift	0	0	0	1	0	92	2	6	207	5	9	281	13	16	313
Not Clear	0	0	0	0	3	2	0	3	1	0	4	1	0	0	1
Total	0	1	0	6	5	97	17	13	213	27	18	292	43	33	329

Table 3-3 shows a summary of line prediction errors that were identified in each of the databases. Due to line blending, doublets, and temperature dependence, the exact number of lines at each temperature is difficult to estimate, but greater than 600 lines were examined for each temperature condition. The "common" column in the table indicates database errors that are common to both HITRAN and HITEMP. Excluding

frequency shift errors, less than 1% of the total lines examined are reported as either MND, DNM, or Not Clear. Database errors between predicted and measured lines mostly occur for intensities less than approximately 1e-23 (cm^{-1}/molecule cm^{-2}). One strong transition located at 6854.163cm^{-1} appears in both models at all elevated temperatures, yet was never observed experimentally (indicated in Figure 3-5 and Figure 3-7 with an "*"). The position and intensity of this transition are computed, not measured, in references [19,83], respectively.

Overall, this study shows that HITEMP is more likely than HITRAN to predict unobserved transitions (MND errors) whereas HITRAN is more likely to omit a measured transition (DNM error), though HITEMP also exhibits this problem. This decrease in MND errors for HITRAN is a result of the combination of the MARVEL line assignment, as described in Section 3.2.6. Essentially, the changes to HITRAN reduced the prediction false-positive rate at the expense of occasionally omitting a weak transition.

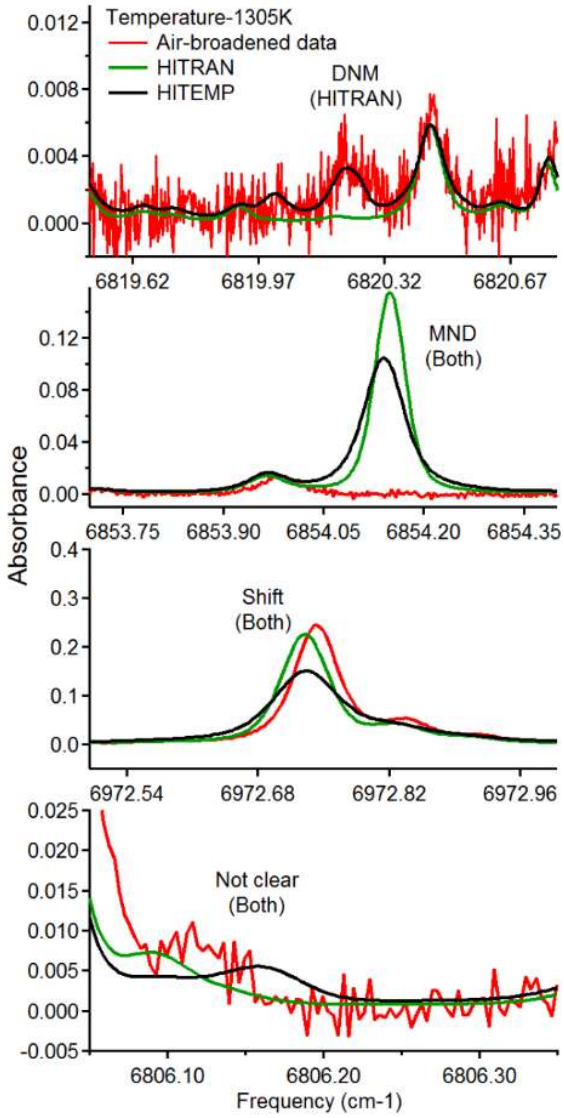

Figure 3-4- Examples of database error types. The MND example is the spurious line indicated by "*" below in Figure 16.

3.3.1.2 Temperature Scaling

The existence of most transitions with intensities stronger than 1E-28 (cm^{-1}/molecule cm^{-2}) is captured by both databases. For these transitions at elevated temperatures, our comparisons show that HITRAN is typically a more accurate predictor of line shape, strength, and position when compared to HITEMP. This is primarily because HITRAN includes improved temperature dependence of air-broadening widths, as discussed below, but also because the updated line assignments in HITRAN correctly locate weak transitions in the wings of the strong features. However, both databases still lack temperature dependence of the self-broadening and air-pressure shift coefficients. We will show below that the inclusion of simple scaling relationships for these parameters greatly improves the accuracy of the model.

Figure 3-5 compares the dual comb spectra with models. The HITEMP and HITRAN databases incorporate standard temperature scaling of air-broadened half width according to [67]:

$$\gamma_{air}(T) = \gamma_{air}(296)\left(\frac{296}{T}\right)^{n}$$

where $\gamma_{air}(296)$ and n are the air-broadening and air-broadening temperature scaling parameters provided by the databases and T is the gas temperature in Kelvin. This relationship is based on the reduction in density of the broadening partner at elevated temperatures. The exponent, n, is transition-

Table 3-4- Differences between the temperature-dependence of the air-broadening coefficient, n, for HITRAN and HITEMP for the transitions examined in Figure 16B. All n values for HITRAN and HITEMP shown here are from [76] and [85], respectively. The lines indicated with "J" avg." are values from [76] averaged over J" while "B&W" lines correspond to transitions with the same rotational quantum assignments. Bold, italic entries indicate a doublet. The source for all HITEMP n values here is complex Robert-Bonamy calculations. Table key: ν-line center, $S(296K)$-Linestrength, n-air-broadening temperature dependent exponent, src.- source.

HITRAN				HITEMP		
ν (cm^{-1})	$S(296K)$	n	Src.	ν (cm^{-1})	$S(296K)$	n
Column 1 Lines						
6972.739031	***2.100E-23***	***0.39***	***J" avg.***	***6972.739319***	***2.106E-23***	***-0.24***
6972.747618	***6.306E-23***	***0.39***	***J" avg.***	***6972.748591***	***6.323E-23***	***-0.24***
6972.809860	1.727E-23	0.61	J" avg.	6972.809860	1.727E-23	0.5
6972.845120	6.858E-23	0.29	B&W	6972.845120	6.858E-23	-0.2
6972.920820	2.445E-23	0.21	B&W	6972.920820	2.445E-23	-0.2
Column 2 Lines						
7047.684236	***1.031E-21***	***0.56***	***J" avg.***	***7047.684017***	***1.034E-21***	***-0.07***
7047.687745	***3.430E-22***	***0.56***	***J" avg.***	***7047.688450***	***3.439E-22***	***-0.07***
7047.692971	2.068E-25	0.48	J" avg.	7047.693923	2.074E-25	0.41
7047.694842	4.566E-26	0.24	J" avg.	7047.698879	4.578E-26	0.45

and broadening- partner specific so a unique value is provided for each categorized line. The improvement shown in Figure 3-5 of HITRAN over HITEMP is primarily based on the work in HITRAN to improve the temperature-scaling exponent values. The values contained in HITEMP are largely theoretical calculations based on complex Robert-Bonamy theory [86]. For example, Table 3-4, shows the significant difference between the CRB values from HITEMP and those presented in HITRAN. Detailed views of the line shape improvement at 1305K due to these changes in n are shown for two representative absorption features in Figure 3-5, Panel B. These improvements are representative of other transitions across the spectra.

In addition to the temperature dependence of the air-broadening half width, there is a similar temperature dependence to both the self-broadening half width and air-pressure shift. Power-law scaling exponents for neither of these effects are listed in HITRAN or HITEMP. It should be noted that the most recent version of HITRAN Online makes accommodation for a linear pressure scaling defined as $\delta(T) = \delta(T_o) + (T - T_o)\delta'$ where T_o and δ' is a reference temperature and shifting coefficient, respectively. Each of these parameters can be published for one of four defined temperature ranges [12]. As of the publication of this dissertation, there was no δ' data for any of the transitions in our spectral region for either the 200-400K or >400K ranges, so the linear relation was overlooked in favor of the power law. Other authors have used the power law for some water/air lines to reliably fit pressure shifts up to 25atm at 1050K and showed that most lines tended toward an exponent near unity [15]. Importantly, an accepted temperature scaling relation valid for large temperature ranges for the pressure shift coefficient has yet to be determined [75] and a power law relation is easily approximated by linear segments if desired. The refinement shown in Figure 3-5 for HITRAN_TS and HITEMP_TS was accomplished by including additional power-law scaling relations for these line shape parameters. We applied constant power-law temperature scaling relations since they are commonly used in the community, though they have been reported to be inaccurate over large temperature ranges [87].

Temperature dependence of air-pressure shift was included in the _TS models according to [67]:

$$\delta_{air}(T) = \delta_{air}(296)\left(\frac{296}{T}\right)^{1}$$

where $\delta_{air}(T)$ is the HITRAN provided air-pressure shift coefficient in units of cm^{-1}/atm. Line-center shifts due to air-pressure occur when collisions distort the intermolecular potential of an absorber thus

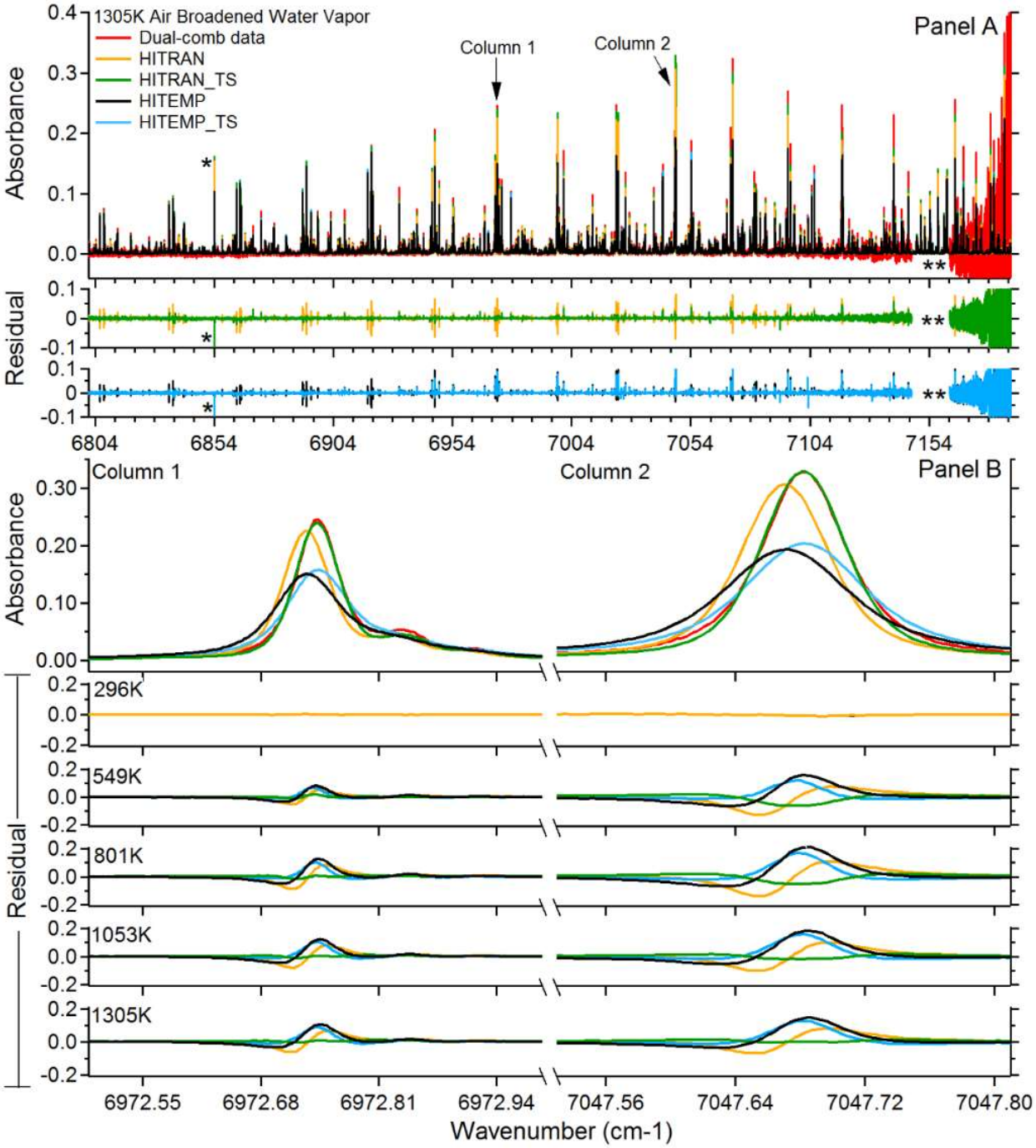

Figure 3-5-Panel A shows HITRAN and HITEMP, and HITRAN and HITEMP with additional temperature scaling parameters (HITRAN_TS and HITEMP_TS) compared to the measured spectrum at 1305K. The line marked with "*" was the strong, temperature dependent line predicted by both databases that was not observed in the data; its residual peak is clipped in order to visualize the residual structure elsewhere. Panel B shows two examples of the agreement between the temperature-scaled HITRAN model and the high temperature data. Most strong lines across the spectrum have similar agreement. Panel B also shows the development of the residual structure for all the models at each measured temperature.

changing the amount of energy required to transition between states (shifting transition line centers). As temperature increases, the gas becomes less dense which results in fewer line-shifting collisions. The unity exponent was chosen since other authors' correlations, which tend to predict values between 0.5 and

1, do not cover our spectral window and/or gas temperatures, nor have they been widely adopted as standards [86,88,89]. Figure 3-6 shows the normalized, bandwide root-mean-squared (RMS) of the residual between the HITRAN model and the measured air-water mixture absorbance data for different values of the air shift temperature-scaling exponent. The analysis was performed with the 1305K data, where the effect of the temperature dependence of the air shift is most significant. One can see that the RMS of the bandwide residual is minimized around 1.0. The residual remains low for exponent values >1.0 because the power-law temperature scaling asymptotes at increasingly higher values of the exponent.

We found that omission of the temperature dependence of the air shift term contributed to the majority of the recorded shift errors in Table 3-3 at every elevated temperature. The shift between unscaled HITRAN in Figure 3-5B, (gold trace) and the measured feature, is of typical magnitude of a "Shift" error (approximately 0.0133cm^{-1}). When the above expression is included, many predicted transition locations are significantly improved and brought within the +/- 0.0033cm^{-1} point spacing of the spectrometer. Since transition peaks were manually selected in this chapter, the shift data should be interpreted as a qualitative analysis of the magnitude of each shift. Nonetheless, these results support the inclusion of simple temperature scaling for air-pressure shift parameters at elevated temperature.

The second addition to the _TS models was the temperature dependence of the self-broadening width [67]:

$$\gamma_{self}(T) = \gamma_{self}(296K)\left(\frac{296}{T}\right)^{1/2}$$

where $\gamma_{self}(T)$ is the HITRAN provided self-broadening coefficient in cm^{-1}/atm. From simplified kinetic theory, collisions transfer energy between available modes and reduce the lifetime of an excited state of an absorber, thus broadening the transition. As temperature increases, these collisions become less frequent thereby reducing this effect and narrowing the transition. When calculating γ_{self} for these assumptions relative to a reference temperature, the $1/2$ exponent results from assuming a constant optical cross-section [67]. Figure 3-6 also shows the bandwide RMS of the residual between the HITRAN model and the 1305K measured absorbance data for different values of the self-broadening temperature-scaling exponent. The choice of 1/2 for the self-broadening term minimizes the residual.

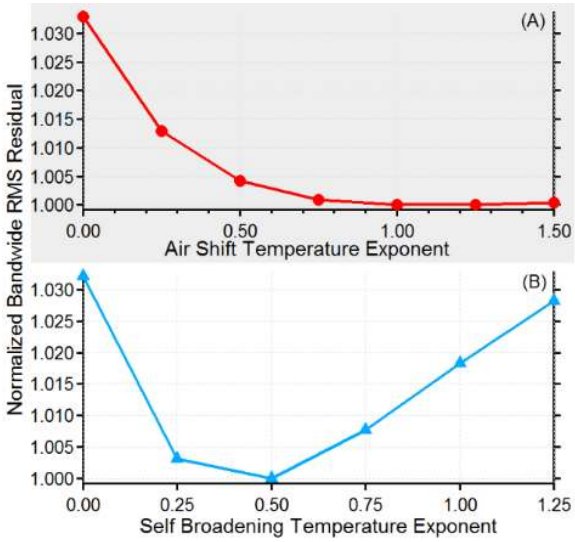

Figure 3-6-A qualitative examination of different exponent values for both air-shift (A) and self-broadening (B). The normalized RMS error was calculated for the entire residual for the 1305K spectra.

This self-broadening temperature-scaling expression narrows the collisional width from water vapor self-broadening by 47.6% at 1305K and improves the model/data match. Water vapor comprises only 2% of the mixture but since water vapor self-broadening coefficients are approximately an order of magnitude larger than corresponding air-broadening coefficients, appropriate temperature scaling quickly becomes important as water concentration increases. The systematic underprediction of absorbance peaks across the spectrum for HITRAN is due, in part, to the exclusion of the self-broadening temperature scaling and was present for all temperatures above room temperature.

As seen in Figure 3-5, with the inclusion of these additional temperature-scaled parameters, the HITRAN_TS model (green trace) is the most accurate predictor of line shape and absorbance magnitude. The left column in Figure 3-5, Panel B displays a strong line slightly blended with a weak neighbor. The strong feature is well predicted by the scaled HITRAN model though there is still a significant residual between the weak feature for all variants of the databases.

As shown in this section, HITRAN line shape parameters should be favored for strong transitions over HITEMP for air-broadened water measurements up to 1305K. HITRAN more accurately models the measured spectra, thanks in large part to the improved the prediction of n, the MARVEL inversion line assignment technique, and inclusion of simple temperature scaling expressions for air-pressure shift and self-broadening. The databases would further benefit from measurements of transition-specific values for the self-broadening and air-pressure shift temperature scaling exponents.

3.3.2 Pure Water Mixture

In this section, we investigate the predictive capability of HITRAN and HITEMP for low-pressure pure water vapor (9Torr) at all five previously listed temperatures. Typically, for intensities greater than approximately 1e-23 (cm^{-1}/molecule cm^{-2}), similarity between the databases is identical or minimally different, with both adequately predicting measured spectra up to 1305K. Noticeable differences begin to occur when examining intensities weaker than 1e-23 cm^{-1}/molecule cm^{-2} since the MARVEL line assignment work frequently supplants the BT2 data. Again, both databases suffer at high temperatures from a lack of a self-broadening temperature-scaling exponent, resulting in models with broader transitions than the measured spectra. Temperature dependence of self-shift was not considered here both because of the lack of self-pressure shift coefficient and relatively low cell pressure of 9Torr (so that self-pressure shift is negligible).

Figure 3-7 displays a spectrum-wide comparison of measured and modeled spectra at 1305K with expanded views of standard examples of strong transitions. Slight systematic underprediction is present for almost all resolvable lines of the unscaled models, which results from the lack of a temperature scaling exponent for self-broadening. Bandwide residuals are reduced when temperature scaling is included, as shown in the HITRAN_TS and HITEMP_TS see Figure 3-7, Panel A. Panel B shows an expanded view of two sets of lines where temperature scaling corrects the slightly underpredicted peaks. The agreement between the simple temperature-scaled models and the measured spectra is impressive given the lack of high temperature validation measurements in HITRAN or HITEMP and the constant self-broadening exponent used on all transitions.

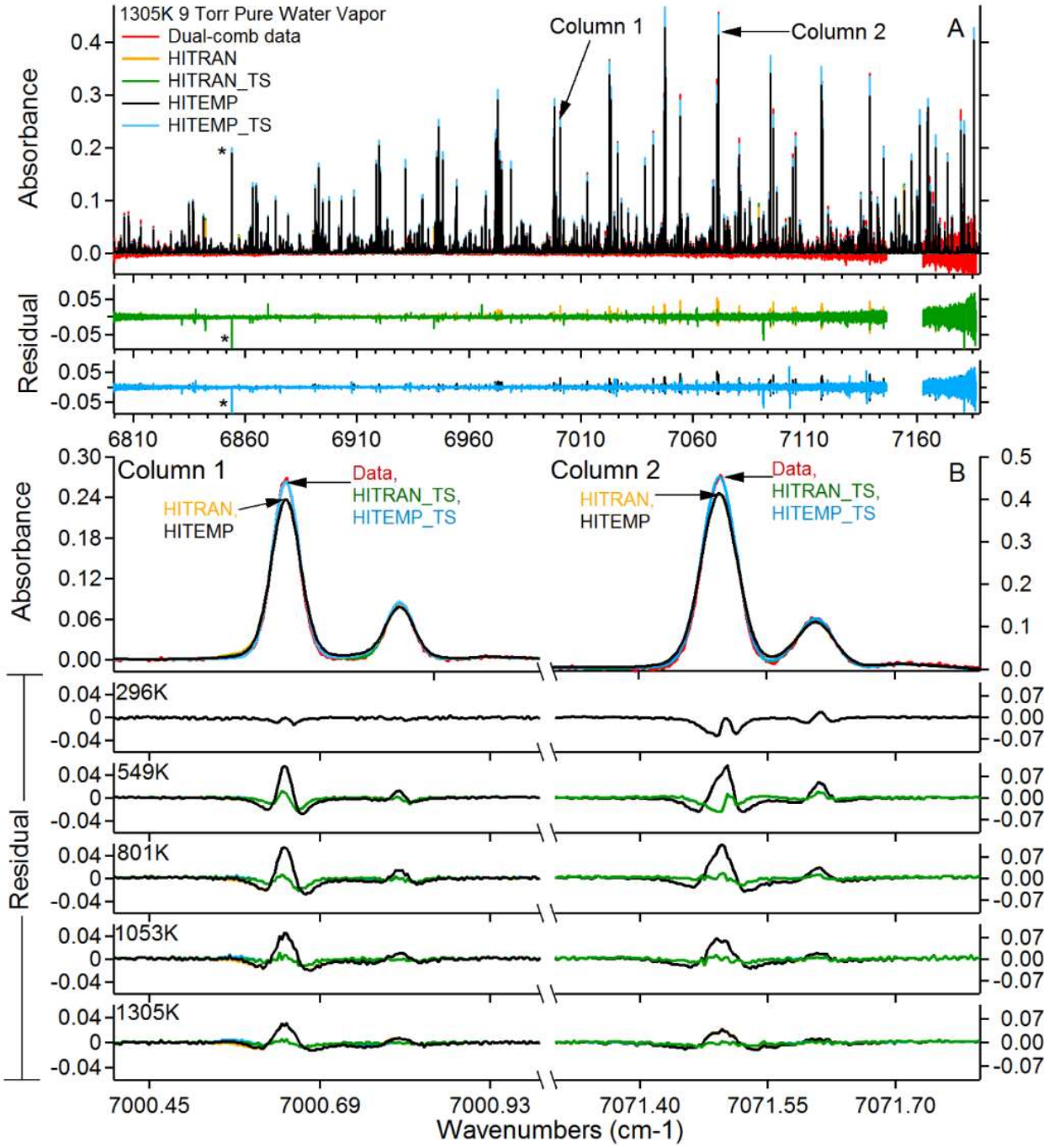

Figure 3-7-Panel A shows model comparisons to measured pure water vapor spectrum at 9Torr and 1305K over the entire spectrum. HITRAN and HITEMP both have almost identical self-broadening values across the spectrum, which is why the HITRAN/HITEMP traces overlay exactly. Panel B shows expanded views of two example lines. As in Figure 6, Panel B shows the residual structure for all temperatures up to the maximum of 1305K.

3.4 Conclusion

We performed the first high temperature comparison of HITRAN2012 and HITEMP2010 models to broadband, high resolution experimental spectra under carefully controlled conditions. The data was collected with a dual comb spectrometer, leveraging the high resolution, absolute wavelength scale, and broadband nature of the combs.

HITRAN is a more accurate predictor of strong, near-infrared water vapor absorption for air-broadened water vapor spectra up to 1305K, producing fewer line shape and intensity prediction errors than HITEMP. The improvement for the strong features is a result of improved air-broadening temperature scaling coefficients in HITRAN. The accuracy of the line shape predictions is increased further when simple temperature scaling relations are used to modify air-pressure shift and self-broadening coefficients. Concerning weak transitions with intensities below approximately 1e-23 (cm^{-1}/molecule cm^{-2}) and above the minimum resolvable intensity for our absorption spectra of 1e-28 (cm^{-1}/molecule cm^{-2}), we show that HITEMP more often predicted a transition that was not observed while HITRAN more often failed to produce a modeled transition for an observed line. This is a result of MARVEL line assignment work and the large reduction of transitions in HITRAN as compared to HITEMP (2.2 million in HITEMP, reduced to 46,314 here, compared to 5,737 in HITRAN). Inclusion of the simple temperature-scaling relationship for self-broadening improves the pure water vapor predictive capability of HITRAN and HITEMP. Therefore, until measured, line-by-line temperature-scaling parameters are available for air-pressure shift and self-broadening, simple scaling relationships should be included for modeling of high temperature pure and air-broadened water spectra.

Since this chapter represents the first instance of a broad, high temperature comparison, the efficacy of the databases outside our spectral region or above our measured temperature is unknown. Our results provide valuable information regarding the accuracy of both models at elevated temperatures and test simple temperature scaling relationships for air-pressure shift and self-broadening in each database. We expect further improvements in the future by employing multispectral fitting techniques to extract line-specific temperature scaling parameters from this data.

The published version of this chapter can be cited as:

Schroeder, P. J., D. J. Pfotenhauer, J. Yang, F. R. Giorgetta, W. C. Swann, I. Coddington, N. R. Newbury, and G. B. Rieker. 2017. “High Temperature Comparison of the HITRAN2012 and HITEMP2010 Water Vapor Absorption Databases to Frequency Comb Measurements.” *Journal of Quantitative Spectroscopy and Radiative Transfer*.

3.5 Acknowledgements

Support for this chapter was provided by the National Science Foundation under grants CBET 1336643 and 1454496. The authors wish to thank J. Steinbrenner, S. Coburn, and N. Hoghooghi for help with the preparation of this chapter.

4 Multispectral fitting validation of the speed dependent Voigt profile for high temperature water vapor absorption with a dual frequency comb spectrometer

A majority of text in this chapter is identical to the published version of the published paper.

4.1 Introduction

As stated in 1.1.1, absorption spectroscopy is a useful diagnostic tool used in many fields of research, from planetary/exoplanetary science to combustion, that rely on accurate measurements in high-temperature gaseous environments. Absorption spectroscopy is useful for remotely investigating these high-temperature systems [6–8], but its accuracy is entirely linked to the existence of well-vetted spectroscopic databases (e.g. HITRAN2012 [10]) and lineshape models to enable interpretation of measured spectra. Voigt profiles are traditionally used to describe the lineshapes of individual absorption transitions, and opacity models involve summations over many of these transitions. Unfortunately, the Voigt model neglects several collisional effects, such as the frequency of velocity-changing collisions, also known as Dicke narrowing, and speed dependence of the collisional broadening coefficient. These omissions can limit data/model agreement to about 2% at the line center of transitions for pure water [90,91] and up to 10% for air- or N_2-broadened water [69,89]. Additionally, the temperature dependence of the lineshapes is not adequately captured in the simple Voigt profile. Conventionally, temperature scaling has been incorporated through a power law $(296K/T)^n$ to scale broadening and pressure-shift coefficients with temperature. This expression has only been experimentally investigated for high-temperatures in a few studies, and has been shown to produce non-physical, negative values for the transition-specific temperature-scaling exponent n when using Voigt profiles with air [76,92] and water [14] as the broadening partners above approximately 400K. Prior to the present chapter, it was unknown if these same failings would occur with water self-broadening using beyond-Voigt line shapes or if a single exponent could model broad temperature ranges. Here, our data suggests that the higher order collisional effects not modeled by the Voigt profile may be the culprit for past water vapor temperature-scaling inaccuracies. This chapter is the first broadband, high resolution, multispectral fit data set to separately examine the effectiveness of advanced profiles for high temperature water vapor, and helps to inform water self-broadening theory at a larger temperature range than previous studies. We achieve this using the DCS described in 1.1.4.1 measuring water vapor from 296-1305K, 1-17Torr, and 6800-7200cm^{-1}.

4.2 Experimental Setup

Reference [66] and section 3.2 describe the technique, spectrometer, and system in detail. The collection of the data in this chapter was completed prior to the advent of the mobile DCS systems described in section 2.2 and [65], so the DCS described in 3.2 was utilized, Figure 4-1 and Figure 3-1. The spectrometer has a point spacing of 0.0033cm^{-1}, absolute frequency accuracy of <3.34e-7cm^{-1}, tooth linewidths of <3.34e-6cm^{-1}, and can span from 5800-7400cm^{-1} (filtered here to span 6800-7200cm^{-1}) [66].

4.3 Spectral Analysis

Advanced lineshapes incorporating velocity-changing collisions and speed dependence are a potential remedy [13] for more accurate and physically reasonable temperature scaling. However, the efficacy of these higher order collisional mechanisms and scaling over large temperature ranges is largely unexplored in water due to the lack of broadband, high-resolution spectra at high temperatures. For

example, prior to the present work, it was unknown if non-physical temperature-scaling exponents would occur for water self-broadening using advanced lineshapes or if a single exponent could model broad temperature ranges. Here we compare the ability of speed dependence and velocity-changing collision mechanisms to model high-temperature spectra. Briefly, velocity-changing collisions reduce the Doppler width of a transition when there are multiple collisions over the distance traveled by a molecule following photon absorption [93,94] and are represented here by the Rautian profile in the hard collision limit [95]. Speed dependence accounts for long-range dipole-dipole coupling and the effect of relative broadener/absorber velocities on the absorber relaxation rate. Absorption profiles are narrowed due the longer lifetimes of slower moving molecules in their excited states relative to fast moving molecules [96]. Here, we compute this profile using a quadratic speed dependent Voigt (qSDVP). It utilizes the quadratic speed dependence model, which is the community standard due to its accurate yet efficient computation [13,97]. These narrowing effects particularly influence the transition- and molecule-dependent collisional broadening parameter γ_{self} and its temperature-scaling exponent n_{self}. These parameters can be predicted by the broadly utilized complex Robert-Bonamy theory (CRB) [86], but the accuracy of these predictions was, until now, widely un-validated by experiment. We show that current CRB theory and our data match only when using a qSDVP and that the transition-dependent temperature-scaling exponents clearly trend as expected with the total rotational momentum quantum number J". Therefore, this work is a vital first step towards improved theoretical understanding and accurate measurement of high-temperature systems.

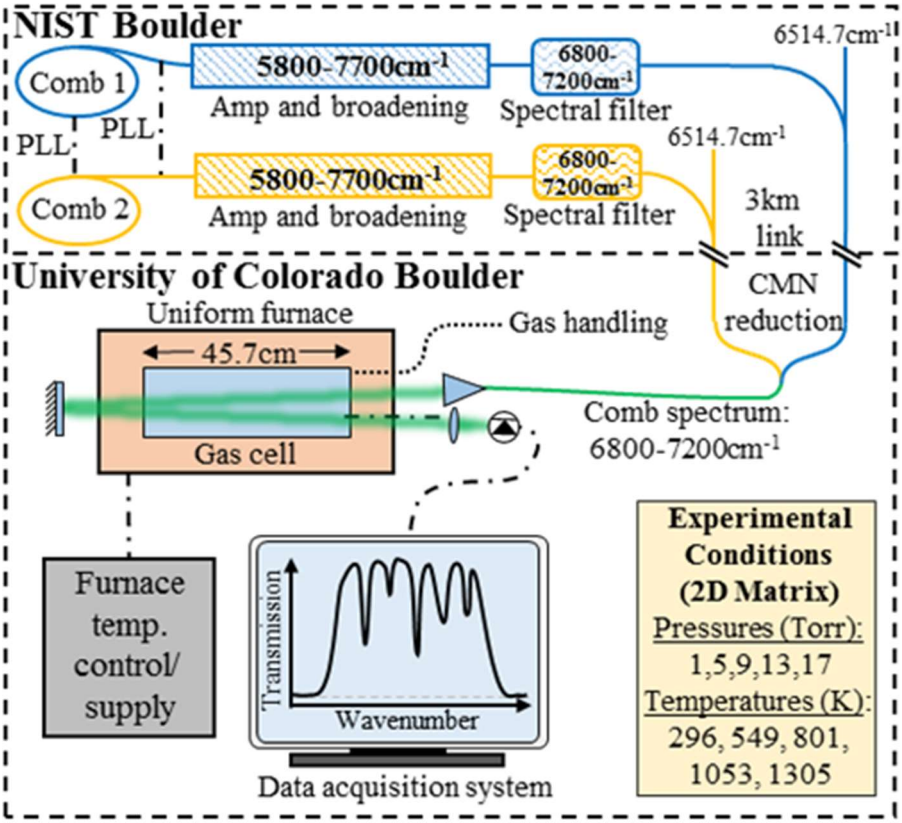

Figure 4-1- Simplified schematic of the dual comb spectrometer housed at NIST Boulder and the link to the high-temperature furnace housed at CU Boulder. Solid lines are fiber optic, dot-dashed lines are electrical and dotted lines are gas handling. CMN-common mode noise, PLL-phase locked loop.

Experimental data for temperature-scaling exponents of broadening coefficients is not widely available owing to difficulty of making high-resolution measurements of many transitions over wide temperature ranges. Spectrometers that are capable of broad spectral coverage usually have difficulty measuring high-temperature gases, >400K, due to blackbody contamination [98,99]. Conversely, instruments that can probe high-temperatures are either low resolution [100,101] or cannot investigate many lines at once [14,102], thus limiting their ability to examine trends of various lineshape models. The work presented here is the first broadband, high-

resolution data set to separately examine the effectiveness of advanced profiles for high-temperature water vapor, and helps to inform water self-broadening theory at a 3-fold higher temperature range than previous studies. We achieve this using a dual frequency comb spectrometer and high-temperature optical cell facility to measure pure water absorption from 296-1305K, 1-17Torr, in a 2D matrix (25 total spectra), each spanning 6800-7200cm^{-1}.

Extraction of the subtle narrowing effects due to velocity-changing collisions and speed dependence by single-spectrum fitting (i.e. fitting the spectrum for each condition individually) is prone to non-physical results due to correlation among lineshape parameters and the requirement of secondary and tertiary fits to extract pressure- and temperature- dependence. Multispectral fitting routines have therefore been recommended as reliable methods for fitting advanced lineshapes [13]. To analyze the 25 spectra, we employ the multispectral fitting program described in [103,104]. It fits a single set of lineshape parameters for each transition to all of the measured spectra at multiple pressure and temperature conditions simultaneously. The outcome is a single set of transition-dependent parameters that minimize the fit residual across all experimental conditions [103].

The base lineshape function currently employed in the fitting routine is the symmetric quadratic speed-dependent Rautian profile, which can be simplified to the Voigt, Rautian, and speed-dependent Voigt profiles by fixing certain parameters to zero, discussed later. When simplified for a single species without self-shift, the function takes the form:

$$F(x,y,S,\nu_{vc}) = \frac{2}{\pi^{3/2}}\int_{-\infty}^{+\infty} \nu e^{-\nu^2} \arctan\left[\frac{x+\nu}{y\left(1+S(\nu^2-3/2)\right)+\left(T_{ref}/T\right)\nu_{vc}}\right] d\nu, \qquad (1a)$$

Where ν is the molecular speed normalized by the most probable speed, $x = (\sigma - \sigma_o)/\gamma_{Doppler}$ is the optical frequency offset from the line center σ_o normalized to the Doppler width $\gamma_{Doppler}$ [104,105], T is the lineshape at the temperature of interest, T_{ref} is the reference temperature, in this work 296K, and ν_{vc} is the velocity-changing collisions coefficient. y is the nondimensionalized self-broadening half-width (shown in Eqn. 1b) and S is the ratio of the speed dependence to collisional self-broadening width, $S = \Gamma_2/\Gamma_0$.

This form assumes the temperature dependence of y and S are equal, as derived in [106] and implemented in [107]. Previous authors have experienced difficulty obtaining reliable temperature dependencies of the speed dependence value when treating self-broadening and speed dependence as independent fitting parameters with separate temperature-scaling exponents due to the dominant influence of self-broadening and inadequate signal-to-noise ratios [14]. Authors with very high signal-to-noise ratio spectrometers have been able to show that separately measured temperature-scaling exponents for self-broadening and speed dependence are similar [108], thus supporting the constraint presented in eqn. (1a).

The temperature dependence of ν_{vc} is fixed at T_{ref}/T as per [109,110] since the temperature dependence of velocity-changing collisions is identical for all transitions of a molecule [93]. The temperature-dependence of the broadening and speed dependence broadening (through S) is captured by:

$$y = \frac{p\gamma_{self}\left(T_{ref}\right)}{\gamma_{Doppler}}\left(\frac{T_{ref}}{T}\right)^{n_{self}} \qquad (1b)$$

Where p is system pressure, γ_{self} is the self-broadening coefficient at T_{ref}, T is the temperature of the system, and n_{self} is the temperature-scaling exponent.

The difference between the velocity-changing collisions and speed dependence narrowing effects require very high SNR to directly discern [38], as the differences are subtle and as there are no broadly accepted methods of relating/constraining the terms when both are floating in a fit. Therefore, we did not employ the full speed dependent Rautian here. Instead, we explored the qSDVP (eqn. (1a) with $\nu_{vc} = 0$), the Rautian profile (eqn. (1a) with $S = 0$), and the Voigt profile (eqn. (1a) with $\nu_{vc} = S = 0$). We float line center, linestrength, self-broadening coefficient, temperature-scaling exponent, and S or ν_{vc} for all transitions. HITRAN2012 data was used to supplement the parameters for weak or unfit lines.

4.4 Results and Discussion

Figure 4-2 shows examples of the multispectral fit results at 296 and 1305K for each lineshape profile. The qSDVP clearly captures the measured data more accurately across our temperature range than the Voigt and Rautian. As shown in eqn. (1a), our Rautian profile employs a transition-independent $1/T$ temperature scaling of ν_{vc} [109], while the qSDVP utilizes a transition-specific exponent identical to that used for the self-broadening term. The Rautian fits suggests that additional molecule- or transition-

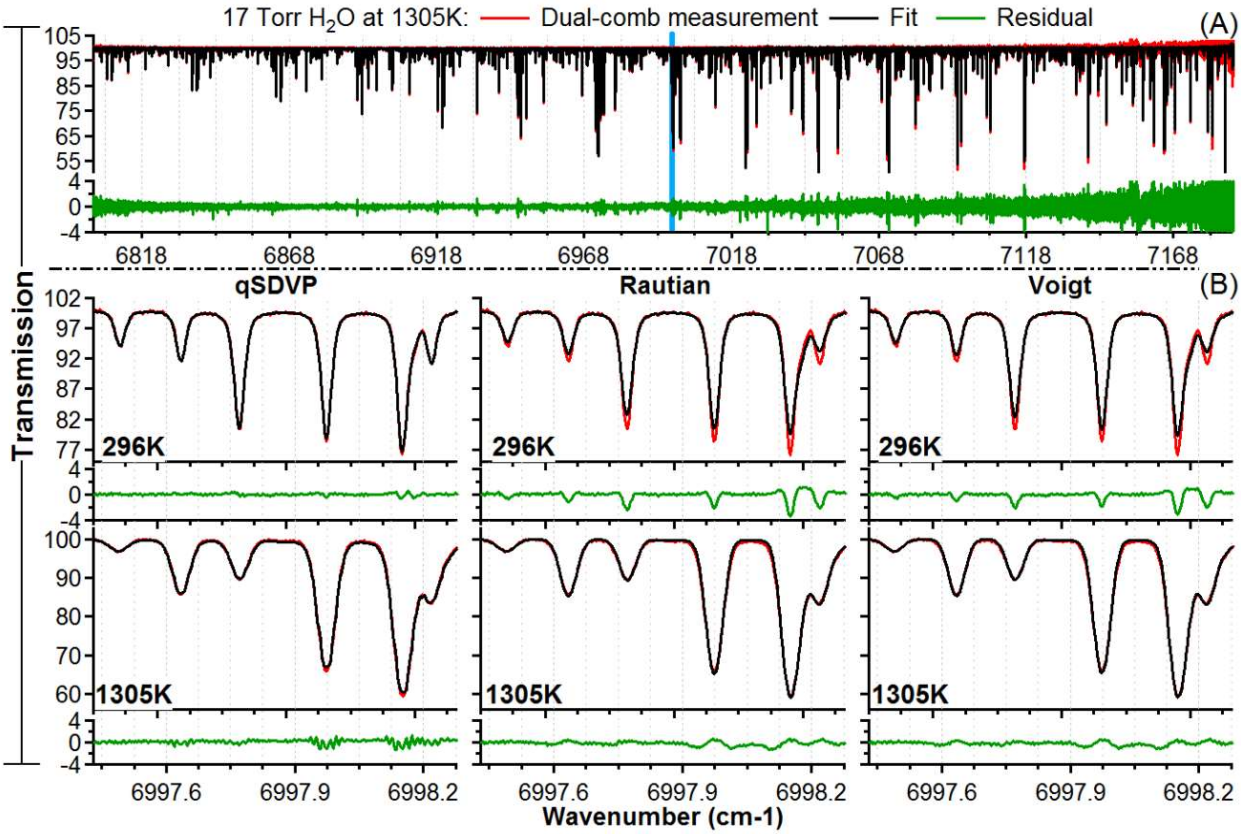

Figure 4-2- Dual-comb measurement and multispectral fit results using the qSDVP, Rautian, and Voigt profiles. Panel A shows the full bandwide measurements and fit with the qSDVP at 1305K and 17Torr H_2O. Panel B highlights the area indicated in blue on Panel A for 296K and 1305K. The residual structure for the qSDVP is the smallest, while the Rautian and Voigt are similar. The high frequency oscillations on the residual of the 1305K qSDVP are numerical noise and do not influence retrieved parameters.

specific broadening temperature exponents may be required, contrary to theory. For all transitions, the qSDVP produced a smaller residual structure than the Rautian or Voigt. The residual for some transitions fit with a Rautian profile matched the qSDVP residual, but for others the result was more similar to the Voigt. This shows that residual analysis in general, and particularly residual analysis on a small number of lines, is not sufficient for determining the dominant narrowing mechanism for our conditions.

To expand the investigation, Figure 4-3 shows the 232 extracted temperature-scaling exponents using the Voigt, Rautian, and qSDVP, organized by J". The systematic uncertainty of the values is approximated as: $\Delta n > \sqrt{2}(\Delta\gamma/\gamma)\ln(T_{max.}/T_{min.})$ [111], where $\Delta\gamma$ is the accuracy of the transition width measurement. Though the equation was derived for single-spectrum fits, it accounts for the decreased uncertainty for fitting temperature-scaling exponents over a broad temperature range [112]. Using this equation, we estimate a systematic uncertainty range of 0.3% and 3.6% for the extracted exponents. The statistical uncertainty varies depending on the absorption strength and fit uncertainty of each line. We only present lines where the temperature-scaling exponent fit uncertainty (which we approximate as the statistical uncertainty) was less than 25%.

The data are plotted in Figure 4-3 together with the upper and lower bounds for the temperature-scaling exponent predicted by CRB theory in Antony et al. [113]. Only the data extracted from the qSDVP agrees with the CRB theory. For the qSDVP lineshapes, the individual temperature-scaling exponents, their average at each J", and standard deviation are all within Antony et al.'s theoretical bounds and closely follow the expected and predicted decrease with increasing J". The Voigt and Rautian resulted in negative exponents that should not occur for water at the J" values explored here [113–115]. Furthermore, for 40 of the investigated lines, the multi-spectral fits with the Voigt and Rautian were not stable. These results point toward speed dependence as the most important and dominant narrowing mechanism for our conditions.

The ratio of the optical collision radius to the potential radius can also reveal the relative influence of speed dependence over velocity-changing collisions on the lineshape [116]. For water, the potential radius is 2.65Å based on the Stockmayer potential for polar molecules [109]. We compute an optical collision radius of 4.52Å from our average measured Γ_2 values (0.05 cm^{-1}/atm across all temperatures). The larger optical collision radius further suggests that speed dependence is the dominant narrowing mechanism at our conditions [116,117].

The large scatter and non-physical results of the Voigt and Rautian results would have a negative impact if a database were created with these data. For example, for a typical J"=9 transition examined here, $n_{Voigt} = 0.954$, $n_{Rautian} = 1.37$, and $n_{qSDVP} = 0.604$. Taking the qSDVP as the true value, the percent differences in the broadening width at 1305K are 50%, and 103%, respectively. This illustrates the importance of using the temperature-scaling exponents from this study or from Antony *et al.* exclusively with the qSDVP, as mixing the exponents with a Voigt profile at elevated temperatures will induce significant error. Therefore, only the qSDVP adequately models temperature behavior of pure water transitions over this temperature range and strongly supports the qSDVP as the preferred advanced lineshape profile of those studied here.

Additionally, we found that the use of a single temperature-scaling exponent to span from 296-1305K adequately modeled the spectra when fit with a qSDVP. The residual structure was almost within noise for the 232 lines that were strong enough to be reliably fit, spanning a linestrength range from 1e-24 to 1.35e-20 (cm^{-1}/molecule cm^{-2}). The average root mean squared error for all residuals was ~3% lower for the qSDVP as compared to both the Voigt and Rautian. Antony et al.'s results also employ a single temperature-scaling exponent to adequately fit their calculated data from 200-500K.

To account for systems that do not follow the power law, like pure H_2 [118], the next version of the HITRAN database will allow up to four broadening temperature-scaling exponents for the following temperature regions: 0-100K, 100-200K, 200-400K, and >400K [12]. Our data shows that this segmentation is not required for pure water over our temperature range. Some authors have postulated that the power law breaks down over large temperature ranges or at high temperatures owing to the

complex broadening behavior of water and competing temperature dependent mechanisms [14,91]. Our data suggests this assertion is incorrect within our range (296-1305K).

Finally, the measurements suggest that the extracted broadening parameters are independent of vibrational band, and thus the trends may carry for vibrational bands not measured here. All of the 232 transitions from six vibrational bands of water investigated here using the qSDVP fall within the Antony *et al.* prediction (which only studied three of these transitions from the (101)-(000) vibrational band). The results do not show a trend among the vibrational bands. This is expected for pure water collisions, since there are always resonant transitions that facilitate energy transfer and prevent the energy defect thought to be responsible for strong vibrational dependence and anomalous temperature behavior with foreign molecule collisions (like with N_2 [113,114,119]).

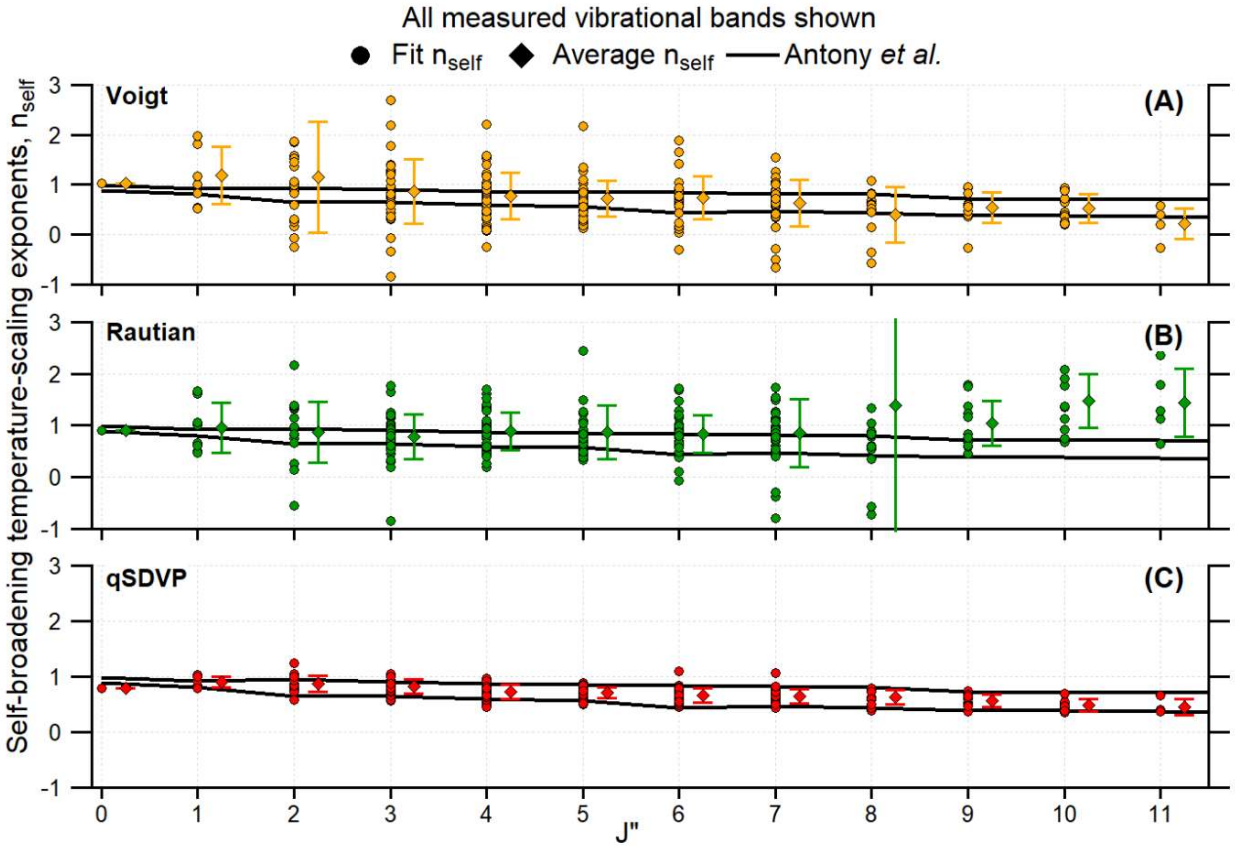

Figure 4-3- Extracted temperature-scaling exponents using Voigt, Rautian, and qSDVP. Data using the qSDVP clearly follow Antony et al.'s bounds (black traces). J"=0 falls outside of the trend since there was only a single measured transition. The averages for all plots are offset for clarity and error bars on the averages are standard deviations of all data at each J".

4.5 Conclusion

In conclusion, we utilized a high-resolution, broadband dual frequency comb spectrometer to measure pure water in a uniform furnace at temperatures up to 1305K. We examined the effect of using a Voigt, Rautian, and qSDVP to extract absorption parameters, and in particular the temperature-scaling exponents of the self-broadening coefficient for 232 transitions. These results validate CRB calculations

conducted by Antony *et al.* and show that their theoretical formalism is accurate for J"≤11 over a much wider temperature range than their original calculations. The temperature-scaling exponents extracted using the qSDVP agree well with the theoretical values, while results obtained using a Voigt or Rautian profile resulted in non-physical and highly scattered values. Additionally, we show that a qSDVP allows accurate fitting over a large temperature range using only a single transition-dependent, power law temperature-scaling exponent. Validity of the power law over such a range for numerous transitions was previously unexplored and this work supports the feasibility of single power law exponents with advanced lineshapes. The systematically better fit and less scatted temperature-scaling exponents suggest that speed dependence is the dominant influence at our conditions despite the effects of velocity-changing collisions and speed dependence narrowing being indistinguishable based solely on residual structure for our SNR of 2000:1.

All lineshapes investigated here are limit cases of the Hartmann-Tran profile so the results are applicable to current and future spectroscopic databases that adopt this formalism. The databases that serve the remote sensing and combustion research communities currently lack temperature dependence information from high-resolution spectra. The line-by-line database extracted from the multispectral fits to our data will be published in an upcoming work, however the results and validation of complex Robert-Bonamy theory lends confidence to the utilization of theoretically computed temperature exponents *provided a speed dependent lineshape is also adopted* for vibrational bands beyond those studied here. The same is true for the speed dependence and single exponent power-law results.

Overall, the work presented here extends our understanding of high-temperature water vapor absorption, with implications ranging from planetary/exoplanetary science to combustion research.

This chapter has been accepted to Physical Review A as:

Schroeder, P.J., Cich, M.J., Yang, J., Swann, W.C., Coddington, I., Newbury, N.R., Drouin, B.J., Rieker, G.B., "Broadband, high-resolution investigation of advanced absorption lineshapes at high temperature". *Physical Review A*

4.6 Acknowledgments

Support for this work was provided by the National Science Foundation under grants CBET 1336643 and 1454496, and by the Air Force Office of Scientific Research under FA9550-17-1-0224. Portions of the research described in this paper were performed at the Jet Propulsion Laboratory, California Institute of Technology, under contract with the National Aeronautics and Space Administration. Government sponsorship acknowledged. The authors would also like to thank J. Steinbrenner, and N. N. Hoghooghi for their help in the preparation of this chapter.

5 Speed-dependent Voigt Line shape Parameter Database from Dual Frequency Comb Measurements at up to 1300K: Part I. Pure H_2O, 6800-7200cm^{-1}

5.1 Introduction

Combustors [2], propulsion engines [3], gasification reactors [1], and planetary atmospheres [7,9] are among the many water-laden, high-temperature environments that benefit from optical diagnostic measurements. The temperature and concentration of water vapor in these systems can be used to assess chemical kinetic processes and atmospheric conditions. Absorption spectroscopy is a quantitative and non-intrusive method commonly used to measure water in such systems. It leverages resonance between ro-vibrational transitions of the molecule and specific frequencies of the light. The amount of light that is absorbed by each transition is a unique but predictable function of temperature and pressure. The measured strength and shape of the absorption profiles of the transitions can thus be used to calculate thermodynamic conditions in unknown environments.

Important parameters of the lineshape profiles, such as line center (ν_o), linestrength (I), broadening coefficients with various collision partners (γ), shift coefficients (δ), and quantum mechanical assignments, are catalogued in databases such as HITRAN2012 [10] and HITEMP2010 [11]. These databases contain lineshape data for thousands of transitions for many molecules and are widely used in the spectroscopic community for retrievals of physical conditions from measured spectra. Though they are largely based on data collected near room temperature and only include temperature dependence for air broadening, we recently showed that they are accurate at predicting the existence and location of >99% of strong water vapor absorption features up to 1305K [66]. However, the databases are built around the Voigt lineshape profile, do not include broadening and shift coefficients for collision partners other than air, and do not include temperature dependence of many lineshape parameters (shift, self- or foreign-broadening). The lack of temperature dependence causes significant departures in line position and width at high temperature [66], which is exacerbated for environments composed of mixtures for which the foreign-broadening coefficients are unknown. The use of a Voigt profile can limit the agreement between high-resolution spectra and the model to between 2 [90,91] and 10% [69,89] (depending on broadening partner) because the profile lacks high order broadening effects such as collisional narrowing and speed dependence.

HITRAN2012 and HITEMP2010 had a fixed format [10] that could not incorporate additional lineshape parameters even if they were measured. HITRAN Online, the next generation database structure, allows inclusion of parameters required to generate advanced lineshapes and include foreign-broadening and shift and temperature dependencies with broadening partners beyond air. In addition, the spectroscopic community has developed advanced lineshape mechanisms that can account for higher order collisional effects. The efficacy of these various lineshapes at conditions relevant to high temperature systems has only been explored recently [14,120], and few coefficients have been measured. Thus, broadband measurements from room to high temperatures (>500K) present an opportunity to begin filling in the many un-measured parameters for these advanced databases [13].

A large fraction of data in the HITRAN2012 (HITRAN) database was collected with large Fourier transform spectrometers (FTS). These instruments excel at broadband, high resolution measurements, but can be sensitive to background infrared radiation at elevated temperatures, thus limiting their ability to explore high temperature regimes. Here, we employ a dual frequency comb spectrometer (DCS) to make the requisite high accuracy, high resolution measurements of water spectra

at temperatures up to 1300K. A DCS is insensitive to background radiation, and yet can have a broad spectral bandwidth, resolution exceeding most large FTS, and near-perfect frequency axis. To date, frequency comb spectrometers (single or dual comb designs) have been used to extract parameters from room temperature gases [38,41,121]. This work is the first instance of a DCS being used to extract spectral parameters from a wide range of temperature and pressure conditions, thereby bringing the unique capabilities of a DCS to lineshape data.

The major results of this work are as follows:

1. Water vapor speed dependence coefficients and their temperature scaling are measured for the first time, spanning 6800-7200cm^{-1} over the largest temperature range yet investigated with a broadband spectrometer, 296-1305K.
2. Intensity, linecenter, self-broadening coefficients, and the self-broadening temperature-scaling exponents are measured for 625 transitions and compared to HITRAN2012 data.
3. 300 of the 302 measured line centers are within ±0.001cm^{-1} of their HITRAN2012 value (measured with <3.34e-6cm^{-1} comb tooth absolute frequency accuracy).
4. 606 of 625 measured linestrengths exhibit uncertainties that are less than their HITRAN2012 values.
5. 203 of the 254 measured self-broadening coefficients have lower uncertainties than their associated HITRAN2012 value.

Additionally, we collected argon-broadened water data with the same spectrometer over the same spectral and temperature ranges. Water-argon pressure shifts, broadening coefficients, and their associated temperature dependencies are published in the companion to this paper.

5.2 Experimental Setup

Since these measurements were completed prior to the creation of mobile DCS systems [64,65], we utilized the DCS, BRAN link, and furnace apparatus described in Sections 1.1.4.1 and 3.2 to enable the precision, high temperature measurements presented in this chapter. As in the previous chapters in this dissertation, we use the heterodyne technique described in section 1.1.3.2 to resolve each tooth across the spectrum. The DCS used here was set to span 6800 to 7200 cm^{-1} with a repetition rate (point spacing) of 0.0033cm^{-1} and further detail about the spectral properties can be found in Section 3.2.5. We averaged data for 90 minutes for each temperature/pressure condition to achieve approximately 2000:1 absorbance single-to-noise ratio and acquired background scans at each temperature with the cell under vacuum before and after the five pure water data sets [66]. This allowed us to account for water vapor in the free-space beam line outside of the spectroscopic cell. The data was post processed as explained in Section 3.2.4 to create normalized transmission spectra that we simultaneously fit with multispectral fitting software to acquire the data presented in this chapter.

5.3 Spectral Analysis

As noted in the previous section and by many researchers, the Voigt profile does not take narrowing mechanisms into account [13], such as Dicke narrowing and speed dependence. See Chapter 11 for more details on these mechanisms. To incorporate these mechanisms, the multispectrum fitting program used here employs the quadratic speed dependent Rautian profile [104] that when simplified for a pure gas takes the form:

$$F(x,y,S,\nu_{vc}) = \frac{2}{\pi^{3/2}} \int_{-\infty}^{\infty} ve^{-v^2} \arctan\left(\frac{x+v}{y\left(1+S(v^2-3/2)\right)+\left(T_{ref}/T\right)\nu_{vc}}\right) dv$$

The function is integrated over molecular speed normalized by the most probable speed; here from v=-4 to 4 in 16 steps at each frequency across each transition [104]. $x = (\sigma - \sigma_0 - \Delta_{\text{self}})/\gamma_{Doppler}$ is the frequency of the transition offset from line center adjusting for self-shift (if applicable) normalized by the Doppler width where σ is the frequency where the transition is to be calculated, σ_o is the transition line center, $\gamma_{Doppler}$ is the computed Doppler width, T_{ref} is a reference temperature, here set to 296K, T is the temperature of interest, S is the ratio of speed dependence to self-broadening, ν_{vc} is the frequency of velocity changing collisions, and Δ_{self} is the pressure induced line shift:

$$\Delta_{self} = \frac{p\delta_{self}\left(T_{ref}\right)}{\gamma_{Doppler}}\left(\frac{T_{ref}}{T}\right)^{m_{self}}$$

Where p is system pressure, $\delta_{Self}(T_{ref})$ is the pressure shift coefficient at T_{ref} and m_{self} is the transition-specific pressure shift temperature-scaling exponent. The power law was chosen for the shift parameter because the linear formulation proposed for the next generation databases [12] failed over our temperature range. $y\left(1+S(v^2-3/2)\right)$ is the formalization of quadratic speed dependence [104,105,122–124]. ν_{vc} is the frequency of velocity changing collisions (Dicke narrowing) and as per [13,109] whereby the temperature dependence of ν_{vc} is fixed to its theoretical value of $1/T$. The temperature dependencies of collisional and speed dependent broadening are expressed as a power law of the form:

$$y = \frac{p\mathrm{X}_{self}\gamma_{self}\left(T_{ref}\right)}{\gamma_{Doppler}}\left(\frac{T_{ref}}{T}\right)^{n_{self}}$$

where X_{self} is the molar fraction of the absorbing molecule, $\gamma_{self}(T_{ref})$ is the self-broadening coefficient at the reference temperature, n_{self} is the transition specific broadening temperature-scaling exponent. Generally, speed dependence scales linearly with pressure and is temperature scaled with the power law using a transition- and broadener-specific exponent. For simplicity, fit robustness, and according to measurements by [108], and theory by [106,110], we equate the temperature dependence of the speed dependent coefficient with the collisional term as seen in the line shape equation and power law scaling above.

In previous work, our group showed that speed dependence was the dominant narrowing mechanism at the conditions encountered in these measurements [120]. Briefly stated, speed dependence stems from the dependence of energy transfer between rotational states on the relative speed of the colliding and absorbing molecules. In a Maxwell-Boltzmann distribution, there are larger numbers of slowly moving molecules and these slow molecules, because of their fewer collisions per unit time, remain in their excited state longer compared to fast molecules. A transition will therefore slightly narrow due to the tradeoff between time and energy in the Heisenberg uncertainty principle. Speed-independent profiles, like the Voigt or Rautian, assume all molecules have the same, average molecular velocity, which is known to be inaccurate. The accepted formal solution to incorporate speed dependent molecular collisions utilizes hypergeometric functions. However, a quadratic approximation [122,123] is preferred in the community due to its computational efficiency, flexibility, and accuracy [13,110]. We implement only the quadratic form for speed dependence in this work to maintain compatibility with current database standards.

Currently, the most advanced and standardized line shape profile in the spectroscopic community is the Hartmann-Tran Profile (HTP) [13]. The HTP uses the quadratic speed dependence model and when the correlation parameter η (see [13]) is set to zero, it reduces to the profile used in this work. Therefore, the data presented here can be included with future implementations of databases built around the HTP. Given that our absorbance SNR was not large enough to directly discern Dicke narrowing from speed dependence, and our previous finding that speed dependence is the dominant narrowing mechanism at our conditions [120], we simplify the quadratic speed dependent Rautian to the quadratic speed dependent Voigt profile (qSDVP) by setting ν_{vc} in the lineshape equation to zero. All broadening terms were computed using this profile. We used a Voigt profile with HITRAN broadening data to extract the linestrength and/or linecenter when fitting for broadening terms was not feasible on certain transitions that lacked sufficient SNR at some temperature/pressure conditions. Since our pressure range was limited to a maximum of 17Torr, we used the symmetric form of the qSDVP that did not account for second-order speed dependent line shifting effects. For more details on Dicke narrowing and speed dependence, the reader is referred to [94,125–129] and [87,96,107,122,130,131], respectively.

The following analysis techniques were employed to improve the quality of the presented parameters. If a transition was saturated with absorbance approximately greater than 2.6 at any temperature/pressure combination, all of its lineshape results were deemed unreliable and discarded. There were 21 of these transitions over our spectral range and the lineshape parameters for the saturated transitions were set back to HITRAN values after removal. For all other transitions, the fits are performed iteratively, increasing the number of floating parameters at each iteration when justified. We start by floating only linestrength, then line center, followed by broadening coefficients and their temperature dependencies, and finally, if possible, self-shift. As each additional parameter is set to float, the fit for some transitions becomes unstable because the SNR across all of the conditions is not sufficient to extract all parameters. When the fit for a transition becomes unstable, we return the most recent parameter that was floated for that transition to the HITRAN2012 value if available or zero if the parameter is not presented in HITRAN, and repeat the fit to return to stability. Thus only the transitions that remain strong across many of the 25 conditions enable all parameters to be extracted. We additionally constrained 42 doublets where the transitions are too close together to reliably extract all parameters. The level of constraint depended on the stability of the fit, and included (as required): float line centers but constrain their difference to the difference in HITRAN; float linestrengths but constrain their relative ratio to the HITRAN ratio; float self-broadened widths, self-broadened temperature-scaling exponents, and speed dependent parameters but constrain the values of the doublet to be equal. Prior to publication, the fit was iterated >10 times to ensure that all values were stable. An example of the resultant fit is shown in Figure 5-1 for both 296 and 1305K data. The residuals are almost within noise for the shown transitions and with the larger structure in the 1305K residual resulting from numerical noise. This expanded section was typical of all transitions across the broad spectral bandwidth. The table in Chapter 10 presents all extracted data with the indicators of special constraints in the “Notes” column with Table 5-1 showing a summary of all parameters extracted and their associated vibrational bands.

Table 5-1- Listing of the number of line parameters extracted for each vibrational bands within the measurement region. Constrained and saturated lines are excluded. The (101-000), (200-000), and (121-000) bands provide most of the data in our study. If a line is presented with a self-broadening coefficient it was always fit along with a broadening temperature exponent and a speed dependent parameter to ensure that only broadening parameters with a qSDVP are presented. The units of linestrength are HITRAN units of cm^{-1}/molecule cm^{-2}.

Vibrational Bands	Total	Min. J"	Max. J"	Fit Linecenters	Fit Linestrengths	Maximum Linestrength	Minimum Linestrength	Fit self-broadening coefficients	Fit broadening temperature exponent	Fit self-shifts	Fit speed dependence values
120-000	38	0	9	5	38	1.1971E-25	1.67E-22	4	4	0	4
101-000	206	2	17	103	206	5.9993E-30	2.55E-21	82	82	1	82
200-000	167	1	15	101	167	1.0279E-26	1.62E-21	86	86	2	86
021-000	165	0	14	85	165	2.6124E-30	1.41E-21	80	80	5	80
111-010	24	4	12	4	24	1.2436E-27	2.56E-24	0	0	0	0
002-000	13	6	11	3	13	2.0065E-26	5.89E-23	1	1	0	1
031-010	8	3	8	0	8	4.1283E-26	1.35E-24	0	0	0	0
040-000	2	5	6	0	2	1.918E-24	2.17E-23	1	1	0	1
210-010	2	5	11	1	2	1.5049E-26	7.99E-26	0	0	0	0
Total	625	N/A	N/A	302	625	N/A	N/A	254	254	8	254

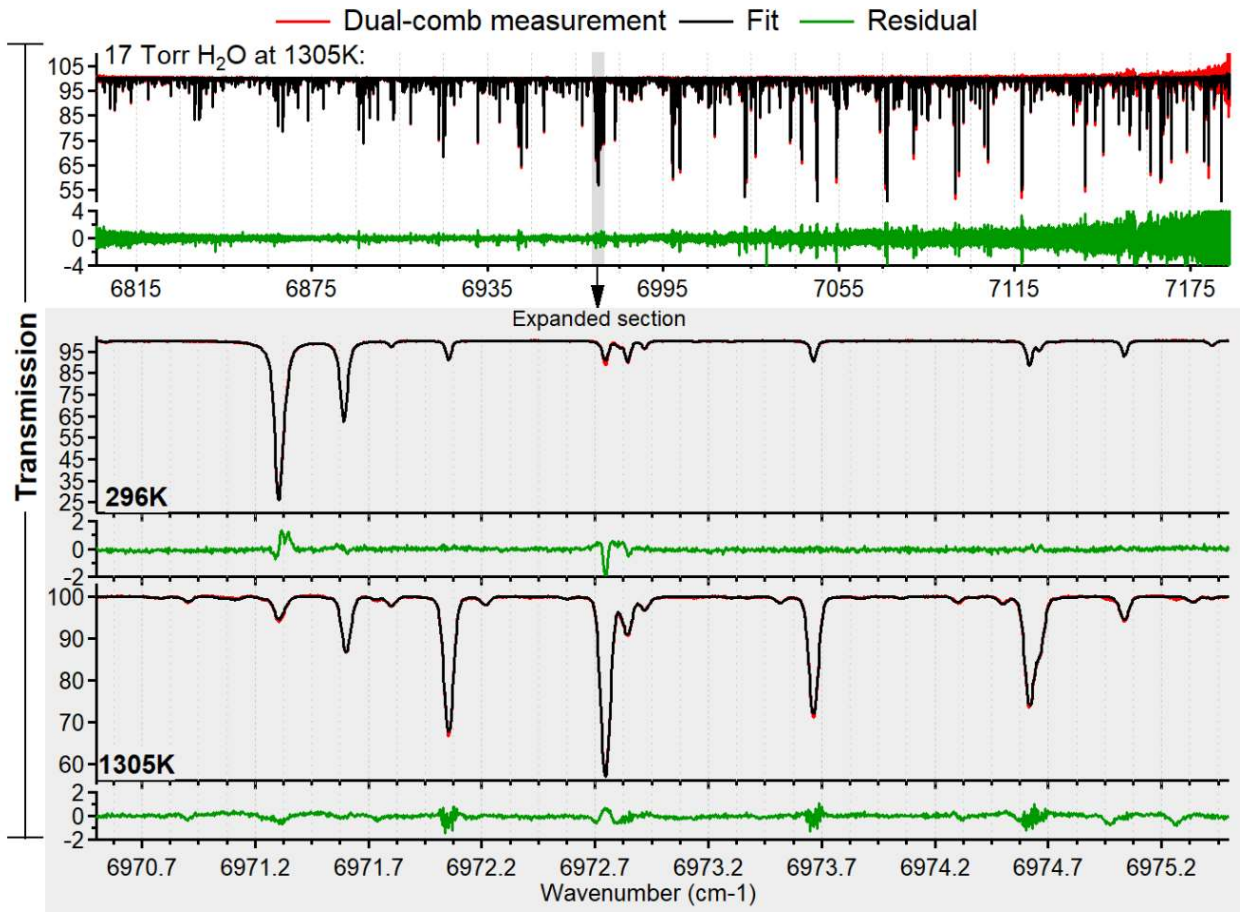

Figure 5-1-Measured transmission spectrum, corresponding fits, and residuals for water vapor at 17Torr at 1305K in the upper panel and for 296K and 1305K in the expanded panel below. The oscillatory residual structure in the 1305K residual in the lower panel is numerical oscillation and does not influence fit results.

5.4 Results and Discussion

5.4.1 Line Positions

Figure 5-2 shows the difference between the fit line centers and HITRAN line centers as a function of HITRAN linestrengths. The statistical uncertainty on the extracted line centers is shown as the uncertainty bars in the figure and presented as the precision of these line center measurements. The precision is given for each on the 321 fit linecenters in Chapter 10. Of the 321 linecenter fits, 106 are between 1e-5cm^{-1} and 5e-5cm^{-1}, 101 are between 5e-5cm^{-1} and 1e-4cm^{-1}, 107 are between 1e-4cm^{-1} and 5e-4cm^{-1}, 5 are between 5e-4cm^{-1} and 1e-3cm^{-1}, and 2 are between 1e-3cm^{-1} and 5e-3cm^{-1}. Of the fits, 267 of 321 are more precise than their respective HITRAN uncertainty codes and the uncertainty bars for 61 of 321 encompass a zero Fit-HITRAN difference, implying that their linecenters are statistically indiscernible to those in HITRAN. The data presented here span a pressure range from 1 to 17Torr. This pressure range was insufficient to fit most self-pressure shift values and associated self-shift temperature-scaling exponents. Inclusion of these parameters would likely improve the precision of the fits since they would allow compensation of slight shifts in linecenter with varying pressure and temperature. The

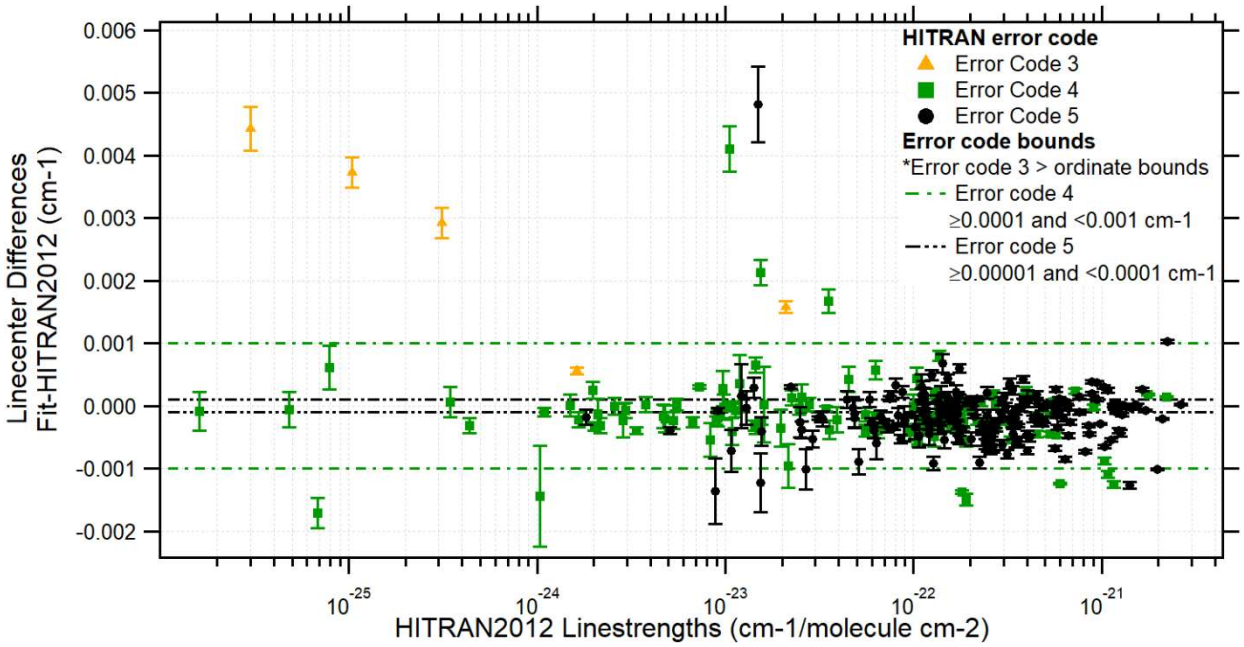

Figure 5-2- Difference between measured and HITRAN line centers. The uncertainty bars are the statistical fit uncertainty and the points are color coded by the respective HITRAN line center uncertainty code. Most transitions are within +/- 0.001cm^{-1} of HITRAN linecenter. The HITRAN uncertainty bounds for the gold points (error code 3) is too large at 0.01cm^{-1} to be shown on the plot. The increased scatter with lower linestrengths is expected due to lower SNR for these features over the measured pressure and temperature range.

systematic uncertainty of the measurements is governed by the resolution, i.e. comb tooth linewidth, and frequency accuracy of the spectrometer. As described in section 1.1.4 and [66], the linewidth of the comb teeth at the measurement cell is <3.34e-6cm^{-1}. The absolute frequency accuracy of each tooth is <3.34e-6cm^{-1} so both the resolution and frequency axis uncertainty are negligible compared to our lowest precision value of 1.14e-5cm^{-1}.

5.4.2 Linestrengths

Figure 5-3 presents all linestrengths from this work fit with a speed dependent Voigt profile compared against the published HITRAN2012 values. The lines indicated by "b" in Chapter 10 are doublets whose linestrengths were floated but constrained to the ratio found in the HITRAN data. Typically, the ratio was 3:1 and results from ortho/para spin states. The uncertainty bars on Figure 5-3 are the statistical fit uncertainties for each point from the fit. More than 96% of the lines measured have fit uncertainties less than 10%. The accuracies of the retrieved linestrengths are related to systematic uncertainty in the number density of water molecules in the spectroscopic cell. We discuss this in further detail in [66] for these measurements, but estimate their fractional uncertainties as 1.70%, 1.71%, 1.65%, 1.69%, and 1.64% for the 296K, 549K, 801K, 1053K, and 1305K, respectively.

Of the 646 measured linestrengths, 97% of our values agreed to within their respective HITRAN published uncertainty codes, <10% or 20% depending on transition, which can be seen in Figure 5-3. These 97% of lines would be preferred over the HITRAN values since they incorporate data over a larger temperature range than much of the HITRAN data. The HITRAN uncertainty codes are larger than both the precision of most lines and systematic uncertainty estimates for all lines. The inset shows an average offset of approximately 1.5% below the 1:1 line compared to HITRAN. The source of this offset is

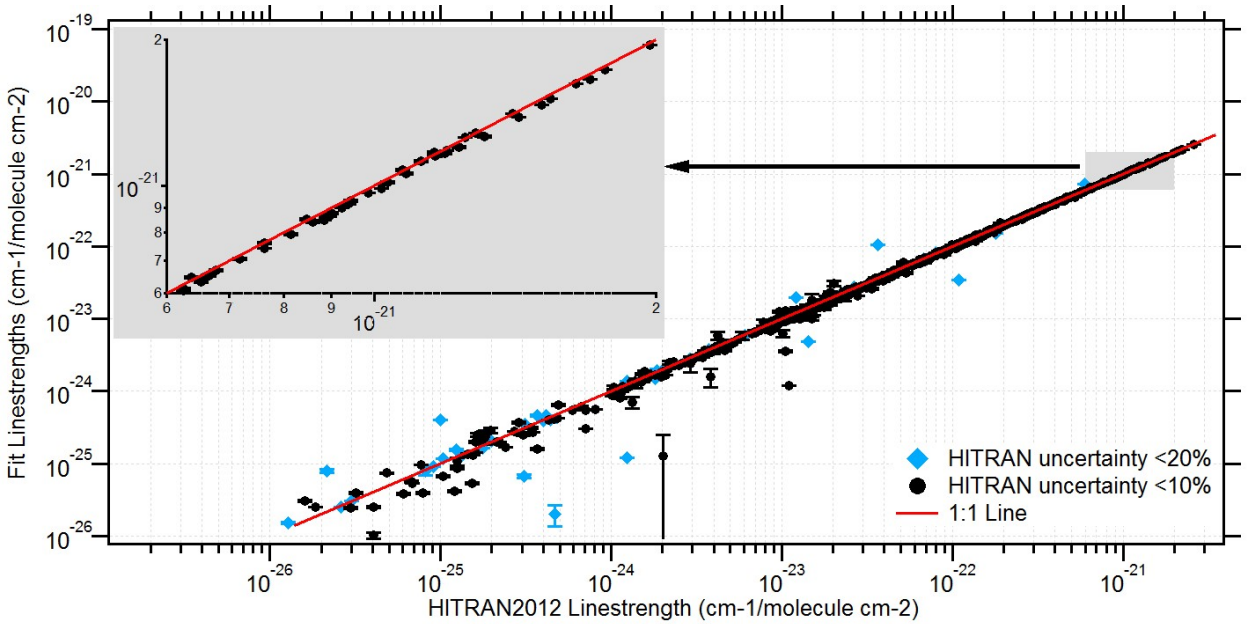

Figure 5-3- Displayed are extracted linestrengths versus HITRAN2012 linestrengths with an expanded inset. The data is color coded by HITRAN2012 linestrength uncertainty and the red line is a 1:1 slope. There is an approximately 1.5% systematic bias lower than HITRAN and is visible in the inset. The offset is less than the most common error code associated with the ≥5% and <10% HITRAN uncertainty code. Uncertainties are presented for each point though often they are too small to be resolved on top of the marker.

unknown though it is within all HITRAN uncertainties for transitions in this range, which are typically much larger than the offset [10,132].

5.4.3 Self-broadening and speed dependence coefficients

Self-broadening and speed dependence coefficients were extracted for 254 transitions over our spectral region using a qSDVP. Values were retained only if they produced small residual structure (<1.0% peak), were stable over >10 iterations of the fitting routine, were physically realistic ($0<n<1$ for pure water vapor), and resulted in a coefficient statistical fit uncertainty <25%. Figure 5-4 shows groupings of A-Type ($\Delta Ka = 0$, 57 lines shown) and B-Type ($\Delta Ka = \pm 1$, 26 lines shown) transitions, following the formalism of Toth *et al.* [133]. Within each type, "families" are plotted to better illustrate parameter trend as a function of $J"$ and $Ka"$ quantum numbers. In the figure, m is plotted as $-J"$ for P branch and $J"$ for R branch transitions. The criteria for inclusion in a family require ΔJ, ΔKa, $Ka"$, and $\gamma"=Ka" + Kc" - J"$ to be equal and $\gamma"$ must be 0 or 1 for all transitions within each family. As per [70,133–135], transitions with the same rotational quanta but reversed upper and lower states, tend to exhibit similar broadening coefficient values. Transitions exhibiting this rotational reversal are therefore also plotted to clarify the trend similarity with Toth *et al.* This allowed reversal is illustrated by the double-sided arrows in the example transition quantum numbers in the figure. Clear from Figure 5-4 is the decreased sensitivity of the self- and speed dependence broadening coefficient on $J"$ with increasing $Ka"$ family. This is due to the increased amount of angular momentum in the Ka projection reducing the effective collisional cross section. The $Ka" = 0$ and $Ka" = 1$ families exhibit a clear decreasing trend with increasing J" whereas $Ka" = 3$ and $Ka" = 4$ are nearly flat. This is much clearer with the A-Type transitions than B-Type, though this may be due to the fewer data points presented for B-Type transitions. Figure 5-4 also shows that the trends are similar between Toth [134] and this work for the same vibrational bands. The trend is also similar for other bands investigated by Toth that were not investigated here. This supports the assertion that the broadening parameters for pure water are

insensitive to the vibrational state of the transition due to the highly efficient coupling of rotational energy between like molecules during collisions.

Exact agreement between self-broadening coefficients extracted with Voigt profiles and those measured here with the qSDVP is not expected due to the coupled effect of speed dependence on retrieved self-broadening coefficients. It has been shown that for isolated lines, the narrowing effect of speed dependence should result in collisional broadening coefficients up to 3% larger than those extracted with Voigt profiles [111]. An offset due to the qSDVP is not expected in our data, since our data is forced to fit over a much larger temperature range than the typical room temperature studies of the self-broadening coefficient. This larger temperature range likely induces enough scatter to obscure the offset that other researchers have noted when comparing coefficients calculated using a Voigt to those calculated using a qSDVP near room temperature. Also shown in Figure 5-4 are the measured speed dependence broadening coefficients extracted with $\Gamma_2 = S * \Gamma_0$; Γ_0 and S are the fit parameters in this work. The ratio of Γ_2 to Γ_0 is nearly constant up to J" of 11 for this data, see Figure 5-5. This is expected since all transitions efficiently couple energy between states in self-perturbed collisions so the relative importance of speed dependence should be constant for all J" states. For dissimilar perturber/absorber pairs this is not the case since the inaccessibility of high energy, high J" transitions more heavily weights the relative speed of interacting molecules [14].

The fit uncertainty for the extracted self-broadening coefficients is reported as the statistical uncertainty of the results. Greater than 98% of extracted coefficients had statistical uncertainties less than 10%, with the minimum linestrength of a fit line being 6.161e-24 (cm^{-1}/molecule cm^{-1}). These uncertainties are shown as the uncertainty bars for each fit parameter in Figure 5-4 and in Chapter 10. Since Γ_2 was computed from $S = \Gamma_2/\Gamma_1$, the uncertainty for Γ_2 was computed as the quadrature sum of the uncertainties of the fit parameters S and Γ_0 as $\sigma_{\Gamma_2} = \Gamma_2\sqrt{\left((\sigma_S/S)^2 + \left(\sigma_{\Gamma_0}/\Gamma_0\right)^2\right)}$ where σ_S and σ_{Γ_0} are the statistical uncertainties from the fit. The average fit uncertainty for Γ_2 was 25%. The systematic uncertainty of both Γ_0 and Γ_2 is dominated by the gas pressure uncertainty of 0.15-1.7%. The pressure uncertainty propagates linearly to the linewidth and minimally to the speed dependence. The fit uncertainty dominates the pressure uncertainty, so the presented data is not likely subject to significant systematic bias relative to the statistical uncertainty.

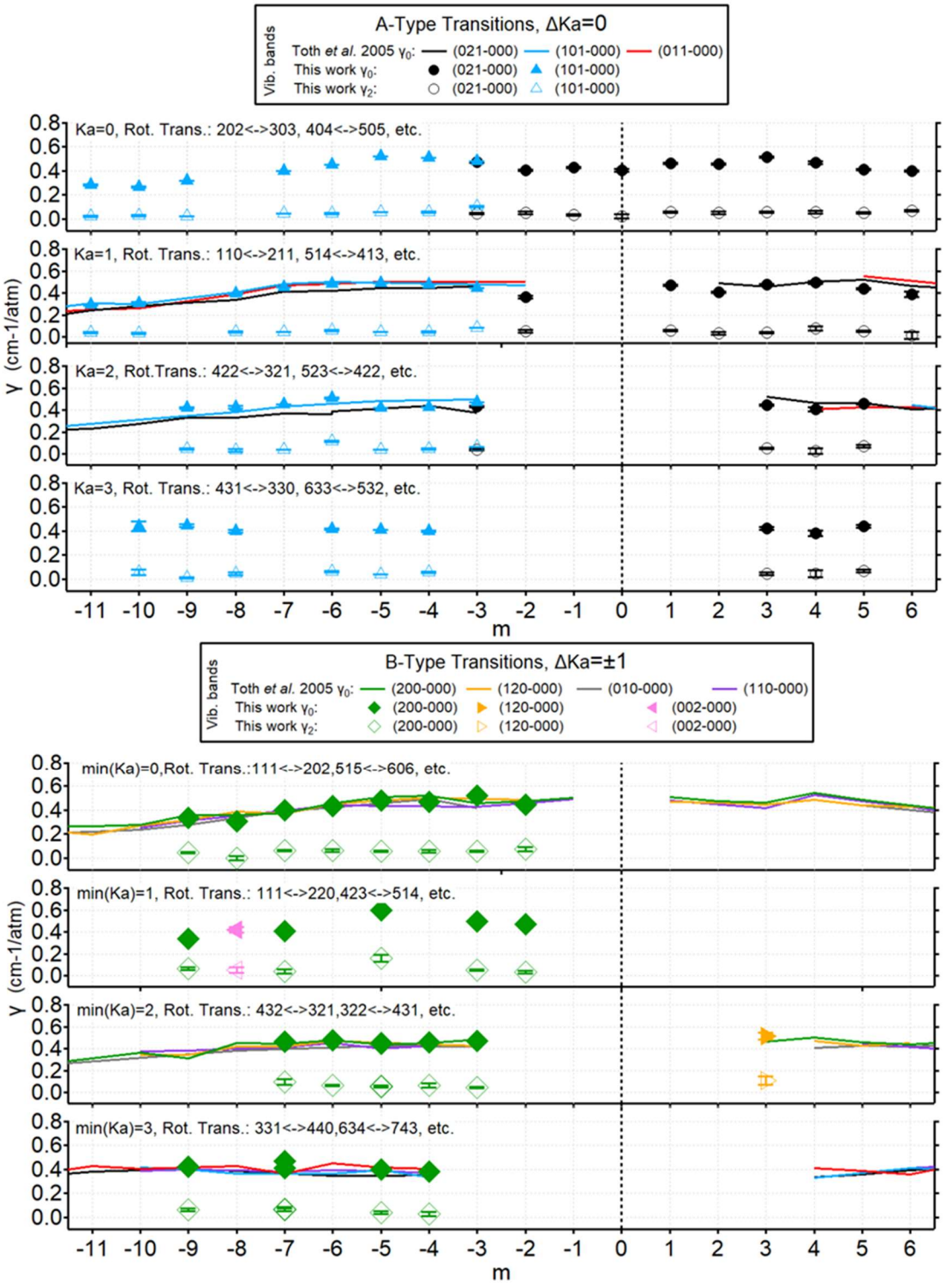

Figure 5-4- Self-broadening and speed dependent parameters, separated by transition family (Markers: this work; Lines: Toth et al.). Each panel provides examples of transitions that meet the criteria to be included in a family. Vibrational bands similar between the Toth study and this one are similarly colored. The insensitivity of these parameters on vibrational band is clear from the similarity across bands. Uncertainty bars representing the statistical fit uncertainty are included, though they are sometimes too small to be resolved.

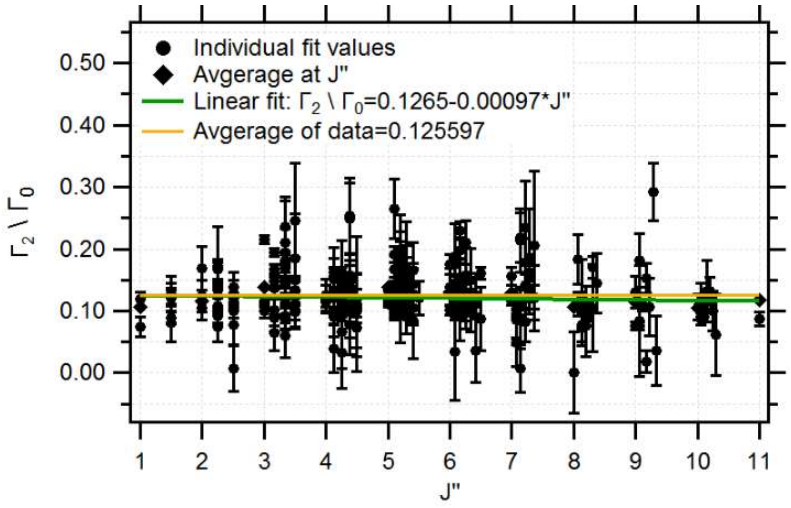

Figure 5-5-All fit values for the ratio of speed dependence broadening to self-broadening. The trend of the average values is clear and is nearly unvarying across all J" values. Fit values are offset by J"+½*Ka"/J" for clarity.

5.4.4 Self-shift coefficients

We extracted 8 self-shift parameters across all lines as shown in Table 5-1 and presented in Chapter 10. The experimental difficulty in heating the entire gas-handling manifold to allow water pressures greater than saturation pressure at room temperature (17 torr) prevented more widespread extraction of self-shift parameters. We attempted to use the HITRAN linear pressure shift model, $\delta_{self}(T) = \delta_{self}(T_o) + (T - T_o)\delta_{self}'$ where δ'_{self} is the temperature shift coefficient, but found the multispectrum fitting algorithm unable to fit any transition over our temperature range; we therefore used power law temperature scaling with the exponent fixed at unity due to lack of tightly constrained shift values for all temperatures [66]. All transitions that allowed extraction of a self-shift parameter were strong, with linestrength >2.18e-21 (cm-1/molecule cm-2).

The fit uncertainty of these values is on average 5.4% and ranges from 0.47 to 10.6% (7 of the 8 parameters were >1.67%). We assume the systematic uncertainty of these values is governed by inaccuracy in true line center stemming from uncertainty in furnace temperature and system pressure. As per Section 5.4.1, we can approximate the systematic uncertainty of line center as the uncertainty in the DCS as negligible compared to the large uncertainty in the fits.

5.4.5 Temperature-scaling of self-broadening and speed dependence coefficients

Classically, a simple power law of the form, $\gamma_{self}(T) = \gamma_{self}(296K)(296K/T)^n$, where $\gamma_{self}(T)$ is the self-broadening coefficient at a specified temperature, is the most common method of scaling the coefficient to non-ambient temperatures [13,110]. The temperature-scaling exponent, n, needs to be individually measured for each transition and broadening partner due to its dependence on ro-vibrational transition and various absorber-broadener combinations. The temperature-scaling exponent of the self-broadening coefficient and the speed dependence term S, were defined to be equal and floated together; a simplification utilized in previous formalisms of this speed dependent Voigt [103,104]. Some authors have measured individual temperature-scaling exponents for self-broadening coefficients and speed dependence terms separately, and have found the exponents to be similar [14,136], further supporting this simplification.

The extracted exponents from our data set are presented in Figure 5-6 with the average of all exponent values (red dashed line) plotted for reference. The average value is 0.702. The separation of the data into families is discussed in section 5.4.3, and is used here again to better show dependencies on rotational quantum numbers. The data do not show strong vibrational band dependence, which is supported in [120]. The general agreement of broadening coefficients collected at room temperature by Toth *et al.* lends support to the accuracy of our temperature exponents since exponent inaccuracy would directly impact the extracted room temperature self-broadening value. It is clear that the upper two families

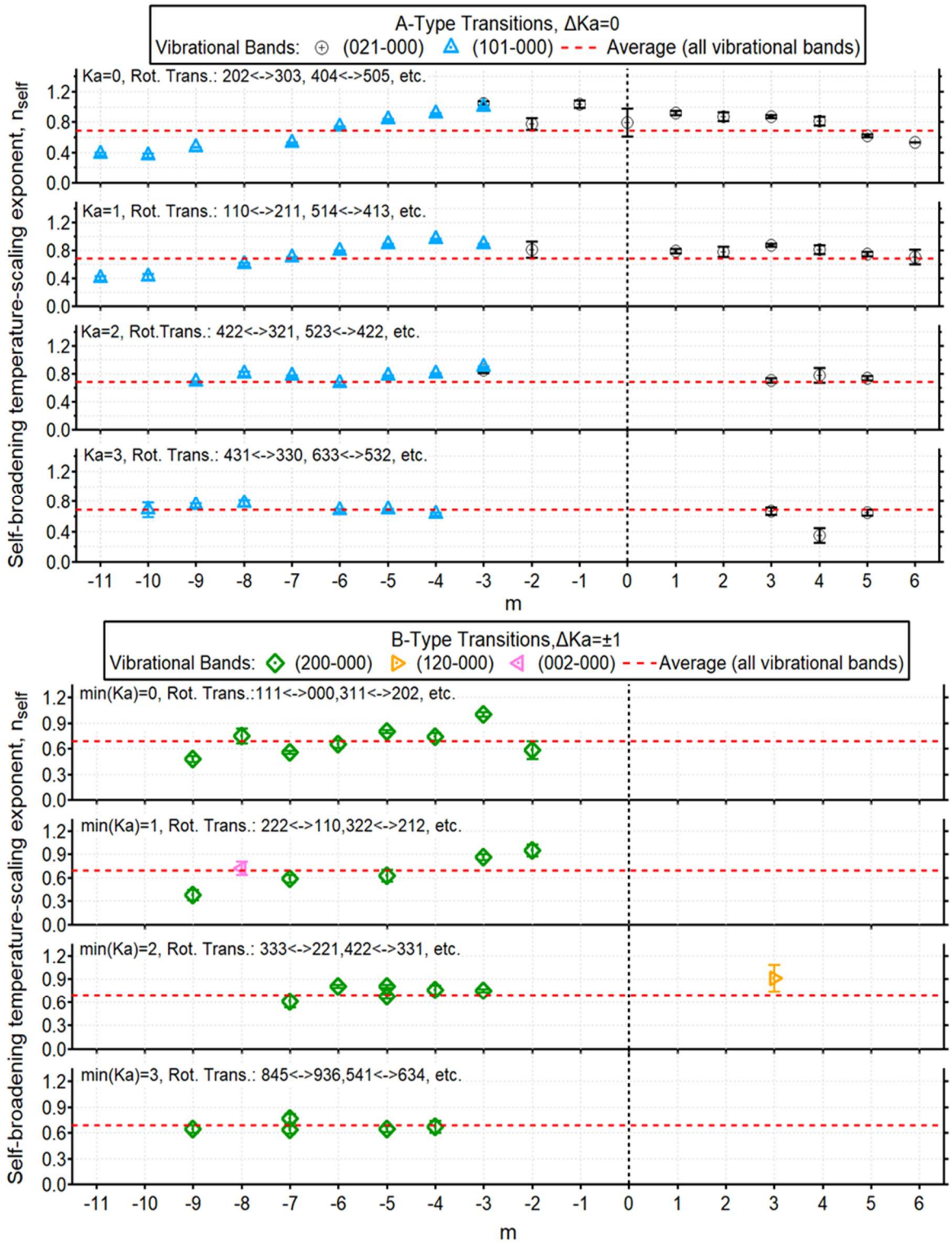

Figure 5-6- Temperature-scaling exponent for the broadening coefficient plotted by the same family structure as the previous figure. The temperature-scaling exponent has not been experimentally studied over similar temperature ranges so there is no data for comparison. The dashed red line is included for reference and is the average of all extracted exponent values of 0.702. Fit uncertainty bars are included in the figure though they are sometimes too small to be resolvable.

show dependence on J". Exponent values become less sensitive to J" with increasing Ka" values as expected from the results plotted in Figure 5-4 and accompanying explanation. Similar to Figure 5-4, A-Type transitions show a clearer dependence on J" than B-Type, though this could again be a result of the fewer total B-Type transitions.

The validity of the power-law temperature scaling has been questioned over large temperature ranges, though not many experiments have been able to accurately probe numerous transitions at these temperatures to explore this theory. The present work studies many of these unique values and shows that only a single exponent is required to span large temperature ranges given the correct lineshape profile is used (qSDVP in this case), thus supporting the use of the simple power law [120]. Approximately 88% of our lines show fit uncertainties of <15% for their temperature-scaling exponent. These uncertainties and are shown in Figure 5-6 and are used as the uncertainties in 10; the lines have linestrengths > 8.319e-24 (cm^{-1}/molecule cm^{-2}).

5.4.6 Extension of the results to other vibrational bands

If the reader wishes to utilize the data from this paper as a reference for other vibrational bands, they should first use lineshape parameters from transitions that are matched by rotational quantum number assignment (found in Chapter 10) with the transitions from the new band. Sometimes this is not possible, so we present Figure 5-7 to facilitate usage of this data beyond the specific transitions studied. Panel A presents the self-broadening coefficient versus the temperature-scaling exponent, colored based on J". A linear trend emerges in the data, though there is significant scatter as expected when combining all rotational and vibrational bands into a single plot. The slope and intercept are presented on the figure and the best-fit line is shown in red. This equation should be favored over a single fixed exponent when transition-specific measurements or rotational quantum number matching are not possible.

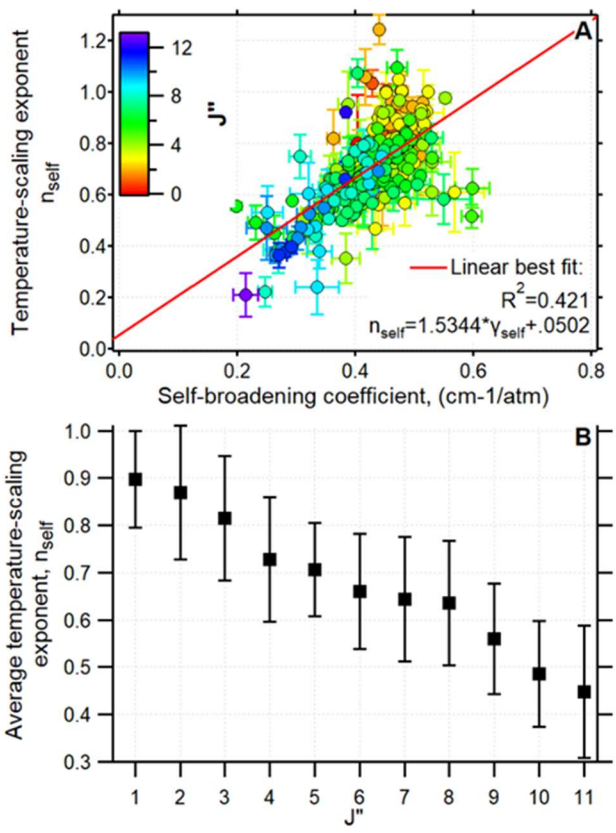

Figure 5-7 Panel A: Self-broadening coefficients versus self-broadening temperature-scaling exponents. The red line is a linear fit to the data. The R^2 of 0.431 is low but the trend is apparent. Panel B: Average temperature-scaling exponents plotted versus J".

Panel B of Figure 5-7 shows the average temperature-scaling exponent versus J". The uncertainty bars on the plot are the standard deviations of all temperature-scaling exponents at each J". The trend is clear and could be used if only the lower state J" is known.

5.5 Conclusion

We present spectral absorption parameters extracted from dual frequency comb spectrometer data spanning 296K to 1300K for pure water vapor at multiple pressures. The spectral range encompasses 6800-7200cm^{-1} at a point spacing of 0.0033cm^{-1}. We report self-broadening coefficients, speed dependent broadening coefficients, and broadening temperature-scaling exponents for 254 transitions using multispectrum fitting techniques and quadratic speed dependent

Voigt profiles. This is the first instance of lineshape parameters of numerous transitions being studied with advanced lineshapes over such a large temperature range. We provide these data on a line-by-line basis for use by other researchers. The use of the quadratic speed dependent Voigt profile allows reliable extraction of single-exponent power-law temperature scaling of self- and speed-dependent broadening coefficients. The temperature-scaling exponents show similar trends as the self-broadening coefficients with increasing J" when examined within families of transitions. We show that our extracted ratio of speed dependence to self-broadening coefficient is nearly constant for J"≤11, as expected for single molecule collision systems. Where HITRAN data already exists, much of the new measured data falls within HITRAN published uncertainties, and exhibits similar trends when comparing within transition families. We also provide interpretations of the data to facilitate its use beyond the vibrational bands investigated. We will publish similar extracted parameters from argon-water mixtures collected with the same spectrometer and experimental apparatus in a companion paper.

5.6 Acknowledgments

Support for this work was provided by the National Science Foundation under grants CBET 1336643 and 1454496, and by the Air Force Office of Scientific Research under FA9550-17-1-0224. Portions of the research described in this paper were performed at the Jet Propulsion Laboratory, California Institute of Technology, under contract with the National Aeronautics and Space Administration. Government sponsorship acknowledged.

6 Dual comb spectroscopy in a research coal gasifier

Below is a first draft of an unpublished manuscript detailing measurements that were taken in the entrained flow gasifier at Colorado School of Mines. The figures and tables below will be finalized when the paper is submitted in a letter-type format.

6.1 Introduction

The demand for various sources of efficient energy generation grows as the energy needs of the world increase. Gasification stands to fill a niche in this area since it can accept a variety of biomass and coal feedstock and produce energy via synthetic natural gas (syngas) combustion while efficiently sequestering greenhouse gasses like CO_2 [137–140]. In particular, the Integrated Gasification Combined Cycle (IGCC) shows promise to meet the growing energy needs of the developing world since it is more efficient and cleaner than standard coal combustion [141,142]. It is a process by which coal particles are pyrolyzed to generate syngas that can power a Brayton turbine while allowing for effective waste product sequestration [137,138]. However, the IGCC cycle relies heavily on particle pore diffusion for which kinetics are not well characterized, particularly at 40atm and 1900K where gasifiers typically operate. Accurate kinetics measurements would assist in optimal reactor sizing for a desired electrical output without wasting capital. The work presented here takes a first step towards characterizing an experimental scale coal gasifier that will enable more accurate understanding of these diffusion kinetics. We show direct measurements of temperature and water concentration through the core of an entrained flow coal gasifier at up to 1673K and 15bar. These measurements will enable experimental validation of temperature profiles in the gasifier core computed via computational fluid dynamics. These validated profiles will enable understanding of the gasification process as function of pore size, system gas pressure, temperature, and feed stock.

Despite the importance of measuring gasification reaction kinetics in the core of a gasifier, measurements of temperature and concentration in this region are sparse. Sun *et al.* [143] measured temperature in an experimental gasifier core but not concentrations whereas Sepman *et al.* [144] measured concentration only. As expected, direct measurements of both quantities are vital to accurate knowledge of gasifier core conditions. Sur *et al.* [143] have measured temperature and concentrations in a gasifier but downstream from the core. These measurements are useful for measuring resultant syngas composition and properties but do not directly elucidate reaction kinetics. The previous authors also did not measure in argon-laden environments like the gasifier investigated here. Therefore, these measurements are not only the first simultaneous temperature and concentration retrievals but also the first in an argon environment.

6.2 Experimental Setup

To conduct these measurements we utilize the DCS described in 1.1.4.2. The spectrometer was set to span from 6806 to 7158cm^{-1}, with a point spacing of 0.0067cm^{-1}, spectra were averaged for 30 minutes, with a pathlength of 4.8cm through the gasifier core. The laser probes a position in the core where a gasifying particle of interest will sit on a ceramic pedestal [145]. This measurement will enable a temperature reading nearby where the particle will be gasifying to give the best understanding of the influence of temperature on the gasification process. A schematic of the experimental setup can be seen in Figure 6-1.

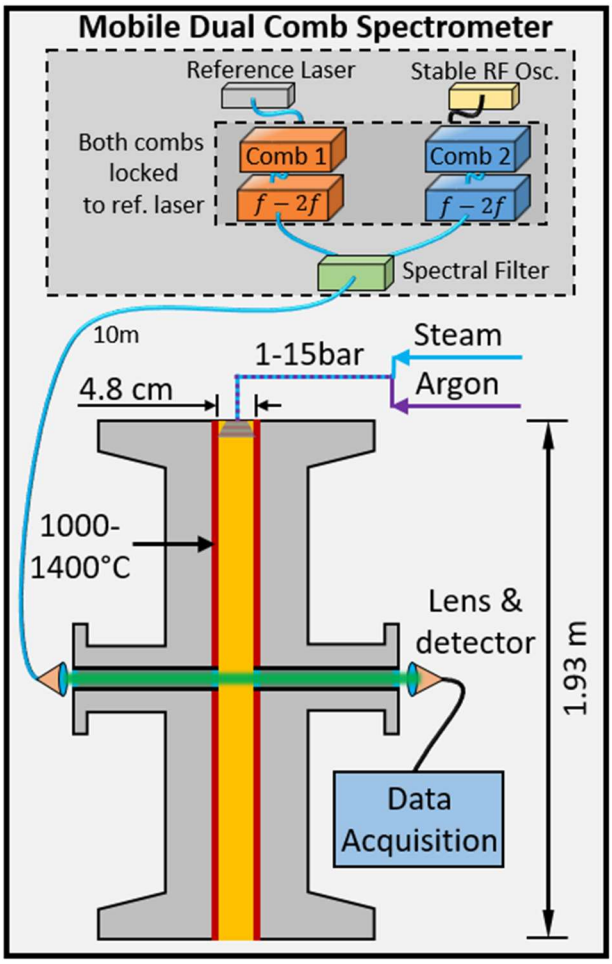

Figure 6-1-Experimental setup for the measurement. The dual comb spectrometer is a mobile version similar to that shown in Chapter 2. $f-2f$ is the method used to stabilize the carrier offset frequency.

6.3 Spectral Analysis

Many research scale gasifiers utilize argon as the entrainment gas since it is completely inert at all gasification relevant conditions. Spectral analysis of water vapor in such an argon-laden environment is impossible with current spectral databases like HITRAN2012 or HITEMP2010. Both databases utilize air as the primary broadener, which means that the broadening and shifting coefficients are invalid for non-air broadened systems. Therefore, prior to this study, we undertook a separate study to measure pure and argon broadening coefficients of water with a 2% mixture, from 100-600 Torr, 296-1300K, spanning from 6800-7200 cm^{-1} [146,147]. We utilize this in-house argon database for the absorption parameters required to accurately interpret collected spectra from the gasifier. This database incorporates a quadratic speed dependent Voigt (qSDVP) profile owing to its increased accuracy and predictable behavior over large temperature ranges [120].

6.4 Results and Discussion

We remove the slowly varying intensity background of the combs to properly normalize the spectra using techniques outlined in [66] and Section 3.2.4. For this work, we utilized a 17^{th} order polynomial over 1 THz windows across the spectrum with subsequent manual inspection to ensure that no spectral information was removed. After normalization, the entire band was simultaneously fit for temperature and concentration using the qSDVP and the in-house database. The improvement to the fit of the data is shown in Figure 6-2. The Voigt/HITRAN trace was generated based on the results of the qSDVP/in-house fit. Typical residuals, fits, and normalized data for the whole band and an arbitrarily chosen expanded section are shown in Figure 6-3. Figure 6-2 and Figure 6-3 clearly illustrate that the fit is improved when compared to models generated with HITRAN and HITEMP and Voigt profiles. However, there is clearly room for improvement. Since the gasifier is not a precise spectroscopic instrument, it is difficult to determine if the residual structure seen in the figure is due to uncertainties in the gasifier conditions or in the fits to the DCS data based on extrapolation beyond the conditions that were used to generate the database. Investigation of these discrepancies are an ongoing area of investigation in the group.

The lower panel in Figure 6-3 shows the fits to data collected at 15bar. As expected, the extrapolation of the spectral data to 15bar from where it was validated (at 1bar), resulted in poorer fit of the data when compared to the fits of the 1bar data. Again, it is difficult to determine if the mismatch results from uncertain conditions in the gasifier or model uncertainty though it is likely a combination of both. It is clear from Table 6 that the result from the 15bar data significantly under predicts mixture

concentration while the temperature extractions much more closely recreate the set temperature of the gasifier. This is likely because the temperature can be inferred from the relative peak heights of the entire band while the concertation measurement requires accurate measurements of absolute absorption. With the 15 bar data, the underlying baseline is difficult to retrieve when the absorption model is not highly accurate so overall absorption area is likely being removed during the fitting procedure. Improvement of this measurement will likely require validated high pressure spectral data rather than reliance on extrapolation to these conditions. The results of the high pressure fits are still to be finalized so the published version of this chapter may be slightly different from what is shown here.

The extracted temperature and mole fractions from the fits can be seen in Table 6-1. The values in the table are the result of iterating the fits 10 times to ensure their results were stable. Uncertainties in the table are the standard deviations of the iterated results. Exact agreement between the gasifier set temperature and the DCS spectroscopy measurements is not expected since the set temperature is based on thermocouple measurements imbedded in the walls of the gasifier. These results will allow experimental validation and incorporation to the CFD models that currently exist, which will be published in separate work.

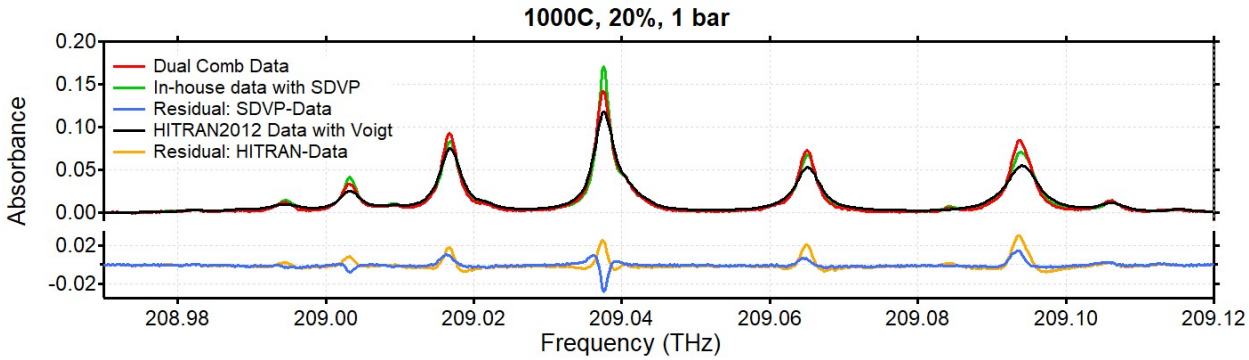

Figure 6-2-Example lines showing the improved agreement to the data using the SDVP fit and in-house database. The Voigt trace was generated using HITRAN2012 data at the fit conditions extracted using the SDVP fit. It is clear that there are still improvements to be done with the argon broadened database.

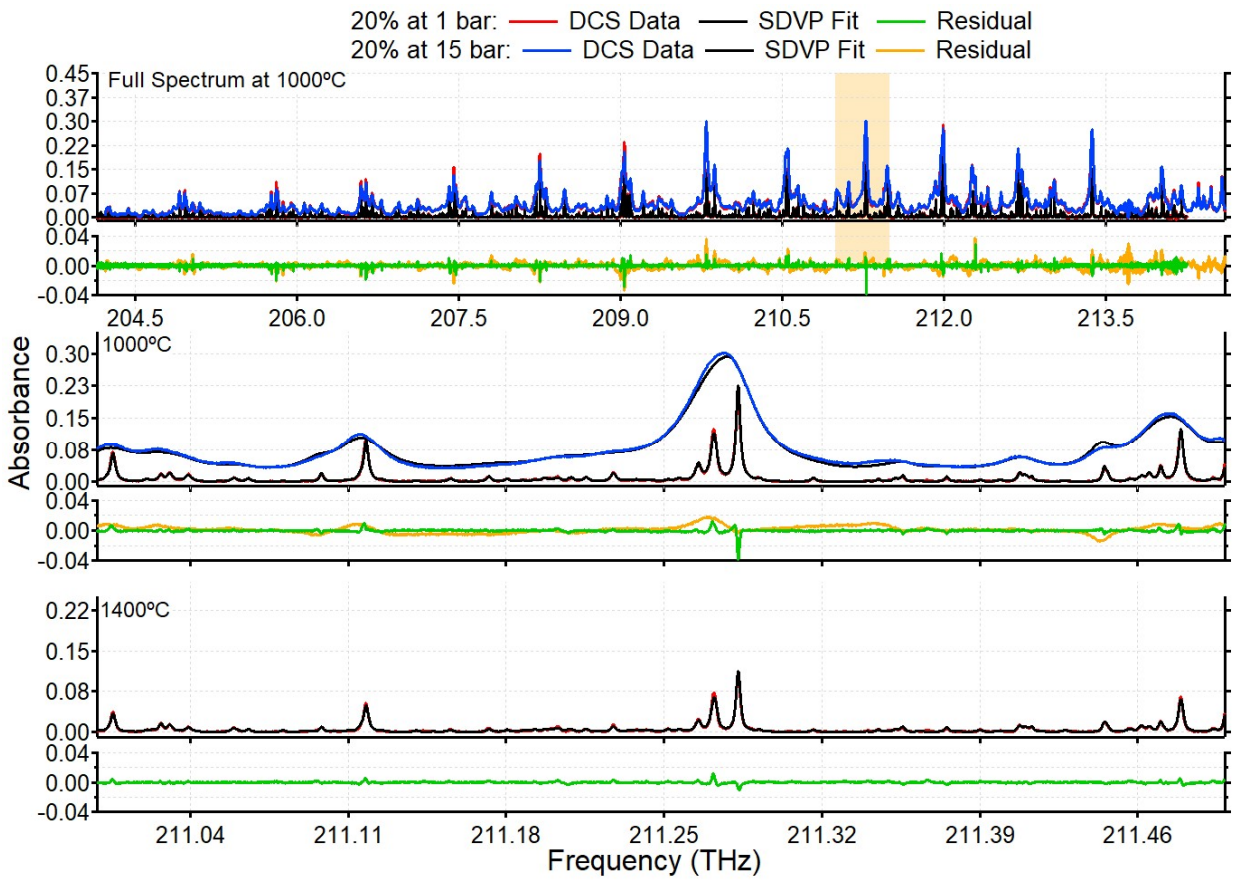

Figure 6-3-Fits, data, and residuals for the entire measured band. All lines were fit simultaneously across this band. The orange box is expanded below the figure to show the agreement between the fit and the data. The expanded panel also shows the results from fitting the 15 bar data.

Table 6-1-Results of the fit using the SDVP and the in-house database versus the gasifier set conditions. It is clear that the temperature retrievals are all near their set points but concentration retrievals vary far more. The values in parentheses are the precisions of the retrieved values. % diff. refers to the absolute percent difference between the set and retrieved values.

Pressure (bar)	Set Temp. (°C)	Fit Temp. (°C)	% diff.	Set X (%)	Fit X (%)	% diff.
1	1000 (9.0)	1020 (17.7)	1.8	20	25.4 (0.43)	23.7
1	1400 (11.0)	1397 (5.7)	0.17	20	21.1 (0.13)	5.5
1	1000 (9.0)	1039 (4.0)	3.84	50	36.4 (0.47)	31.6
15	1000 (9.0)	970 (19.9)	3.0	20	14.4 (0.3)	32.6

6.5 Conclusion

Prior to these measurements and database development, broadband absorption spectroscopy measurements in argon-laden environments were impossible owing to the lack of reliable broadening and shifting coefficients. We leverage the broad nature of a dual frequency comb spectrometer to measure many transitions at once to show precise temperature measurements of the water vapor in the gasifier core. There are still discrepancies between the fit and data but this is to be expected with the first utilization of an in-house database outside of its original physical conditions. Despite the discrepancies, we were able to extract temperatures up to 1400°C at concentrations of 21% steam with high precision in the gasifier core. These results will assist in computed temperature profile validation for the gasifier to enable more accurate kinetics studies.

6.6 Acknowledgements

The authors would like to acknowledge the National Science Foundation (NSF) CAREER award CBET 1454496 and CBET 1336643.

7 Dissertation Summary and Future Directions

7.1 Dissertation Summary

The preceding work will comprise my dissertation. It shows the first implementation of a dual frequency comb spectrometer untethered from the optics laboratory and utilized in industrial environments. The broadband, highly accurate spectra will help to further optimize and understand harsh industrial combustion systems like natural gas turbines and coal gasifiers. It will also add to the current knowledge of high temperature behavior of water vapor to further enable accurate spectroscopic measurements of temperature and species in these harsh environments.

The resultant first-author publications resulting from this dissertation are as follows:

1-Chapter 2 has been accepted to the Proceedings of the Combustion Institute (peer reviewed and indexed journal publication).

Citation: Schroeder PJ, Wright RJ, Coburn S, Sodergren B, Cossel KC, Droste S, Truong GW, Baumann E, Giorgetta FR, Coddington I, Newbury NR., G.B. Rieker. Dual frequency comb laser absorption spectroscopy in a 16 MW gas turbine exhaust. Proceedings of the Combustion Institute. 2017 Dec 31;36(3):4565-73.

2-Chapter 3 has been accepted and is in press to the Journal of Quantitative Spectroscopy and Radiative Transfer (JQSRT): HITRAN special edition.

Title: High temperature comparison of the HITRAN2012 and HITEMP2010 water vapor absorption databases to frequency comb measurements

Author List: P.J. Schroeder[1], D.J. Pfotenhauer[1], J. Yang[1], F.R. Giorgetta[2], W.C. Swann[2], I. Coddington[2], N.R. Newbury[2], G.B. Rieker[1]

[1]Precision Laser Diagnostics Laboratory, University of Colorado Boulder

[2]Applied Physics Division, National Institute of Standards and Technology, Boulder, CO

3-Chapter 4 has been submitted to Physical Review A and is in review for acceptance.

Title: Multispectral fitting validation of the speed dependent Voigt profile for high temperature water vapor absorption with a dual frequency comb spectrometer

Author List: Paul J. Schroeder[1], Matthew Cich[2], Jinyu Yang[1], William C. Swann[3], Ian Coddington[3], Nathan R. Newbury[3], Brian Drouin[2], Gregory B. Rieker[1]

[1]Precision Laser Diagnostics Laboratory, University of Colorado Boulder

[2]Jet Propulsion Laboratory - NASA, California Institute of Technology, 4800, Oak Grove Drive, Pasadena, CA 91109-8099, USA

[3]Applied Physics Division, National Institute of Standards and Technology, Boulder, CO

4-Chapter 5 has been written and is in internal review. It will be sent to JPL and NIST by the end of May 2017. The data will result in two companion papers, one for pure water and one for argon-broadened water. They will also be submitted to JQSRT as a separate publications with myself as the first author on the pure water work and Jinyu Yang as the first author with me second on the second argon-water data.

Title: Speed-dependent Voigt Line shape Parameter Database from Dual Frequency Comb Measurements at up to 1300K: Part I. Pure H2O, 6800-7200cm-1

Extraction of pure water vapor pressure and temperature dependent parameters up to 1300K employing dual frequency comb spectroscopy, Part 1

Author List: Paul J. Schroeder[1], Matthew Cich[2], Jinyu Yang[1], Fabrizio R. Giorgetta[3], William C. Swann[3], Ian Coddington[3], Nathan R. Newbury[3], Brian Drouin[2], Gregory B. Rieker[1]
[1] Precision Laser Diagnostics Laboratory, University of Colorado Boulder
[2] Jet Propulsion Laboratory - NASA, California Institute of Technology, 4800, Oak Grove Drive, Pasadena, CA 91109-8099, USA
[3]Applied Physics Division, National Institute of Standards and Technology, Boulder, CO

5- Chapter 6 is currently composed of unpublished, preliminary results that will be published following the publication of this dissertation. The final results will likely be slightly different than those presented here.

7.2 Future Research Directions

7.2.1 Mid-infrared dual comb spectroscopy

The entirety of this dissertation focused on spectroscopy in the near infrared region (NIR) of light, up to about 1.5 μm. Building instruments in this region is desirable owing to the large number of readily available and robust optical components. However, this region is not ideal for spectroscopy of many important molecules. Considering the pathlengths easily achieved in the laboratory or field measurements, not many molecules besides H_2O, CO_2, and CH_4 are easily measured in this region of light. Measurement of these molecules provides some information about certain combustion systems though almost all other gas-phase molecules of scientific, commercial, or industrial interest absorb orders of magnitude more strongly in the mid infrared region (MIR), >2 μm to approximately 8 μm. A robust dual comb spectrometer operating in this region would allow sensing of lower concentrations of the previously mentioned molecules and sensing of many atmospherically and combustions relevant molecules like NOx, SO_2, CO, N_2O, among many others, that are either inactive in the NIR or are too weak to practically measure.

Operation in the MIR does incur significant challenges. For example, when measuring high temperature systems, the blackbody curve is typically very strong in the MIR so the detector can be more easily saturated by coupled radiation. Additionally, optical components in the MIR region are more expensive and less robust than components in the NIR, which are significant considerations when building a field ready instrument.

7.2.2 High pressure, high temperature conditions

All chapters in this dissertation, except for Chapter 6, focused on system pressures less than or equal to 1 bar at highly elevated temperatures. However, many systems like combustors or exoplanets exist at high temperatures while being at high pressures. Most current data used to interpret spectra was collected at room temperature and room pressure and the spectral parameters do not reliably extrapolate to conditions relative to the above systems. Therefore, to make accurate measurements, the spectroscopic models need to be developed and validated at relevant conditions. Some experimenters have explored high temperatures [14,76,92] like those in this dissertation but few have examined high pressures and fewer still have examined both conditions simultaneously. High temperatures present many problems with accurately scaling broadening and shifting coefficients while high pressures can induce less studied

physical mechanisms like line mixing, collisional induced absorption, and the breakdown of the impact approximation. The temperature and pressure effects are not completely orthogonal so measurements must be conducted at a combination of both regimes to obtain an accurate representation of the spectra. It is highly likely that once these regimes are explored, the current models and databases will completely fail thereby necessitating modifications to the theoretical arguments to bring models and measurements together.

To begin to address this question, we have built a spectroscopic cell capable of 1000°C operation at 100 bar with a 45.7cm pathlength. As of the publication of this dissertation, the system has been constructed and our group is in the process of collecting the first spectra. Coupling this cell with our DCS will allow measurement of hundreds of transitions as they broaden. The broadband, highly resolved nature of the DCS coupled with multispectral fitting algorithms will allow us to track transitions from room pressure, room temperature, where they are isolated and well characterized, to the high pressure, high temperature regimes where the physical models are unvalidated. At pressures greater than approximately 20 bar the transitions broaden into a continuous spectrum that completely removes all nonabsorbing baseline. Measurement of nonabsorbing baseline is vital to accurate retrievals of full lineshapes and absolute peak heights. Therefore, the system not only employs a quartz cell to house the gas of interest, but an additional, identical cell immediately adjacent filled with nonabsorbing gas that will allow continuous measurement of the laser intensity baseline. The spectra collected with this system will likely follow a similar analysis process as that outlined in Chapters 4 and 5 though will require special consideration for the high pressure spectroscopic models. This combination of the DCS with high pressure and high temperature spectra are unmatched in the field and presents an impactful path of research for the group.

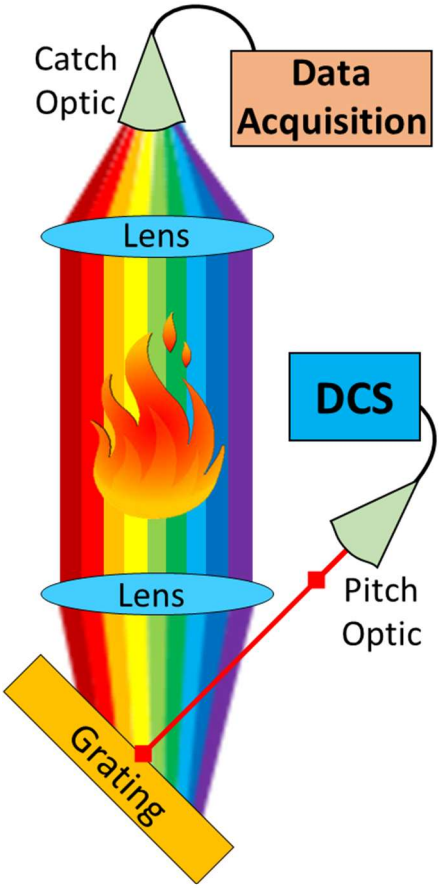

Figure 7-1-Top view of the schematic of the optical setup to spatially resolve temperature gradients in a flame or nonuniform source.

7.2.3 Spatial temperature profiling with dual comb spectroscopy

Owing to the large spectral bandwidth and dense point spacing of DCS, the possibility exists to use the technique to spatially profile a flame or other nonuniform, high-temperature system. Currently, spatially resolved temperature profiles are acquired by translating the pitch and catch optics across the flame width. This technique works well if the flame is known to be stable in time so that measurements through one part of the flame correspond to later measurements from another part of the flame. However, transients in the flame can nullify this assumption. DCS could begin to answer this question with a very simple optical setup shown in Figure 7-1. In the setup, the combined DCS beam is directed onto a diffraction grating. This grating will separate the constituent wavelengths of the light by the grating equation, $dsin(\Theta_m) = m\lambda$, where d is the distance between grating slits, Θ_m is the angle of mth mode of light diffracted, m is the diffraction mode, and λ is the wavelength of light. Therefore, the width of the diffracted beam would be transformed from a width in frequency to a width in space. The comb tooth spacing would then correspond to the smallest resolvable length difference

within that beam. For example, if the beam is expanded to a 50mm wide ribbon that spans 400cm^{-1} in spectral bandwidth, the spacing between each resolvable comb tooth would map to a physical separation of 8.3e-3mm using a 200MHz comb repetition rate. The limitation in spatial accuracy of this technique would be the measurement of the ribbon width. Nonuniform temperature measurements would use fits of single transitions to retrieve of a slice of the flame, shown by the various colors in Figure 7-1. In the figure, each color would encompass a few transitions of a molecule of interest since the frequency bandwidth corresponds to a physical length. These transitions would therefore yield the temperature measurement of that particular slice.

8 References

[1] Sur R, Sun K, Jeffries JB, Hanson RK. Multi-species laser absorption sensors for in situ monitoring of syngas composition. Appl Phys B 2013;115:9–24. doi:10.1007/s00340-013-5567-2.

[2] Ebert V, Fitzer J, Gerstenberg I, Pleban K-U, Pitz H, Wolfrum J, et al. Simultaneous laser-based in situ detection of oxygen and water in a waste incinerator for active combustion control purposes. Symposium (International) on Combustion 1998;27:1301–8. doi:10.1016/S0082-0784(98)80534-1.

[3] Rieker GB, Jeffries JB, Hanson RK, Mathur T, Gruber MR, Carter CD. Diode laser-based detection of combustor instabilities with application to a scramjet engine. Proceedings of the Combustion Institute 2009;32:831–838.

[4] Akiya N, Savage PE. Roles of Water for Chemical Reactions in High-Temperature Water. Chem Rev 2002;102:2725–50. doi:10.1021/cr000668w.

[5] Docquier N, Candel S. Combustion control and sensors: a review. Progress in Energy and Combustion Science 2002;28:107–50. doi:10.1016/S0360-1285(01)00009-0.

[6] Goldenstein CS, Spearrin RM, Jeffries JB, Hanson RK. Infrared laser-absorption sensing for combustion gases. Progress in Energy and Combustion Science 2017;60:132–176.

[7] Grillmair CJ, Burrows A, Charbonneau D, Armus L, Stauffer J, Meadows V, et al. Strong water absorption in the dayside emission spectrum of the planet HD 189733b. Nature 2008;456:767–9. doi:10.1038/nature07574.

[8] Konopacky QM, Barman TS, Macintosh BA, Marois C. Detection of Carbon Monoxide and Water Absorption Lines in an Exoplanet Atmosphere. Science 2013;339:1398–401. doi:10.1126/science.1232003.

[9] Tinetti G, Vidal-Madjar A, Liang M-C, Beaulieu J-P, Yung Y, Carey S, et al. Water vapour in the atmosphere of a transiting extrasolar planet. Nature 2007;448:169–71. doi:10.1038/nature06002.

[10] Rothman LS, Gordon IE, Babikov Y, Barbe A, Chris Benner D, Bernath PF, et al. The HITRAN2012 molecular spectroscopic database. Journal of Quantitative Spectroscopy and Radiative Transfer 2013;130:4–50. doi:10.1016/j.jqsrt.2013.07.002.

[11] Rothman LS, Gordon IE, Barber RJ, Dothe H, Gamache RR, Goldman A, et al. HITEMP, the high-temperature molecular spectroscopic database. Journal of Quantitative Spectroscopy and Radiative Transfer 2010;111:2139–50. doi:10.1016/j.jqsrt.2010.05.001.

[12] Hill C, Gordon IE, Kochanov RV, Barrett L, Wilzewski JS, Rothman LS. HITRANonline: An online interface and the flexible representation of spectroscopic data in the HITRAN database. Journal of Quantitative Spectroscopy and Radiative Transfer 2016;177:4–14. doi:10.1016/j.jqsrt.2015.12.012.

[13] Tennyson J, Bernath PF, Campargue A, Császár AG, Daumont L, Gamache RR, et al. Recommended isolated-line profile for representing high-resolution spectroscopic transitions (IUPAC Technical Report). Pure and Applied Chemistry 2014;86:1931–1943. doi:10.1515/pac-2014-0208.

[14] Goldenstein CS, Hanson RK. Diode-laser measurements of linestrength and temperature-dependent lineshape parameters for H2O transitions near 1.4 μm using Voigt, Rautian, Galatry, and speed-dependent Voigt profiles. Journal of Quantitative Spectroscopy and Radiative Transfer 2015;152:127–39. doi:10.1016/j.jqsrt.2014.11.008.

[15] Liu X, Jeffries JB, Hanson RK. Measurements of spectral parameters of water-vapour transitions near 1388 and 1345 nm for accurate simulation of high-pressure absorption spectra. Meas Sci Technol 2007;18:1185. doi:10.1088/0957-0233/18/5/004.

[16] Zhou X, Liu X, Jeffries JB, Hanson RK. Development of a sensor for temperature and water concentration in combustion gases using a single tunable diode laser. Meas Sci Technol 2003;14:1459. doi:10.1088/0957-0233/14/8/335.

[17] Sun K, Chao X, Sur R, Jeffries JB, Hanson RK. Wavelength modulation diode laser absorption spectroscopy for high-pressure gas sensing. Applied Physics B 2012;110:497–508. doi:10.1007/s00340-012-5286-0.
[18] Cai T, Jia H, Wang G, Chen W, Gao X. A sensor for measurements of temperature and water concentration using a single tunable diode laser near 1.4 μm. Sensors and Actuators A: Physical 2009;152:5–12. doi:10.1016/j.sna.2009.03.004.
[19] Barber RJ, Tennyson J, Harris GJ, Tolchenov RN. A high-accuracy computed water line list. MNRAS 2006;368:1087–94. doi:10.1111/j.1365-2966.2006.10184.x.
[20] Fiadzomor PA, Baker DM, Keen AM, Grant RB, Orr-Ewing AJ. Pressure Broadening of H2O Absorption Lines in the 1.3 μm Region Measured by Continuous Wave-Cavity Ring-Down Spectroscopy: Application in the Trace Detection of Water Vapor in N2, SiH4, CF4, and PH3. Applied Spectroscopy 2008;62:1354–1362.
[21] Sajid MB, Es-sebbar E, Farooq A. Measurements of linestrengths, N 2-, Ar-, He-and self-broadening coefficients of acetylene in the ν 4+ ν 5 combination band using a cw quantum cascade laser. Journal of Quantitative Spectroscopy and Radiative Transfer 2014;148:1–12.
[22] Ultrashort-pulsed lasers | Cundiff Laboratory https://jila.colorado.edu/cundiff/research/ultrashort-pulsed-lasers (accessed April 15, 2016).
[23] Keilmann F, Gohle C, Holzwarth R. Time-domain mid-infrared frequency-comb spectrometer. Optics Letters 2004;29:1542–1544.
[24] Brehm M, Schliesser A, Keilmann F. Spectroscopic near-field microscopy using frequency combs in the mid-infrared. Opt Express 2006;14:11222–11233.
[25] Coddington I, Swann WC, Newbury NR. Coherent Multiheterodyne Spectroscopy Using Stabilized Optical Frequency Combs. Phys Rev Lett 2008;100:013902. doi:10.1103/PhysRevLett.100.013902.
[26] Roy J, Deschênes J-D, Potvin S, Genest J. Continuous real-time correction and averaging for frequency comb interferometry. Optics Express 2012;20:21932–21939.
[27] Udem T, Holzwarth R, Hänsch TW. Optical frequency metrology. Nature 2002;416:233–237.
[28] Hall JL. Nobel Lecture: Defining and measuring optical frequencies*. Rev Mod Phys 2006;78:1279–95. doi:10.1103/RevModPhys.78.1279.
[29] Diddams SA. The evolving optical frequency comb [Invited]. Journal of the Optical Society of America B 2010;27:B51. doi:10.1364/JOSAB.27.000B51.
[30] Bruker Corporation: IFS 125HR - Overview https://www.bruker.com/products/infrared-near-infrared-and-raman-spectroscopy/ftir-research-spectrometers/ifs-125hr/overview.html (accessed April 7, 2016).
[31] Long DA, Fleisher AJ, Douglass KO, Maxwell SE, Bielska K, Hodges JT, et al. Multiheterodyne spectroscopy with optical frequency combs generated from a continuous-wave laser. Optics Letters 2014;39:2688–2690.
[32] Potvin S, Genest J. Dual-comb spectroscopy using frequency-doubled combs around 775 nm. Optics Express 2013;21:30707–30715.
[33] Boudreau S, Levasseur S, Perilla C, Roy S, Genest J. Chemical detection with hyperspectral lidar using dual frequency combs. Optics Express 2013;21:7411–7418.
[34] Bernhardt B, Ozawa A, Jacquet P, Jacquey M, Kobayashi Y, Udem T, et al. Cavity-enhanced dual-comb spectroscopy. Nature Photonics 2010;4:55–57.
[35] Schliesser A, Brehm M, Keilmann F, van der Weide D. Frequency-comb infrared spectrometer for rapid, remote chemical sensing. Optics Express 2005;13:9029–9038.
[36] Ideguchi T, Poisson A, Guelachvili G, Picqué N, Hänsch TW. Adaptive real-time dual-comb spectroscopy. Nature Communications 2014;5.
[37] Zolot AM, Giorgetta FR, Baumann E, Nicholson JW, Swann WC, Coddington I, et al. Direct-comb molecular spectroscopy with accurate, resolved comb teeth over 43 THz. Optics Letters 2012;37:638. doi:10.1364/OL.37.000638.

[38] Baumann E, Giorgetta FR, Swann WC, Zolot AM, Coddington I, Newbury NR. Spectroscopy of the methane ν_{3} band with an accurate midinfrared coherent dual-comb spectrometer. Physical Review A 2011;84. doi:10.1103/PhysRevA.84.062513.
[39] Rieker GB, Giorgetta FR, Swann WC, Kofler J, Zolot AM, Sinclair LC, et al. Frequency-comb-based remote sensing of greenhouse gases over kilometer air paths. Optica 2014;1:290. doi:10.1364/OPTICA.1.000290.
[40] Coddington I, Swann WC, Newbury NR. Coherent dual-comb spectroscopy at high signal-to-noise ratio. Physical Review A 2010;82:043817.
[41] Zolot AM, Giorgetta FR, Baumann E, Swann WC, Coddington I, Newbury NR. Broad-band frequency references in the near-infrared: Accurate dual comb spectroscopy of methane and acetylene. Journal of Quantitative Spectroscopy and Radiative Transfer 2013;118:26–39. doi:10.1016/j.jqsrt.2012.11.024.
[42] Bernhardt B, Sorokin E, Jacquet P, Thon R, Becker T, Sorokina IT, et al. Mid-infrared dual-comb spectroscopy with 2.4 μm Cr2+:ZnSe femtosecond lasers. Applied Physics B 2010;100:3–8. doi:10.1007/s00340-010-4080-0.
[43] Ultrashort Laser Pulse Phenomena, 2nd Edition | Jean-Claude Diels, Wolfgang Rudolph | ISBN 9780122154935 http://store.elsevier.com/Ultrashort-Laser-Pulse-Phenomena/JeanClaude-Diels/isbn-9780122154935/ (accessed April 18, 2016).
[44] Sinclair LC, Coddington I, Swann WC, Rieker GB, Hati A, Iwakuni K, et al. Operation of an optically coherent frequency comb outside the metrology lab. Optics Express 2014;22:6996. doi:10.1364/OE.22.006996.
[45] Zirngibl M, Stulz LW, Stone J, Hugi J, DiGiovanni D, Hansan PB. 1.2 ps pulses from passively mode-locked laser diode pumped Er-doped fibre ring laser. Electronics Letters 1991;27:1734. doi:10.1049/el:19911079.
[46] Sinclair LC, Deschênes J-D, Sonderhouse L, Swann WC, Khader IH, Baumann E, et al. Invited Article: A compact optically coherent fiber frequency comb. Review of Scientific Instruments 2015;86:081301. doi:10.1063/1.4928163.
[47] Ideguchi T, Poisson A, Guelachvili G, Hänsch TW, Picqué N. Adaptive dual-comb spectroscopy in the green region. Optics Letters 2012;37:4847–4849.
[48] Kuse N, Ozawa A, Kobayashi Y. Comb-resolved dual-comb spectroscopy stabilized by free-running continuous-wave lasers. Applied Physics Express 2012;5:112402.
[49] Coddington I, Newbury N, Swann W. Dual-comb spectroscopy. Optica, OPTICA 2016;3:414–26. doi:10.1364/OPTICA.3.000414.
[50] Ideguchi T. Dual-Comb Spectroscopy. Optics and Photonics News 2017;28:32–39.
[51] Alrahman CA, Khodabakhsh A, Schmidt FM, Qu Z, Foltynowicz A. Cavity-enhanced optical frequency comb spectroscopy of high-temperature H 2 O in a flame. Optics Express 2014;22:13889–13895.
[52] Adler F, Maslowski P, Foltynowicz A, Cossel KC, Briles TC, Hartl I, et al. Mid-infrared Fourier transform spectroscopy with a broadband frequency comb. Opt Express 2010;18:21861–21872.
[53] Langridge JM, Laurila T, Watt RS, Jones RL, Kaminski CF, Hult J. Cavity enhanced absorption spectroscopy of multiple trace gas species using a supercontinuum radiation source. Optics Express 2008;16:10178. doi:10.1364/OE.16.010178.
[54] Kovalenko SA, Dobryakov AL, Ruthmann J, Ernsting NP. Femtosecond spectroscopy of condensed phases with chirped supercontinuum probing. Phys Rev A 1999;59:2369–84. doi:10.1103/PhysRevA.59.2369.
[55] Jayaraman V, Cole GD, Robertson M, Uddin A, Cable A. High-sweep-rate 1310 nm MEMS-VCSEL with 150 nm continuous tuning range. Electronics Letters 2012;48:867–869.
[56] Liu X, Zhou X, Jeffries JB, Hanson RK. Experimental study of H2O spectroscopic parameters in the near-IR (6940–7440 cm−1) for gas sensing applications at elevated temperature. Journal of Quantitative Spectroscopy and Radiative Transfer 2007;103:565–77. doi:10.1016/j.jqsrt.2006.07.008.

[57] Sanders ST. Wavelength-agile fiber laser using group-velocity dispersion of pulsed super-continua and application to broadband absorption spectroscopy. Appl Phys B 2002;75:799–802. doi:10.1007/s00340-002-1044-z.
[58] Farooq A, Jeffries JB, Hanson RK. High-pressure measurements of CO2 absorption near 2.7 μm: Line mixing and finite duration collision effects. Journal of Quantitative Spectroscopy and Radiative Transfer 2010;111:949–60. doi:10.1016/j.jqsrt.2010.01.001.
[59] Goldenstein CS, Strand CL, Schultz IA, Sun K, Jeffries JB, Hanson RK. Fitting of calibration-free scanned-wavelength-modulation spectroscopy spectra for determination of gas properties and absorption lineshapes. Appl Opt 2014;53:356–67. doi:10.1364/AO.53.000356.
[60] Arita Y, Stevens R, Ewart P. Multi-mode absorption spectroscopy of oxygen for measurement of concentration, temperature and pressure. Applied Physics B 2008;90:205–211.
[61] Mihalcea RM, Baer DS, Hanson RK. Advanced diode laser absorption sensor for in situ combustion measurements of CO 2, H 2 O, and gas temperature. Symposium (International) on Combustion, vol. 27, Elsevier; 1998, p. 95–101.
[62] Sun K, Sur R, Jeffries JB, Hanson RK, Clark T, Anthony J, et al. Application of wavelength-scanned wavelength-modulation spectroscopy H2O absorption measurements in an engineering-scale high-pressure coal gasifier. Appl Phys B 2014;117:411–21. doi:10.1007/s00340-014-5850-x.
[63] Schliesser A, Picqué N, Hänsch TW. Mid-infrared frequency combs. Nature Photonics 2012;6:440–9. doi:10.1038/nphoton.2012.142.
[64] Truong G-W, Waxman EM, Cossel KC, Baumann E, Klose A, Giorgetta FR, et al. Accurate frequency referencing for fieldable dual-comb spectroscopy. Optics Express 2016;24:30495–30504.
[65] Schroeder PJ, Wright RJ, Coburn S, Sodergren B, Cossel KC, Droste S, et al. Dual frequency comb laser absorption spectroscopy in a 16 MW gas turbine exhaust. Proceedings of the Combustion Institute 2016.
[66] Schroeder PJ, Pfotenhauer DJ, Yang J, Giorgetta FR, Swann WC, Coddington I, et al. High temperature comparison of the HITRAN2012 and HITEMP2010 water vapor absorption databases to frequency comb measurements. Journal of Quantitative Spectroscopy and Radiative Transfer 2017.
[67] Hanson RK, Spearrin RM, Goldenstein CS. Spectroscopy and Optical Diagnostics for Gases. Cham: Springer International Publishing; 2016.
[68] Rothman LS, Gordon IE, Barbe A, Benner DC, Bernath PF, Birk M, et al. The HITRAN 2008 molecular spectroscopic database. Journal of Quantitative Spectroscopy and Radiative Transfer 2009;110:533–72. doi:10.1016/j.jqsrt.2009.02.013.
[69] Toth RA, Brown LR, Smith MAH, Malathy Devi V, Chris Benner D, Dulick M. Air-broadening of H2O as a function of temperature: 696–2163 cm−1. Journal of Quantitative Spectroscopy and Radiative Transfer 2006;101:339–66. doi:10.1016/j.jqsrt.2005.11.022.
[70] Toth RA. Air- and N2-Broadening Parameters of Water Vapor: 604 to 2271 cm−1. Journal of Molecular Spectroscopy 2000;201:218–43. doi:10.1006/jmsp.2000.8098.
[71] Brown LR, Toth RA, Dulick M. Empirical Line Parameters of H216O near 0.94 μm: Positions, Intensities and Air-Broadening Coefficients. Journal of Molecular Spectroscopy 2002;212:57–82. doi:10.1006/jmsp.2002.8515.
[72] Predoi-Cross A, McKellar ARW, Benner DC, Devi VM, Gamache RR, Miller CE, et al. Temperature dependences for air-broadened Lorentz half-width and pressure shift coefficients in the 30013←00001 and 30012←00001 bands of CO2 near 1600 nm This article is part of a Special Issue on Spectroscopy at the University of New Brunswick in honour of Colan Linton and Ron Lees. Can J Phys 2009;87:517–35. doi:10.1139/P08-137.
[73] Rothman LS, Jacquemart D, Barbe A, Benner DC, Birk M, Brown LR, et al. The HITRAN 2004 molecular spectroscopic database. Journal of Quantitative Spectroscopy and Radiative Transfer 2005;96:139–204.

[74] Rothman LS, Barbe A, Benner DC, Brown LR, Camy-Peyret C, Carleer MR, et al. The HITRAN molecular spectroscopic database: edition of 2000 including updates through 2001. Journal of Quantitative Spectroscopy and Radiative Transfer 2003;82:5–44.
[75] Tennyson J, Bernath PF, Brown LR, Campargue A, Császár AG, Daumont L, et al. IUPAC critical evaluation of the rotational–vibrational spectra of water vapor, Part III: Energy levels and transition wavenumbers for H216O. Journal of Quantitative Spectroscopy and Radiative Transfer 2013;117:29–58. doi:10.1016/j.jqsrt.2012.10.002.
[76] Birk M, Wagner G. Temperature-dependent air broadening of water in the 1250–1750 cm−1 range. Journal of Quantitative Spectroscopy and Radiative Transfer 2012;113:889–928. doi:10.1016/j.jqsrt.2011.12.013.
[77] Rutkowski L, Khodabakhsh A, Johansson AC, Valiev DM, Lodi L, Qu Z, et al. Measurement of H 2 O and OH in a Flame by Optical Frequency Comb Spectroscopy. CLEO: Science and Innovations, Optical Society of America; 2016, p. SW4H–8.
[78] Zhu F, Mohamed T, Strohaber J, Kolomenskii AA, Udem T, Schuessler HA. Real-time dual frequency comb spectroscopy in the near infrared. Applied Physics Letters 2013;102:121116. doi:10.1063/1.4799282.
[79] BRAN - Boulder Research and Administration Network http://www.branfiber.net/ (accessed March 20, 2016).
[80] Adams RO. A review of the stainless steel surface. Journal of Vacuum Science & Technology A 1983;1:12–8. doi:10.1116/1.572301.
[81] Truong G-W. Effects of Phase Noise on Coherent Dual-Comb Spectroscopy, In preparation 2017.
[82] Tennyson J. Experimental Energy Levels of the Water Molecule. Journal of Physical and Chemical Reference Data 2001;30:735. doi:10.1063/1.1364517.
[83] Gordon IE. Line positions generated from the database of experimentally-determined energy levels. (This is reference 43 ("H2O [1]", "Positions" section) from the HITRAN reference list but does not correspond to a published paper). HITRAN/HITEMP Reference List 2008.
[84] Toth RA. Linelist of water vapor parameters from 500 to 8000 cm-1 http://mark4sun.jpl.nasa.gov/h2o.html (accessed March 20, 2016).
[85] Gordon IE, Rothman LS, Gamache RR, Jacquemart D, Boone C, Bernath PF, et al. Current updates of the water-vapor line list in HITRAN: A new "Diet" for air-broadened half-widths. Journal of Quantitative Spectroscopy and Radiative Transfer 2007;108:389–402.
[86] Robert D, Bonamy J. Short range force effects in semiclassical molecular line broadening calculations. Journal de Physique 1979;40:923–943.
[87] Hartmann J-M, Rosenmann L, Perrin M-Y, Taine J. Accurate calculated tabulations of CO line broadening by H 2 O, N 2, O 2, and CO 2 in the 200–3000-K temperature range. Applied Optics 1988;27:3063–3065.
[88] Labani B, Bonamy J, Robert D, Hartmann JM, Taine J. Collisional broadening of rotation–vibration lines for asymmetric top molecules. I. Theoretical model for both distant and close collisions. The Journal of Chemical Physics 1986;84:4256–4267.
[89] Grossmann BE, Browell EV. Spectroscopy of water vapor in the 720-nm wavelength region: Line strengths, self-induced pressure broadenings and shifts, and temperature dependence of linewidths and shifts. Journal of Molecular Spectroscopy 1989;136:264–94. doi:10.1016/0022-2852(89)90336-6.
[90] Tran H, Ngo NH, Hartmann J-M, Gamache RR, Mondelain D, Kassi S, et al. Velocity effects on the shape of pure H2O isolated lines: Complementary tests of the partially correlated speed-dependent Keilson-Storer model. The Journal of Chemical Physics 2013;138:034302.
[91] Ngo NH, Tran H, Gamache RR, Hartmann JM. Pressure effects on water vapour lines: beyond the Voigt profile. Philosophical Transactions of the Royal Society of London A: Mathematical, Physical and Engineering Sciences 2012;370:2495–2508.
[92] Wagner G, Birk M, Gamache RR, Hartmann J-M. Collisional parameters of H2O lines: effect of temperature. Journal of Quantitative Spectroscopy and Radiative Transfer 2005;92:211–230.

[93] Dicke RH. The effect of collisions upon the Doppler width of spectral lines. Physical Review 1953;89:472.
[94] Varghese PL, Hanson RK. Collisional narrowing effects on spectral line shapes measured at high resolution. Applied Optics 1984;23:2376–2385.
[95] Rautian SG, Sobel'man II. The effect of collisions on the Doppler broadening of spectral lines. Soviet Physics Uspekhi 1967;9:701.
[96] Hartmann J-M, Boulet C, Robert D. Collisional effects on molecular spectra: laboratory experiments and models, consequences for applications. Elsevier; 2008.
[97] De Vizia MD, Castrillo A, Fasci E, Amodio P, Moretti L, Gianfrani L. Experimental test of the quadratic approximation in the partially correlated speed-dependent hard-collision profile. Physical Review A 2014;90:022503.
[98] Toth RA. Extensive measurements of H 2 16 O line frequencies and strengths: 5750 to 7965 cm-1. Applied Optics 1994;33:4851–4867.
[99] Michaels CA, Masiello T, Chu PM. Fourier Transform Spectrometry with a Near-Infrared Supercontinuum Source. Appl Spectrosc, AS 2009;63:538–43.
[100] Hult J, Watt RS, Kaminski CF. High bandwidth absorption spectroscopy with a dispersed supercontinuum source. Optics Express 2007;15:11385. doi:10.1364/OE.15.011385.
[101] Zobov NF, Shirin SV, Ovsyannikov RI, Polyansky OL, Barber RJ, Tennyson J, et al. Spectrum of hot water in the 4750–13 000 cm−1 wavenumber range (0.769–2.1 μm). MNRAS 2008;387:1093–8. doi:10.1111/j.1365-2966.2008.13234.x.
[102] Larcher G, Tran H, Schwell M, Chelin P, Landsheere X, Hartmann J-M, et al. CO2 isolated line shapes by classical molecular dynamics simulations: Influence of the intermolecular potential and comparison with new measurements. The Journal of Chemical Physics 2014;140:084308. doi:10.1063/1.4866449.
[103] Benner DC, Rinsland CP, Devi VM, Smith MAH, Atkins D. A multispectrum nonlinear least squares fitting technique. Journal of Quantitative Spectroscopy and Radiative Transfer 1995;53:705–21. doi:10.1016/0022-4073(95)00015-D.
[104] Drouin BJ, Benner DC, Brown LR, Cich MJ, Crawford TJ, Devi VM, et al. Multispectrum analysis of the oxygen A-band. Journal of Quantitative Spectroscopy and Radiative Transfer 2017;186:118–38. doi:10.1016/j.jqsrt.2016.03.037.
[105] Ciurylo R. Shapes of pressure-and Doppler-broadened spectral lines in the core and near wings. Physical Review A 1998;58:1029.
[106] Lisak D, Cygan A, Wcislo P, Ciurylo R. Quadratic speed dependence of collisional broadening and shifting for atmospheric applications. Journal of Quantitative Spectroscopy and Radiative Transfer 2015;151:43–48.
[107] Boone CD, Walker KA, Bernath PF. Speed-dependent Voigt profile for water vapor in infrared remote sensing applications. Journal of Quantitative Spectroscopy and Radiative Transfer 2007;105:525–32. doi:10.1016/j.jqsrt.2006.11.015.
[108] Forthomme D, Cich MJ, Twagirayezu S, Hall GE, Sears TJ. Application of the Hartmann–Tran profile to precise experimental data sets of 12 C 2 H 2. Journal of Quantitative Spectroscopy and Radiative Transfer 2015;165:28–37.
[109] Hirschfelder J, Bird RB, Curtiss CF. Molecular theory of gases and liquids 1964.
[110] Ngo NH, Lisak D, Tran H, Hartmann J-M. An isolated line-shape model to go beyond the Voigt profile in spectroscopic databases and radiative transfer codes. Journal of Quantitative Spectroscopy and Radiative Transfer 2013;129:89–100.
[111] Priem D, Rohart F, Colmont J-M, Wlodarczak G, Bouanich J-P. Lineshape study of the J= 3← 2 rotational transition of CO perturbed by N 2 and O 2. Journal of Molecular Structure 2000;517:435–454.
[112] Gamache RR, Arié E, Boursier C, Hartmann J-M. Pressure-broadening and pressure-shifting of spectral lines of ozone. Spectrochimica Acta Part A: Molecular and Biomolecular Spectroscopy 1998;54:35–63.

[113] Antony BK, Neshyba S, Gamache RR. Self-broadening of water vapor transitions via the complex Robert–Bonamy theory. Journal of Quantitative Spectroscopy and Radiative Transfer 2007;105:148–63. doi:10.1016/j.jqsrt.2006.10.005.
[114] Hartmann JM, Taine J, Bonamy J, Labani B, Robert D. Collisional broadening of rotation–vibration lines for asymmetric-top molecules. II. H2O diode laser measurements in the 400–900 K range; calculations in the 300–2000 K range. The Journal of Chemical Physics 1987;86:144–56. doi:10.1063/1.452605.
[115] Tsao CJ, Curnutte B. Line-widths of pressure-broadened spectral lines. Journal of Quantitative Spectroscopy and Radiative Transfer 1962;2:41–91.
[116] Amodio P, Moretti L, Castrillo A, Gianfrani L. Line-narrowing effects in the near-infrared spectrum of water and precision determination of spectroscopic parameters. The Journal of Chemical Physics 2014;140:044310.
[117] D'Eu J-F, Lemoine B, Rohart F. Infrared HCN lineshapes as a test of Galatry and speed-dependent Voigt profiles. Journal of Molecular Spectroscopy 2002;212:96–110.
[118] Wcisło P, Gordon IE, Tran H, Tan Y, Hu S-M, Campargue A, et al. The implementation of non-Voigt line profiles in the HITRAN database: H2 case study. Journal of Quantitative Spectroscopy and Radiative Transfer 2016;177:75–91. doi:10.1016/j.jqsrt.2016.01.024.
[119] Gamache RR, Hartmann J-M. Collisional parameters of H 2 O lines: effects of vibration. Journal of Quantitative Spectroscopy and Radiative Transfer 2004;83:119–147.
[120] Schroeder PJ, Cich MJ, Yang J, Swann WC, Coddington I, Newbury NR, et al. Broadband, high-resolution investigation of advanced absorption lineshapes at high temperature. Physical Review A, accepted 2017
[121] Wójtewicz S, Cygan A, Maslowski P, Domyslawska J, Lisak D, Trawiński RS, et al. Spectral line shapes of self-broadened P-branch transitions of oxygen B band. Journal of Quantitative Spectroscopy and Radiative Transfer 2014;144:36–48.
[122] Berman PR. Speed-dependent collisional width and shift parameters in spectral profiles. Journal of Quantitative Spectroscopy and Radiative Transfer 1972;12:1331–1342.
[123] Ward J, Cooper J, Smith EW. Correlation effects in the theory of combined Doppler and pressure broadening—I. Classical theory. Journal of Quantitative Spectroscopy and Radiative Transfer 1974;14:555–590.
[124] Pine AS, Looney JP. N 2 and air broadening in the fundamental bands of HF and HCl. Journal of Molecular Spectroscopy 1987;122:41–55.
[125] Rao DR, Oka T. Dicke narrowing and pressure broadening in the infrared fundamental band of HCl perturbed by Ar. Journal of Molecular Spectroscopy 1987;122:16–27.
[126] Bui TQ, Long DA, Cygan A, Sironneau VT, Hogan DW, Rupasinghe PM, et al. Observations of Dicke narrowing and speed dependence in air-broadened CO2 lineshapes near 2.06 μ m. The Journal of Chemical Physics 2014;141:174301.
[127] Pine AS. Line shape asymmetries in Ar-broadened HF (v= 1–0) in the Dicke-narrowing regime. The Journal of Chemical Physics 1994;101:3444–3452.
[128] Hodges JT, Lisak D, Lavrentieva N, Bykov A, Sinitsa L, Tennyson J, et al. Comparison between theoretical calculations and high-resolution measurements of pressure broadening for near-infrared water spectra. Journal of Molecular Spectroscopy 2008;249:86–94. doi:10.1016/j.jms.2008.02.022.
[129] Pine AS. Asymmetries and correlations in speed-dependent Dicke-narrowed line shapes of argon-broadened HF. Journal of Quantitative Spectroscopy and Radiative Transfer 1999;62:397–423. doi:10.1016/S0022-4073(98)00112-5.
[130] Rohart F, Mäder H, Nicolaisen H-W. Speed dependence of rotational relaxation induced by foreign gas collisions: studies on CH3F by millimeter wave coherent transients. The Journal of Chemical Physics 1994;101:6475–6486.
[131] De Vizia MD, Rohart F, Castrillo A, Fasci E, Moretti L, Gianfrani L. Speed-dependent effects in the near-infrared spectrum of self-colliding H 2 O 18 molecules. Physical Review A 2011;83:052506.

[132] Toth RA, Sung K, Brown LR. H 2 16 O line strengths revisited: ν 2 and 2ν 2–ν 2 at 6μm. Journal of Molecular Spectroscopy 2011;265:59–68.
[133] Toth RA, Brown LR, Plymate C. Self-broadened widths and frequency shifts of water vapor lines between 590 and 2400cm- 1. Journal of Quantitative Spectroscopy and Radiative Transfer 1998;59:529–562.
[134] Toth RA. Measurements of positions, strengths and self-broadened widths of H2O from 2900 to 8000 cm−1: line strength analysis of the 2nd triad bands. Journal of Quantitative Spectroscopy and Radiative Transfer 2005;94:51–107. doi:10.1016/j.jqsrt.2004.08.042.
[135] Toth RA. Water Vapor Measurements between 590 and 2582 cm−1: Line Positions and Strengths. Journal of Molecular Spectroscopy 1998;190:379–96. doi:10.1006/jmsp.1998.7611.
[136] Cich MJ, McRaven CP, Lopez GV, Sears TJ, Hurtmans D, Mantz AW. Temperature-dependent pressure broadened line shape measurements in the ν1+ν3 band of acetylene using a diode laser referenced to a frequency comb. Appl Phys B 2012;109:373–84. doi:10.1007/s00340-011-4829-0.
[137] Descamps C, Bouallou C, Kanniche M. Efficiency of an Integrated Gasification Combined Cycle (IGCC) power plant including CO2 removal. Energy 2008;33:874–81. doi:10.1016/j.energy.2007.07.013.
[138] Emun F, Gadalla M, Majozi T, Boer D. Integrated gasification combined cycle (IGCC) process simulation and optimization. Computers & Chemical Engineering 2010;34:331–8. doi:10.1016/j.compchemeng.2009.04.007.
[139] Minchener AJ. Coal gasification for advanced power generation. Fuel 2005;84:2222–35. doi:10.1016/j.fuel.2005.08.035.
[140] Kanniche M, Bouallou C. CO2 capture study in advanced integrated gasification combined cycle. Applied Thermal Engineering 2007;27:2693–702. doi:10.1016/j.applthermaleng.2007.04.007.
[141] Park WC, Atreya A, Baum HR. Experimental and theoretical investigation of heat and mass transfer processes during wood pyrolysis. Combustion and Flame 2010;157:481–94. doi:10.1016/j.combustflame.2009.10.006.
[142] Van Oost G, Hrabovsky M, Kopecky V, Konrad M, Hlina M, Kavka T, et al. Pyrolysis of waste using a hybrid argon–water stabilized torch. Vacuum 2006;80:1132–7. doi:10.1016/j.vacuum.2006.01.046.
[143] Sur R, Sun K, Jeffries JB, Hanson RK, Pummill RJ, Waind T, et al. TDLAS-based sensors for in situ measurement of syngas composition in a pressurized, oxygen-blown, entrained flow coal gasifier. Applied Physics B 2014;116:33–42.
[144] Sepman A, Ögren Y, Gullberg M, Wiinikka H. Development of TDLAS sensor for diagnostics of CO, H2O and soot concentrations in reactor core of pilot-scale gasifier. Appl Phys B 2016;122:29. doi:10.1007/s00340-016-6319-x.
[145] Kelley MA, Jakulewicz MS, Dreyer CB, Parker TE, Porter JM. System overview and characterization of a high-temperature, high-pressure, entrained-flow, laboratory-scale gasifier. Review of Scientific Instruments 2015;86:055106. doi:10.1063/1.4921196.
[146] Schroeder PJ, Cich MJ, Yang J, Giorgetta FR, Swann WC, Coddington I, et al. Speed-dependent Voigt Lineshape Parameter Database from Dual Frequency Comb Measurements at up to 1300K: Part I. Pure H2O, 6800-7200cm-1. In Preparation 2017
[147] Yang J, Schroeder PJ, Cich MJ, Giorgetta FR, Swann WC, Coddington I, et al. Speed-dependent Voigt Lineshape Parameter Database from Dual Frequency Comb Measurements at up to 1300K: Part 2. Argon Broadened Water, 6800-7200cm-1. In Preparation 2017
[148] Letchworth KL, Benner DC. Rapid and accurate calculation of the Voigt function. Journal of Quantitative Spectroscopy and Radiative Transfer 2007;107:173–192.
[149] Rohart F, Ellendt A, Kaghat F, Mäder H. Self and polar foreign gas line broadening and frequency shifting of CH3F: effect of the speed dependence observed by millimeter-wave coherent transients. Journal of Molecular Spectroscopy 1997;185:222–233.

[150] Long DA, Bielska K, Lisak D, Havey DK, Okumura M, Miller CE, et al. The air-broadened, near-infrared CO2 line shape in the spectrally isolated regime: Evidence of simultaneous Dicke narrowing and speed dependence. The Journal of Chemical Physics 2011;135:064308.
[151] Cygan A, Lisak D, Wójtewicz S, Domyslawska J, Hodges JT, Trawiński RS, et al. High-signal-to-noise-ratio laser technique for accurate measurements of spectral line parameters. Physical Review A 2012;85:022508.
[152] Galatry L. Simultaneous effect of Doppler and foreign gas broadening on spectral lines. Physical Review 1961;122:1218.
[153] Nelkin M, Ghatak A. Simple binary collision model for Van Hove's G s (r, t). Physical Review 1964;135:A4.
[154] Tran H, Ngo NH, Hartmann J-M. Efficient computation of some speed-dependent isolated line profiles. Journal of Quantitative Spectroscopy and Radiative Transfer 2013;129:199–203.

9 Appendix for Chapter 3

9.1 Detailed Descriptions of Uncertainty Calculations

The following section details the uncertainty considerations and calculations for the experimental conditions presented in the accompanying paper.

9.1.1 Pressure

Pressure measurements of water vapor in the spectroscopic cell were taken using a 20 Torr capacitance manometer (MKS Baratron 626C) and total mixture pressure measurements were taken with a heated diaphragm, 1000 Torr capacitance manometer (MKS Baratron 628C). The reported uncertainty is a combination of manufacture's specification (0.25% of the measured value), the inability to zero the gauge with an ultra-high vacuum source, and the measured pressure drift over the course of a data run. These sources were combined in quadrature and presented in the manuscript.

9.1.2 Temperature

Temperature of the spectroscopic cell was acquired with a standard accuracy Type K thermocouple probe. The furnace was set to the five temperatures listed in the manuscript and allowed to stabilize overnight. Upon stabilization, readings were taken at the middle and both ends of the cell with the probe in physical contact with the internal furnace wall followed by the spectroscopic cell wall at each cell measurement location for a total of six measurements. Each of the six locations was measured for 1 hour and averaged. The reported temperature is the average of the six thermocouple averaged measurement locations for 1 hour of data acquisition.. The reported temperature uncertainty is the quadrature sum of the thermocouple manufacturer's uncertainty specification (0.75% of the reading or 2.2ºC, whichever is greater) and the standard deviation of the temperature at the six measurement locations.

9.1.3 Cell Length

The cell length measurements were taken using a 61cm long Starrett caliper accurate to 0.0025 cm. The path length was calculated as the average distance measured at the top and bottom of the cell after subtracting out window thicknesses. The actual error of the measurement is estimated as 0.10 cm, due to the inability to directly measure the internal dimensions of the cell and parallax between the edge of the clear cell and the caliper jaws. The thermal expansion of 0.5mm at 1305K of the cell was negligible. The resultant uncertainty in cell length is 0.1cm over the 91.4cm cell (0.109%).

9.1.4 H_2O Number Density

Water vapor number density for the air-broadened spectra were calculated at each temperature based on the integrated absorbance of four transitions for which the HITRAN and HITEMP values had been previously verified to within 5% at high temperature [20,35]. At elevated temperatures, additional transitions appear and overlap with the dominant feature so Voigt profiles were fit to each blended feature. We float both the Doppler and Lorentz width in the Voigt fit to obtain the lowest residual and most accurate integrated area calculations. The absorbance areas of all fit features were summed to calculate number density using the Beer-Lambert Law. Table 9-1 lists the calculated number densities at each temperature for each measured line. The number density uncertainty is reported as the standard deviation of the number densities retrieved from the fit to each transition. The uncertainty thus incorporates both the fit error and any line-to-line bias in the HITRAN/HITEMP intensity parameters (which is confirmed to be below the HITRAN/HITEMP error codes as verified in the previous works referenced in the main text).

All experiments were performed with a single, large volume mixture that was created in a stainless steel mixing tank prior to testing.

Table 9-1- Number densities measured using HITRAN and HITEMP linestrengths from four lines. Lines 1 and 4 are composed of two indistinguishable adjacent lines that form a single feature. At 296K, Line 1 was too weak to accurately resolve above noise. The number density standard deviation was used as the uncertainty.

	HITRAN H_2O Number density /1e17				HITEMP H_2O Number density /1e17					
Exp. Temp (K)	**Line 1 (cm^{-1})** 6919.947474 6919.948133	**Line 2(cm^{-1})** 7134.981550	**Line 3(cm^{-1})** 7136.093500	**Line 4(cm^{-1})** 7139.089130 7139.610090	**Line 1(cm^{-1})** 6919.947474 6919.948133	**Line 2(cm^{-1})** 7134.981550	**Line 3(cm^{-1})** 7136.093500	**Line 4(cm^{-1})** 7139.089130 7139.610090	**Average**	**Standard Deviation**
296	N/A	3.49	3.49	3.54	N/A	3.49	3.49	3.60	3.52	0.048
549	1.84	1.83	1.84	1.82	1.85	1.84	1.84	1.85	1.84	0.010
801	1.30	1.28	1.29	1.26	1.28	1.28	1.25	1.27	1.28	0.014
1053	0.94	0.91	0.92	0.91	0.95	0.96	0.94	0.91	0.93	0.022
1305	0.77	0.73	0.75	0.77	0.76	0.76	0.74	0.75	0.75	0.013

9.2 Tables of Recorded Database Errors

We tabulate transitions exhibiting the four types of errors classified in the main text. Examples of each are shown in the body of the paper. Though the instrument resolution and wavelength accuracy are better than 100 kHz (see Section 3.2), the reported shift errors and differences have a precision of 50MHz due to the manual identification of errors and manual estimation of shift differences. Fitting of the line shapes to extract line centers in the future will achieve much higher precision. Occasionally there are instances that could not be clearly classified but obviously produced incorrect predictions in measured spectroscopic data. Errors associated with saturated transitions in the measurements were not counted as errors in this work. All errors were obtained using unscaled database parameters using only data published in HITRAN, i.e. only employing the temperature dependence of air half width.

Table 9-2- Categorized database errors from the air-broadened mixture measurements. The shift difference represents the frequency difference between the line centers of the database predicted, non-temperature scaled line centers and measured DCS transition line center. The line centers were manually selected as the nearest comb tooth as reflected by the significant figures in the tables. These shifts should be used as qualitative values. To obtain a more exact frequency shift would require fitting of each line, which was beyond the scope of this work. Amplitude is in units of absorbance while the SNR gives the reader a relative scale of the size of the error examined. All SNR values retained were >2.5.

9.2.1 296K

Error Quantification for a 1.86% Water-Air Mixture at296K

Line center (cm-1)	Peak absorbance	SNR	Error Type	Shift difference (model-measured) (cm-1)	Database
6944.311	0.00351	3.44	Not Clear	N/A	Not clear
6965.578	0.00274	2.69	DNM	N/A	HITRAN 2012

9.2.2 549K

Error Quantification for a 1.82% Water-Air Mixture at 549K

Line center (cm-1)	Peak absorbance	SNR	Error Type	Shift difference (model-measured) (cm-1)	Database
6806.022	0.00587	5.17	Shift	-0.013	Both
6807.825	0.00816	7.19	Shift	-0.010	Both
6826.856	0.00447	3.94	Shift	-0.016	Both
6834.981	0.02276	20.05	Shift	-0.010	Both
6836.670	0.01499	13.21	Shift	-0.017	Both
6837.118	0.00971	8.55	Shift	-0.013	Both
6839.067	0.01046	9.22	Shift	-0.013	Both
6846.811	0.00893	7.86	Shift	-0.007	Both
6854.149	0.01100	9.69	MND	N/A	Both
6861.923	0.05585	49.21	Shift	-0.003	Both
6862.053	0.00585	5.15	MND	N/A	Both
6862.550	0.00669	5.89	Shift	-0.013	Both
6863.408	0.02485	21.89	Shift	-0.010	Both
6864.971	0.03206	28.24	Shift	-0.007	Both
6865.458	0.01868	16.46	Shift	-0.013	Both
6867.030	0.02376	20.93	Shift	-0.007	Both
6868.836	0.00736	6.48	Shift	-0.020	Both
6869.447	0.00820	7.23	Shift	-0.010	Both
6870.298	0.00780	6.88	Not Clear	N/A	HITRAN 2012
6879.074	0.01395	12.29	Shift	-0.010	Both
6891.182	0.06230	54.89	Shift	-0.010	Both

6891.282	0.01892	16.67	Shift	-0.013	Both
6891.736	0.01842	16.23	Shift	-0.017	Both
6892.731	0.06239	54.97	Shift	-0.007	Both
6894.366	0.02881	25.38	Shift	-0.007	Both
6894.704	0.02266	19.97	Shift	-0.013	Both
6897.534	0.02567	22.62	Shift	-0.010	Both
6901.954	0.00985	8.68	Shift	-0.007	Both
6907.675	0.00404	3.56	MND	N/A	HITEMP 2010
6909.171	0.01364	12.02	Shift	-0.010	Both
6915.653	0.01792	15.78	Shift	-0.013	Both
6918.471	0.06405	56.44	Shift	-0.007	Both
6918.755	0.02420	21.32	Shift	-0.007	Both
6919.940	0.11101	97.81	Shift	-0.010	Both
6920.524	0.05013	44.16	Shift	-0.007	Both
6920.928	0.03701	32.61	Shift	-0.007	Both
6922.771	0.02570	22.64	Shift	-0.007	Both
6923.138	0.01239	10.91	Shift	-0.010	Both
6923.658	0.02861	25.21	Shift	-0.007	Both
6929.787	0.00808	4.90	MND	N/A	HITRAN 2012
6933.579	0.01240	7.52	DNM	N/A	HITEMP 2010
6935.672	0.01526	9.25	Shift	-0.010	Both
6937.835	0.02100	12.74	Shift	-0.007	Both
6944.311	0.02052	12.44	Not Clear	N/A	HITRAN 2012
6944.846	0.02966	17.99	Shift	-0.007	Both
6945.477	0.10304	62.49	Shift	-0.007	Both
6946.568	0.16817	101.98	Shift	-0.010	Both
6946.788	0.03946	23.93	Shift	-0.007	Both
6947.226	0.04686	28.42	Shift	-0.013	Both
6948.441	0.08115	49.21	Shift	-0.010	Both
6949.700	0.00692	4.19	DNM	N/A	HITRAN 2012
6954.002	0.03491	21.17	Shift	-0.003	Both
6954.169	0.01693	10.27	Shift	-0.013	Both
6965.582	0.02345	14.22	Not Clear	N/A	HITRAN 2012
6967.405	0.07622	46.22	Shift	-0.003	Both
6969.037	0.02805	17.01	Not Clear	N/A	Both
6971.594	0.08519	51.66	Shift	-0.010	Both
6971.791	0.01808	10.96	Shift	-0.010	Both
6972.045	0.15398	93.38	Shift	-0.007	Both
6972.739	0.27558	167.12	Shift	-0.010	Both
6972.833	0.08617	52.26	Shift	-0.003	Both
6973.661	0.12025	72.92	Shift	-0.007	Both
6980.748	0.05177	31.40	Shift	-0.003	Both
6981.525	0.11058	67.06	Shift	-0.003	Both

6984.947	0.08188	49.66	Shift	-0.003	Both
6994.898	0.04945	29.99	Shift	-0.007	Both
6997.648	0.08234	49.94	Shift	-0.013	Both
6997.782	0.09698	58.81	Shift	-0.007	Both
6997.989	0.21834	132.41	Shift	-0.007	Both
6998.163	0.34024	206.33	Shift	-0.007	Both
6998.223	0.16561	100.43	Not Clear	N/A	Both
6999.972	0.05698	34.55	Shift	-0.003	Both
7001.941	0.11017	66.81	Shift	-0.003	Both
7005.740	0.01002	6.08	Shift	-0.003	Both
7006.124	0.06539	39.66	Shift	-0.003	Both
7012.690	0.13799	83.68	Shift	-0.003	Both
7013.157	0.01485	9.01	Shift	-0.010	Both
7014.456	0.06381	38.70	Shift	-0.007	Both
7016.635	0.00413	2.50	Shift	-0.020	Both
7021.803	0.09881	59.92	Shift	-0.007	Both
7022.073	0.03671	22.26	Shift	-0.007	Both
7022.708	0.44132	267.63	Shift	-0.007	Both
7023.315	0.15723	95.35	Shift	-0.007	Both
7023.452	0.40853	247.74	Shift	-0.010	Both
7028.763	0.05498	33.34	Shift	-0.003	Both
7031.637	0.01548	9.39	Shift	-0.003	Both
7032.351	0.02005	12.16	Shift	-0.010	Both
7034.802	0.02042	12.39	Shift	-0.007	Both
7038.434	0.20757	125.88	Shift	-0.006	Both
7041.522	0.06867	41.64	Shift	-0.007	Both
7045.835	0.11220	68.04	Shift	-0.003	Both
7046.806	0.02041	12.38	Shift	-0.007	Both
7047.677	0.71719	434.92	Shift	-0.007	Both
7057.358	0.11831	31.40	Shift	-0.007	Both
7075.587	0.01051	2.79	Shift	-0.010	Both
7079.857	0.01402	3.72	Shift	-0.017	Both
7080.097	0.03881	10.30	Shift	-0.007	Both
7080.364	0.03537	9.39	Shift	0.010	Both
7081.342	0.03577	9.49	Shift	-0.010	Both
7082.500	0.01388	3.68	Shift	-0.010	Both
7089.351	0.03279	8.70	Shift	-0.010	Both
7089.437	0.01107	2.94	MND	N/A	HITEMP 2010
7097.375	0.22168	58.83	Shift	-0.007	Both
7103.207	0.02782	7.38	MND	N/A	HITEMP 2010
7130.032	0.01280	3.40	MND	N/A	Both
7137.493	0.04912	13.04	Shift	0.026	HITEMP 2010
7137.600	0.03538	9.39	MND	N/A	HITEMP 2010

7142.961	0.02961	7.86	Shift	-0.013	Both

9.2.3 801K

Error Quantification for a 1.83% Water-Air Mixture at 801K					
Line center (cm-1)	Peak absorbance	SNR	Error Type	Shift difference (model-measured) (cm-1)	Database
6807.832	0.03701	24.25	Shift	-0.017	Both
6808.039	0.02473	16.21	Shift	-0.017	Both
6808.209	0.00847	5.55	Shift	-0.013	Both
6810.499	0.01505	9.86	Shift	-0.013	Both
6811.093	0.01058	6.93	Shift	-0.013	Both
6812.385	0.01202	7.87	Not Clear	N/A	Not clear
6813.403	0.01954	12.81	Shift	-0.017	Both
6819.148	0.01712	11.22	Shift	-0.010	Both
6823.962	0.00384	2.51	Shift	-0.013	Both
6826.856	0.01497	9.81	Shift	-0.016	Both
6829.119	0.00860	5.63	Shift	-0.020	Both
6829.747	0.00517	3.39	Shift	-0.010	Both
6831.726	0.00689	4.51	Shift	-0.013	Both
6831.973	0.00592	3.88	Shift	-0.013	Both
6834.981	0.05787	37.92	Shift	-0.013	Both
6835.265	0.02156	14.13	Shift	-0.013	Both
6836.673	0.05802	38.02	Shift	-0.020	Both
6837.118	0.03238	21.22	Shift	-0.013	Both
6837.508	0.00902	5.91	MND	N/A	Both
6837.915	0.01210	7.93	DNM	N/A	Both
6838.746	0.00987	6.47	Shift	-0.010	Both
6839.070	0.02864	18.77	Shift	-0.017	Both
6839.501	0.01409	9.23	Shift	-0.013	Both
6839.611	0.00628	4.11	Shift	-0.013	Both
6841.280	0.02980	19.53	Shift	-0.013	Both
6844.728	0.01043	6.83	Shift	-0.013	Both
6846.815	0.01034	6.78	Shift	-0.010	Both
6849.024	0.00732	4.80	Shift	-0.010	Both
6853.507	0.01421	9.31	Shift	-0.007	Both
6854.149	0.06581	43.13	MND	N/A	Both
6857.320	0.01370	8.98	Shift	-0.013	Both
6857.423	0.00449	2.94	MND	N/A	HITEMP 2010
6858.058	0.00845	5.53	Shift	-0.010	Both

6859.686	0.00687	4.50	Shift	-0.013	Both
6860.244	0.01681	11.02	Shift	-0.007	Both
6861.926	0.05679	37.21	Shift	-0.007	Both
6862.057	0.01311	8.59	MND	N/A	Both
6862.550	0.02216	14.52	Shift	-0.013	Both
6863.412	0.07395	48.46	Shift	-0.013	Both
6864.483	0.00796	5.22	Shift	-0.010	Both
6864.974	0.09346	61.24	Shift	-0.010	Both
6865.462	0.05257	34.45	Shift	-0.017	Both
6866.670	0.00570	3.74	Shift	-0.010	Both
6867.030	0.03736	24.48	Shift	-0.010	Both
6867.501	0.01912	12.53	Shift	-0.007	Both
6868.829	0.01431	9.37	Shift	-0.013	Both
6869.451	0.01751	11.48	Shift	-0.013	Both
6870.305	0.02672	17.51	Not Clear	N/A	HITRAN 2012
6873.670	0.04686	30.70	Shift	-0.007	Both
6875.402	0.01849	12.11	Shift	-0.013	Both
6878.203	0.00676	4.43	Shift	-0.017	Both
6879.074	0.03829	25.09	Shift	-0.010	Both
6880.757	0.01163	7.62	Shift	-0.013	Both
6884.302	0.01126	7.38	Shift	-0.017	Both
6884.832	0.01017	6.67	Shift	-0.010	Both
6890.451	0.04141	27.13	Shift	-0.007	Both
6891.182	0.10004	65.56	Shift	-0.013	Both
6891.288	0.03580	23.46	Shift	-0.016	Both
6891.733	0.03845	25.19	Shift	-0.013	Both
6892.734	0.13902	91.10	Shift	-0.010	Both
6893.094	0.01184	7.76	Shift	-0.013	Both
6893.298	0.02920	19.14	Shift	-0.010	Both
6894.370	0.04831	31.66	Shift	-0.010	Both
6894.704	0.05862	38.41	Shift	-0.013	Both
6895.211	0.02697	17.67	Shift	-0.017	Both
6897.538	0.05859	38.39	Shift	-0.013	Both
6901.957	0.02582	16.92	Shift	-0.013	Both
6906.657	0.01099	7.20	Shift	-0.020	Both
6906.711	0.02154	14.12	Shift	-0.003	Both
6907.565	0.01254	8.22	Shift	-0.016	HITRAN 2012
6907.565	0.01254	8.22	DNM	N/A	HITEMP 2010
6907.675	0.00926	6.07	MND	N/A	HITEMP 2010
6909.168	0.02284	14.96	Shift	-0.010	Both
6910.606	0.01215	7.96	Shift	-0.013	Both
6914.148	0.00856	5.61	Shift	-0.010	Both
6915.653	0.02300	15.07	Shift	-0.013	Both

6918.471	0.12551	82.25	Shift	-0.010	Both
6918.758	0.04131	27.07	Shift	-0.013	Both
6919.943	0.20266	132.80	Shift	-0.013	Both
6920.527	0.10329	67.69	Shift	-0.010	Both
6920.931	0.04852	31.80	Shift	-0.010	Both
6921.028	0.01972	12.93	Shift	-0.010	Both
6921.565	0.01102	7.22	Shift	-0.010	Both
6922.777	0.03328	21.81	Shift	-0.013	Both
6923.141	0.02299	15.06	Shift	-0.013	Both
6923.665	0.04828	31.64	Shift	-0.013	Both
6929.787	0.00887	4.34	MND	N/A	HITRAN 2012
6933.105	0.01221	5.98	Shift	-0.007	Both
6933.586	0.01562	7.65	DNM	N/A	HITEMP 2010
6933.586	0.01562	7.65	Shift	-0.010	Both
6935.672	0.02708	13.27	Shift	-0.013	Both
6936.831	0.01674	8.20	Shift	-0.007	Both
6937.835	0.03722	18.24	Shift	-0.007	Both
6944.311	0.02981	14.61	Not Clear	N/A	HITRAN 2012
6944.846	0.04997	24.48	Shift	-0.007	Both
6945.480	0.16474	80.72	Shift	-0.010	Both
6946.572	0.25753	126.18	Shift	-0.013	Both
6946.788	0.04430	21.70	Shift	-0.007	Both
6947.269	0.05637	27.62	Shift	-0.017	Both
6947.439	0.02057	10.08	Shift	-0.006	Both
6948.444	0.13823	67.72	Shift	-0.013	Both
6948.811	0.01335	6.54	Shift	-0.010	Both
6949.703	0.01154	5.65	DNM	N/A	HITRAN 2012
6951.151	0.00768	3.76	Shift	-0.020	Both
6952.710	0.00995	4.88	Shift	-0.007	Both
6954.005	0.05711	27.98	Shift	-0.006	Both
6954.166	0.02375	11.64	Shift	-0.010	Both
6954.389	0.11440	56.05	Shift	-0.006	Both
6960.756	0.02695	13.20	Shift	-0.010	Both
6961.917	0.00553	2.71	Shift	-0.013	Both
6962.922	0.01095	5.36	Shift	-0.010	Both
6964.928	0.00626	3.07	Shift	-0.007	Both
6965.582	0.03813	18.68	Not Clear	N/A	HITRAN 2012
6967.405	0.10239	50.17	Shift	-0.003	Both
6969.031	0.04273	20.94	Shift	-0.010	Both
6971.598	0.08876	43.49	Shift	-0.013	Both
6971.795	0.01829	8.96	Shift	-0.010	Both
6972.048	0.21031	103.04	Shift	-0.010	Both
6972.743	0.35496	173.91	Shift	-0.013	Both

6972.836	0.08852	43.37	Shift	-0.007	Both
6973.661	0.16599	81.33	Shift	-0.007	Both
6979.843	0.02228	10.92	Shift	-0.007	Both
6979.980	0.01435	7.03	Shift	-0.007	Both
6980.751	0.04656	22.81	Shift	-0.007	Both
6981.525	0.08598	42.13	Shift	-0.003	Both
6984.950	0.05561	27.25	Shift	-0.007	Both
6985.675	0.01631	7.99	Shift	-0.013	Both
6987.457	0.02334	11.44	Shift	-0.010	Both
6994.901	0.04647	22.77	Shift	-0.007	Both
6995.389	0.01271	6.23	Shift	-0.007	Both
6995.518	0.00564	2.76	Shift	-0.016	Both
6997.652	0.09606	47.06	Shift	-0.017	Both
6997.786	0.08706	42.66	Shift	-0.010	Both
6997.989	0.25465	124.77	Shift	-0.007	Both
6998.166	0.37765	185.03	Shift	-0.010	Both
6998.219	0.18285	89.59	MND	N/A	HITRAN 2012
6998.219	0.18285	89.59	DNM	N/A	HITEMP 2010
6998.807	0.11496	56.33	Shift	-0.003	Both
7001.117	0.01038	5.09	Shift	-0.010	Both
7001.500	0.01425	6.98	Shift	-0.013	Both
7002.225	0.02037	9.98	Shift	-0.003	Both
7003.100	0.01732	8.49	Shift	-0.007	Both
7004.969	0.01126	5.52	Shift	-0.010	Both
7005.743	0.01242	6.09	Shift	-0.010	Both
7008.384	0.01513	7.42	DNM	N/A	HITRAN 2012
7011.191	0.03090	15.14	Shift	-0.010	Both
7011.836	0.00874	4.28	Shift	-0.013	Both
7013.154	0.01296	6.35	Shift	-0.017	Both
7014.456	0.07044	34.51	Shift	-0.007	Both
7015.918	0.06117	29.97	Shift	-0.003	Both
7016.639	0.00651	3.19	Shift	-0.023	Both
7016.879	0.00656	3.22	Shift	-0.017	Both
7017.210	0.05196	25.46	Shift	-0.006	Both
7017.948	0.09319	45.66	Shift	-0.003	Both
7021.806	0.07960	39.00	Shift	-0.010	Both
7022.073	0.02821	13.82	Shift	-0.007	Both
7022.708	0.43149	211.41	Shift	-0.007	Both
7023.319	0.14929	73.15	Shift	-0.010	Both
7023.452	0.39836	195.18	Shift	-0.010	Both
7024.397	0.00655	3.21	Shift	-0.013	Both
7024.684	0.00761	3.73	MND	N/A	HITEMP 2010
7024.791	0.00853	4.18	Shift	-0.010	Both

7025.899	0.01610	7.89	Shift	-0.024	Both
7028.136	0.11685	57.25	Shift	-0.003	Both
7028.306	0.04457	21.84	Shift	-0.003	Both
7028.766	0.04116	20.16	Shift	-0.007	Both
7030.449	0.00575	2.82	Shift	-0.013	HITRAN 2012
7030.562	0.00517	2.53	MND	N/A	HITEMP 2010
7031.237	0.05075	24.87	Shift	-0.007	Both
7031.641	0.01816	8.90	Shift	-0.007	Both
7032.351	0.02104	10.31	Shift	-0.010	Both
7034.799	0.04008	19.64	Shift	-0.007	Both
7036.511	0.02700	13.23	Shift	-0.007	Both
7038.434	0.20115	98.55	Shift	-0.006	Both
7039.148	0.01957	9.59	Shift	-0.010	HITRAN 2012
7040.220	0.01011	4.95	Shift	-0.013	Both
7041.522	0.05537	27.13	Shift	-0.007	Both
7043.998	0.05011	24.55	Shift	-0.007	Both
7045.223	0.02954	14.47	Shift	-0.010	Both
7045.841	0.08177	40.06	Shift	-0.010	Both
7046.803	0.02208	10.82	Shift	-0.007	Both
7047.093	0.13209	64.72	Shift	-0.006	Both
7047.316	0.36427	178.48	Shift	-0.003	Both
7048.034	0.01275	6.25	Shift	-0.364	Both
7049.757	0.00931	4.56	Shift	-0.010	Both
7050.011	0.01392	6.82	Shift	-0.013	Both
7050.114	0.01736	8.51	Shift	-0.010	Both
7050.768	0.01824	8.94	Shift	-0.013	Both
7051.843	0.03724	18.24	Shift	-0.003	Both
7052.020	0.01093	5.35	DNM	N/A	HITEMP 2010
7052.157	0.00728	3.57	MND	N/A	HITEMP 2010
7053.933	0.09653	47.30	Shift	-0.003	Both
7054.884	0.03740	18.32	Shift	-0.007	Both
7055.068	0.00989	4.85	Shift	-0.020	Both
7056.336	0.01008	4.94	Shift	-0.010	Both
7056.536	0.00748	3.67	Shift	-0.010	Both
7057.361	0.10622	27.55	Shift	-0.010	Both
7057.685	0.03500	9.08	Shift	-0.007	Both
7057.775	0.02825	7.33	Shift	-0.020	Both
7058.923	0.02376	6.16	Shift	-0.007	Both
7059.244	0.01187	3.08	Shift	-0.010	Both
7061.557	0.01421	3.68	Shift	-0.010	Both
7063.683	0.01139	2.95	Shift	-0.010	Both
7064.077	0.03962	10.28	Shift	-0.010	Both
7065.536	0.02580	6.69	Shift	-0.017	HITEMP 2010

7068.524	0.07258	18.82	Shift	-0.007	Both
7068.604	0.05560	14.42	Shift	-0.006	Both
7069.215	0.04406	11.43	DNM	N/A	Both
7071.491	0.68977	178.88	Shift	-0.010	Both
7071.598	0.19159	49.69	Not Clear	N/A	Not clear
7074.245	0.02887	7.49	Shift	-0.007	Both
7074.643	0.01458	3.78	Shift	-0.010	Both
7075.591	0.03273	8.49	Shift	-0.013	Both
7076.512	0.02532	6.57	Shift	-0.010	Both
7079.850	0.01613	4.18	Shift	-0.010	Both
7080.101	0.05861	15.20	Shift	-0.010	Both
7080.364	0.05798	15.04	Shift	-0.010	HITRAN 2012
7080.364	0.05798	15.04	Shift	0.007	HITEMP 2010
7081.075	0.04055	10.52	Shift	-0.006	Both
7081.349	0.08862	22.98	Shift	-0.013	Both
7082.247	0.02883	7.48	Shift	-0.007	Both
7082.500	0.02063	5.35	Shift	-0.010	Both
7083.225	0.06948	18.02	Shift	-0.007	Both
7085.245	0.11688	30.31	Shift	-0.007	Both
7089.351	0.07543	19.56	Shift	-0.013	Both
7089.437	0.02239	5.81	MND	N/A	HITEMP 2010
7090.792	0.01025	2.66	Shift	-0.013	Both
7091.417	0.03642	9.45	Not Clear	N/A	Both
7097.375	0.17375	45.06	Shift	-0.007	Both
7099.485	0.01113	2.89	Shift	-0.013	Both
7100.116	0.03440	8.92	Shift	-0.010	Both
7101.561	0.03105	8.05	Shift	-0.003	Both
7103.207	0.06066	15.73	MND	N/A	HITEMP 2010
7103.110	0.05540	14.37	Shift	-0.007	HITRAN 2012
7113.649	0.02674	6.94	Shift	-0.003	Both
7120.131	0.01980	5.14	DNM	N/A	HITEMP 2010
7128.013	0.03890	10.09	Shift	-0.010	Both
7128.964	0.03907	10.13	Shift	-0.010	Both
7129.876	0.02990	7.75	Shift	-0.007	HITRAN 2012
7130.032	0.02539	6.59	DNM	N/A	HITEMP 2010
7137.523	0.02834	7.35	MND	N/A	HITEMP 2010
7137.603	0.04246	11.01	MND	N/A	HITEMP 2010
7142.967	0.05318	13.79	Shift	-0.020	Both
7143.084	0.02350	6.10	Shift	-0.017	Both
7164.896	0.40847	105.93	Shift	-0.003	Both

9.2.4 1053K

Error Quantification for a 1.77% Water-Air Mixture at 1053K					
Line center (cm-1)	Peak absorbance	SNR	Error Type	Shift difference (model-measured) (cm-1)	Database
6801.613	0.01494	7.63	Shift	-0.010	Both
6804.343	0.02873	14.67	Shift	-0.007	Both
6806.029	0.05446	27.82	Shift	-0.020	Both
6807.832	0.06327	32.31	Shift	-0.017	Both
6808.039	0.04110	20.99	Shift	-0.017	Both
6808.209	0.01429	7.30	Shift	-0.013	Both
6810.499	0.02429	12.40	Shift	-0.013	Both
6810.933	0.00507	2.59	Shift	-0.010	Both
6811.093	0.01414	7.22	Shift	-0.013	Both
6812.449	0.01834	9.37	DNM	N/A	Both
6813.407	0.03487	17.81	Shift	-0.020	Both
6819.151	0.02833	14.47	Shift	-0.013	Both
6821.274	0.00784	4.00	Shift	-0.020	Both
6821.785	0.01310	6.69	Shift	-0.007	Both
6823.965	0.00926	4.73	Shift	-0.013	Both
6824.225	0.00585	2.99	Shift	-0.024	Both
6826.856	0.02317	11.83	Shift	-0.013	Both
6829.099	0.00887	4.53	Shift	0.024	Both
6829.733	0.01291	6.59	Shift	0.017	Both
6831.723	0.01176	6.01	Shift	-0.010	Both
6831.973	0.00825	4.22	Shift	-0.013	Both
6834.804	0.00788	4.03	Shift	-0.017	Both
6834.981	0.08205	41.90	Shift	-0.017	Both
6835.268	0.03244	16.57	Shift	-0.013	Both
6836.673	0.08729	44.58	Shift	-0.020	Both
6837.121	0.05127	26.19	Shift	-0.017	Both
6837.504	0.01359	6.94	MND	N/A	Both
6837.918	0.01670	8.53	DNM	N/A	Both
6838.749	0.01421	7.26	Shift	-0.013	Both
6839.070	0.03308	16.90	Shift	-0.017	Both
6839.501	0.01705	8.71	Shift	-0.013	Both
6839.611	0.00727	3.71	Shift	-0.013	Both
6841.280	0.04437	22.66	Shift	-0.013	Both
6844.728	0.01565	8.00	Shift	-0.013	Both
6846.818	0.00627	3.20	Shift	-0.013	Both
6847.749	0.01035	5.29	Shift	-0.013	Both
6849.028	0.01178	6.02	Shift	-0.013	Both

6849.926	0.00744	3.80	Shift	-0.017	Both
6853.517	0.01439	7.35	Shift	-0.013	Both
6853.985	0.01030	5.26	Shift	-0.016	Both
6854.149	0.12932	66.05	DNM	N/A	Both
6855.374	0.00777	3.97	Shift	-0.017	Both
6857.323	0.02288	11.69	Shift	-0.017	Both
6857.423	0.00644	3.29	MND	N/A	HITEMP 2010
6858.061	0.00912	4.66	Shift	-0.017	Both
6859.690	0.01143	5.84	Shift	-0.016	Both
6861.926	0.04003	20.44	Shift	-0.007	Both
6862.557	0.03132	16.00	Shift	-0.020	Both
6863.412	0.09564	48.84	Shift	-0.013	Both
6864.487	0.01055	5.39	Shift	-0.017	Both
6864.977	0.11889	60.72	Shift	-0.013	Both
6865.462	0.06976	35.63	Shift	-0.017	Both
6866.670	0.00735	3.76	Shift	-0.010	Both
6867.034	0.03654	18.66	Shift	-0.010	Both
6867.504	0.01883	9.62	Shift	-0.010	Both
6868.829	0.01703	8.70	Shift	-0.016	Both
6869.451	0.02373	12.12	Shift	-0.013	Both
6869.554	0.01742	8.90	Shift	-0.017	Both
6870.305	0.04260	21.76	Shift	-0.010	Both
6870.922	0.00841	4.29	Shift	-0.010	Both
6873.670	0.06454	32.96	Shift	-0.007	Both
6875.402	0.02276	11.62	Shift	-0.013	Both
6878.203	0.01344	6.87	Shift	-0.017	Both
6878.954	0.01326	6.77	Shift	-0.013	Both
6879.074	0.05005	25.56	Shift	-0.010	Both
6880.767	0.01476	7.54	Shift	-0.024	Both
6884.299	0.02273	11.61	Shift	-0.013	Both
6884.832	0.01234	6.30	Shift	-0.007	Both
6890.451	0.03314	16.93	Shift	-0.007	Both
6891.185	0.10805	55.19	Shift	-0.017	Both
6891.288	0.03920	20.02	Shift	-0.016	Both
6891.733	0.04420	22.58	Shift	-0.013	Both
6892.734	0.15946	81.44	Shift	-0.010	Both
6893.094	0.01397	7.14	Shift	-0.013	Both
6893.301	0.03191	16.30	Shift	-0.013	Both
6894.370	0.04461	22.78	Shift	-0.010	Both
6894.500	0.01031	5.26	Shift	-0.010	Both
6894.707	0.07091	36.22	Shift	-0.017	Both
6895.207	0.02576	13.15	Shift	-0.013	Both
6901.957	0.03570	18.23	Shift	-0.013	Both

6905.966	0.01998	10.21	Shift	-0.013	Both
6906.654	0.01466	7.49	Shift	-0.013	Both
6906.714	0.02726	13.92	Shift	-0.007	Both
6907.565	0.01663	8.49	Shift	-0.013	HITRAN 2012
6907.675	0.01148	5.86	MND	N/A	HITEMP 2010
6908.537	0.00625	3.19	Shift	-0.030	Both
6909.165	0.02531	12.92	Shift	-0.010	Both
6909.929	0.01112	5.68	Shift	-0.013	Both
6910.319	0.01026	5.24	Shift	-0.013	Both
6910.606	0.02048	10.46	Shift	-0.013	Both
6912.282	0.01399	7.15	Shift	-0.007	Both
6912.766	0.00753	3.85	Shift	-0.010	Both
6914.145	0.01011	5.16	Shift	-0.007	Both
6915.653	0.02110	10.78	Shift	-0.013	Both
6916.842	0.00544	2.78	MND	N/A	HITEMP 2010
6918.475	0.13780	70.38	Shift	-0.010	Both
6918.755	0.04431	22.63	Shift	-0.007	Both
6919.943	0.20947	106.98	Shift	-0.013	Both
6920.527	0.11161	57.00	Shift	-0.010	Both
6920.931	0.04105	20.97	Shift	-0.010	Both
6921.028	0.01593	8.14	Shift	-0.007	Both
6921.565	0.01071	5.47	Shift	-0.010	Both
6922.453	0.03309	16.90	Shift	-0.007	Both
6922.777	0.02826	14.43	Shift	-0.013	Both
6923.138	0.02641	13.49	Shift	-0.010	Both
6923.665	0.05105	26.07	Shift	-0.013	Both
6926.065	0.01267	6.47	Shift	-0.007	Both
6929.787	0.00767	3.90	MND	N/A	HITRAN 2012
6932.351	0.01671	8.49	Shift	-0.010	Both
6933.109	0.02084	10.59	Shift	-0.010	Both
6933.589	0.01534	7.79	Shift	-0.013	HITRAN 2012
6933.589	0.01534	7.79	DNM	N/A	HITEMP 2010
6934.120	0.01499	7.62	Shift	-0.010	Both
6934.588	0.01312	6.67	Shift	-0.010	Both
6935.672	0.02953	15.01	Shift	-0.010	Both
6936.834	0.02795	14.20	Shift	-0.010	Both
6937.835	0.04183	21.26	Shift	-0.007	Both
6940.523	0.01666	8.46	Shift	-0.010	Both
6942.152	0.00703	3.57	Shift	-0.017	Both
6943.200	0.00714	3.63	Shift	-0.013	Both
6944.311	0.02881	14.64	Not Clear	N/A	HITRAN 2012
6944.849	0.04917	24.99	Shift	-0.010	Both
6945.483	0.16012	81.36	Shift	-0.013	Both

6946.572	0.24642	125.21	Shift	-0.013	Both
6946.792	0.03641	18.50	Shift	-0.010	Both
6947.059	0.04729	24.03	Shift	-0.003	Both
6947.272	0.05596	28.43	Shift	-0.020	Both
6947.443	0.01777	9.03	Shift	-0.010	Both
6948.444	0.14169	72.00	Shift	-0.013	Both
6948.815	0.01209	6.14	Shift	-0.013	Both
6949.706	0.01049	5.33	Not Clear	N/A	HITRAN 2012
6951.145	0.00918	4.66	Shift	-0.013	Both
6951.549	0.02845	14.46	Shift	-0.007	Both
6952.714	0.01395	7.09	Shift	-0.010	Both
6954.005	0.05779	29.36	Shift	-0.006	Both
6954.166	0.02151	10.93	Shift	-0.010	Both
6954.389	0.11110	56.45	Shift	-0.006	Both
6956.723	0.00580	2.95	Shift	-0.010	Both
6957.701	0.01352	6.87	Shift	-0.007	Both
6960.024	0.02125	10.80	Shift	-0.007	Both
6960.107	0.01349	6.86	Shift	-0.020	Both
6960.759	0.03285	16.69	Shift	-0.013	Both
6961.913	0.00926	4.71	Shift	-0.010	Both
6962.925	0.02071	10.52	Shift	-0.013	Both
6963.169	0.01056	5.36	Shift	-0.007	Both
6963.376	0.00789	4.01	Shift	-0.013	Both
6964.217	0.00622	3.16	Shift	-0.010	Both
6964.431	0.00682	3.47	Shift	-0.057	HITEMP 2010
6964.431	0.00682	3.47	DNM	N/A	HITRAN 2012
6964.928	0.00829	4.21	Shift	-0.007	Both
6965.582	0.03791	19.27	Not Clear	N/A	HITRAN 2012
6966.961	0.00778	3.95	Shift	-0.013	Both
6967.408	0.09665	49.11	Shift	-0.007	Both
6969.031	0.04052	20.59	Shift	-0.013	Both
6970.903	0.00752	3.82	Shift	-0.017	Both
6971.598	0.07483	38.02	Shift	-0.013	Both
6971.798	0.01461	7.42	Shift	-0.013	Both
6972.052	0.19369	98.42	Shift	-0.013	Both
6972.743	0.31123	158.15	Shift	-0.010	Both
6973.664	0.15427	78.39	Shift	-0.010	Both
6974.301	0.00530	2.69	DNM	N/A	HITRAN 2012
6975.033	0.03068	15.59	Shift	-0.003	Both
6976.989	0.00913	4.64	Shift	-0.010	Both
6979.843	0.01649	8.38	Shift	-0.007	Both
6980.537	0.02725	13.84	Shift	-0.003	Both
6980.751	0.03355	17.05	Shift	-0.007	Both

6981.528	0.05877	29.86	Shift	-0.007	Both
6984.329	0.05291	26.89	Shift	-0.007	Both
6984.950	0.03397	17.26	Shift	-0.007	Both
6985.157	0.00946	4.81	Shift	-0.013	Both
6985.678	0.01669	8.48	Shift	-0.010	Both
6987.337	0.00876	4.45	Shift	-0.013	Both
6987.457	0.03399	17.27	Shift	-0.010	Both
6987.771	0.01350	6.86	Shift	-0.010	Both
6990.384	0.00656	3.33	Shift	-0.010	Both
6993.265	0.01900	9.65	Shift	-0.007	Both
6994.240	0.01313	6.67	Shift	-0.007	Both
6994.901	0.03543	18.01	Shift	-0.010	Both
6995.389	0.02055	10.44	Shift	-0.007	Both
6995.522	0.01743	8.86	Shift	-0.020	Both
6995.963	0.00836	4.25	Shift	-0.013	Both
6996.066	0.01648	8.38	Shift	-0.007	Both
6997.078	0.00542	2.76	Shift	-0.027	HITEMP 2010
6997.078	0.00542	2.76	DNM	N/A	HITRAN 2012
6997.652	0.07993	40.62	Shift	-0.013	Both
6997.788	0.06507	33.06	Shift	-0.010	Both
6997.992	0.21448	108.98	Shift	-0.010	Both
6998.169	0.30786	156.43	Shift	-0.013	Both
6998.219	0.14912	75.77	Not Clear	N/A	Not clear
6998.540	0.01060	5.39	MND	N/A	HITEMP 2010
6998.680	0.01264	6.43	DNM	N/A	HITEMP 2010
6999.972	0.05891	29.94	Shift	-0.003	Both
7000.640	0.22051	112.05	Shift	-0.003	Both
7001.120	0.00992	5.04	Shift	-0.013	Both
7002.228	0.02856	14.51	Shift	-0.007	Both
7002.956	0.00512	2.60	DNM	N/A	HITRAN 2012
7003.103	0.01359	6.90	Shift	-0.013	Both
7004.972	0.01180	6.00	Shift	-0.013	Both
7005.193	0.01189	6.04	Shift	-0.010	Both
7005.743	0.01160	5.90	Shift	-0.007	Both
7006.361	0.00814	4.14	Shift	-0.010	Both
7007.032	0.04956	25.18	Shift	-0.003	Both
7008.073	0.03054	15.52	Shift	-0.006	Both
7008.387	0.01488	7.56	Not Clear	N/A	HITRAN 2012
7008.711	0.00909	4.62	Shift	-0.007	Both
7008.981	0.00553	2.81	Shift	-0.010	Both
7011.191	0.04409	22.40	Shift	-0.010	Both
7011.839	0.00954	4.85	Shift	-0.017	Both
7012.353	0.00839	4.26	Shift	-0.010	Both

7013.147	0.01212	6.16	Shift	-0.010	Both
7013.611	0.00973	4.94	Shift	-0.010	Both
7014.459	0.05689	28.91	Shift	-0.010	Both
7015.918	0.04107	20.87	Shift	-0.007	Both
7016.178	0.02165	11.00	Shift	-0.007	Both
7016.642	0.00852	4.33	Shift	-0.026	Both
7016.879	0.01566	7.96	Shift	-0.017	Both
7017.210	0.04418	22.45	Shift	-0.006	Both
7017.951	0.06860	34.86	Shift	-0.007	Both
7018.125	0.00845	4.29	Shift	-0.010	Both
7020.431	0.00516	2.62	Shift	-0.017	HITRAN 2012
7020.431	0.00516	2.62	DNM	N/A	HITEMP 2010
7020.558	0.00688	3.50	MND	N/A	HITEMP 2010
7020.661	0.00863	4.38	Shift	-0.013	Both
7021.096	0.00534	2.72	MND	N/A	Both
7021.806	0.05612	28.52	Shift	-0.010	Both
7022.077	0.02045	10.39	Shift	-0.010	Both
7022.711	0.33729	171.38	Shift	-0.010	Both
7023.319	0.11415	58.00	Shift	-0.010	Both
7023.456	0.30629	155.64	Shift	-0.010	Both
7024.394	0.00767	3.90	Shift	-0.010	Both
7024.684	0.01580	8.03	MND	N/A	HITEMP 2010
7024.791	0.01626	8.26	Shift	-0.010	HITRAN 2012
7024.791	0.01626	8.26	DNM	N/A	HITEMP 2010
7025.899	0.03357	17.06	Shift	-0.024	Both
7025.986	0.01788	9.08	Shift	-0.010	Both
7028.139	0.09230	46.90	Shift	-0.007	Both
7028.306	0.03607	18.33	Shift	-0.003	Both
7028.766	0.02672	13.57	Shift	-0.007	Both
7030.289	0.01206	6.13	DNM	N/A	Both
7030.449	0.01079	5.48	Shift	-0.013	HITRAN 2012
7030.449	0.01079	5.48	DNM	N/A	HITEMP 2010
7030.562	0.00930	4.72	MND	N/A	HITEMP 2010
7030.669	0.00887	4.51	MND	N/A	Both
7031.237	0.05615	28.53	Shift	-0.007	Both
7031.641	0.01592	8.09	Shift	-0.007	Both
7032.996	0.00520	2.64	MND	N/A	Both
7034.465	0.03846	19.54	Shift	-0.010	Both
7034.799	0.04964	25.22	Shift	-0.007	Both
7036.511	0.01778	9.03	Shift	-0.007	Both
7036.761	0.01523	7.74	Shift	-0.010	Both
7038.434	0.15326	77.88	Shift	-0.006	Both
7039.145	0.02300	11.69	Shift	-0.010	HITRAN 2012

7039.145	0.02300	11.69	Shift	0.007	HITEMP 2010
7040.223	0.01318	6.70	Shift	-0.017	Both
7041.522	0.04036	20.51	Shift	-0.007	Both
7043.998	0.03066	15.58	Shift	-0.007	Both
7044.265	0.01367	6.94	Shift	-0.010	Both
7045.016	0.01547	7.86	Not Clear	N/A	Both
7045.227	0.01786	9.07	Shift	-0.013	Both
7045.841	0.05474	27.81	Shift	-0.010	Both
7046.806	0.01834	9.32	Shift	-0.010	Both
7047.093	0.09923	50.42	Shift	-0.006	Both
7047.320	0.27814	141.33	Shift	-0.007	Both
7047.684	0.46299	235.26	Shift	-0.013	Both
7047.994	0.01690	8.59	Shift	-0.010	Both
7049.760	0.00994	5.05	Shift	-0.013	Both
7050.011	0.01357	6.89	Shift	-0.013	Both
7050.117	0.01963	9.97	Shift	-0.013	Both
7050.772	0.01724	8.76	Shift	-0.017	Both
7052.100	0.00641	3.26	MND	N/A	HITEMP 2010
7052.157	0.01244	6.32	MND	N/A	HITEMP 2010
7052.024	0.01394	7.08	DNM	N/A	HITEMP 2010
7053.656	0.02111	10.73	Shift	-0.017	HITRAN 2012
7053.656	0.02111	10.73	Shift	0.013	HITEMP 2010
7053.933	0.07846	39.87	Shift	-0.007	Both
7054.888	0.06013	30.55	Shift	-0.010	Both
7055.061	0.01029	5.23	Shift	-0.013	Both
7057.361	0.07617	19.74	Shift	-0.010	Both
7057.685	0.04375	11.34	Shift	-0.010	Both
7057.775	0.03024	7.84	Shift	-0.020	Both
7058.636	0.01057	2.74	Shift	-0.010	Both
7061.560	0.02093	5.42	Shift	-0.013	Both
7061.654	0.01750	4.54	DNM	N/A	Both
7062.035	0.01434	3.72	MND	N/A	Both
7064.979	0.03226	8.36	Shift	-0.007	Both
7065.553	0.02320	6.01	Shift	-0.007	HITRAN 2012
7065.553	0.02320	6.01	Shift	-0.040	HITEMP 2010
7067.693	0.05585	14.48	Shift	-0.010	Both
7068.524	0.05309	13.76	Shift	-0.007	Both
7068.607	0.03170	8.22	Shift	-0.010	Both
7069.001	0.04105	10.64	Shift	-0.020	Both
7070.784	0.30410	78.82	Shift	-0.010	Both
7070.914	0.05300	13.74	Shift	-0.024	Both
7071.491	0.47624	123.44	Shift	-0.010	Both
7071.598	0.14105	36.56	Shift	-0.010	Both

7074.245	0.02274	5.89	Shift	-0.007	Both
7074.482	0.04812	12.47	Shift	-0.007	Both
7075.591	0.05312	13.77	Shift	-0.013	Both
7076.515	0.03404	8.82	Shift	-0.013	Both
7078.852	0.05267	13.65	Shift	-0.003	Both
7080.104	0.06691	17.34	Shift	-0.013	Both
7080.277	0.04741	12.29	Shift	-0.007	Both
7080.361	0.06384	16.55	Shift	-0.007	Both
7080.361	0.06384	16.55	Shift	0.007	Both
7081.075	0.02783	7.21	Shift	-0.006	Both
7081.205	0.02661	6.90	Shift	-0.007	Both
7081.349	0.11684	30.28	Shift	-0.013	Both
7082.247	0.02043	5.30	Shift	-0.007	Both
7082.504	0.01829	4.74	Shift	-0.013	Both
7083.225	0.07654	19.84	Shift	-0.007	Both
7084.323	0.01774	4.60	Shift	-0.007	Both
7085.248	0.10984	28.47	Shift	-0.010	Both
7089.353	0.08934	23.16	Shift	-0.013	Both
7089.434	0.02696	6.99	MND	N/A	HITEMP 2010
7090.796	0.01702	4.41	Shift	-0.013	Both
7093.246	0.01462	3.79	Shift	-0.010	Both
7093.586	0.01687	4.37	Shift	-0.010	Both
7094.064	0.11223	29.09	Shift	-0.007	Both
7094.682	0.40553	105.11	Shift	-0.007	Both
7095.673	0.03524	9.14	Shift	-0.013	Both
7097.375	0.11777	30.53	Shift	-0.007	Both
7098.093	0.02031	5.27	Shift	-0.007	Both
7100.116	0.04543	11.77	Shift	-0.010	Both
7101.565	0.04143	10.74	Shift	-0.007	Both
7103.110	0.06497	16.84	Shift	-0.007	HITRAN 2012
7103.110	0.06497	16.84	DNM	N/A	HITEMP 2010
7103.207	0.06979	18.09	MND	N/A	HITEMP 2010
7120.175	0.02411	6.25	Not Clear	N/A	Not clear
7122.381	0.03017	7.82	Shift	-0.010	Both
7128.964	0.04017	10.41	Shift	-0.010	Both
7129.869	0.02943	7.63	DNM	N/A	HITEMP 2010
7130.032	0.02837	7.35	MND	N/A	HITEMP 2010
7137.523	0.02041	5.29	MND	N/A	HITEMP 2010
7137.603	0.03870	10.03	MND	N/A	HITEMP 2010
7139.085	0.34334	88.99	Shift	-0.007	Both
7139.606	0.10744	27.85	Shift	-0.007	Both
7142.964	0.05951	15.43	Shift	-0.017	Both
7164.899	0.36371	94.27	Shift	-0.007	Both

7173.782	0.17392	45.08	Shift	-0.013	Both

9.2.5 1305K

Error Quantification for a 1.76% Water-Air Mixture at 1305K

Line center (cm-1)	Peak absorbance	SNR	Error Type	Shift difference (model-measured) (cm-1)	Database
6801.620	0.02222	9.19	Shift	-0.020	Both
6804.253	0.01122	4.64	Shift	-0.007	Both
6804.350	0.01982	8.20	Shift	-0.017	Both
6806.029	0.06319	26.13	Shift	-0.017	Both
6806.116	0.01097	4.54	Not Clear	N/A	Not clear
6807.832	0.07350	30.40	Shift	-0.017	Both
6808.039	0.04834	19.99	Shift	-0.017	Both
6808.209	0.01398	5.78	Shift	-0.013	Both
6810.502	0.02279	9.42	Shift	-0.017	Both
6810.936	0.00964	3.99	Shift	-0.013	Both
6811.093	0.01246	5.15	Shift	-0.017	Both
6812.391	0.01915	7.92	Shift	-0.016	Both
6812.806	0.02204	9.12	Shift	-0.010	Both
6813.407	0.04336	17.93	Shift	-0.020	Both
6819.151	0.03356	13.88	Shift	-0.017	Both
6821.274	0.01406	5.82	Shift	-0.020	Both
6821.789	0.01282	5.30	Shift	-0.010	Both
6823.965	0.01372	5.68	Shift	-0.013	Both
6824.225	0.01242	5.14	Shift	-0.017	Both
6826.859	0.02865	11.85	Shift	-0.020	Both
6829.123	0.00941	3.89	Shift	-0.024	Both
6829.747	0.02085	8.62	Shift	-0.013	Both
6830.952	0.00919	3.80	Shift	-0.013	Both
6831.977	0.00862	3.57	Shift	-0.020	Both
6834.807	0.01146	4.74	Shift	-0.020	Both
6834.981	0.08788	36.35	Shift	-0.017	Both
6835.268	0.03990	16.50	Shift	-0.013	Both
6836.550	0.00649	2.69	DNM	N/A	HITRAN 2012
6836.673	0.09564	39.55	Shift	-0.020	Both
6837.121	0.05799	23.98	Shift	-0.017	Both
6837.508	0.01478	6.11	MND	N/A	Both
6837.918	0.01502	6.21	DNM	N/A	Both
6838.749	0.01484	6.14	Shift	-0.013	Both
6839.073	0.03260	13.48	Shift	-0.020	Both

6839.501	0.01812	7.49	Shift	-0.013	Both
6841.280	0.05219	21.59	Shift	-0.013	Both
6842.161	0.02106	8.71	Shift	-0.010	Both
6844.725	0.01990	8.23	Shift	-0.010	Both
6849.028	0.01113	4.60	Shift	-0.013	Both
6849.926	0.00833	3.45	Shift	-0.017	Both
6853.517	0.01198	4.95	Shift	-0.013	Both
6853.985	0.01477	6.11	Shift	-0.016	Both
6854.149	0.16180	66.92	MND	N/A	Both
6855.374	0.01111	4.60	Shift	-0.017	Both
6857.323	0.02970	12.28	Shift	-0.017	Both
6857.423	0.00703	2.91	MND	N/A	HITEMP 2010
6859.690	0.01069	4.42	Shift	-0.016	Both
6860.247	0.01444	5.97	Shift	-0.010	Both
6860.795	0.01026	4.24	Shift	-0.013	Both
6861.923	0.03215	13.30	Shift	-0.003	Both
6862.117	0.00705	2.91	Shift	-0.060	Both
6862.554	0.02985	12.35	Shift	-0.017	Both
6863.412	0.09796	40.51	Shift	-0.013	Both
6864.487	0.00887	3.67	Shift	-0.017	Both
6864.977	0.11595	47.95	Shift	-0.013	Both
6865.462	0.07105	29.38	Shift	-0.017	Both
6867.030	0.03326	13.75	Shift	-0.007	Both
6867.501	0.01450	6.00	Shift	-0.007	Both
6868.823	0.01881	7.78	Shift	-0.013	Both
6869.451	0.02498	10.33	Shift	-0.013	Both
6869.554	0.01607	6.64	Shift	-0.017	Both
6870.305	0.04764	19.70	Shift	-0.010	Both
6870.926	0.00819	3.39	Shift	-0.013	Both
6873.670	0.07113	29.41	Shift	-0.007	Both
6875.402	0.02348	9.71	Shift	-0.013	Both
6875.646	0.01009	4.17	Shift	-0.020	Both
6878.207	0.01770	7.32	Shift	-0.020	Both
6878.954	0.01744	7.21	Shift	-0.017	Both
6879.074	0.04995	20.66	Shift	-0.010	Both
6879.485	0.00692	2.86	Shift	-0.013	Both
6880.763	0.01402	5.80	Shift	-0.024	Both
6884.299	0.02942	12.17	Shift	-0.017	Both
6884.836	0.01078	4.46	Shift	-0.013	Both
6890.451	0.02486	10.28	Shift	-0.007	Both
6891.185	0.10239	42.35	Shift	-0.020	Both
6891.288	0.03562	14.73	Shift	-0.020	Both
6891.733	0.04329	17.90	Shift	-0.013	Both

6892.400	0.00728	3.01	DNM	N/A	HITRAN 2012
6892.734	0.14896	61.60	Shift	-0.013	Both
6893.094	0.01529	6.33	Shift	-0.013	Both
6893.301	0.03000	12.41	Shift	-0.013	Both
6894.370	0.03836	15.86	Shift	-0.010	Both
6894.503	0.00851	3.52	Shift	-0.013	Both
6894.707	0.07021	29.04	Shift	-0.017	Both
6895.114	0.01387	5.74	Shift	-0.013	Both
6895.207	0.02259	9.34	Shift	-0.013	Both
6897.538	0.07165	29.63	Shift	-0.013	Both
6901.954	0.03396	14.05	Shift	-0.010	Both
6905.970	0.02492	10.31	Shift	-0.017	Both
6906.657	0.01555	6.43	Shift	-0.020	Both
6906.714	0.02594	10.73	Shift	-0.010	Both
6907.565	0.01381	5.71	Shift	-0.016	HITRAN 2012
6907.565	0.01381	5.71	DNM	N/A	HITEMP 2010
6907.672	0.01122	4.64	MND	N/A	HITEMP 2010
6908.523	0.00855	3.54	Shift	-0.016	Both
6909.165	0.02265	9.37	Shift	-0.010	Both
6909.929	0.01306	5.40	Shift	-0.013	Both
6910.322	0.01301	5.38	Shift	-0.016	Both
6910.606	0.02522	10.43	Shift	-0.013	Both
6911.962	0.01904	7.87	Shift	-0.010	Both
6912.286	0.01668	6.90	Shift	-0.010	Both
6912.770	0.00863	3.57	Shift	-0.010	Both
6914.145	0.01257	5.20	Shift	-0.010	Both
6914.970	0.01011	4.18	Shift	-0.013	Both
6915.653	0.01722	7.12	Shift	-0.016	Both
6916.946	0.01385	5.73	Shift	-0.010	Both
6918.475	0.12394	51.26	Shift	-0.013	Both
6918.758	0.03814	15.77	Shift	-0.013	Both
6919.946	0.18031	74.57	Shift	-0.016	Both
6920.527	0.10118	41.84	Shift	-0.010	Both
6920.931	0.03304	13.66	Shift	-0.010	Both
6921.028	0.01234	5.10	Shift	-0.010	Both
6921.565	0.00729	3.02	Shift	-0.010	Both
6922.450	0.02956	12.22	Shift	-0.003	Both
6922.777	0.02243	9.28	Shift	-0.017	Both
6923.138	0.02337	9.66	Shift	-0.010	Both
6923.665	0.04396	18.18	Shift	-0.013	Both
6925.805	0.02924	12.09	Shift	-0.007	Both
6929.784	0.00600	3.28	MND	N/A	HITRAN 2012
6931.146	0.00678	3.71	Shift	-0.074	HITEMP 2010

6931.146	0.00678	3.71	DNM	N/A	Both
6932.348	0.01903	10.42	Shift	-0.007	Both
6933.109	0.02444	13.38	Shift	-0.013	Both
6933.586	0.01319	7.22	Shift	-0.010	HITRAN 2012
6933.586	0.01319	7.22	DNM	N/A	HITEMP 2010
6934.120	0.01748	9.57	Shift	-0.007	Both
6934.581	0.01143	6.26	Shift	-0.010	Both
6935.676	0.02336	12.78	Shift	-0.017	Both
6935.859	0.00642	3.51	DNM	N/A	HITRAN 2012
6936.000	0.00642	3.51	Shift	-0.017	Both
6936.838	0.03400	18.61	Shift	-0.013	Both
6937.835	0.03620	19.81	Shift	-0.007	Both
6938.283	0.00936	5.12	Shift	-0.010	Both
6938.703	0.00465	2.55	Shift	-0.033	HITEMP 2010
6938.703	0.00465	2.55	DNM	N/A	HITRAN 2012
6938.777	0.00485	2.65	DNM	N/A	HITRAN 2012
6939.184	0.07222	39.53	Shift	-0.003	Both
6940.089	0.00996	5.45	Shift	-0.010	Both
6940.523	0.01272	6.96	Shift	-0.010	Both
6942.021	0.00971	5.32	Shift	-0.013	Both
6942.155	0.00604	3.30	Shift	-0.017	Both
6943.197	0.00654	3.58	Shift	-0.010	Both
6944.849	0.04303	23.55	Shift	-0.010	Both
6945.480	0.13565	74.25	Shift	-0.010	Both
6946.345	0.00888	4.86	MND	N/A	HITEMP 2010
6946.572	0.20715	113.38	Shift	-0.017	Both
6946.792	0.02819	15.43	Shift	-0.010	Both
6947.272	0.04668	25.55	Shift	-0.017	Both
6947.439	0.01240	6.79	Shift	-0.010	Both
6947.910	0.00653	3.57	MND	N/A	HITEMP 2010
6948.044	0.00608	3.33	DNM	N/A	Both
6948.448	0.12115	66.31	Shift	-0.017	Both
6948.811	0.00777	4.25	Shift	-0.010	Both
6949.710	0.01083	5.93	Shift	0.020	HITRAN 2012
6951.759	0.00550	3.01	MND	N/A	HITEMP 2010
6951.759	0.00550	3.01	DNM	N/A	HITRAN 2012
6952.710	0.01383	7.57	Shift	-0.007	Both
6953.244	0.00617	3.38	Shift	-0.016	HITEMP 2010
6953.244	0.00617	3.38	DNM	N/A	HITRAN 2012
6953.588	0.01053	5.77	Shift	-0.010	Both
6954.005	0.04878	26.70	Shift	-0.010	Both
6954.166	0.01909	10.45	Shift	-0.010	Both
6954.389	0.09232	50.53	Shift	-0.006	Both

6956.726	0.00721	3.95	Shift	-0.013	Both
6957.861	0.01794	9.82	Shift	-0.007	Both
6958.532	0.02727	14.92	Shift	-0.013	Both
6958.966	0.00699	3.82	Shift	-0.007	Both
6960.027	0.02474	13.54	Shift	-0.010	Both
6960.107	0.01344	7.36	Shift	-0.020	Both
6961.913	0.01152	6.31	Shift	-0.013	Both
6962.925	0.02652	14.52	Shift	-0.013	Both
6963.172	0.00585	3.20	Shift	-0.013	Both
6963.376	0.00964	5.28	Shift	-0.010	Both
6964.217	0.00616	3.37	Shift	-0.010	Both
6964.427	0.01125	6.16	Shift	-0.050	HITEMP 2010
6964.427	0.01125	6.16	DNM	N/A	HITRAN 2012
6964.928	0.00890	4.87	Shift	-0.010	Both
6966.964	0.00581	3.18	Shift	-0.016	Both
6967.405	0.07969	43.62	Shift	-0.003	Both
6969.047	0.03313	18.13	Shift	-0.023	Both
6969.391	0.01711	9.37	Shift	-0.010	Both
6969.588	0.00590	3.23	Shift	-0.013	Both
6970.903	0.00682	3.73	Shift	-0.020	Both
6971.601	0.05851	32.03	Shift	-0.017	Both
6971.801	0.01184	6.48	Shift	-0.020	Both
6972.052	0.15907	87.07	Shift	-0.013	Both
6972.743	0.24569	134.48	Shift	-0.013	Both
6972.836	0.05252	28.75	DNM	N/A	HITEMP 2010
6973.661	0.12446	68.12	Shift	-0.007	Both
6974.305	0.00860	4.71	DNM	N/A	HITRAN 2012
6975.033	0.02276	12.46	Shift	-0.010	Both
6976.678	0.00719	3.94	Shift	-0.010	Both
6976.985	0.00991	5.42	Shift	-0.007	Both
6978.487	0.01660	9.08	Shift	-0.010	Both
6979.843	0.01198	6.56	Shift	-0.010	Both
6979.983	0.00829	4.54	Shift	-0.010	Both
6980.537	0.01968	10.77	Shift	-0.007	Both
6980.754	0.02525	13.82	Shift	-0.006	Both
6981.111	0.01454	7.96	Shift	-0.007	Both
6981.532	0.03886	21.27	Shift	-0.010	Both
6982.433	0.00973	5.33	Shift	-0.007	Both
6984.326	0.04180	22.88	Shift	-0.003	Both
6984.953	0.02174	11.90	Shift	-0.010	Both
6985.160	0.01377	7.54	Shift	-0.017	Both
6985.681	0.01405	7.69	Shift	-0.013	Both
6985.748	0.02370	12.97	Shift	-0.007	Both

6986.302	0.00556	3.04	DNM	N/A	Both
6986.472	0.00556	3.04	MND	N/A	HITEMP 2010
6987.123	0.02858	15.64	Shift	-0.013	HITRAN 2012
6987.457	0.03740	20.47	Shift	-0.010	Both
6987.771	0.01428	7.82	Shift	-0.010	Both
6990.384	0.00848	4.64	Shift	-0.013	Both
6991.369	0.00670	3.67	MND	N/A	HITEMP 2010
6991.493	0.00555	3.04	DNM	N/A	Both
6992.594	0.01142	6.25	Shift	-0.007	Both
6994.240	0.01586	8.68	Shift	-0.007	Both
6994.901	0.02653	14.52	Shift	-0.010	Both
6995.389	0.02424	13.27	Shift	-0.007	Both
6995.522	0.02390	13.08	Shift	-0.020	Both
6995.966	0.00894	4.89	Shift	-0.020	Both
6996.063	0.01907	10.44	Shift	-0.007	Both
6996.400	0.00746	4.09	Shift	-0.010	Both
6997.074	0.00797	4.36	Shift	-0.024	HITEMP 2010
6997.074	0.00797	4.36	DNM	N/A	HITRAN 2012
6997.508	0.01571	8.60	Shift	-0.013	Both
6997.652	0.06292	34.44	Shift	-0.017	Both
6997.788	0.04752	26.01	Shift	-0.010	Both
6997.992	0.16539	90.52	Shift	-0.010	Both
6998.169	0.23453	128.37	Shift	-0.013	Both
6998.537	0.01342	7.35	MND	N/A	HITEMP 2010
6998.676	0.01579	8.64	Shift	-0.010	HITRAN 2012
6998.676	0.01579	8.64	DNM	N/A	HITEMP 2010
6998.807	0.07772	42.54	Shift	-0.007	Both
6999.765	0.00666	3.65	MND	N/A	HITEMP 2010
6999.972	0.04471	24.47	Shift	-0.003	Both
7000.640	0.17218	94.24	Shift	-0.003	Both
7001.120	0.00835	4.57	Shift	-0.013	Both
7001.498	0.00940	5.14	Shift	-0.017	Both
7001.941	0.02808	15.37	Shift	-0.003	Both
7002.081	0.00785	4.30	DNM	N/A	Both
7002.228	0.02940	16.09	Shift	-0.010	Both
7002.953	0.00691	3.78	Shift	-0.013	HITEMP 2010
7002.953	0.00691	3.78	DNM	N/A	HITRAN 2012
7003.100	0.01063	5.82	Shift	-0.013	Both
7004.972	0.01194	6.54	Shift	-0.017	Both
7005.193	0.01728	9.46	Shift	-0.013	Both
7005.370	0.00676	3.70	Shift	-0.024	Both
7005.743	0.00974	5.33	Shift	-0.007	Both
7006.127	0.01787	9.78	Shift	-0.007	Both

7007.602	0.01142	6.25	Shift	-0.010	Both
7008.070	0.03285	17.98	Shift	-0.003	Both
7008.387	0.01159	6.35	DNM	N/A	HITRAN 2012
7008.708	0.01184	6.48	Shift	-0.007	Both
7008.985	0.00565	3.09	Shift	-0.017	Both
7009.806	0.00729	3.99	Shift	-0.017	HITEMP 2010
7009.806	0.00729	3.99	DNM	N/A	HITRAN 2012
7010.273	0.00635	3.47	MND	N/A	HITEMP 2010
7010.807	0.00586	3.21	Shift	0.053	HITEMP 2010
7010.807	0.00586	3.21	DNM	N/A	HITRAN 2012
7011.191	0.04568	25.00	Shift	-0.010	Both
7011.839	0.00878	4.80	Shift	-0.020	Both
7012.072	0.00892	4.88	Shift	-0.013	Both
7012.356	0.00850	4.65	Shift	-0.016	HITRAN 2012
7012.356	0.00850	4.65	Shift	0.003	HITEMP 2010
7013.154	0.00960	5.26	Shift	-0.020	Both
7013.611	0.01372	7.51	Shift	-0.010	Both
7014.459	0.04367	23.90	Shift	-0.010	Both
7014.569	0.02077	11.37	Shift	-0.007	Both
7015.541	0.00518	2.83	Shift	-0.017	Both
7015.624	0.00879	4.81	Shift	-0.013	Both
7015.915	0.02580	14.12	Shift	-0.007	Both
7016.178	0.01573	8.61	Shift	-0.007	Both
7016.646	0.00828	4.53	Shift	-0.030	Both
7016.879	0.02437	13.34	Shift	-0.017	Both
7017.210	0.03369	18.44	Shift	-0.006	Both
7017.647	0.02027	11.10	Shift	-0.003	Both
7017.948	0.04797	26.26	Shift	-0.003	Both
7018.829	0.00748	4.09	Shift	-0.006	Both
7019.223	0.00593	3.25	Shift	-0.013	Both
7020.425	0.00780	4.27	Shift	-0.010	HITRAN 2012
7020.425	0.00780	4.27	DNM	N/A	HITEMP 2010
7020.558	0.00901	4.93	MND	N/A	HITEMP 2010
7020.658	0.01359	7.44	Shift	-0.010	Both
7021.092	0.00820	4.49	MND	N/A	Both
7021.492	0.00460	2.52	Shift	-0.016	HITRAN 2012
7021.492	0.00460	2.52	DNM	N/A	HITEMP 2010
7021.810	0.03627	19.85	Shift	-0.013	Both
7022.080	0.01457	7.97	Shift	-0.013	Both
7022.511	0.01226	6.71	MND	N/A	HITEMP 2010
7022.711	0.24651	134.92	Shift	-0.010	Both
7023.322	0.08323	45.55	Shift	-0.013	Both
7023.452	0.22420	122.71	Shift	-0.010	Both

7024.223	0.00473	2.59	Shift	-0.017	Both
7024.390	0.00680	3.72	Shift	-0.007	Both
7024.684	0.02204	12.06	MND	N/A	HITEMP 2010
7024.794	0.02388	13.07	Shift	-0.013	HITRAN 2012
7024.794	0.02388	13.07	DNM	N/A	HITEMP 2010
7025.048	0.04634	25.37	Shift	-0.007	Both
7025.899	0.04257	23.30	Shift	-0.013	Both
7025.982	0.01668	9.13	Shift	-0.007	Both
7028.139	0.06859	37.54	Shift	-0.007	Both
7028.306	0.02606	14.26	Shift	-0.003	Both
7028.613	0.00667	3.65	Shift	-0.013	Both
7028.766	0.01828	10.01	Shift	-0.010	Both
7030.289	0.01696	9.28	DNM	N/A	Both
7030.449	0.01274	6.97	Shift	-0.013	HITRAN 2012
7030.449	0.01274	6.97	DNM	N/A	HITEMP 2010
7030.566	0.01151	6.30	MND	N/A	HITEMP 2010
7030.669	0.01322	7.24	MND	N/A	Both
7031.237	0.05075	27.78	Shift	-0.007	Both
7031.644	0.01202	6.58	Shift	-0.013	Both
7032.699	0.00682	3.73	DNM	N/A	HITRAN 2012
7032.996	0.00808	4.42	MND	N/A	Both
7034.468	0.02696	14.76	Shift	-0.017	Both
7034.802	0.05007	27.40	Shift	-0.010	Both
7036.515	0.00926	5.07	Shift	-0.010	Both
7036.765	0.01341	7.34	Shift	-0.010	Both
7038.434	0.10887	59.59	Shift	-0.006	Both
7039.011	0.00721	3.95	DNM	N/A	HITRAN 2012
7039.145	0.02735	14.97	Shift	-0.010	HITRAN 2012
7039.145	0.02735	14.97	Shift	0.007	HITEMP 2010
7039.279	0.03378	18.49	Shift	-0.003	Both
7040.220	0.01539	8.42	Shift	-0.010	Both
7041.525	0.02748	15.04	Shift	-0.013	Both
7043.037	0.00566	3.10	Not Clear	N/A	Not clear
7044.002	0.01650	9.03	Shift	-0.010	Both
7044.265	0.01004	5.49	Shift	-0.010	Both
7044.826	0.01367	7.48	Shift	-0.010	Both
7045.016	0.01672	9.15	Shift	-0.017	Both
7045.223	0.01324	7.25	Shift	-0.034	Both
7045.845	0.03760	20.58	Shift	-0.010	Both
7046.809	0.01375	7.53	Shift	-0.013	Both
7047.093	0.07069	38.69	Shift	-0.006	Both
7047.320	0.20481	112.10	Shift	-0.003	Both
7047.684	0.32792	179.49	Shift	-0.013	Both

7049.760	0.01114	6.10	Shift	-0.013	Both
7050.117	0.01642	8.99	Shift	-0.013	Both
7050.488	0.00573	3.14	DNM	N/A	Both
7050.772	0.01344	7.35	Shift	-0.020	Both
7051.843	0.03128	17.12	Shift	-0.007	Both
7052.027	0.01392	7.62	Shift	-0.024	HITRAN 2012
7052.027	0.01392	7.62	MND	N/A	HITEMP 2010
7052.097	0.00734	4.02	MND	N/A	HITEMP 2010
7052.157	0.01540	8.43	MND	N/A	HITEMP 2010
7053.649	0.02343	12.83	Shift	-0.013	HITRAN 2012
7053.649	0.02343	12.83	Shift	0.016	HITEMP 2010
7053.933	0.05806	31.78	Shift	-0.007	Both
7054.230	0.18871	103.29	Shift	-0.003	Both
7054.888	0.06944	38.01	Shift	-0.010	Both
7055.068	0.00949	5.20	Shift	-0.020	Both
7057.358	0.05373	14.99	Shift	-0.007	Both
7057.685	0.04300	12.00	Shift	-0.010	Both
7057.778	0.02530	7.06	Shift	-0.020	Both
7058.643	0.00993	2.77	Shift	-0.017	Both
7058.770	0.01100	3.07	Shift	-0.013	Both
7061.560	0.02473	6.90	Shift	-0.013	Both
7061.657	0.01952	5.45	DNM	N/A	Both
7062.031	0.01870	5.22	MND	N/A	Both
7065.559	0.02034	5.67	Shift	-0.010	HITRAN 2012
7065.559	0.02034	5.67	Shift	-0.050	HITEMP 2010
7067.689	0.03196	8.92	Shift	-0.007	Both
7069.001	0.04210	11.75	Shift	-0.020	Both
7070.781	0.21010	58.62	Shift	-0.007	Both
7070.917	0.04898	13.67	Shift	-0.020	Both
7071.491	0.32336	90.22	Shift	-0.010	Both
7071.602	0.10148	28.31	Shift	-0.017	Both
7074.245	0.01706	4.76	Shift	-0.010	Both
7074.482	0.03375	9.42	Shift	-0.007	Both
7075.594	0.05720	15.96	Shift	-0.020	Both
7076.518	0.03663	10.22	Shift	-0.020	Both
7080.104	0.06006	16.76	Shift	-0.013	Both
7080.361	0.05802	16.19	Shift	-0.007	HITRAN 2012
7080.361	0.05802	16.19	Shift	0.007	HITEMP 2010
7080.575	0.13656	38.10	Shift	-0.007	Both
7081.078	0.01848	5.16	Shift	-0.010	Both
7081.212	0.01869	5.21	Shift	-0.010	Both
7081.349	0.11366	31.71	Shift	-0.013	Both
7082.250	0.01177	3.28	Shift	-0.013	Both

7082.507	0.01423	3.97	Shift	-0.016	Both
7083.228	0.06962	19.43	Shift	-0.010	Both
7084.637	0.02063	5.76	Shift	-0.007	Both
7085.248	0.09356	26.11	Shift	-0.010	Both
7089.353	0.08101	22.60	Shift	-0.016	Both
7089.434	0.02625	7.33	MND	N/A	HITEMP 2010
7090.796	0.01622	4.52	Shift	-0.013	Both
7091.417	0.04958	13.83	Not Clear	N/A	Both
7094.067	0.07397	20.64	Shift	-0.010	Both
7094.682	0.26471	73.86	Shift	-0.007	Both
7095.676	0.02632	7.34	Shift	-0.017	Both
7097.375	0.07905	22.06	Shift	-0.007	Both
7098.093	0.01255	3.50	Shift	-0.007	Both
7100.116	0.04460	12.44	Shift	-0.010	Both
7101.565	0.03502	9.77	Shift	-0.010	Both
7103.110	0.05991	16.72	Shift	-0.007	HITRAN 2012
7103.207	0.06277	17.51	MND	N/A	HITEMP 2010
7107.093	0.01780	4.97	Shift	-0.030	Both
7108.712	0.02593	7.24	Shift	-0.007	Both
7117.418	0.24608	68.66	Shift	-0.007	Both
7117.755	0.20633	57.57	Shift	-0.010	Both
7120.168	0.02731	7.62	Not Clear	N/A	Not clear
7122.381	0.02949	8.23	Shift	-0.013	Both
7127.596	0.01070	2.99	Shift	-0.017	Both
7128.961	0.02558	7.14	Shift	-0.010	Both
7130.032	0.02538	7.08	MND	N/A	HITEMP 2010
7137.523	0.01473	4.11	MND	N/A	HITEMP 2010
7137.600	0.03083	8.60	MND	N/A	HITEMP 2010
7139.082	0.21167	59.06	Shift	-0.003	Both
7164.899	0.25576	71.36	Shift	-0.007	Both

10 Appendix for Chapter 5

Table 10-1-This is a listing of all data extracted with the multispectral fitting routine explained in Chapter 5. The "Notes" column uses letters to indicate the following special constraints: a: line center, b: linestrengths, c: self-broadened width, d: temperature-scaling exponent, e: pressure shift, f: speed dependence parameter, g: self-shift temperature-scaling. The uncertainties presented are the fit uncertainties for each line.

Vibrational upper	Vibrational lower	Rotational upper	Rotational lower	Line center (cm-1)	Line center uncert. (cm-1)	Linestrength (cm-1/molecule cm-1)	Linestrength uncert. (cm-1/molecule cm-1)	E"(cm-1)	Self-broadening (cm-1/atm)	Self-broadening uncert. (cm-1/atm)	Temperature-scaling expoent	Temperature-scaling exponent uncert.	Self shift (cm-1/atm)	Self shift uncert. (cm-1/atm)	Speed dependence ratio Γ2/Γ0	Speed dependence ratio uncert. (Γ2/Γ1)	Notes
021	000	202	303	6804.40072	2.91E-05	1.1236E-21	2.5E-24	136.7617	0.473	0.0036	1.0485	0.0276			0.10046	0.012	
120	000	211	202	6806.66956		1.6846E-23	1.1E-24	70.0908	0.437		0.694						
021	000	212	313	6812.81062	6.98E-05	3.2709E-22	1.9E-24	142.2785	0.4428	0.0091	0.9212	0.0713			0.06478	0.029	
021	000	220	321	6816.39305	4.92E-05	4.7003E-22	1.9E-24	212.1564	0.4301	0.0065	0.8511	0.0449			0.09139	0.020	
120	000	111	000	6818.311		1.1878E-24	5.4E-27	0	0.461		0.694						b
021	000	331	432	6819.27622	7.52E-05	2.2952E-22	1.6E-24	382.5169	0.3679	0.0106	0.6944	0.0626			0.11655	0.033	
021	000		322	6821.04856	1.14E-04	1.6819E-22	1.8E-24	206.3014	0.4394	0.0183	0.5596	0.1034			0.23563	0.042	
021	000	110	211	6824.39499	7.90E-05	2.429E-22	1.8E-24	95.1759	0.3634	0.0110	0.8179	0.1132			0.13801	0.034	
021	000	101	202	6825.0564	6.28E-05	3.52E-22	1.9E-24	70.0908	0.4052	0.0084	0.7722	0.0782			0.12426	0.026	
101	000	1349	14410	6831.7246	3.50E-04	3.8892E-26	6.4E-28	2880.8325	0.235		0.694						
101	000	1267	1368	6831.97711		3.8322E-26	1.0E-27	2748.0986	0.25		0.694						
200	000	652	761	6833.13129		3.1606E-23	2.9E-25	1216.1945	0.3151	0.0268	0.5661	0.0953			0.10452	0.063	
021	000	111	212	6834.17172	3.81E-05	7.6217E-22	2.2E-24	79.4964	0.4969	0.0049	0.9398	0.0368			0.10727	0.015	
021	000	550	651	6834.99274		7.1857E-24	1.2E-25	888.6326	0.371		0.694						
021	000	551	652	6835.00517		2.1517E-23	3.7E-25	888.5986	0.371		0.694						b
101	000	1257	1358	6835.26868		2.816E-25	1.7E-27	2629.333	0.34		0.694						
120	000	212	101	6835.57969		4.187E-23	1.1E-24	23.7944	0.453		0.694						
101	000	16016	17017	6836.67528		9.052E-26	4.5E-28	2981.3574	0.195		0.694						bcdf
101	000	16116	17117	6836.6777	3.45E-04	3.0177E-26	1.5E-28	2981.3584	0.195		0.694						
101	000	14212	15213	6837.12344		1.292E-25	7.1E-28	2872.2732	0.221		0.694						
120	000	422	413	6837.14281	6.07E-04	1.508E-23	1.0E-24	275.4971	0.45		0.694						
200	000	744	853	6837.67671		6.633E-24	1.5E-25	1255.9115	0.354		0.694						
101	000	14312	15313	6837.91784		3.8812E-26	6.6E-28	2872.5806	0.221		0.694						
031	010	331	330	6838.91197		1.1515E-24	1.9E-26	1907.6158	0.34		0.694						
101	000	13310	14311	6838.9686		5.6435E-26	1.1E-27	2739.4277	0.336		0.694						
200	000	14014	15115	6839.07501	2.43E-04	1.1585E-25	1.3E-27	2358.3005	0.35		0.694						

200	000	14114	15015	6839.0751	2.43E-04	3.4773E-25	3.9E-27	2358.2996	0.35		0.694					abcd
101	000	533	652	6840.95441		2.3875E-23	4.1E-25	888.5986	0.388		0.694					
120	000	752	845	6841.2224		1.2879E-24	2.1E-25	1122.7083	0.31		0.694					
101	000	13410	14411	6841.28334		2.0145E-25	1.1E-27	2746.0225	0.265		0.694					
200	000	743	854	6841.42701	1.36E-04	2.4446E-23	2.6E-25	1255.1666	0.4142	0.0379	0.7379	0.1085		0.10529	0.070	
200	000	1258	1349	6842.163		2.0327E-25	2.2E-27	2533.7932	0.25		0.694					
120	000	523	514	6842.24736		2.1764E-23	1.4E-24	399.4575	0.3744	0.0973	1.1389	0.7188		0.00015	0.344	
101	000	826	945	6842.32832		2.4837E-24	1.2E-25	1360.235	0.56		0.694					
021	000	313	312	6843.36021	9.25E-05	2.4056E-22	1.8E-24	173.3658	0.4954	0.0131	0.874	0.0822		0.10235	0.036	
200	000	1037	1148	6843.95107		6.0405E-25	2.4E-26	1843.0288	0.425		0.694					
101	000	955	972	6847.32246		2.8474E-25	2.6E-26	1810.5876	0.26		0.694					
021	000	000	101	6847.7256	4.00E-05	6.5361E-22	2.1E-24	23.7944	0.4288	0.0048	1.0308	0.0529		0.07469	0.016	
120	000	313	202	6850.2027		1.7154E-23	1.0E-24	70.0908	0.435		0.694					
120	000	404	313	6852.29726		1.0986E-23	1.0E-24	142.2785	0.42		0.694					
120	000	221	212	6855.50978		1.672E-23	1.1E-24	79.4964	0.485		0.694					
021	000	212	211	6859.9136	1.52E-04	1.4384E-22	2.2E-24	95.1759	0.5102	0.0264	0.7508	0.1539		0.17784	0.057	
021	000	524	523	6859.97885	1.73E-04	9.9728E-23	1.8E-24	446.5107	0.4514	0.0287	0.7425	0.1141		0.12121	0.073	
200	000	550	661	6861.93209	8.78E-05	6.3823E-23	4.7E-25	1045.0577	0.2635	0.0159	0.4487	0.0686		0.08718	0.051	
200	000	15114	15213	6862.07427		1.0279E-26	1.0E-27	2872.2732	0.221		0.694					
210	010	440	551	6862.10592	1.22E-03	7.9898E-26	4.1E-27	2406.1411	0.391		0.694					
101	000	14213	15214	6863.40558		1.4193E-25	5.6E-28	2631.2822	0.221		0.694					
101	000	14113	15114	6863.41814		4.2491E-25	1.7E-27	2631.2671	0.3		0.694					b
120	000	414	303	6863.68961		4.2009E-23	1.1E-24	136.7617	0.46		0.694					
021	000	881	982	6864.48905		1.5239E-25	3.8E-27	2009.8051	0.315		0.694					
021	000	880	981	6864.48943		4.5717E-25	1.1E-26	2009.8047	0.315		0.694					b
101	000	15115	16116	6864.97936		3.932E-25	1.2E-27	2660.9441	0.149		0.694					
101	000	15015	16016	6864.97944		1.31E-25	4.0E-28	2660.9448	0.208		0.694					b
101	000	13211	14212	6865.4252		1.9823E-25	7.5E-28	2550.8816	0.254		0.694					
101	000	13311	14312	6865.46835		5.488E-25	2.1E-27	2551.4822	0.217		0.694					b
200	000	13013	14114	6867.03664		1.0491E-24	1.1E-26	2073.5137	0.2		0.694					
200	000	643	752	6867.15891	1.05E-04	5.2994E-23	4.5E-25	1059.8353	0.3697	0.0221	0.6334	0.073		0.12052	0.052	
200	000	12211	13112	6867.50601		1.0031E-24	2.1E-26	2042.3098	0.188	0.0790	0.0611	0.3388		0.14056	0.161	
200	000	642	753	6868.27321	2.90E-04	1.9339E-23	4.6E-25	1059.6466	0.4288	0.0645	0.5655	0.1778		0.20521	0.120	
101	000	1249	13410	6869.45153	2.46E-04	2.7306E-25	3.3E-27	2426.1953	0.25		0.694					
101	000	1248	1349	6870.30686	1.18E-04	4.0625E-25	2.4E-27	2533.7932	0.25		0.694					
021	000	111	110	6871.29684	3.29E-05	9.1982E-22	2.4E-24	42.3717	0.4661	0.0042	0.8361	0.0354		0.12388	0.013	
101	000	431	550	6871.35454		1.7997E-23	5.8E-25	742.0762	0.34		0.694					
101	000	1239	13310	6873.67367	7.03E-05	1.0361E-24	3.8E-27	2414.7219	0.303		0.694					
021	000	423	422	6875.59442	1.11E-04	8.1146E-23	1.0E-24	315.7795	0.48		0.694					
101	000	1074	1175	6875.6427		1.5944E-25	4.7E-27	2321.8118	0.281		0.694					
101	000	1157	1258	6879.07744		1.2985E-24	6.0E-27	2275.3718	0.317		0.694					
021	000	110	111	6882.43443	7.19E-05	3.0505E-22	1.9E-24	37.1371	0.4506	0.0101	0.8224	0.0917		0.12741	0.028	
101	000	1139	1156	6884.04218		2.4607E-25	1.4E-26	1998.9948	0.315		0.694					

021	000	322	321	6885.91384	4.27E-05	5.5576E-22	1.9E-24	212.1564	0.4469	0.0055	0.762	0.037		0.08712	0.017	
021	000	735	734	6887.82855		2.4903E-23	4.6E-25	842.3565	0.431		0.694					
120	000	606	515	6888.10921		8.9452E-24	8.9E-25	326.6255	0.385		0.694					
200	000	634	743	6890.45216	7.55E-05	1.0587E-22	6.5E-25	931.237	0.4114	0.0143	0.6348	0.0445		0.15282	0.033	
200	000	625	734	6890.94662		6.1879E-23	1.2E-24	842.3565	0.4646	0.0353	0.6735	0.1073		0.15614	0.065	
120	000	616	505	6890.94963		1.9805E-23	2.2E-24	325.3479	0.391		0.694					
021	000	221	220	6891.18605	5.38E-05	4.2743E-22	1.9E-24	136.1639	0.4616	0.0075	0.9605	0.0651		0.12801	0.021	
101	000	13212	14213	6891.19028		1.6669E-24	5.8E-27	2327.9126	0.235		0.694					
101	000	13112	14113	6891.29376		5.6629E-25	4.7E-27	2327.8826	0.235		0.694					
031	010	413	312	6891.69064		1.3472E-24	3.5E-26	1772.4135	0.425		0.694					
101	000	1064	1165	6891.73865	1.16E-04	1.6498E-24	9.3E-27	2144.0459	0.281		0.694					
200	000	734	845	6891.86566		3.8612E-23	2.4E-25	1122.7083	0.43		0.694					
101	000	524	643	6892.04178		4.344E-23	5.5E-25	756.7247	0.415		0.694					
120	000	221	110	6892.63485	2.02E-04	4.6187E-23	1.1E-24	42.3717	0.46		0.694					
101	000	14014	15015	6892.73934	6.01E-05	1.568E-24	4.9E-27	2358.2996	0.2		0.694					
021	000	211	212	6893.24116	5.82E-05	4.0453E-22	1.9E-24	79.4964	0.4784	0.0081	0.8128	0.0625		0.12584	0.022	
021	000	220	221	6893.64765	2.58E-05	1.2866E-21	2.5E-24	134.9016	0.4703	0.0030	0.7618	0.0224		0.11464	0.010	
200	000	12012	13113	6894.37068		1.1857E-24	8.8E-27	1806.67	0.25		0.694					
200	000	12112	13013	6894.37562		3.5541E-24	2.6E-26	1806.6694	0.345		0.694					b
101	000	12210	13211	6894.71136	6.97E-05	1.8487E-24	6.7E-27	2246.8838	0.244		0.694					
021	000	101	000	6895.14719	8.69E-05	2.3389E-22	1.8E-24	23.1181	0.404	0.0114	0.7977	0.1872		0.05566	0.036	
200	000	11110	12211	6895.21283		3.0095E-24	3.0E-26	1774.7502	0.23		0.694					
200	000	542	651	6895.65082	1.29E-04	3.8149E-23	5.4E-25	888.6326	0.339		0.694					
120	000	431	422	6895.66484		1.0189E-23	1.2E-24	315.7795	0.412		0.694					
200	000	541	652	6895.89457	7.31E-05	1.1618E-22	7.0E-25	888.5986	0.3647	0.0128	0.6011	0.0455		0.12499	0.035	
031	010	606	505	6896.47638		1.0799E-24	1.9E-26	1920.7657	0.395		0.694					
021	000	321	322	6897.3115	1.06E-04	1.8918E-22	1.8E-24	206.3014	0.4848	0.0167	0.566	0.0878		0.19387	0.039	
101	000	1148	1249	6897.54105	6.04E-05	3.155E-24	1.0E-26	2124.95	0.31		0.694					
101	000	606	725	6898.51689	5.13E-04	1.166E-23	5.3E-25	782.4098	0.454		0.694					
120	000	220	111	6898.93961		1.4512E-23	1.0E-24	37.1371	0.47		0.694					
021	000	634	633	6901.66324		2.4462E-23	6.4E-25	661.5489	0.43		0.694					
101	000	1138	1239	6901.96239	1.27E-04	1.5158E-24	1.1E-26	2105.8667	0.37		0.694					
120	000	330	321	6902.47866		4.3061E-23	9.9E-25	212.1564	0.425		0.694					
200	000	1038	1129	6902.51417		2.5169E-24	4.0E-26	1690.6636	0.32		0.694					
120	000	707	616	6902.8993		1.3238E-23	8.2E-25	447.2523	0.39		0.694					
101	000	1055	1156	6902.99553	5.95E-05	4.7418E-24	1.6E-26	1998.9948	0.372		0.694					
021	000	422	423	6905.0573	1.27E-04	1.3666E-22	1.5E-24	300.3623	0.3878	0.0170	0.95	0.1285		0.03232	0.057	
101	000	973	1074	6906.71429	1.74E-04	1.3189E-24	1.2E-26	2054.3447	0.265		0.694					
120	000	331	322	6908.31033		2.0331E-23	9.3E-25	206.3014	0.375		0.694					
101	000	1046	1147	6908.70976	6.05E-05	8.3185E-24	3.6E-26	1899.0074	0.3826	0.0269	0.6585	0.0655		0.10619	0.033	
021	000	312	313	6909.21229		6.5344E-23	1.0E-24	142.2785	0.44		0.694					
120	000	322	211	6910.17454		1.2806E-23	1.1E-24	95.1759	0.392		0.694					
021	000	533	532	6910.21933	8.02E-05	1.9867E-22	1.6E-24	508.812	0.4156	0.0135	0.6822	0.0535		0.14122	0.035	

200	000	633	744	6911.16721		2.7431E-23	3.7E-25	927.7439	0.37		0.694						
120	000	432	423	6911.38475	1.32E-04	1.3992E-22	1.6E-24	300.3623	0.4628	0.0204	0.6906	0.1033			0.1626	0.051	
200	000	404	533	6911.6312		8.4724E-24	7.9E-25	503.9681	0.45		0.694						
200	000	515	624	6913.13988		1.4447E-23	7.1E-25	602.7735	0.48		0.694						
021	000	432	431	6914.54889	1.04E-04	1.5307E-22	1.5E-24	383.8425	0.3571	0.0144	0.6601	0.09			0.07752	0.048	
210	010	10110	11011	6914.96807		1.5049E-26	5.9E-28	2915.8743	0.281		0.694						
200	000	927	1038	6915.65664		1.0231E-23	9.0E-26	1446.1279	0.36		0.694						
101	000	515	634	6915.69392		2.6663E-23	6.7E-25	648.9787	0.43		0.694						
021	000	331	330	6916.37357	4.88E-05	1.0176E-21	2.1E-24	285.4186	0.4015	0.0031	0.5964	0.0208	4.75E-02	1.99E-03	0.10999	0.011	
021	000	330	331	6916.73317	5.70E-05	3.4385E-22	1.7E-24	285.2193	0.4126	0.0080	0.5765	0.0468			0.13286	0.023	
021	000	431	432	6916.94385	4.10E-05	4.7504E-22	1.7E-24	382.5169	0.4009	0.0057	0.5719	0.0302			0.13981	0.017	
021	000	202	101	6917.36811	5.27E-05	1.2569E-21	2.6E-24	23.7944	0.4604	0.0031	0.9165	0.0295	4.00E-02	2.57E-03	0.11913	0.010	
120	000	818	707	6917.62783		8.0515E-24	7.0E-25	586.2435	0.4		0.694						
021	000	212	111	6917.95186	7.91E-05	2.9327E-22	1.9E-24	37.1371	0.5003	0.0107	0.7826	0.0875			0.07999	0.030	
101	000	12111	13112	6918.47713	8.08E-05	6.161E-24	8.0E-26	2042.3098	0.2143	0.0213	0.2089	0.0843			0.14663	0.029	
200	000	1267	1358	6918.48305		7.9073E-26	1.0E-26	2629.333	0.25		0.694						
101	000	12211	13212	6918.76109	1.20E-04	2.0358E-24	1.2E-26	2042.3727	0.16		0.694						
021	000	532	533	6919.03288		6.6526E-23	7.9E-25	503.9681	0.37		0.694						
101	000	523	642	6919.4793		5.5232E-23	5.6E-25	757.7801	0.474		0.694						
101	000	13013	14014	6919.94747		1.992E-24	5.8E-27	2073.5142	0.2956	0.0080	0.685	0.0015			0.08519	0.025	
101	000	13113	14114	6919.94813		5.9564E-24	1.7E-26	2073.5137	0.2956	0.0080	0.685	0.0015			0.08519	0.025	bcdf
101	000	1139	12310	6920.53051	4.19E-05	7.9449E-24	1.9E-26	1962.5062	0.28		0.694						
200	000	11011	12112	6920.93621	1.01E-04	1.0405E-23	6.2E-26	1557.847	0.257		0.694						
200	000	1019	11210	6921.5701		3.0635E-24	6.5E-26	1525.135	0.261		0.694						
021	000	946	945	6921.7057		4.0053E-24	1.1E-25	1360.235	0.403		0.694						
101	000	1129	12210	6922.45606	1.30E-04	2.3834E-24	1.7E-26	1960.2061	0.263		0.694						
021	000	523	524	6922.77915		4.2462E-23	1.0E-24	416.2087	0.435		0.694						
200	000	1029	11110	6922.77936	1.36E-04	8.4049E-24	8.0E-26	1524.8473	0.281		0.694						
101	000	963	1064	6923.1419	2.38E-04	1.6716E-24	2.2E-26	1875.4613	0.28		0.694						
200	000	441	550	6923.45894	5.75E-05	2.1452E-22	1.3E-24	742.0762	0.3343	0.0093	0.5021	0.0365			0.12149	0.027	
200	000	440	551	6923.49867		6.868E-23	1.3E-24	742.073	0.3119	0.0267	0.5432	0.1122			0.13903	0.079	
101	000	964	1065	6923.66848	9.74E-05	5.0869E-24	3.6E-26	1874.9727	0.2499	0.0348	0.4675	0.1239			0.0618	0.065	
120	000	423	312	6924.78039		2.9422E-23	1.0E-24	173.3658	0.48		0.694						
021	000	633	634	6924.82294		7.6513E-23	6.8E-25	648.9787	0.43		0.694						
101	000	1047	1148	6925.80922	1.23E-04	3.5912E-24	2.5E-26	1843.0288	0.327		0.694						
101	000	423	542	6926.45166		2.2984E-23	7.0E-25	610.1144	0.454		0.694						
021	000	413	414	6929.64019	1.93E-04	1.0419E-22	1.7E-24	224.8384	0.5144	0.0295	0.7934	0.1571			0.13027	0.073	
021	000	211	110	6930.36592	3.33E-05	8.5238E-22	2.2E-24	42.3717	0.4725	0.0042	0.7932	0.0352			0.12043	0.013	
120	000	321	212	6930.73626	1.27E-04	1.6739E-22	1.8E-24	79.4964	0.5034	0.0189	0.7891	0.1366			0.12462	0.048	
200	000	533	642	6930.86934		1.9453E-23	5.4E-25	757.7801	0.44		0.694						
101	000	1037	1138	6931.59243		1.7174E-23	4.9E-26	1813.2227	0.4005	0.0177	0.6541	0.0423			0.11381	0.021	
111	010	937	1038	6932.35411		2.5062E-26	3.4E-28	3072.7258	0.298		0.694						
101	000	615	734	6932.64083		2.7475E-23	4.6E-25	842.3565	0.455		0.694						

200	000	532	643	6933.70903	6.81E-05	1.6898E-22	9.3E-25	756.7247	0.4307	0.0113	0.7591	0.0392		0.09601	0.031	
111	010	844	945	6934.12486	3.11E-04	3.008E-26	4.5E-28	2998.7661	0.315		0.694					
200	000	826	937	6934.60175		9.5241E-24	1.7E-25	1216.2311	0.315		0.694					
101	000	954	1055	6935.6759	1.32E-04	4.7553E-24	3.6E-26	1724.7047	0.311		0.694					
021	000	734	735	6935.85259		9.1969E-24	4.6E-25	816.6942	0.392		0.694					
120	000	716	625	6936.74669		5.9264E-24	7.2E-25	552.9114	0.387		0.694					
111	010	11111	12112	6936.83679		2.5111E-26	2.3E-28	3144.5781	0.265		0.694					
111	010	11011	12012	6936.87584		8.3388E-27	7.7E-29	3144.5681	0.265		0.694					b
021	000	313	212	6937.22939	2.84E-05	1.1519E-21	2.5E-24	79.4964	0.496	0.0036	0.8396	0.0259		0.09223	0.011	
021	000	303	202	6937.33786	4.96E-05	4.8453E-22	2.1E-24	70.0908	0.4598	0.0070	0.8713	0.0567		0.10518	0.020	
101	000	871	972	6937.83936		2.9506E-24	2.1E-26	1810.5876	0.35		0.694					
101	000	872	973	6937.85003		9.8383E-25	7.1E-27	1810.583	0.35		0.694					bcd
101	000	955	1056	6939.19133	5.96E-05	1.4818E-23	6.4E-26	1718.7185	0.3231	0.0213	0.5226	0.0629		0.09953	0.033	
200	000	524	633	6939.75997	1.26E-04	5.6976E-23	6.7E-25	661.5489	0.435		0.694					
031	010	919	818	6939.81165		2.1686E-25	4.6E-27	2337.6665	0.333		0.694					
002	000	963	1074	6940.34359		3.0906E-25	1.1E-26	2054.3447	0.243		0.694					
021	000	744	743	6940.52278	2.00E-04	3.7814E-23	6.3E-25	931.237	0.4164	0.0387	0.5874	0.114		0.17947	0.085	
101	000	945	1046	6941.78073	8.37E-05	1.0254E-23	5.3E-26	1616.4524	0.378		0.694					
101	000	422	541	6942.02326	1.13E-04	1.2845E-22	1.2E-24	610.3411	0.4827	0.0188	0.7092	0.0603		0.16631	0.044	
021	000	624	625	6942.40269		5.0104E-23	7.6E-25	552.9114	0.45		0.694					
101	000	937	954	6942.49587		2.2956E-24	7.5E-26	1477.2972	0.34		0.694					
021	000	643	642	6944.18672		3.3448E-23	5.2E-25	757.7802	0.33		0.694					
101	000	936	1037	6944.31736		4.88E-24	6.3E-26	1538.1488	0.298		0.694					
101	000	11110	12111	6944.85163		6.4698E-24	3.1E-26	1774.6154	0.25		0.694					
101	000	11210	12211	6945.48522		2.1102E-23	5.5E-26	1774.7502	0.2369	0.0115	0.3268	0.044		0.10972	0.021	
021	000	642	643	6945.98724	1.15E-04	1.0073E-22	1.3E-24	756.7247	0.3504	0.0195	0.5535	0.0709		0.14929	0.051	
021	000	542	541	6946.03203	6.12E-05	2.5147E-22	1.7E-24	610.3411	0.3609	0.0097	0.5466	0.0389		0.14299	0.026	
021	000	541	542	6946.4116	7.37E-05	8.4996E-23	7.2E-25	610.1144	0.34		0.694					
101	000	12112	13113	6946.55753	2.82E-05	6.7264E-24	1.1E-26	1806.67	0.25		0.694					
101	000	12012	13013	6946.5795	2.82E-05	2.0554E-23	3.4E-26	1806.6694	0.25		0.694					abcdf
200	000	10110	11011	6946.79411		2.1418E-23	1.2E-25	1327.1096	0.27		0.694					
021	000	441	440	6947.02045	8.65E-05	1.88E-22	1.9E-24	488.1342	0.3209	0.0135	0.5281	0.0667		0.1206	0.040	
021	000	440	441	6947.06518	3.40E-05	5.5956E-22	2.0E-24	488.1077	0.312	0.0050	0.4979	0.0267		0.10668	0.016	
120	000	743	734	6947.18846		4.6229E-24	4.5E-25	842.3565	0.365		0.694					
200	000	918	1029	6947.22601		2.3514E-23	1.4E-25	1293.6337	0.266		0.694					
101	000	1038	1139	6947.27678		8.5559E-24	4.1E-26	1695.0677	0.3		0.694					
200	000	10010	11111	6947.44661	2.05E-04	9.2984E-24	1.2E-25	1327.1165	0.26		0.694					
120	000	625	514	6948.384		1.2898E-23	8.8E-25	399.4575	0.433		0.694					
101	000	1028	1129	6948.44887	2.75E-05	2.8884E-23	5.0E-26	1690.6636	0.322		0.694					
200	000	928	1019	6948.81246	2.75E-04	7.4133E-24	1.3E-25	1293.0173	0.315		0.694					
021	000	844	845	6949.29927	2.64E-04	1.1544E-23	2.1E-25	1122.7083	0.3		0.694					
200	000	303	432	6951.03616		2.0325E-23	9.1E-25	382.5169	0.48		0.694					
200	000	725	836	6951.55259	9.74E-05	6.6382E-23	5.1E-25	1006.1157	0.415	0.0203	0.791	0.0639		0.07648	0.049	

021	000	835	836	6952.30746		6.622E-24	2.9E-25	1006.1157	0.387		0.694					
021	000	514	515	6953.09871		1.6231E-23	9.3E-25	326.6255	0.454		0.694					
111	010	753	854	6953.59218		2.5302E-26	5.9E-28	2919.6323	0.333		0.694					
101	000	862	963	6954.00933	8.12E-05	1.2975E-23	7.9E-26	1631.3831	0.2509	0.0267	0.5291	0.1015			0.03657	0.056
101	000	863	964	6954.16989	1.89E-04	4.3189E-24	4.7E-26	1631.2452	0.268		0.694					
101	000	946	1047	6954.39173	4.25E-05	3.3284E-23	1.1E-25	1581.3357	0.3475	0.0152	0.5489	0.0426			0.13266	0.022
021	000	414	313	6954.44362	5.33E-05	4.5115E-22	2.0E-24	142.2785	0.4813	0.0076	0.6794	0.0501			0.13955	0.020
021	000	404	303	6955.15567	4.71E-05	1.4066E-21	2.6E-24	136.7617	0.5171	0.0031	0.8739	0.0206	5.78E-02	2.02E-03	0.1152	0.010
021	000	312	211	6956.31526	5.89E-05	3.6862E-22	1.8E-24	95.1759	0.4069	0.0076	0.7819	0.0699			0.07371	0.024
101	000	322	441	6957.47124	2.54E-04	5.9968E-23	1.4E-24	488.1077	0.4105	0.0383	0.6816	0.1672			0.11199	0.109
200	000	432	541	6957.86289	5.84E-05	2.5018E-22	1.2E-24	610.3411	0.399	0.0087	0.6426	0.035			0.1052	0.026
120	000	642	633	6958.05939		2.4273E-24	6.1E-25	661.5489	0.36		0.694					
200	000	431	542	6958.77614	1.33E-04	1.0164E-22	1.2E-24	610.1144	0.3956	0.0201	0.7432	0.0841			0.08401	0.061
111	010	928	1029	6960.02909	2.41E-04	5.3985E-26	6.3E-28	2904.428	0.298		0.694					
101	000	836	853	6960.29657		2.2876E-24	1.4E-25	1255.9115	0.34		0.694					
200	000	1056	1147	6960.75301	1.27E-04	2.8338E-24	2.1E-26	1899.0074	0.419		0.694					
111	010	826	927	6960.80796		9.6995E-26	8.8E-28	2818.3977	0.315		0.694					
101	000	505	624	6961.17248		1.2235E-23	7.1E-25	602.7735	0.475		0.694					
021	000	322	303	6961.30828		5.5012E-23	1.8E-24	136.7617	0.5471	0.0641	0.6922	0.3306			0.18353	0.136
111	010	10110	11111	6961.91693		2.4211E-26	5.9E-28	2915.8933	0.281		0.694					
200	000	863	872	6962.01874		2.3353E-25	5.0E-26	1590.6901	0.23		0.694					
101	000	414	533	6962.26746		1.7796E-23	8.1E-25	503.9681	0.444		0.694					
031	010	726	625	6962.30791		3.6989E-25	8.3E-27	2161.2859	0.371		0.694					
002	000	818	927	6962.78751		2.8111E-24	1.7E-25	1201.921	0.384		0.694					
021	000	322	221	6963.16826	4.19E-05	6.4773E-22	2.1E-24	134.9016	0.4953	0.0055	0.7209	0.0344			0.10456	0.016
101	000	321	440	6963.73787	3.16E-04	2.6482E-23	8.5E-25	488.1342	0.443		0.694					
101	000	936	1037	6965.58402	1.05E-04	1.4299E-23	1.1E-25	1538.1495	0.439	0.0396	0.6883	0.0949			0.13253	0.050
120	000	541	532	6965.80233		1.3046E-23	7.8E-25	508.812	0.395		0.694					
200	000	624	735	6967.33554	2.16E-04	4.9678E-23	9.2E-25	816.6942	0.55	0.0447	0.5808	0.096			0.23461	0.076
101	000	853	954	6967.41081		4.0276E-23	9.3E-26	1477.2972	0.3		0.694					
021	000	321	220	6967.44911		2.1954E-22	2.0E-24	136.1639	0.5042	0.0161	0.7137	0.0942			0.15792	0.038
021	000	1046	1047	6967.90523	8.01E-04	1.1257E-24	5.5E-26	1581.3357	0.377		0.694					
101	000	854	955	6969.06962	1.27E-04	1.3969E-23	1.4E-25	1474.9803	0.3355	0.0367	0.2391	0.1054			0.29181	0.047
021	000	423	404	6969.32087		2.0776E-23	1.0E-24	222.0528	0.46		0.694					
111	010	744	845	6969.39153	2.82E-04	7.3803E-26	1.0E-27	2764.6973	0.333		0.694					
120	000	643	634	6970.14661		1.3002E-23	6.5E-25	648.9787	0.44		0.694					
021	000	515	414	6971.30229	5.15E-05	1.1712E-21	3.2E-24	224.8384	0.4656	0.0039	0.7238	0.0208	1.26E-01	2.11E-03	0.09055	0.011
200	000	414	523	6971.33472		1.0968E-22	1.6E-24	446.5107	0.45		0.694					
120	000	441	432	6971.57797		1.8244E-23	3.8E-24	382.5169	0.412		0.694					
021	000	505	404	6971.59156	1.29E-04	3.8586E-22	4.6E-24	222.0528	0.4706	0.0091	0.8169	0.0575			0.12614	0.026
101	000	1029	11210	6971.60321		2.0728E-23	8.8E-26	1525.135	0.281		0.694					
200	000	817	928	6971.80289		1.9787E-23	2.4E-25	1080.3853	0.33		0.694					
101	000	1019	11110	6972.05394	2.75E-05	6.4852E-23	1.3E-25	1524.8473	0.2922	0.0083	0.3968	0.0279			0.14045	0.014

101	000	11011	12012	6972.74061	8.91E-05	2.0426E-23	3.7E-26	1557.8436	0.3847	0.0057	0.9199	0.0011			0.02011	0.015	
101	000	11111	12112	6972.74762		6.1336E-23	1.1E-25	1557.847	0.3847	0.0057	0.9199	0.0011			0.02011	0.015	bcdf
101	000	735	752	6972.80986		1.7441E-23	3.2E-25	1059.8353	0.33		0.694						
200	000	909	10110	6972.84512		7.0022E-23	3.5E-25	1114.5493	0.3054	0.0125	0.5773	0.0025			0.08962	0.036	
200	000	919	10010	6972.92082		2.4964E-23	1.2E-25	1114.5312	0.3054	0.0125	0.5773	0.0025			0.08962	0.036	bcdf
101	000	937	1038	6973.66499		7.6602E-23	1.6E-25	1446.1279	0.3521	0.0093	0.5429	0.027			0.12408	0.014	
101	000	844	945	6974.61702		9.3151E-23	2.7E-25	1360.235	0.3684	0.0097	0.5538	0.028			0.12734	0.016	
101	000	927	1028	6974.6633		3.0176E-23	2.1E-25	1437.9678	0.3329	0.0224	0.4916	0.0689			0.17248	0.037	
120	000	845	836	6974.73829		3.5705E-24	3.1E-25	1006.1157	0.335		0.694						
200	000	827	918	6975.03665	9.97E-05	5.3346E-23	4.3E-25	1079.0792	0.3392	0.0206	0.378	0.0661			0.18186	0.043	
101	000	514	633	6975.4241		2.021E-23	6.5E-25	661.5489	0.47		0.694						
021	000	615	616	6977.58841		2.8042E-23	8.6E-25	447.2523	0.395		0.694						
021	000	954	955	6977.78043		1.4061E-24	7.5E-26	1474.9803	0.3		0.694						
021	000	854	853	6977.819		3.4842E-24	1.5E-25	1255.9115	0.365		0.694						
021	000	1055	1056	6977.89414		1.3606E-24	3.4E-26	1718.7185	0.31		0.694						
031	010	817	716	6978.45736		1.9858E-25	5.1E-27	2309.73	0.352		0.694						
101	000	12012	12211	6978.49814		1.1569E-24	2.9E-26	1774.7502	0.235		0.694						
101	000	835	936	6978.6122	8.25E-05	1.1372E-22	7.3E-25	1282.9188	0.4447	0.0099	0.7462	0.0247			0.01817	0.017	
101	000	12112	12111	6978.61231		4.1572E-25	1.0E-26	1774.6154	0.265		0.694						b
021	000	853	854	6978.62887		6.1631E-24	7.2E-25	1255.1666	0.333		0.694						
200	000	11110	1129	6979.29951		1.6934E-24	3.7E-26	1690.6636	0.275		0.694						
021	000	752	753	6979.74033	2.76E-04	1.2505E-23	2.6E-25	1059.6466	0.352		0.694						
021	000	753	752	6979.84675	1.32E-04	2.722E-23	2.5E-25	1059.8353	0.286		0.694						
021	000	652	651	6979.98721		3.1936E-23	3.9E-25	888.6326	0.33		0.694						
120	000	918	827	6979.99627		1.1971E-25	1.5E-27	885.6002	0.333		0.694						b
200	000	423	532	6980.5407	4.75E-05	3.9684E-22	1.5E-24	508.812	0.45	0.0072	0.6781	0.0275			0.13625	0.019	
021	000	651	652	6980.75506	7.94E-05	9.5629E-23	6.5E-25	888.5986	0.2317	0.0127	0.4901	0.0657			0.03606	0.051	
021	000	413	312	6981.11281	3.75E-05	1.0606E-21	3.3E-24	173.3658	0.4748	0.0044	0.8722	0.0252			0.08802	0.012	
021	000	524	505	6981.14118		4.1884E-23	1.8E-24	325.3479	0.391		0.694						
021	000	551	550	6981.52762		2.3692E-22	1.5E-24	742.0762	0.2372	0.0079	0.4074	0.0392	-3.37E-02	6.00E-03	0.06894	0.029	
021	000	550	551	6981.55237		7.7681E-23	1.4E-24	742.073	0.2257	0.0248	0.6459	0.1333			0.06029	0.098	
040	000	1056	1029	6983.17972		1.918E-24	1.3E-25	1293.6337	0.298		0.694						
101	000	845	946	6983.30656	8.44E-05	3.0586E-23	2.1E-25	1340.8845	0.3522	0.0253	0.6178	0.08			0.1063	0.046	
111	010	817	918	6983.3661		1.6953E-25	1.5E-27	2688.0796	0.315		0.694						
200	000	523	634	6983.66764	5.95E-05	2.5457E-22	1.2E-24	648.9787	0.4873	0.0100	0.8365	0.0327			0.1228	0.025	
101	000	761	862	6984.29946		7.3488E-24	1.3E-25	1411.6418	0.25		0.694						
101	000	762	863	6984.33504	1.02E-04	2.3497E-23	2.1E-25	1411.6113	0.2695	0.0250	0.3833	0.0904			0.1447	0.047	
200	000	331	440	6984.81787	1.01E-04	1.6413E-22	1.5E-24	488.1342	0.3802	0.0147	0.668	0.0673			0.07203	0.046	
200	000	330	441	6984.95323	3.82E-05	5.1591E-22	1.7E-24	488.1077	0.3956	0.0056	0.59	0.0242			0.11987	0.016	
021	000	423	322	6985.07193	8.40E-05	2.5887E-22	1.9E-24	206.3014	0.4029	0.0114	0.7304	0.0759			0.05956	0.036	
021	000	616	515	6987.08508	7.76E-05	2.803E-22	2.3E-24	326.6255	0.4033	0.0125	0.6597	0.058			0.12037	0.033	
021	000	606	505	6987.14402	3.25E-05	8.435E-22	2.6E-24	325.3479	0.4109	0.0048	0.6197	0.0231			0.12455	0.014	
111	010	919	10110	6987.46481		1.6139E-25	1.3E-27	2705.1392	0.298		0.694						

021	000	946	1029	6988.30659	2.10E-04	9.5425E-24	1.3E-25	1293.6337	0.35		0.694				
021	000	422	321	6993.26295	4.17E-05	6.6762E-22	2.2E-24	212.1564	0.4471	0.0055	0.7047	0.0316		0.1233	0.016
200	000	716	827	6994.9034	6.71E-05	1.2965E-22	6.9E-25	885.6002	0.3496	0.0121	0.6256	0.044		0.07705	0.034
101	000	633	652	6995.93845		7.1774E-24	3.9E-25	888.5986	0.385		0.694				
200	000	808	919	6997.51242	1.68E-04	4.423E-23	6.3E-25	920.2098	0.3209	0.0314	0.6014	0.1206		0.08437	0.090
101	000	918	1019	6997.65415	5.14E-05	6.0543E-23	2.4E-25	1293.0173	0.3033	0.0134	0.4278	0.0457		0.11825	0.027
200	000	818	909	6997.79013	5.26E-05	1.5837E-22	6.8E-25	920.168	0.3336	0.0097	0.4762	0.0345		0.12994	0.025
101	000	928	1029	6997.9935	2.26E-05	1.6716E-22	2.7E-25	1293.6337	0.3079	0.0059	0.472	0.0199		0.10134	0.012
101	000	10010	11011	6998.17016	3.22E-05	1.7517E-22	4.1E-25	1327.1096	0.2811	0.0055	0.3752	0.0193		0.08644	0.012
101	000	752	853	6998.19624		2.6688E-23	4.2E-25	1255.9115	0.333		0.694				
101	000	10110	11111	6998.23909	5.61E-05	5.8173E-23	3.0E-25	1327.1165	0.2717	0.0133	0.3637	0.0485		0.13549	0.028
101	000	753	854	6998.8096	3.84E-05	9.5397E-23	2.7E-25	1255.1666	0.3334	0.0100	0.4378	0.0316		0.17033	0.018
021	000	836	919	6998.99018		9.1986E-24	3.6E-25	920.2098	0.33		0.694				
120	000	432	321	6999.59079	2.06E-04	1.1161E-22	2.0E-24	212.1564	0.5154	0.0346	0.9162	0.1664		0.21074	0.074
101	000	836	937	6999.9765	4.02E-05	6.5763E-23	1.9E-25	1216.2311	0.36		0.694				
101	000	826	927	7000.64192	2.01E-05	2.6825E-22	3.7E-25	1201.921	0.4197	0.0055	0.6845	0.0147		0.11029	0.009
200	000	845	936	7000.80231	5.23E-05	6.3727E-23	2.5E-25	1282.9188	0.4243	0.0161	0.6421	0.042		0.15298	0.024
200	000	726	817	7001.57273	1.42E-04	3.5179E-23	4.2E-25	882.8903	0.357		0.694				
101	000	726	743	7001.6848		1.4184E-23	3.6E-25	931.237	0.43		0.694				
200	000	422	533	7001.84401	1.29E-04	1.4511E-22	1.8E-24	503.9681	0.4947	0.0228	0.7606	0.0713		0.15291	0.052
021	000	707	606	7001.9245	4.34E-05	1.953E-22	6.1E-25	446.6966	0.4003	0.0057	0.5334	0.0025		0.17551	0.015
021	000	717	616	7001.9489	4.34E-05	5.5966E-22	1.7E-24	447.2523	0.4003	0.0057	0.5334	0.0025		0.17551	0.015 abcdf
111	010	633	734	7002.23027		6.7074E-26	3.0E-27	2462.8752	0.352		0.694				
002	000	716	845	7003.10452		2.2505E-23	2.2E-25	1122.7085	0.4		0.694				
101	000	313	432	7003.73115	1.72E-04	1.246E-22	1.9E-24	382.5169	0.5298	0.0301	0.6095	0.0914		0.24934	0.058
021	000	514	413	7004.22718	8.93E-05	2.7587E-22	2.0E-24	275.4971	0.4972	0.0136	0.8102	0.0598		0.15075	0.034
021	000	220	101	7004.75508		1.4291E-23	1.3E-24	23.7944	0.47		0.694				
021	000	524	423	7006.12704	3.97E-05	7.0631E-22	2.2E-24	300.3623	0.4459	0.0054	0.6544	0.0261		0.13835	0.015
101	000	835	854	7006.36405		7.2051E-24	1.5E-25	1255.1666	0.396		0.694				
101	000	743	844	7007.03542	4.44E-05	7.4161E-23	2.3E-25	1131.7755	0.32		0.694				
200	000	909	918	7008.315	2.33E-04	1.4839E-23	2.4E-25	1079.0792	0.327		0.694				
200	000	955	1046	7008.39679		1.4836E-24	6.3E-26	1616.4531	0.298		0.694				
101	000	413	532	7008.40005	1.17E-04	8.3466E-23	1.2E-24	508.8121	0.47		0.694				
101	000	734	835	7010.54736	4.98E-05	1.2304E-22	4.7E-25	1050.1576	0.4001	0.0121	0.7695	0.0376		0.11464	0.025
111	010	551	652	7011.13838		6.6785E-26	2.1E-27	2552.8572	0.371		0.694				
111	010	808	909	7011.19393		4.0225E-25	2.6E-27	2512.2825	0.283		0.694				
111	010	818	919	7011.23336		1.3567E-25	2.5E-27	2512.3752	0.315		0.694				
021	000	726	707	7012.1068		1.3634E-23	7.5E-25	586.2435	0.37		0.694				
101	000	744	845	7012.69443	2.82E-05	2.0446E-22	4.1E-25	1122.7083	0.3595	0.0067	0.6108	0.0215		0.09909	0.014
120	000	533	422	7012.84136		4.6791E-23	1.1E-24	315.7795	0.425		0.694				
021	000	1064	1065	7013.14817		8.0061E-25	2.2E-26	1874.9727	0.298		0.694				
021	000	432	331	7013.172	1.96E-04	1.1376E-22	2.0E-24	285.2193	0.4344	0.0298	0.4643	0.1259		0.18465	0.073
021	000	431	330	7014.04199	7.39E-05	3.321E-22	2.1E-24	285.4186	0.425	0.0105	0.6677	0.0518		0.10176	0.030

021	000	937	10110	7014.11637	3.33E-04	1.0223E-23	2.2E-25	1114.5493	0.27		0.694					
101	000	660	761	7014.46039		4.0425E-23	1.3E-25	1216.1945	0.3		0.694					
101	000	661	762	7014.46515		1.3478E-23	4.5E-26	1216.1897	0.3		0.694					bcdf
200	000	322	431	7014.56482	9.12E-05	2.4382E-22	1.9E-24	383.8425	0.4603	0.0139	0.7617	0.0575		0.14667	0.036	
200	000	615	726	7015.84058	9.21E-05	8.557E-23	6.8E-25	709.6082	0.411		0.694					
021	000	808	707	7015.91991		3.2201E-22	1.1E-24	586.2435	0.3348	0.0079	0.4854	0.03		0.1295	0.023	
021	000	818	717	7015.9649		1.0573E-22	3.8E-25	586.4792	0.3348	0.0079	0.4854	0.03		0.1295	0.023	bcdf
021	000	863	862	7016.12935		3.2742E-24	2.8E-26	1411.6418	0.333		0.694					
021	000	862	863	7016.182		9.6396E-24	8.3E-26	1411.6113	0.26		0.694					b
021	000	762	761	7017.21229		2.9615E-23	1.3E-25	1216.1945	0.23		0.694					
021	000	761	762	7017.22204		9.2321E-24	4.1E-26	1216.1897	0.23		0.694					bcd
101	000	404	523	7017.92654		9.371E-23	1.2E-24	446.5107	0.5		0.694					
021	000	661	660	7017.95395		2.7099E-23	1.0E-25	1045.0583	0.371		0.694					
021	000	660	661	7017.95436		8.1255E-23	3.1E-25	1045.0577	0.371		0.694					bcdf
200	000	707	818	7021.81134	4.21E-05	3.167E-22	1.0E-24	744.1627	0.3651	0.0069	0.5735	0.0259		0.11063	0.019	
200	000	717	808	7022.0805	1.12E-04	9.9306E-23	9.3E-25	744.0637	0.3061	0.0178	0.748	0.0846		0.00077	0.066	
200	000	313	422	7022.47145		9.767E-23	1.2E-24	315.7795	0.44		0.694					
101	000	817	918	7022.7091		4.5587E-22	6.4E-25	1079.0792	0.3148	0.0043	0.5439	0.0025		0.02652	0.012	
200	000	321	432	7022.72122		6.0668E-22	3.7E-24	382.5169	0.4655	0.0096	0.354	0.0538		0.16682	0.025	
101	000	827	928	7022.72849		1.4269E-22	2.0E-25	1080.3853	0.3148	0.0043	0.5439	0.0025		0.02652	0.012	bcdef
021	000	817	818	7023.18064		5.9613E-24	7.8E-25	744.1627	0.333		0.694					
021	000	523	422	7023.2083	1.56E-04	1.6127E-22	2.4E-24	315.7795	0.4073	0.0211	0.7847	0.1049		0.06623	0.060	
101	000	909	10010	7023.32352	3.71E-05	1.4498E-22	4.2E-25	1114.5312	0.265	0.0077	0.362	0.0309		0.10617	0.020	
101	000	919	10110	7023.45825	1.70E-05	4.2663E-22	5.1E-25	1114.5493	0.2755	0.0034	0.3858	0.0136		0.0877	0.009	
101	000	725	826	7025.04848	4.56E-05	1.6973E-22	5.8E-25	982.9116	0.4229	0.0102	0.7982	0.0314		0.07278	0.023	
021	000	615	514	7025.38326	4.59E-05	5.3641E-22	1.9E-24	399.4575	0.4374	0.0065	0.7482	0.0295		0.1148	0.019	
021	000	735	716	7025.97109		1.0167E-23	6.4E-25	704.214	0.41		0.694					
120	000	634	523	7026.0151		3.0859E-23	1.0E-24	446.5107	0.44		0.694					
021	000	625	524	7026.27279	1.33E-04	1.5233E-22	1.8E-24	416.2087	0.4129	0.0199	0.5611	0.0806		0.14968	0.054	
101	000	735	836	7026.52917	2.08E-05	4.4159E-22	6.3E-25	1006.1157	0.3842	0.0044	0.6012	0.0138		0.10768	0.010	
101	000	651	752	7028.1408	3.64E-05	1.7369E-22	4.8E-25	1059.8353	0.2955	0.0074	0.4279	0.028		0.1223	0.018	
101	000	652	753	7028.31123		5.6819E-23	2.7E-25	1059.6466	0.3		0.694					
021	000	919	818	7028.7685	7.96E-05	1.3773E-22	9.8E-25	744.1627	0.2471	0.0122	0.2217	0.0575		0.18262	0.040	
200	000	625	716	7029.08939	1.11E-04	1.6253E-22	1.8E-24	704.214	0.4086	0.0166	0.5851	0.0519		0.09544	0.040	
021	000	909	808	7029.12045		5.5658E-23	1.6E-24	744.0637	0.2733	0.0369	0.0794	0.1323		0.23879	0.095	
101	000	11210	1129	7029.57168	2.67E-04	2.6036E-24	3.8E-26	1690.6636	0.264		0.694					
002	000	1046	1157	7030.44377		1.0772E-25	1.4E-26	1985.7842	0.35		0.694					
101	000	14114	14113	7030.68603		1.8008E-29	4.1E-30	4172.1523	0.235		0.694					
101	000	14113	14114	7030.68603		5.9993E-30	1.4E-30	4172.1523	0.235		0.694					
002	000	717	826	7031.23806	1.24E-04	5.8884E-23	5.7E-25	982.9116	0.4208	0.0275	0.7244	0.0835		0.12585	0.058	
040	000	945	818	7031.47378		2.1686E-23	6.2E-25	744.1627	0.2698	0.0628	0.6441	0.2362		0.04549	0.215	
101	000	10010	1029	7031.64593		1.0853E-23	1.3E-25	1293.6337	0.27		0.694					
101	000	10110	1019	7032.33879		4.8879E-24	2.1E-25	1293.0173	0.255		0.694					

200	000	818	827	7032.3603	1.90E-04	3.6164E-23	5.4E-25	885.6002	0.36		0.694					
111	010	625	726	7032.40889		2.4577E-25	4.7E-27	2318.5398	0.352		0.694					
021	000	753	836	7033.56679		1.8559E-23	3.0E-25	1006.1157	0.3		0.694					
002	000	753	862	7034.44734		6.9609E-25	1.2E-25	1411.6418	0.333		0.694					
200	000	514	625	7034.47468	5.08E-05	4.4555E-22	1.8E-24	552.9114	0.4616	0.0074	0.7631	0.0266		0.12625	0.019	
120	000	955	946	7034.78917		1.2794E-25	1.3E-25	1340.8845	0.315		0.694					
200	000	808	817	7034.83715	6.06E-04	9.9454E-24	4.4E-25	882.8903	0.427		0.694					
021	000	533	432	7036.51449	6.03E-05	3.7528E-22	1.9E-24	382.5169	0.3948	0.0086	0.5171	0.039		0.15803	0.024	
200	000	743	752	7036.75734	5.17E-04	7.1538E-24	2.7E-25	1059.8353	0.345		0.694					
200	000	643	652	7038.39576		9.9016E-24	6.1E-25	888.5986	0.4		0.694					
101	000	524	541	7038.4254		3.0883E-23	2.8E-24	610.3411	0.391		0.694					
101	000	642	743	7038.43735	3.62E-05	4.7221E-22	1.5E-24	931.237	0.353	0.0047	0.5335	0.0164		0.12484	0.012	
200	000	918	927	7038.93855		1.4512E-23	1.8E-25	1201.921	0.345		0.694					
021	000	532	431	7039.15797	1.64E-04	1.2449E-22	1.8E-24	383.8425	0.3842	0.0236	0.351	0.0981		0.1245	0.068	
200	000	634	725	7039.27942	1.35E-04	8.8604E-23	9.9E-25	782.4098	0.4646	0.0261	0.6091	0.072		0.21415	0.052	
101	000	643	744	7039.55539	6.76E-05	1.274E-22	6.7E-25	927.7439	0.3866	0.0133	0.5289	0.0418		0.16269	0.029	
101	000	212	331	7040.00847	2.85E-04	8.7834E-23	2.1E-24	285.2193	0.5684	0.0501	0.6093	0.1558		0.2462	0.092	
200	000	954	1047	7040.44802	2.09E-04	4.5802E-24	5.6E-26	1581.3357	0.36		0.694					
021	000	10110	919	7041.51507		2.6988E-23	1.3E-25	920.2098	0.235		0.694					
021	000	10010	909	7041.52984		7.8707E-23	3.7E-25	920.168	0.283		0.694					b
101	000	633	734	7042.1806		9.0183E-22	1.1E-24	842.3565	0.3998	0.0033	0.6791	0.0113		0.12641	0.008	
200	000	541	550	7042.41613	4.75E-04	1.3478E-23	5.8E-25	742.0762	0.333		0.694					
200	000	744	835	7043.43037	1.24E-04	3.1931E-23	2.9E-25	1050.1576	0.425		0.694					
200	000	221	330	7044.00112	3.33E-05	1.0157E-21	2.5E-24	285.4186	0.47	0.0043	0.7529	0.0219		0.09853	0.013	
021	000	716	615	7044.83557	1.72E-04	1.0117E-22	1.4E-24	542.9058	0.3899	0.0245	0.7129	0.1054		0.03474	0.079	
021	000	1275	1276	7045.01784		5.3879E-26	1.6E-27	2612.7991	0.265		0.694					
200	000	606	717	7045.22679	8.67E-05	1.8613E-22	1.4E-24	586.4792	0.3666	0.0130	0.6629	0.0559		0.08579	0.040	
021	000	726	625	7045.43871	6.03E-05	3.0184E-22	1.5E-24	552.9114	0.3892	0.0090	0.5689	0.0363		0.13295	0.026	
200	000	616	707	7045.84398	3.47E-05	5.6869E-22	1.5E-24	586.2435	0.4022	0.0053	0.5547	0.0206		0.15542	0.014	
031	010	937	836	7046.18702		4.1283E-26	1.5E-27	2630.1924	0.333		0.694					
200	000	220	331	7046.40293	9.85E-05	2.6141E-22	2.1E-24	285.2193	0.4993	0.0148	0.7216	0.0615		0.14902	0.036	
200	000	836	845	7046.80869		2.2787E-23	2.2E-25	1122.7083	0.333		0.694					
101	000	716	817	7047.09539	3.14E-05	3.5259E-22	8.1E-25	882.8903	0.3931	0.0058	0.6043	0.0193		0.11397	0.014	
101	000	726	827	7047.3214	1.59E-05	9.6695E-22	1.0E-24	885.6002	0.3549	0.0028	0.5058	0.0103		0.10051	0.007	
200	000	827	836	7048.00069		3.4203E-23	5.4E-25	1006.1157	0.3548	0.0395	0.4352	0.1285		0.19451	0.083	
021	000	624	523	7048.8035	5.71E-05	3.9005E-22	1.8E-24	446.5107	0.4574	0.0088	0.74	0.0349		0.16208	0.022	
101	000	1019	1038	7050.77384		6.7879E-24	8.6E-26	1446.1279	0.323		0.694					
200	000	413	524	7051.56336	1.00E-04	2.2977E-22	1.9E-24	416.2087	0.5304	0.0163	0.741	0.0536		0.17489	0.036	
021	000	652	735	7051.92559	8.10E-05	1.3381E-22	8.7E-25	816.6942	0.3816	0.0143	0.5774	0.0491		0.13812	0.036	
021	000	872	871	7053.09553		2.7621E-24	1.6E-26	1590.6906	0.333		0.694					
021	000	871	872	7053.0966		8.2872E-24	4.7E-26	1590.6901	0.198		0.694					b
021	000	11111	10110	7053.13941		3.3368E-23	3.5E-25	1114.5493	0.24		0.694					
021	000	11011	10010	7053.16775	4.54E-04	1.0464E-23	2.5E-25	1114.5312	0.244		0.694					

101	000	634	735	7053.76398	6.34E-05	1.7211E-22	8.7E-25	816.6942	0.3595	0.0109	0.6551	0.0418			0.08205	0.031	
021	000	770	771	7053.93826		8.0555E-24	3.5E-26	1394.8141	0.352		0.694						
021	000	771	770	7053.93875		2.4163E-23	1.0E-25	1394.8141	0.352		0.694						bc
101	000	624	725	7054.23272	1.48E-05	1.4661E-21	1.5E-24	782.4098	0.4487	0.0027	0.7706	0.0092			0.08606	0.007	
101	000	515	532	7055.86056		3.8751E-23	9.3E-25	508.812	0.49		0.694						
101	000	211	330	7056.38424		1.1207E-23	1.1E-24	285.4186	0.43		0.694						
200	000	717	726	7056.53615		2.763E-23	6.3E-25	709.6082	0.4		0.694						
101	000	550	651	7057.33564	4.67E-05	7.3508E-23	1.7E-25	888.6326	0.2938	0.0007	0.5748	0.0019			0.11085	0.016	
101	000	551	652	7057.36808	4.67E-05	2.1453E-22	4.8E-25	888.5986	0.2938	0.0007	0.5748	0.0019			0.11085	0.016	abcdf
101	000	909	928	7057.47024		9.9718E-24	2.5E-25	1080.3853	0.325		0.694						
200	000	735	744	7057.54153		1.721E-23	3.8E-25	927.7439	0.378		0.694						
111	010	606	707	7057.68743		1.5812E-24	8.0E-27	2180.6428	0.37		0.694						
200	000	524	615	7058.40349		6.4725E-23	8.8E-25	542.9058	0.458		0.694						
101	000	919	918	7058.92867		2.6339E-23	2.5E-25	1079.0792	0.305		0.694						
021	000	634	533	7059.24404	1.83E-04	9.6454E-23	1.5E-24	503.9681	0.4131	0.0286	0.5798	0.1087			0.17118	0.074	
002	000	606	735	7061.1766	3.48E-04	1.8804E-23	5.1E-25	816.6942	0.391		0.694						
200	000	707	716	7061.76038	9.49E-05	8.4022E-23	6.9E-25	704.214	0.435		0.694						
021	000	817	716	7063.1294	8.01E-05	1.6499E-22	1.1E-24	704.214	0.3539	0.0125	0.5832	0.0502			0.0953	0.038	
021	000	827	726	7063.68266	1.24E-04	5.3662E-23	6.4E-25	709.6082	0.345		0.694						
021	000	12112	11111	7064.01253		3.617E-24	1.2E-25	1327.1165	0.25		0.694						
021	000	12012	11011	7064.08387	1.62E-04	1.2913E-23	1.2E-25	1327.1096	0.25		0.694						
101	000	422	441	7064.25675	2.03E-04	4.9989E-23	9.6E-25	488.1077	0.44		0.694						
200	000	634	643	7064.96451		9.449E-23	1.1E-24	756.7247	0.4		0.694						
021	000	633	532	7064.98926	9.27E-05	2.8071E-22	2.4E-24	508.812	0.4412	0.0121	0.6501	0.0425			0.15811	0.028	
200	000	212	321	7065.53163	4.98E-05	6.1142E-22	2.3E-24	212.1564	0.4946	0.0067	0.8691	0.036			0.10939	0.019	
101	000	303	422	7066.50865		7.525E-23	1.2E-24	315.7795	0.488		0.694						
101	000	523	542	7067.14506		3.6105E-23	7.7E-25	610.1144	0.446		0.694						
111	010	422	523	7067.55025	1.29E-04	1.8144E-24	1.2E-26	2053.9685	0.375		0.694						
200	000	505	616	7067.69482	2.92E-05	9.29E-22	2.1E-24	447.2523	0.4473	0.0042	0.6536	0.0184			0.14483	0.012	
200	000	726	735	7067.7692		2.6606E-23	5.2E-25	816.6942	0.34		0.694						
021	000	542	441	7068.26585	1.26E-04	1.327E-22	1.5E-24	488.1077	0.3199	0.0177	0.4568	0.0882			0.10037	0.059	
021	000	541	440	7068.39236	1.77E-04	4.4676E-23	9.2E-25	488.1342	0.334		0.694						
101	000	541	642	7068.5246	4.98E-05	2.5769E-22	1.1E-24	757.7801	0.3555	0.0085	0.5423	0.0317			0.13096	0.023	
200	000	312	423	7068.6113	3.59E-05	8.7856E-22	2.7E-24	300.3623	0.4868	0.0055	0.8066	0.0247			0.12139	0.015	
120	000	441	330	7068.67628		1.3334E-23	1.2E-24	285.4186	0.33		0.694						
101	000	542	643	7069.09472	2.18E-05	7.4198E-22	1.2E-24	756.7247	0.349	0.0035	0.5203	0.0143			0.11213	0.010	
200	000	515	606	7069.21686	7.17E-05	2.9236E-22	1.9E-24	446.6966	0.4324	0.0113	0.657	0.0459			0.1385	0.030	
200	000	817	826	7069.27661		1.363E-23	3.6E-25	982.9116	0.37		0.694						
101	000	615	716	7070.7844	2.51E-05	2.1752E-21	2.1E-24	704.214	0.4517	0.0023	0.6944	0.0082	-1.21E-01	5.80E-04	0.09518	0.006	
000	000	000	000	0	0.00E+00	0	0.0E+00	0	0	0.0000	0	0		0.00E+00	0.08685	0.000	
000	000	000	000	0	0.00E+00	0	0.0E+00	0	0	0.0000	0	0		0.00E+00	0.08685	0.000	
101	000	625	726	7071.61119	2.75E-05	6.3463E-22	1.3E-24	709.6082	0.4051	0.0045	0.6269	0.0167			0.10718	0.012	
021	000	725	624	7073.52373		7.3276E-23	8.0E-25	602.7735	0.46		0.694						

101	000	532	633	7073.77789	3.03E-05	5.8115E-22	1.3E-24	661.5489	0.4158	0.0049	0.6805	0.0187		0.14853	0.013	
101	000	523	624	7074.48586	4.09E-05	4.7294E-22	1.5E-24	602.7735	0.5107	0.0071	0.6706	0.0215		0.22984	0.014	
002	000	514	643	7076.67076		2.3552E-23	5.8E-25	756.7247	0.45		0.694					
200	000	927	936	7078.86791	2.06E-04	1.1325E-23	1.6E-25	1282.9188	0.43		0.694					
200	000	616	625	7079.17597	1.04E-04	1.6324E-22	1.4E-24	552.9114	0.4052	0.0155	0.6558	0.0623		0.09694	0.045	
101	000	826	845	7079.85512		1.9258E-23	2.3E-25	1122.7083	0.42		0.694					
200	000	532	541	7080.09319		5.7506E-23	3.3E-24	610.3411	0.391		0.694					
200	000	432	441	7080.09684		6.1986E-23	4.0E-24	488.1077	0.412		0.694					
111	010	515	616	7080.27839		2.5642E-24	1.3E-26	2042.7533	0.371		0.694					
101	000	533	634	7080.57464	1.79E-05	1.7351E-21	2.4E-24	648.9787	0.4321	0.0027	0.6435	0.0106		0.1214	0.007	
021	000	918	817	7080.61199		2.5358E-23	6.9E-25	882.8903	0.333		0.694					
200	000	431	440	7080.75691		2.2309E-23	8.8E-25	488.1342	0.385		0.694					
021	000	928	827	7081.07837		7.9328E-23	4.4E-25	885.6002	0.305		0.694					
200	000	633	642	7081.13092		2.0172E-23	6.0E-25	757.7801	0.43		0.694					
021	000	735	634	7081.20649	8.45E-05	1.7712E-22	1.3E-24	648.9787	0.408	0.0137	0.6652	0.0512		0.1095	0.038	
111	010	423	524	7081.27766		6.3899E-25	1.4E-26	2024.1523	0.391		0.694					
200	000	936	945	7081.34689		9.8594E-24	1.6E-25	1360.235	0.384		0.694					
101	000	10101	10100	7081.35187		3.9593E-25	1.8E-27	2701.8879	0.6		0.694					
101	000	808	827	7082.25233	7.25E-05	7.201E-23	4.5E-25	885.6002	0.37		0.694					
101	000	414	431	7082.39304		2.093E-23	1.0E-24	383.8425	0.447		0.694					
200	000	734	743	7083.33709		3.7829E-23	4.0E-25	931.237	0.46		0.694					
200	000	625	634	7084.32451	9.60E-05	1.6119E-22	1.3E-24	648.9787	0.4861	0.0168	0.6321	0.0492		0.21123	0.035	
200	000	643	734	7084.63811	8.49E-05	1.2442E-22	8.2E-25	842.3565	0.4682	0.0164	0.7697	0.0492		0.14091	0.036	
101	000	818	817	7085.00831	2.05E-04	2.4636E-23	4.4E-25	882.8903	0.384		0.694					
021	000	881	880	7085.25152		2.779E-24	8.9E-27	1789.0426	0.333		0.694					
021	000	880	881	7085.25153		8.336E-24	2.7E-26	1789.0426	0.177		0.694					b
200	000	533	624	7085.87615	3.35E-05	5.8209E-22	1.5E-24	602.7735	0.4741	0.0054	0.8069	0.0199		0.13688	0.014	
200	000	211	322	7086.90615	7.19E-05	3.5301E-22	2.1E-24	206.3014	0.466	0.0103	0.7675	0.057		0.14575	0.027	
200	000	606	615	7088.80077	1.52E-04	6.1413E-23	8.8E-25	542.9058	0.45		0.694					
200	000	404	515	7088.97339	5.74E-05	4.3997E-22	2.0E-24	326.6255	0.4952	0.0083	0.8149	0.0373		0.12597	0.022	
101	000	928	927	7089.70644	1.26E-04	2.1834E-23	1.9E-25	1201.921	0.356		0.694					
200	000	423	514	7089.89584	1.56E-04	1.4411E-22	1.9E-24	399.4575	0.5981	0.0285	0.6242	0.076		0.26483	0.049	
200	000	743	836	7090.47821		4.8139E-23	3.2E-25	1006.1157	0.37		0.694					
021	000	734	633	7090.99792		5.515E-23	7.0E-25	661.5489	0.442		0.694					
111	010	734	651	7091.42788		1.2436E-27	6.3E-27	2552.8796	0.371		0.694					
021	000	15115	14114	7091.43264		4.0322E-25	3.2E-26	2073.5137	0.235		0.694					
021	000	643	542	7091.85248		4.4151E-23	7.2E-25	610.1144	0.324		0.694					
021	000	642	541	7092.37107	1.08E-04	1.3416E-22	1.3E-24	610.3411	0.3521	0.0167	0.5706	0.0704		0.12667	0.050	
200	000	414	505	7092.49487	2.76E-05	1.1786E-21	2.4E-24	325.3479	0.4809	0.0037	0.8042	0.0189		0.12063	0.011	
200	000	752	845	7093.24528		2.1544E-23	2.2E-25	1122.7083	0.29		0.694					
101	000	514	615	7094.0672	2.02E-05	1.3866E-21	2.0E-24	542.9058	0.4804	0.0030	0.7871	0.0125		0.1154	0.008	
000	000	000	000	0	0.00E+00	0	0.0E+00	0	0	0.0000	0	0	0.00E+00	0.11627	0.000	
101	000	616	717	7094.73373	2.64E-05	1.264E-21	2.8E-24	586.4792	0.3783	0.0037	0.4978	0.0154		0.1034	0.011	

101	000	817	836	7095.67274		5.5807E-23	3.2E-25	1006.1157	0.315		0.694				
000	000	000	000	0	0.00E+00	0	0.0E+00	0	0	0.0000	0	0	0.00E+00	0.09374	0.000
021	000	826	725	7096.84154	1.09E-04	1.1031E-22	9.6E-25	782.4098	0.5047	0.0209	0.6398	0.0548		0.21908	0.040
111	010	321	422	7097.27248		8.8296E-25	1.9E-26	1922.9004	0.412		0.694				
200	000	524	533	7097.34117		7.6389E-23	1.3E-24	503.9681	0.33		0.694				
101	000	440	541	7097.37712		8.6721E-22	2.9E-24	610.3411	0.3672	0.0043	0.4941	0.0167		0.1501	0.011
021	000	1019	918	7097.38673		3.3544E-23	6.5E-25	1079.0792	0.315		0.694				
101	000	441	542	7097.5244		2.8624E-22	1.3E-24	610.1144	0.3503	0.0082	0.496	0.0349		0.14396	0.024
021	000	1029	928	7097.71344		1.1051E-23	2.4E-25	1080.3853	0.266		0.694				
200	000	716	725	7098.09433	1.08E-04	1.0583E-22	9.1E-25	782.4098	0.4283	0.0187	0.7902	0.065		0.08798	0.050
200	000	515	524	7099.7043	1.90E-04	1.0317E-22	1.7E-24	416.2087	0.4893	0.0308	0.6974	0.1129		0.18442	0.070
200	000	111	220	7100.6436	8.32E-05	3.1959E-22	2.2E-24	136.1639	0.4718	0.0112	0.9539	0.0764		0.07683	0.032
200	000	826	835	7100.67534		1.484E-23	3.1E-25	1050.1576	0.333		0.694				
101	000	313	330	7100.82991		6.2742E-23	1.1E-24	285.4186	0.465		0.694				
021	000	836	735	7102.50599		2.7139E-23	4.8E-25	816.6942	0.34		0.694				
000	000	000	000	0	0.00E+00	0	0.0E+00	0	0	0.0000	0	0	0.00E+00	0.09994	0.000
101	000	202	321	7105.76142	7.74E-05	3.3E-22	2.0E-24	212.1564	0.4881	0.0116	0.8649	0.0219		0.16881	0.027
000	000	000	000	0	0.00E+00	0	0.0E+00	0	0	0.0000	0	0	0.00E+00	0.09625	0.000
101	000	707	726	7105.93991		5.4938E-23	1.3E-24	709.6082	0.4166	0.0443	0.4075	0.1258		0.21681	0.094
200	000	423	432	7106.83651	6.38E-05	3.3146E-22	1.8E-24	382.5169	0.4276	0.0091	0.641	0.0426		0.12855	0.025
200	000	110	221	7107.09284	3.14E-05	1.1651E-21	2.6E-24	134.9016	0.5147	0.0039	0.9549	0.0252		0.10043	0.012
101	000	432	533	7107.84271	2.70E-05	8.4794E-22	1.7E-24	503.9681	0.4092	0.0037	0.6717	0.018		0.11345	0.011
200	000	303	414	7108.71493	2.50E-05	1.6246E-21	2.9E-24	224.8384	0.552	0.0032	0.9758	0.0178		0.12522	0.009
200	000	642	735	7111.22598		3.0861E-23	4.9E-25	816.6942	0.37		0.694				
101	000	717	716	7111.44623	8.21E-05	1.5885E-22	1.0E-24	704.214	0.3886	0.0127	0.7277	0.0506		0.04809	0.039
200	000	322	331	7113.18839		9.7471E-23	1.1E-24	285.2193	0.475		0.694				
101	000	716	735	7113.2918		4.2597E-23	5.0E-25	816.6942	0.394		0.694				
021	000	11210	1029	7113.65622		1.3764E-23	1.4E-25	1293.6337	0.25		0.694				
021	000	744	643	7115.03532		9.4679E-23	5.8E-25	756.7247	0.37		0.694				
200	000	725	734	7115.31214	9.89E-05	1.0671E-22	8.2E-25	842.3565	0.5291	0.0202	0.8189	0.0534		0.17796	0.039
200	000	505	514	7115.48952	5.90E-05	3.6963E-22	1.8E-24	399.4575	0.49	0.0091	0.7486	0.0369		0.16684	0.022
021	000	835	734	7116.06681		7.5585E-23	8.0E-25	842.3565	0.4632	0.0260	0.8407	0.0799		0.18483	0.055
200	000	313	404	7116.19873	5.70E-05	4.393E-22	2.0E-24	222.0528	0.469	0.0079	0.7409	0.0442		0.11911	0.022
021	000	743	642	7116.47652		3.0273E-23	5.4E-25	757.7801	0.36		0.694				
101	000	505	606	7117.24952	1.73E-05	2.1369E-21	2.8E-24	446.6966	0.4516	0.0024	0.7313	0.012		0.10112	0.007
000	000	000	000	0	0.00E+00	0	0.0E+00	0	0	0.0000	0	0	0.00E+00	0.09188	0.000
200	000	414	423	7117.48035	6.52E-05	4.6237E-22	3.0E-24	300.3623	0.45	0.0104	0.5866	0.0424		0.1444	0.025
000	000	000	000	0	0.00E+00	0	0.0E+00	0	0	0.0000	0	0	0.00E+00	0.0924	0.000
200	000	652	743	7118.08869		2.6927E-23	3.8E-25	931.2371	0.395		0.694				
021	000	927	826	7118.67948		1.688E-23	3.3E-25	982.9116	0.41		0.694				
200	000	321	330	7119.81899	9.30E-05	2.3275E-22	1.8E-24	285.4186	0.4604	0.0134	0.8152	0.0716		0.11134	0.037
101	000	827	826	7120.20221		2.0395E-23	3.3E-25	982.9116	0.405		0.694				
101	000	423	524	7120.35728	1.99E-05	1.659E-21	2.4E-24	416.2087	0.4659	0.0026	0.7543	0.0135		0.10913	0.008

200	000	432	523	7121.69417	2.57E-05	9.8637E-22	2.0E-24	446.5107	0.4419	0.0037	0.8123	0.0189			0.1231	0.011	
200	000	651	744	7121.74804		9.1986E-24	4.1E-25	927.7439	0.3		0.694						
200	000	422	431	7121.96966	1.81E-04	1.0776E-22	1.7E-24	383.8425	0.5307	0.0321	0.725	0.1124			0.25299	0.061	
200	000	624	633	7122.481		6.5577E-23	6.8E-25	661.5489	0.42		0.694						
021	000	937	836	7122.55101		4.2368E-23	3.2E-25	1006.1157	0.36		0.694						
200	000	615	624	7122.67553		9.2323E-23	6.5E-25	602.7735	0.45		0.694						
200	000	542	633	7122.73445		4.4626E-23	3.1E-25	661.5489	0.425		0.694						b
200	000	523	532	7123.83445	6.41E-05	2.7994E-22	1.5E-24	508.812	0.4382	0.0095	0.8553	0.0423			0.08964	0.027	
101	000	615	634	7126.01873	7.34E-05	2.012E-22	1.2E-24	648.9787	0.4563	0.0119	0.7941	0.0425			0.11459	0.031	
021	000	652	551	7126.54684		1.0001E-23	5.4E-25	742.073	0.325		0.694						
200	000	202	313	7127.03483	4.51E-05	5.6309E-22	2.1E-24	142.2785	0.4394	0.0061	0.8986	0.046			0.13706	0.018	
021	000	651	550	7127.27788		4.2786E-23	5.3E-25	742.0762	0.254		0.694						
101	000	606	625	7128.01488	5.26E-05	3.2725E-22	1.4E-24	552.9114	0.4491	0.0085	0.668	0.0317			0.19804	0.020	
021	000	12111	11110	7128.96841	3.65E-04	3.5935E-24	1.4E-25	1524.8473	0.281		0.694						
200	000	734	827	7128.97398		2.2982E-23	8.0E-25	885.6002	0.333		0.694						
002	000	542	651	7128.98717		1.8673E-24	6.5E-26	888.6326	0.371		0.694						b
200	000	633	726	7129.30289		2.9695E-23	6.3E-25	709.6082	0.4058	0.0451	1.0336	0.1803				0.144	
002	000	973	982	7129.87645		4.5911E-25	4.3E-27	2009.8051	0.315		0.694						
002	000	972	981	7129.87909		1.379E-24	1.3E-26	2009.8047	0.315		0.694						b
200	000	313	322	7131.94934	1.06E-04	1.9603E-22	1.8E-24	206.3014	0.4333	0.0151	0.7406	0.0972			0.11331	0.042	
101	000	312	331	7132.83906		1.652E-23	9.9E-25	285.2193	0.45		0.694						
101	000	514	533	7133.00491		7.6906E-23	8.6E-25	503.9681	0.475		0.694						
101	000	330	431	7133.90264	2.78E-05	8.6407E-22	1.9E-24	383.8425	0.3973	0.0037	0.6246	0.0211			0.14932	0.011	
101	000	413	432	7134.69536	1.20E-04	1.5732E-22	1.6E-24	382.5169	0.4553	0.0180	0.7603	0.0833			0.12637	0.048	
101	000	331	432	7134.98157	1.60E-05	2.5497E-21	3.3E-24	382.5169	0.4222	0.0019	0.6902	0.012			0.10066	0.007	
200	000	541	634	7135.51501	1.06E-04	1.2692E-22	1.1E-24	648.9787	0.4057	0.0171	0.6611	0.0647			0.15741	0.045	
101	000	1175	1174	7135.62614		5.4771E-25	4.9E-27	2321.905	0.281		0.694						
101	000	321	422	7136.0933	1.83E-05	2.0487E-21	3.0E-24	315.7795	0.4236	0.0022	0.8064	0.0154			0.11108	0.008	
101	000	101	220	7136.8361		6.5343E-23	1.1E-24	136.1639	0.45		0.694						
101	000	937	936	7136.87416	1.12E-04	2.0868E-23	1.6E-25	1282.9188	0.51		0.694						
200	000	532	625	7137.52258	7.31E-05	2.3196E-22	1.4E-24	552.9114	0.4602	0.0114	0.6248	0.0409			0.15379	0.028	
021	000	845	744	7137.68896		1.8079E-23	3.6E-25	927.7439	0.33		0.694						
101	000	616	615	7138.30717	1.40E-04	1.147E-22	1.4E-24	542.9058	0.474	0.0232	0.6542	0.0782			0.18728	0.053	
000	000	000	000	0	0.00E+00	0	0.0E+00	0	0	0.0000	0	0		0.00E+00	0.11062	0.000	
021	000	1028	927	7139.48763		1.6521E-23	1.8E-25	1201.921	0.35		0.694						
000	000	000	000	0	0.00E+00	0	0.0E+00	0	0	0.0000	0	0		0.00E+00	0.1343	0.000	
200	000	404	413	7140.10196	9.38E-05	2.2456E-22	1.7E-24	275.4971	0.4567	0.0126	0.9241	0.0776			0.03839	0.038	
021	000	844	743	7140.77073		5.0314E-23	3.9E-25	931.237	0.41		0.694						
200	000	514	523	7140.87555	4.19E-05	5.6942E-22	2.3E-24	446.5107	0.4849	0.0071	0.8426	0.0273			0.15227	0.016	
200	000	212	303	7140.92654	3.21E-05	1.1593E-21	3.2E-24	136.7617	0.5234	0.0046	0.9982	0.027			0.11062	0.012	
000	000	000	000	0	0.00E+00	0	0.0E+00	0	0	0.0000	0	0		0.00E+00	0.10034	0.000	
200	000	212	221	7142.78656	5.14E-05	5.1873E-22	2.0E-24	134.9016	0.5211	0.0071	0.8326	0.0432			0.10868	0.019	
000	000	000	000	0	0.00E+00	0	0.0E+00	0	0	0.0000	0	0	4.93E-02	0.00E+00	0.13434	0.000	

000	000	000	000	0	0.00E+00	0	0.0E+00	0	0	0.0000	0	0		0.00E+00	0.10592	0.000	
101	000	505	524	7147.73575	1.00E-04	2.1226E-22	1.7E-24	416.2087	0.5969	0.0168	0.5129	0.0459			0.19685	0.033	
111	010	753	752	7149.05801		8.4971E-26	1.2E-27	2724.167	0.352		0.694						
200	000	550	643	7150.26515	2.38E-04	2.3857E-23	5.3E-25	756.7247	0.31		0.694						
101	000	972	973	7150.43505		3.6821E-24	1.1E-26	1810.583	0.315		0.694						
101	000	973	972	7150.47161		1.0585E-23	3.3E-26	1810.5876	0.315		0.694						bcd
101	000	726	725	7150.51269	7.24E-05	1.5698E-22	9.6E-25	782.4098	0.4035	0.0121	1.0722	0.0538			0.00752	0.038	
021	000	752	651	7150.75405		1.4271E-23	3.9E-25	888.6326	0.285		0.694						
002	000	981	990	7150.8044		2.0065E-26	6.6E-27	2225.4182	0.315		0.694						
021	000	753	652	7151.08398		2.6124E-30	8.6E-31	888.5986	0.28		0.694						b
200	000	413	422	7151.99207	6.67E-05	3E-22	1.7E-24	315.7795	0.4474	0.0095	0.9155	0.0562			0.09284	0.027	
200	000	431	524	7152.68315	7.58E-05	1.1869E-22	9.5E-25	416.2087	0.46		0.694						
101	000	881	880	7154.35329		3.7937E-24	1.0E-26	1789.0426	0.333		0.694						
101	000	880	881	7154.35384		1.1378E-23	3.1E-26	1789.0426	0.215		0.694						b
200	000	441	532	7156.72342		1.0573E-22	8.3E-25	508.812	0.39		0.694						
200	000	312	321	7156.81615	5.19E-05	1.0774E-21	2.3E-24	212.1564	0.5206	0.0039	0.9221	0.0228	5.03E-02	2.19E-03	0.18194	0.010	
200	000	211	220	7157.04353	8.71E-05	2.3435E-22	1.7E-24	136.1639	0.4165	0.0111	1.056	0.1079			0.00654	0.037	
200	000	331	422	7157.17342	6.63E-05	1.4252E-22	1.0E-24	315.7795	0.44		0.694						
101	000	871	872	7157.73763		3.3747E-23	5.4E-26	1590.6901	0.304		0.694						
101	000	872	871	7157.74248		1.1259E-23	1.8E-26	1590.6906	0.333		0.694						b
021	000	946	845	7159.2325		2.3258E-23	2.2E-25	1122.7083	0.34		0.694						
200	000	303	312	7160.18685	3.61E-05	1.2021E-21	3.9E-24	173.3658	0.5121	0.0051	0.9287	0.0268			0.14782	0.013	
000	000	000	000	0	0.00E+00	0	0.0E+00	0	0	0.0000	0	0		0.00E+00	0.11517	0.000	
000	000	000	000	0	0.00E+00	0	0.0E+00	0	0	0.0000	0	0		0.00E+00	0.16229	0.000	
200	000	440	533	7161.60359		2.6207E-23	7.6E-25	503.9681	0.34		0.694						
101	000	404	423	7164.07402	3.12E-05	7.9478E-22	1.9E-24	300.3623	0.4694	0.0042	0.8211	0.0244			0.12969	0.012	
200	000	000	111	7164.40342	5.94E-05	3.8661E-22	1.9E-24	37.1371	0.4773	0.0084	1.0006	0.0767			0.122	0.023	
101	000	771	770	7164.90181		3.4635E-23	4.9E-26	1394.8141	0.2		0.694						
101	000	770	771	7164.90199		1.0391E-22	1.5E-25	1394.8141	0.2		0.694						bcdgf
101	000	515	514	7165.21425	3.41E-05	6.4749E-22	1.7E-24	399.4575	0.4941	0.0052	0.7372	0.0226			0.19162	0.012	
000	000	000	000	0	0.00E+00	0	0.0E+00	0	0	0.0000	0	0		0.00E+00	0.14356	0.000	
101	000	836	835	7166.05044		2.1594E-23	2.7E-25	1050.1576	0.37		0.694						
200	000	111	202	7166.71601	9.22E-05	2.1677E-22	1.8E-24	70.0908	0.4454	0.0139	0.5858	0.1085			0.16814	0.035	
101	000	964	963	7167.25845		1.8239E-23	5.3E-26	1631.3831	0.27		0.694						
000	000	000	000	0	0.00E+00	0	0.0E+00	0	0	0.0000	0	0	-1.10E-01	0.00E+00	0.19371	0.000	
021	000	1037	936	7169.21851		1.0542E-23	1.4E-25	1282.9188	0.39		0.694						
111	010	642	643	7169.82584		3.0593E-25	3.7E-27	2398.3816	0.371		0.694						
002	000	707	734	7169.93226	3.27E-03	1.5631E-24	4.4E-25	842.3565	0.352		0.694						
101	000	221	322	7170.2768	1.96E-05	1.9469E-21	3.0E-24	206.3014	0.471	0.0024	0.7856	0.0168			0.16986	0.008	
200	000	330	423	7172.69855	5.89E-05	3.2326E-22	1.6E-24	300.3623	0.4062	0.0082	0.6685	0.0504			0.10814	0.024	
101	000	863	862	7173.77426		2.2383E-23	4.0E-26	1411.6418	0.333		0.694						
101	000	862	863	7173.78056		6.7019E-23	1.2E-25	1411.6113	0.33		0.694						b
021	000	853	752	7173.96018		2.6003E-23	2.6E-25	1059.8353	0.33		0.694						

200	000	202	211	7174.13704	4.05E-05	5.6975E-22	1.9E-24	95.1759	0.4403	0.0057	1.2406	0.0581			0.16675	0.016
101	000	946	945	7175.49242		2.8073E-23	1.2E-25	1360.235	0.375		0.694					
101	000	303	322	7175.98644	7.62E-05	2.6279E-22	1.7E-24	206.3014	0.4531	0.0110	0.9952	0.0798			0.11047	0.030
101	000	625	624	7178.44569	9.92E-05	1.401E-22	1.2E-24	602.7735	0.4706	0.0169	1.0942	0.0701			0.14099	0.043
101	000	762	761	7179.75084	2.26E-05	1.5067E-22	2.6E-25	1216.1945	0.265		0.694					
200	000	321	414	7180.39904	4.18E-05	5.5348E-22	1.8E-24	224.8384	0.4883	0.0060	0.7871	0.0351			0.1548	0.016
120	000	771	762	7181.09959		1.9703E-23	2.4E-25	1216.1897	0.352		0.694					
000	000	000	000	0	0.00E+00	0	0.0E+00	0	0	0.0000	0	0	7.26E-02	0.00E+00	0.21496	0.000
200	000	101	110	7182.2091	4.37E-05	1.5134E-21	2.7E-24	42.3717	0.4531	0.0026	1.0012	0.0263	1.98E-02	2.10E-03	0.08895	0.009
000	000	000	000	0	0.00E+00	0	0.0E+00	0	0	0.0000	0	0	-2.35E-02	0.00E+00	0.16791	0.000
101	000	202	221	7183.01527	5.96E-05	4.1249E-22	2.5E-24	134.9016	0.4794	0.0100	1.0003	0.0635			0.13838	0.023
200	000	523	616	7185.39427		5.9312E-23	9.9E-25	447.2523	0.435		0.694					
101	000	954	955	7185.40077		9.4324E-24	9.5E-26	1474.9803	0.315		0.694					
101	000	660	661	7185.59567	1.28E-05	7.1753E-22	6.9E-25	1045.0577	0.1996	0.0022	0.5535	0.0138			0.16078	0.009
101	000	854	853	7188.1382		3.5841E-23	1.7E-25	1255.9115	0.315		0.694					

11 Appendix: Lineshape Primer

Knowledge of absorption lineshape models and their limitations is vital if one is to perform accurate spectroscopic measurements with modern, high-resolution spectrometers coupled with advanced lineshape profiles. Lineshape models allow us both to use collected spectra to compute system parameters like gas temperature and concentration but also allow us to study the underlying physics present during a collision. However, the extreme flexibility of modern lineshapes often supplies the non-expert user with too many spectroscopic "knobs" to turn. This can lead to erroneous or biased results of either extracted lineshape parameters or gas conditions computed from utilizing the wrong lineshape model or implementing an inappropriate broadening or shifting parameter. For example, self-broadening coefficients extracted with a Voigt profile will be narrower than those extracted with a speed dependent Voigt. If one mixes profiles or lineshape parameters, the prediction of the transition width will be incorrect and yield a biased result. This appendix is designed to give the beginning spectroscopist a primer on the lineshapes in the current literature and important physical mechanisms.

11.1 Voigt Profile

The Voigt profile is the most commonly employed lineshape profile in the spectroscopic community and has been in use for many decades. Because of its ubiquity, it will be discussed in brief here with only details relevant to subsequent discussions presented. The Voigt profile is a convolution of a Gaussian and a Lorentz profile and does not have an analytic solution.

The Gaussian aspect of the profile accounts for the Doppler broadening term that results from absorbing molecules moving with and against the propagation direction of the probe beam from the spectrometer. Molecular velocities are governed by a Maxwell-Boltzmann distribution. The molecule's motion relative to the beam will Doppler-shift the beam frequency from the molecule's perspective. Thus, it will shift the frequency at which the molecule will absorb. The molecules moving towards the beam will absorb slightly blue-shifted light while the molecules moving with the beam will absorb slightly red-shifted light. The profile describing Doppler-broadening is a Gaussian, where the Doppler width is a function of average gas temperature, the mass of the absorber, and the line center of the transition of interest. The computation of the profile width and overall shape is analytic and can be found in many locations including [13,67]. Since Doppler broadening is not pressure dependent, it is most prevalent at low pressures where the pressure dependent collisional width is negligible.

The second part of the Voigt convolution is the contribution of collisions to the lineshape width. Collisions enable the exchange of energy between a broadener and absorber. This energy exchange will increase the uncertainty in energy of a transition thus decreasing its lifetime as per the Heisenberg Uncertainty Principle: $\Delta T \Delta E \geq \hbar/2$. This profile is described with a Lorentzian profile, which is quite simple to compute. However, the effect of collisions on the distribution of energy in a molecule after a collision is extremely difficult or impossible to compute manually so it is measured through experiments or large-scale computer simulations. This effect is encapsulated with the broadening coefficient and is transition, molecule, and broadener specific. The width of a transition will always increase with increasing pressure.

The broadening coefficient,γ, scales linearly with pressure and is the slope of a pressure versus transition width plot, after subtracting the Doppler contribution. With temperature, it scales approximately using a power law, $\gamma(T) = \gamma(296K)(296K/T)^n$, where n is a transition, molecule, and broadener specific exponent. There is still some debate as to the validity of the power law for temperatures <200K, with very light broadeners such as helium or hydrogen, and over larger temperature

ranges of order 1000K. n is usually positive and $0 < n < 1$ though deviations from this using Voigt profiles have been seen for high J" transitions. Despite this, the power law tends to work well for most practical pressures, temperatures, and broadening partners in cases when the correct lineshape model is used, see Chapter 4. For a more in depth discussion on theoretical arguments and limitations of the power law, see [114]. Additionally, during a collision the potential surfaces of each molecule are distorted. This distortion changes the energy level spacing of the molecule and is thus responsible for the first order effect referred to as pressure shift. This effect can shift the transition to a higher or lower frequency depending on the location where the transition is located on the potential surface of the molecule. As pressure increases, the collision frequency increases and the perturbation of the potential surface increases, further shifting the transition. Pressure shift is accounted for with the term $\delta(296K)$. If the spectrum temperature is not room, $\delta(296K)$ can be scaled using the power law mentioned above with a separate exponent, m, that is separate and unique to the transition and broadener. Also a linear scaling over smaller temperature ranges that takes the form: $\delta(T) = \delta(T_o) + (T - T_o)\delta'$, where T is the temperature of interest, T_o is a reference temperature, and δ' is the temperature dependent parameter [12]. For more in depth discussions about the Voigt profile see, [67].

The Voigt lineshape is commonly used because it can be computed with minor computational resources [148] and agrees fairly well with measurements, to within 1-3% at line center for self-broadened transitions and up 10% for foreign transitions. However, as the resolution, SNR, point spacing, and frequency accuracy of spectrometers has improved over the last couple decades, the limitations of the Voigt have become well-known [13]. The most apparent shortcoming of the Voigt is a lineshape narrowing present in many experiments exhibiting peaks that are slightly taller than what is predicted or can be fit using a Voigt. This narrowing is a result of two higher order, semi-coupled physical mechanisms known as Dicke narrowing and speed dependence (both discussed below) that are knowingly not accounted for in the Voigt formalization.

11.2 Speed Dependence

Speed dependence is considered a refinement of Lorentzian broadening and accounts for how the coupling of energy between a broadener and absorber depends on their relative collision speeds. In a gas, the speed of molecules is described by a Maxwell-Boltzmann distribution. In this distribution, slower moving molecules collide with other molecules less frequently than faster moving molecules. Since there are more slowly moving molecules than faster moving molecules in a Maxwell-Boltzmann distribution, a larger fraction of the distribution is allowed to stay in its excited states for longer durations of time. An increased lifetime,ΔT, therefore corresponds to an decreased uncertainty in the energy of that state, ΔE. In the frequency domain, this manifests as a slightly taller peak with correspondingly narrowed width. This effect is usually of order 1-3% at line center and is especially present for molecules with large dipole moments since the radius at which molecules are affected by passing molecules, and thus their associated speeds, is increased. Once these various speed classes are included into the Lorentzian broadening derivation (see [122,123] for details), hypergeometric solutions are required for each transition and velocity class. This has been deemed too computationally expensive so a quadratic approximation for the effect of various velocity classes is favored [13,127,130].

Inclusion of speed dependence in this effect also results in a second-order speed-dependent shifting term, typically referred to as Δ_2, which represents the additional perturbation to the potential surface due to the velocity of collisions. This shifting term is usually small and neglected since the uncertainties in experiments often dominate this effect [130,149–151].

If possible, speed dependence should be included in all fits where Lorentz broadening is significant. It is typically more pronounced in systems with broadener/absorber pairs that have dissimilar rotational energy spacing and is usually stronger for higher J" transitions in those systems. This is because the relative speed of the colliding molecules, and thus energy transferred, governs which transitions are accessible due to the added energy of the faster moving molecules [14]. For pure mixtures, this is not generally the case since rotational transitions are always resonant with an identical molecule so the speed dependence contribution is more constant for all transitions.

The general formulation of the speed dependence treats the speed dependent broadening term, its temperature dependence, the speed dependent shift term, and its temperature dependence all as unique parameters to be extracted in a fit [13]. This type of complex fitting often requires exceptionally large SNR values in the data; it is more robust to fit the parameterized formulation stated in Section 4.3 [136]. The temperature dependence of the speed dependent broadening term is typically incorporated as a power law similar to the collisional broadening dependence mentioned above. The general theory allows for separate n values for both γ_o and γ_2 though the parameterization in Section 4.3 constrains these exponents to be identical, which yields a more robust fitting function.

11.3 Dicke (Confinement) Narrowing: Rautian & Galatry Profiles

The second, higher order broadening effect that narrows transitions and is unaccounted for in the Voigt profile is known as Dicke or confinement narrowing [93]. The Galatry [152] and Rautian [95] (or Nelkin-Ghatak [153]) lineshapes are the two most common profiles that account for this effect though they arrive at the same result of inclusion of a frequency of velocity changing collisions term, ν_{vc}, with different methods. The Galatry profile arrives at this term using a soft collision argument that states that the mass of the absorber is far larger than that of the perturber so it requires many collisions to change the velocity of the absorber. Conversely, the hard collision model, known as the Rautian profile, arrives at the ν_{vc} term by assuming that the absorber has far less mass than the perturber so the collision is sufficiently strong to remove any memory of its previous velocity. The subsequent velocity of the absorber then follows a Maxwell-Boltzmann distribution [13,95].

Dicke narrowing becomes less relevant with increasing pressures since collisional effects dominate the width of transitions. Above approximately 100 Torr, speed-dependence then becomes the dominant narrowing mechanism [94,117]. Dicke narrowing typically occurs when the molecular mean free path is similar to the wavelength of incident, absorbed radiation. In this case, during the lifetime of a transition, the molecule will undergo many collisions that change its velocity. This change in velocity manifests as velocity averaging, which results in a Doppler-shifted velocity nearer to zero. This will narrow the Doppler width. This means that if Doppler broadening is significant for a transition, the transition will narrow and its peak height will increase. At higher pressures, the effect of collisional broadening dominates this effect, so speed dependence is usually the dominant narrowing mechanism. Dicke narrowing is a transition independent process since it is based entirely on kinetic arguments and can be approximately calculated based on the diffusion coefficient of the mixture [13,109].

11.4 Hartman-Tran Profile

Speed dependence and Dicke narrowing are not completely independent processes. As expected, the speed at which molecules collide affects how much their velocities are changed thus coupling the mechanisms. Therefore, the standard profile to incorporate both of these mechanisms along with a correlation parameter η between the two is called the Hartmann-Tran profile [13]. It is the current standard in the field of advanced spectroscopy and lineshape physics studies and its full name is "the

partially correlated quadratic speed-dependent hard collision profile", though it is called the Hartmann-Tran profile in most work. The profile incorporates more physical broadening and shifting mechanisms than are currently required by most spectroscopists to fit spectra to spectrometer noise but was designed to be future-proof as the community advances. It is easily simplified to less complicated profiles and can be computed using two complex Voigt probability calculations [154] with far more details about the profile available in [13].

When the above correlation parameter is set to zero, the Hartmann-Tran profile reduces to the quadratic speed-dependent Rautian profile. Upon exclusion of speed dependence or the Dicke narrowing term, it will further reduce to the Rautian or speed-dependent Voigt, respectively. With all higher order terms zeroed, the Hartmann-Tran profile reduces to the Voigt. Currently, most advanced experimental work is utilizing some simplified form of this profile because of the difficulty in constraining the correlation parameter and reliably separating spectral narrowing due to Dicke-narrowing versus speed-dependence. Often the types of experiments that are able to separate these mechanisms have SNR of >10,000 and are either cavity ring down systems or highly stabilized diode experiments, see previously referenced work in Chapters 4 and 5. In the case of not being able to constrain either Dicke-narrowing or speed-dependence to a known or specifically chosen value, the two parameters should not be fit simultaneously.

As noted in [13], one must take caution when using all the options afforded by the Hartmann-Tran profile. The researchers saw that the values extracted for ν_{vc} were non physical for the HTP and should be regarded as only useful fit parameters. Since parameters like speed dependent broadening necessarily impacts the mean relaxation rate (collisional broadening), one cannot employ parameters extracted with one profile in another regardless of whether or not the profile is increasing or decreasing in complexity. The simplest example of this is speed dependence. Since the γ_2 term is a narrowing term, the γ_o values extracted with the SDV, or a more complex profile utilizing speed dependence, will most likely be larger than those extracted with a Voigt profile. Therefore, use of Voigt profile parameters in a SDV fit, or vice versa, would yield incorrect calculations of the width of the transition. This argument extends to all variations of the profile complexity ladder in that one cannot climb or descend it and interchange parameters.

Finally, the highly correlated nature of the parameters in all advanced profiles beyond the Voigt means that multispectral fitting is required to extract useful spectral information [103]. This fitting technique leverages the physics of the lineshape model in use to extract subtle narrowing or asymmetric effects that would be over-fit with classic single spectrum techniques.